A Thesis Submitted for the Degree of PhD at the University of Warwick

http://go.warwick.ac.uk/wrap/57917

Lubricated Contact Analysis of a Spur Gear Pair with Dynamic Loads

by

Huaiju Liu

A thesis submitted in partial fulfilment of the requirements for the
degree of
Doctor of Philosophy in Mechanical Engineering

School of Engineering, University of Warwick
April 2013

Contents

List of Figures

List of Tables

Acknowledgement

I would like to take this opportunity to acknowledge the help and contribution of the following people and organizations:

Special thanks gives to my PhD supervisor, Dr Ken Mao. Without his kind guidance, this work cannot be finished.

I appreciate the financial support from China Scholarship Council and School of Engineering, University of Warwick.

I had a great time in Coventry with my friends Zhongnan Wang, Guanhua Zhang, Jinghan Zeng, Jiaxuan Du, Xinyao Zhu, Yiming Zhang, Yi Ding, Chunzhi Ju, Lei Wang et al.

I appreciate teachers and friends in Chongqing University, China very much during my PhD period. Thanks goes to Professor Caichao Zhu, Dr Xiangyang Xu, Dr Mingyong Liu, and all my other lovely friends.

I appreciate all the necessary support such as computer technique support, essential software access like Abaqus, Matlab, Endnote, Mathtype, etc., provided by School of Engineering, University of Warwick.

Dr CH Venner from University of Twente, Netherland, and Dr CJ Hooke from University of Birmingham, UK helped me a lot on tribology knowledge.

I love my parents.

Declarations

This is to certify that the work submitted here was carried out by the candidate Huaiju Liu and it has not been submitted for a degree at another university. The work presented in this thesis is original work carried out by the author.

Candidate’s signature and date:

Abstract

In the present research study, a comprehensive spur gear lubrication analysis has been carried out to understand the gear contact behaviour under lubrication conditions. The modelling works have been extended to consider the effects of thermal mechanical, non-Newtonian fluid, surface roughness, transient squeeze and dynamic load conditions.

First, the elastohydrodynamic lubrication theory is studied and relevant numerical approaches are introduced. The reduced Reynolds equation technique is applied to deal with any potential "asperity contacts" or any other ultra-thin film situations. Those situations could be a result of the surface roughness or the dynamic load effect. This approach allows us to capture local information about pressure, traction, film thickness, etc., within the nominal contact zone. Influence of working conditions, i.e. load, rolling speed, as well as the sliding to roll ratio are discussed with those models (Newtonian or non-Newtonian fluids, isothermal or thermal conditions). The non-Newtonian fluid effect has been investigated with a Ree-Eyring fluid model and a power-law fluid model and the thermal effect is studied by solving energy equations of interacting solids and the film numerically with the sequential sweeping technique.

The dynamic effect on contact performance is also studied. The dynamic load is calculated using a two degree-of-freedom lumped parameter system dynamic model in which the varying mesh stiffness is considered as the excitation. The dynamic model is solved using the Runge-Kutta method. The effects of the dynamic load effect on pressure distribution and film thickness in a whole mesh period are discussed. The normal contact stiffness of a spur gear pair is also predicted based on the deterministic tribology models.

The main contributions from the present research could be summarized as

follows:

i. An elastohydrodynamic lubrication model for a spur gear pair is developed by taking into account the effects of transient squeeze, the non-Newtonian fluid, the rough surface and the thermal mechanical contacts which makes the proposed model one of the most advanced models currently evaluating gear lubrication performance. This model can also be applied to bearings, cams, or other gear types with some modifications.

ii. The friction behaviour, which is not investigated as extensively as the film thickness in existing work, is studied. The effects of the working conditions (the load, the rolling speed, the slide/roll ratio), the non-Newtonian conditions, the rough surface conditions, as well as the thermal conditions on friction behaviour are discussed. The conclusions suggest controlling surface topography patterns and working conditions aiming at a reduced friction coefficient and a longer service life.

iii. The dynamic effect on lubrication performance and effect of lubrication on normal contact stiffness of a spur gear pair are studied. The work provides a potential gateway for a more comprehensive evaluation of spur gear pair working performance using a tribology-dynamic coupled method which is the next area this author would like to explore.

Abbreviations

LOA	Line of action
BC	Boundary condition
LPSTC	The lowest point of single tooth contact
HPSTC	The highest point of single tooth contact
DF	Dynamic factor
DTE	Dynamic transmission error
EHL	Elastohydrodynamic lubrication
DOF	Degree-of-freedom
SAP	Start of active profile along the line of action
RMS	Root mean square
FEM	Finite element method
CFD	Computational fluid dynamics

Nomenclature

a, b	two solid surfaces contacting with each other
Amp	the dimensionless amplitude of sinusoidal waviness on surfaces
b	the half Hertzian contact width
b	the gear backlash, m
B	the width of the gear tooth
c	the gear tooth damping factor, Ns/m
d_m	the mean deformation within the nominal contact zone
$d_{\max}$	the maximum deformation within the nominal contact zone
E'	the equivalent elastic modulus, Pa
E_1, E_2	the elastic modulus of the two solids, Pa
F_s	the static load carried only by one gear pair
G	the dimensionless material parameter, $G = \alpha E'$
h	the film thickness or the gap, m
h_0	the rigid body displacement, m
h_x	the grid mesh size in x direction
k	the gear mesh stiffness, N/m
k_c	the gear normal contact stiffness, N/m
H	the dimensionless film thickness or dimensionless gap, $H = hR/b^2$
H_0	the dimensionless rigid body displacement, $H_0 = h_0 R/b^2$
I_1, I_2	the rotational inertia of the pinion and the wheel, respectively
i, k	the grid indices in x and z direction, $i \in [0, n_x]$, $k \in [0, n_z]$
i_g	the gear ratio

K	the kernel for contribution to the elastic deformation
L	the Moes dimensionless speed parameter, $L = G(2U)^{1/4}$
M	the Moes dimensionless load parameter, $M = W(2U)^{-1/2}$
m	the module of the gear pair
m	the power law viscosity index
m_e	the equivalent mass of the lumped parameter system
n	the number of grid points in a direction
n_1, n_2	the rotation speed of the pinion and the wheel, respectively, unit $r/\min$
N_1, N_2	the tooth number of the pinion and the wheel, respectively
n_d	the number of node pairs with a non-zero elastic deformation
n_x	the number of grid points in x direction
n_z	the number of grid points in z direction
n_T	the number of discretized points along the line of action
p_b	the transverse base pitch of the gear
p_H	the Hertzian maximum pressure
p_n	the normal base pitch
P	the dimensionless pressure, $P = p / p_H$
r_{b1}, r_{b2}	the base circle of the pinion and the wheel, respectively
rr	the surface roughness, m
RR	the dimensionless surface roughness, $RR = rrR / b^2$
R_1, R_2	the radius of the two solids, m
R	the equivalent radius, m
R_1, R_2	the radii of the two interacting subjects, respectively

R_q	the root mean square value of surface roughness height, m
R_{qa}, R_{qb}	the root mean square value of two solids' surface roughness height m
s	the viscosity-temperature factor
sr	slide/roll ratio, $sr = u_s / u_r$
S	the viscosity modifying factor for the non-Newtonian fluid
t	the time, s
T	the temperature, $^\circ C$
T_1, T_2	torque of the pinion and the wheel, respectively, Nm
$\bar{t}$	the dimensionless time
$\overline{T}$	the dimensionless temperature
w	the general under-relaxation factor
u	the velocity of the flow, m / s
u_1, u_2	velocity of the lower surface and the upper surface, respectively, m / s
u_r	the rolling velocity m / s
u_s	the sliding velocity, m / s
$\bar{u}$	the dimensionless speed, $\bar{u} = u / u_r$
U	the dimensionless speed parameter, $U = (\eta_0 u_r) / (E' R)$
W	the load per length
W	the dimensionless load parameter, $W = F / (E' R)$
Wav	the dimensionless wavelength of sinusoidal waviness on surfaces
x, y, z	the coordinates, x represents the flow direction, z represents the direction across the film, y represents the direction normal to x and z direction.
X, Y, Z	the dimensionless coordinates, $X = x / b$, $Z = z / h$

z	the pressure-viscosity index
z	the length of the line of action (LOA) of the gear pair
α	the pressure viscosity index, Pa^{-1}
θ_1, θ_2	the rotation angle of the pinion and the wheel, respectively
β	the viscosity-temperature factor
τ_1	the principal shear stress in the subsurface field
τ_{1m}	the maximum shear stress in the subsurface field
σ_x	the principal stress along x direction
σ_z	the principal stress along z direction
δ	the elastic deformation, m
η_0	the viscosity of ambient pressure, Pas
η	viscosity with Newtonian fluid, Pas
η_x	the equivalent viscosity with non-Newtonian fluid, Pas
$\overline{\eta}$	the dimensionless viscosity, $\overline{\eta} = \eta / \eta_0$
$\overline{\lambda}$	the dimensionless parameter in Reynolds equation, $\overline{\lambda} = (12 u_r \eta_0 R^2) / (b^3 p_H)$
$\overline{\varepsilon}$	the dimensionless parameter in Reynolds equation, $\overline{\varepsilon} = \overline{\rho} H^3 / (\overline{\eta} \overline{\lambda})$
ρ	the density of the lubricant, kg / m^3
ρ_0	the density of the lubricant at ambient pressure, kg / m^3
$\overline{\rho}$	the dimensionless density, $\overline{\rho} = \rho / \rho_0$
σ_y	the third principal stress in subsurface field, Pa
τ	the shear stress in the film, Pa
μ	the friction coefficient, $\mu = F / W$
F	the total traction, N

τ the shear stress in the film, Pa

$\bar{\tau}$ the dimensionless shear stress, $\bar{\tau} = \tau / p_H$

τ_0 the Ree-Eyring stress, Pa

τ_1 the shear stress on the interface between the film and the surface of the lower solid, Pa

$\bar{\tau}_1$ the dimensionless form of τ_1, $\bar{\tau}_1 = \tau_1 / p_H$

$\bar{\tau}_0$ the dimensionless Ree-Eyring stress, $\bar{\tau}_0 = \tau_0 / p_H$

υ_1, υ_2 the Poisson ratio of the two solids

λ the lambda ratio, $\lambda = h / \sqrt{R_{q1}^2 + R_{q2}^2}$

Chapter 1 Introduction

1.1. Background

Spur gear drives are extensively used in industries such as the automobile industry, the wind power industry, and others. Mainly, there are two research topics about gear working performance which draw much attention from engineers and researchers: one is the contact (including lubrication) performance of engaging gear teeth and the other is the dynamic behaviour of gear drives. The first determines the tooth surface failures which commonly occur in gear drives, and the latter determines the vibration and noise of the system which influences the service life and the comfortableness. Currently there is little work focusing on the coupling effect of contact performance and dynamic performance of a gear pair. In this work the contact performance, mainly lubricated contact performance of a spur gear pair, and effect of dynamic behaviour on contact performance of a spur gear pair are investigated. This topic is chosen as the subject of this thesis for the following reasons:

i. Gear drives transmit power and movement through the contacting behaviour between teeth of the pinion and the wheel. If the contact performance of a gear pair is not acceptable, it is probable that the service life would be shorted owing to premature surface failures and low transmission accuracy. A complete contact analysis would be the prerequisite for a further surface failure analysis.

ii. Theoretically, solving contact problems, especially lubricated contact problems in which surface roughness effects and thermal effects are considered, requires more advanced algorithms and more computation costs to deal with real contact problems. There is still a long way to go towards developing a more advanced contact model which is accurate enough and requires acceptable computational time. For several decades, the elastohydrodynamic lubrication (EHL) problem, which applies if a spur gear pair is lubricated adequately, has been believed to be one of the most difficult one to handle in the area of tribology. If it reaches to the mixed lubrication situation, which often occurs in gear drives owing to the roughness effect or severe operating conditions such as ultra-low speeds or ultra-heavy loads, the problem becomes even more complicated. Currently, some models are developed to handle mixed lubrication problems, however, a complete, efficient, and physically-meaningful model is yet to be developed. In addition, non-Newtonian effects and thermal effects on lubrication performance of gear pairs also require deep investigation.

iii. Gear drives often experience some dynamic behaviours which would affect the load carried by the engaging gear pairs. This effect will be more evident if the working frequency (meshing frequency) is close to the natural frequency of the system or its harmonic components. The dynamic load effect is assumed to cause significant variation for the film thickness, friction, etc. Also, the lubricated contact performance of the gear pair affects the dynamic performance through the meshing stiffness, transmission error, tooth friction and meshing damping.

Gear tooth contacts have been recognized as one of the most complicated and important applications in the field of tribology. Before conducting a gear contact analysis, several typical characters of gear drives should be recognized first. Gear parameters such as the contact radius, the rolling speed, the slide/roll ratio, and others, all vary during the meshing process, which makes the geometries and the kinematics of gear pairs more complicated than those of rolling bearings. Furthermore, since the contact ratio is not always an integer, the load carried by a gear pair will suddenly change when the meshing makes a transition from the double-gear-pair-engaging zone to the single-gear-pair-engaging zone, or from the single-gear-pair-engaging zone to the double-gear-pair-engaging zone.

Gear tooth contacts are classical forms of non-conformal contacts. That means a small portion on the tooth profile will undertake the load which will lead to high pressures in the contact area. In a lubrication case, high pressures will cause two distinct characteristics: a rapid increase of the fluid viscosity and considerable elastic deformations of tooth surfaces within the nominal contact zone. For a hydrodynamic lubrication (HL) problem, if the two factors are ignored, the predicted film thickness will be too small to maintain a film between two surfaces. It was reported that when the main propulsion gears of the transatlantic linerm the ‘Queen Mary’ were examined after eleven years’ operation, “no wear could be detected on the gear teeth” [1]. With the development of EHL theory, it is now possible to explain the existence of a film between concentrated contacts like the gear tooth contacts.

When dealing with rolling element bearings, it is feasible to ignore the surface topography since finely finished surfaces are used and the amplitude of the surface roughness is small enough compared with the film thickness. Surface roughness will not affect the pressure distribution and the film thickness profile within the nominal contact zone significantly. However, as for gears, the manufacturing processes currently employed tend to leave relatively rough surfaces on gear teeth so that the amplitude of roughness is comparable with film thickness. As a gear meshes with its counterpart, it is possible to make direct asperity contacts happen, or at least cause ultra-thin film at local areas within the nominal Hertzian contact. For a gear lubrication analysis, a model should be able to handle ultra-thin film situations. Fortunately there exist some methods to deal with this which will be introduced in the literature review in detail.

1.2. Objective and Layout of the Thesis

The objectives of the thesis can be summarized into three aspects. First, the working conditions (the load, the speed, the slide/roll ratio) effects, the non-Newtonian effects, surface topography effects and the thermal effects on pressure distribution, film thickness and friction coefficient are studied in detail through a line contact model. Second, a comprehensive lubricated contact analysis of a spur gear pair is proposed based upon the developed mixed lubrication line contact model which incorporates thermal effects, transient squeeze effects, and non-Newtonian effects. Third, this work tries to develop a coupled tribological-dynamic gear model. This objective will be conducted from two works: one is the study of dynamic load effects on the lubrication performance of an engaging gear pair, and the other is the study of effects of contact/lubrication conditions of a gear pair on contact stiffness. To achieve those research objectives, knowledge on contact mechanics, lubrication mechanics, fluid rheology, thermodynamics, and system dynamics should be synthetically used and problems should be solved systematically. A general technique route of this work is depicted in Fig. 1.1.

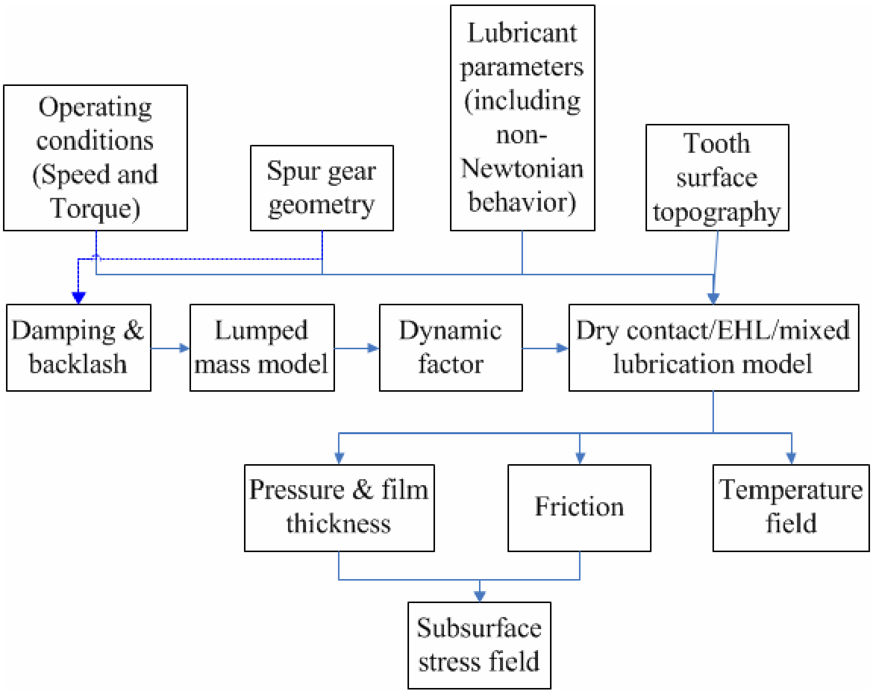

Fig. 1.1 Flow chart of this work

The choices of modelling approach, structural steps, and software strategy are described here. For the numerical modelling of dry contact problems and classical

EHL problems, the distributed relaxation scheme and the hybrid relaxation scheme, introduced by Venner and Lubrecht [2], are used respectively. The generalized Reynolds equation, proposed by Yang et al. [3] is applied for taking the non-Newtonian constitutive equations into the Reynolds equation easily. The reduced Reynolds technique, proposed by Hu and Zhu [4], is used to deal with any potential "asperity contact" within the nominal contact zone which would be caused by surface roughness or a sudden working situation change. For thermal elastohydrodynamic lubrication (TEHL) problems, the temperature field within the solids and the film are calculated by solving energy equations of the solids and the film numerically. A lumped parameter model is developed to predict the dynamic load of a spur gear pair. The mesh stiffness variation is taken as the exclusive excitation of the dynamic system. The Runge–Kutta iterative method is used for solving the dynamic equations of the system with the aid of Matlab. The whole contact/lubrication model is implemented in the C++ frame.

In Chapter 2, a literature review illuminates the development of the lubrication theories and the applications of those theories on gear drives. The highlights of the current proposed model are outlined.

Chapter 3 mainly illuminates the dry contact theory and the classical EHL theory and relevant numerical models. A dry contact model is developed based upon the influential coefficient method which is solved through direct summation since for a line contact problem the calculation cost is acceptable with available computer resources. Essential notices about the multigrid method, used to speed up the convergence process, are presented.

Chapter 4 introduces non-Newtonian effects by deriving lubrication models for the Ree-Eyring fluid and the power-law fluid. The effects of the characteristic Eyring stress for the Ree-Eyring fluid and the effects of power index for the power-law fluid are introduced. The results are compared with Newtonian-based solutions.

Chapter 5 mainly introduces the rough surface EHL and mixed lubrication problems. Rough surfaces may cause asperity contacts within the nominal Hertzian contact zone. The reduced Reynolds technique is applied to handle ultra-thin lubrication problems or mixed lubrication problems. First, regular sinusoidal wavinesses are assumed on contacting surfaces to investigate their wavelength and amplitude on lubrication performance. Second, digitalized surface roughnesses which follow Gaussian distribution, are generated to study the effect of the root mean square (RMS) value of surface roughness.

Chapter 6 studies the thermal effects on the pressure profile and the film thickness, as well as the traction using the developed TEHL model. The energy equation and the Reynolds equation are iteratively solved. With the help of the sequential sweeping technique, energy equations are solved for the solids and the film.

Chapter 7 applies the proposed model in a spur-gear-pair application and its lubrication performance in a whole meshing period is evaluated by getting the pressure distribution, traction, film thickness, and the temperature field at each discretized location along the line of action (LOA).

Chapter 8 studies the effects of the dynamic behaviour of the chosen spur gear pair on its lubrication performance. Dynamic loads are calculated through a two-degree-of-freedom (DOF) dynamic model.

Chapter 9 investigates the normal contact stiffness of a spur gear pair based on the deterministic dry contact model and the EHL model.

Chapter 10 offers the main conclusions of this work and recommendations for future work.

Parts of this thesis work have been published by the author and coworkers [5-7].

Chapter 2 Literature Review

The chapter contains a literature review on the development of contact theory and lubrication theory, and existing gear lubrication analysis. Research on non-Newtonian effects, thermal effects, surface roughness effects, and others, on lubrication and contact performance are introduced. A review on gear lubrication theoretical analysis is also presented. Based on this review, highlights of this work are emphasized.

2.1. Contact Theory and Lubrication Theory

When lubrication is not applied between interacting contact surfaces owing to the working environment requirement, a dry contact situation occurs. Dry contact studies emerged earlier than lubrication studies and relevant work should be introduced back from Hertz's work.

2.1.1. Dry Contact Theory

Based upon some assumptions, Hertz [8] presented the first analytical solution for contact problems. Hertz was attempting to understand how the optical properties of multiple, stacked lenses might change with the force holding them together. Hertzian contact stress refers to the localized stresses that develop as two curved surfaces come into contact and deform slightly under the imposed loads. The amount of deformation is dependent on the modulus of elasticity of the material in contact. It gives the contact stress as a function of the normal contact force, the radii of curvature of both bodies and the modulus of elasticity of both bodies. Hertzian contact stress forms the foundation for the equations of load bearing capabilities and fatigue life in bearings, gears, and any other bodies where two surfaces are in contact. Until now, the Hertz solution has often been used in engineering practice owing to its simple form. Hertz opened the door for a systematic subject called “contact mechanics”. The physical and mathematical formulation of the subject of contact mechanics is based upon the mechanics of materials and continuum mechanics and focuses on computations involving elastic, viscoelastic, and plastic bodies in static or dynamic contact. The central aspects in contact mechanics are the pressures and adhesion acting perpendicular to the contacting bodies' surfaces, the normal direction, and the frictional stresses acting tangentially between the surfaces.

Since Hertz, the development of contact mechanics mainly focuses on eliminating assumptions made by Hertz, such as removing the friction between interacting surfaces. Bowden and Tabor [9] were the first to study the effects of surface roughness on bodies in contact. Through the investigation of the surface roughness, the true contact area between friction partners is found to be less than the apparent contact area. Such understanding also drastically changed the direction of undertakings in tribology. The works of Bowden and Tabor yielded several theories in contact mechanics of rough surfaces. Archard’s work [10] should also be mentioned because he concluded that even for rough elastic surfaces, the contact area is approximately proportional to the normal force. This work was followed by Greenwood and Williamson [11] and others. In the 1970s, Johnson et al. [12], among others, proposed their adhesive elastic contact model. The work by Greenwood and coworkers [13] is used for reference for EHL researchers studying statistical rough surface EHL models, which will be mentioned later.

In the early days, owing to the limit of computation ability, researchers used statistical models [14, 15] as the main tool to study rough surface contact problems. However, statistical models ignore the interaction between neighboring asperity micro-contacts, which becomes prominent at high contact loads [16]. Additionally, those models cannot represent the essentially multiscale nature of surface roughness

[17]. Despite some work [18] which also took the multiscale nature of roughness into account, the asperity interaction effects are nevertheless neglected.

It is fair to argue that if the real surface topography is explicitly considered in the model, the problem occurring in statistical models would disappear. As the development of computer technology progressed, more work focused on the deterministic models, such as work done by Lai and Cheng [19]. Among those numerical methods, two advanced algorithms should be emphasized: the multi-level multi-integration (MLMI) method [20], and the FFT-based method [21, 22]. The MLMI and FFT-based methods have their own advantages and both of them could save computation time significantly compared with the direct summation method.

2.1.2. Elastohydrodynamic Lubrication (EHL)

EHL problems refer to those hydrodynamic lubrication cases in which the viscosity-pressure effect and the elastic deformations of solid surfaces cannot be neglected. This kind of lubrication may occur in gears, bearings, cam drives, etc. Even though researchers agree that the most popular state for gear drives and other components is the mixed lubrication, it is necessary to study the mechanism of EHL to understand mixed lubrication. EHL has been studied extensively since the 1950s, both theoretically and experimentally, and many achievements have been obtained. For example, several empirical formulas of minimum film thickness are developed which are quite useful for engineering practice. However, there is still a great deal of work yet to be done to consider the real fluid rheology behaviours or the relationship between lubricated contact conditions and surface failure behaviours, and other aspects. The development of easy calculation tools is required so that engineers can evaluate lubrication performance more quickly.

Owing to the advanced algorithms and rapid development of computer ability, numerical models and related approaches provide an effective way to study the successful operation mechanism of EHL, as well as failure analyses of EHL. There are many numerical methods which are able to solve EHL problems: the inverse method, the direct method, the Finite Element Method (FEM) [23], the Computer Fluid Dynamics (CFD) method [24], and the multigrid method [25], amongst others. Until now, the multigrid method is believed to be one of the “standard” methods for EHL problems, which is also applied in this work.

2.1.3. Non-Newtonian Behaviour

Rigorously speaking, every lubricant would represent the non-Newtonian behaviour in practice. That is, more or less, the relationship between the shear rate and the shear stress deviates from the linear line, which is the case for a Newtonian fluid. In the early days of EHL studies, a Newtonian fluid is often assumed owing to its simple and straightforward constitutional expression. This is fair when evaluating the minimum film thickness with the Newtonian assumption because people realize that it is the inlet zone condition of the contact region that determines the minimum film thickness the most, whereas non-Newtonian behaviours may affect the film thickness in a more limited way [26]. However, the Newtonian-based solution would overestimate the friction coefficient between the interacting surfaces.

Evans [27] presents four types of friction curves which depend on the rheological behaviour of the lubricant. These curves usually present three distinct regions. In the first part, limited by low shear rates, the shear stress varies linearly with the shear rate, so the lubricant behaves as a Newtonian fluid. In the second region the shear stress deviates from the linear curve at higher shear rates; it increases less rapidly because of non-Newtonian behaviour. Eventually, at even higher shear rates, thermal effects cause a reduction in viscosity, and thus also in the friction. This implies a reduction of the shear stresses. The slope of the linear part of the curves can be described adequately by the viscous Newtonian behaviour of the lubricant. The coefficient of viscosity is given by the viscosity-pressure relation according to Roelands, provided the pressure is not too high. At higher pressures the lubricant starts to behave as a visco-elastic and eventually as an elastic solid material.

Shear-thinning is only a single aspect of non-Newtonian response. Shear-thinning is accompanied by normal stress differences in the principal shear directions. In particular, an extra tensile stress will appear in the direction of motion, which may augment the load capacity of a bearing [28], although the relative improvement has been debated.

Researchers proposed many rheology models to describe the shear behaviour of fluids, such as the Ree-Eyring model, the power-law model, the Johnson-Tevaarwerk model [29], and others. In the following, the Ree-Eyring model and the power-law model are introduced：

i. Ree-Eyring model: The constitutive equation is, in fact, the sinh-law which was mistakenly assumed to be constitutive by Henry Eyring in 1936 [30]. Eyring recognized his error. The constitutive equation accurately describes the thermal reduction of viscosity owing to viscous heating in Poiseuille flow, and is not a description of shear-thinning. The real Ree-Eyring equation was introduced in a series of papers [31, 32] in the 1950s in the Journal of Applied Physics in which many real examples of its use were presented. Among those, the Ree-Eyring model is recommended by many researchers [29, 33, 34] for traction studies and is applied extensively [5, 35, 36] for lubrication performance studies of, for example, gears and cams. The advantage of the Ree-Eyring equation lies in its ability to describe accurately the complex behaviour of mixtures [37].

ii. Power-law model: Compared with those Ree-Eyring literatures, work performed with a power-law fluid assumption is less. Some researchers [38] recommended that for shear stress greater than some critical value, the relationship between viscosity and rate or stress is best described by a power law. Bhattacharjee and Das [39] considered a general solution including EHL for different values of power law exponent. Chu et al. [40] derived a modified Reynolds equation for power-law fluids from the viscous adsorption theory. Recently, Chu et al. [41] analyzed the coupled effects of surface roughness and flow rheology for a homogeneous mixture of Newtonian base oil and power law fluids on EHL performance. However, in Ref. [40] and [41] a particular complicated Reynolds equation is derived which is difficult to modify for a traction study of other rheology models.

2.1.4. Thermal EHL (TEHL)

TEHL theory deals with thermal phenomena in EHL contacts, such as temperature distribution inside solids and the film, a thermal effect on traction and film profile, and other phenomena. A thermal effect within the contact causes frictional heat and may lead to surface failures owing to the film failure. Even though currently a full understanding about this thermal effect on surface failures is not available, it is confirmed that the thermal effect is worth noticing, and in fact, significant achievements on this subject have been obtained [42, 43].

Chang et al. [44] concluded that there are several types of approaches to solve thermal EHL problems:

i. The simplest approach is based upon the concept of “effective viscosity”, which is obtained at the average cross film temperature. The effective viscosity is employed in a generalized Reynolds equation which retains some integral expressions to accommodate the viscosity variation in the transverse direction of the oil film. This approach was used by Chang [45] and others.

ii. A complete model uses discretized energy equations so that the whole temperature field can be calculated. This approach, of course, increases computational costs. Further difficulties appear owing to the instabilities that are initiated when a reverse flow appears at the entrance of the oil film. This approach was used by Yang et al. [46, 47], Sadeghi et al. [48, 49], and others.

iii. The temperature is assumed to have a parabolic variation across the oil film. The quadratic temperature expression is inserted into the energy equation which is next integrated analytically across the film. This approach was used by Salehizadeh and Saka [50] and by Wang et al. [51] and others;

iv. Elrod and Brewe [52] realized that the regular numerical solutions of the full thermal distribution within the flow field are costly and they proposed an alternate approach based on the Labatto points interpolation. This approach was first limited to inlet zone analysis with incompressible lubricants [53]. Moraru then applied this approach to compressible lubricants applications [54].

As the computer technology develops rapidly, it is more reasonable to use the complete numerical model in which energy equations are solved, since this kind of model predicts the most accurate results for the temperature field. In this work this approach is applied.

Several thermal reduction factor formulae [53, 55, 56] are proposed based on numerical or analytical or experimental solutions to help engineers gather a quick consideration of thermal effects in engineering practice.

2.1.5. Rough Surface EHL and Mixed Lubrication

For many components such as gears, the surface topography has a significant influence on EHL performance, especially when the RMS value of the surface is comparable to the film thickness. In this case, direct metal-to-metal contact may occur within the nominal Hertzian contact zone. This situation is referred to as the mixed lubrication. The concept of mixed lubrication first appeared at the proceedings of the eleventh Leeds-Lyon Symposium on Tribology, with the topic “Mixed lubrication and lubricated wear”. Mixed lubrication occurs between boundary and hydrodynamic lubrication, as the name would suggest. The fluid film thickness is slightly greater than the surface roughness, so there is very little asperity (high point) contact, but the surfaces are still close enough together to affect each other. In a mixed lubrication system, the surface asperities themselves can form miniature non-conformal contacts.

Rough surface EHL and mixed lubrication have been studied in the last decades mainly with two types of approaches. The first is the statistical approach. In the early days of rough surface EHL studies, owing to the limitation of computing abilities and lack of advanced algorithms, some statistical parameters of the surface topography were used to describe the roughness effect on contact performances. This is why this type is called the statistical approaches. Greenwood and Williamson [11] proposed a basic elastic model considering rough surfaces. They based this on the assumption that all asperities can be represented by paraboloids, and calculated the separation of the surfaces, as well as the nominal pressure between two surfaces. This nominal pressure is not the real pressure, but should be interpreted as the average statistical pressure. In their calculations, they gave the asperities a Gaussian height distribution. The model works well when the load is such that the asperity tips of the rough materials are compressed within the elastic limit. Using the G-W model it is important to know its restrictions. One of the most important features of the model is that it is a statistical analysis, and therefore a very large number of asperity contacts are expected within the nominal contact area. Accordingly, the model deals with the part of the roughness spectrum where the wavelengths are small compared with the contact area. Another assumption made in the GW model is that the asperities deform independently from each other, so the asperities may therefore not merge. The GW model is also extended by others. Greenwood and Tripp [13] extended this model to the contact of two nominally flat rough surfaces, and the Chang-Etsion-Bogy model [57] can separate the plastic and the elastic supported loads, to name a few. Asperity interactions can also be treated with the statistical approach. Johnson et al. [58] used the Fourier series to study a bi-sinusoidal isotropic surface in contact with a flat plate case, while Vergne et al. [59] used an integral formulation of the elasticity theory to study the elastic contact between two and three asperities and a flat plate. Zhao and Chang [60] modelled the asperity interaction in elastic-plastic contact of rough surfaces using the Saint Venant's Principle and Love's formula [61]. The average flow model, first proposed by Patir and Cheng [62], is also used extensively. Zhu et al. [63] developed a mixed line contact EHL model, and Zhu and Cheng [64] subsequently studied mixed point contact EHL. In the two studies the metal-to-metal asperity pressure was computed using the GT model. Epstein et al. [65] used an improved flow factor method in a micro-macro approach to study the effect of roughness on the fatigue life in a mixed EHL contact. Reference [66] contains a detailed review on progresses in the area of probabilistic EHL modelling, as well as a review on the most recent EHL studies that utilized probabilistic modelling.

The second approach is the deterministic approach. Owing to the rapid development of computer ability and advanced numerical algorithms, the deterministic approach has been widely used recently. This approach can capture details of asperity deformation and interaction because the roughness information is expressed in the model explicitly; however, it requires more computation time. When the roughness does not have a definite lay direction, the analysis requires the use of a three-dimensional roughness profile. In the case of a heavily loaded line contact, the Hertzian contact width can be wider than 1 mm, while the length of the line contact is several centimeters. A typical measurement performed on an optical profilometer at 1 μm lateral resolution gives about 5 MB of double precision data for less than half a square millimetre of rough surface [66]. Despite this, the deterministic approach can provide detailed information inside the nominal contact area, which is a must for a further surface failure analysis.

Key issues encountered when developing mixed EHL models are discussed by Zhu [67]:

i. How to handle surface roughness. Two main approaches are used when dealing with surface roughness: stochastic and deterministic. Stochastic approaches use a small number of statistic parameters to describe the rough surface characteristics and their influences on contact and lubrication. They cannot predict localized details and peak values within nominal contact regions. This information may be directly correlated to surface failures such as micropitting. The other methods are the deterministic approaches, which have drawn more attention in the last twenty years owing to advancements in computer technologies.

ii. How to model surface contact and hydrodynamic lubrication simultaneously. Currently there are two types of models. One simulates contact and lubrication separately with different approaches. For instance, a dry contact model can be used for asperity contact areas and the Reynolds equation applies to the areas where the lubricant exists. In this approach, it may be difficult to determine borders and handle boundary conditions between contact and lubrication areas, especially when random or irregular surface roughness is involved. The other approach is the unified way proposed by Hu and Zhu [4]. This approach based upon the fact that dry contact is a special case of lubricated contact at ultra-low viscosity or ultra-low speed. Therefore, dry contact can be simulated with lubrication models as long as the numerical solver is sufficiently robust to handle ultra-low viscosity and ultra-low speed.

The progress of mixed lubrication studies mainly relies on the development of knowledge in two fields: an integrative knowledge of fluid film and boundary lubrication, and a sufficient recognition of rough surface interaction.

2.2. Lubrication Analysis of Spur Gear Pairs

In order to protect gear tooth surface and reduce the frictional power loss, lubrication is also applied between the interacting gear tooth. Gear lubrication problems have been studied for a long time. After obtaining their first numerical solution for EHL line contacts. Dowson and Higginson [68] applied the empirical minimum film thickness formula into spur gear lubrication problems. Since more advanced algorithms and more advanced lubrication models have been proposed, the gear lubrication analysis continues. Initially, researchers could only deal with two-dimensional steady-state isothermal lubrication models for spur gears; now, researchers can handle the three-dimensional transient thermal non-Newtonian models for non-spur gear pairs with surface roughness. Table 2.1 lists some of works on lubrication studies of gear drives.

Table 2.1 Some of works on lubrication studies of gear drives

Reference	Effects	Notes
1966 Dowson, Higginson [69]	Thermal: No Transient: No Roughness: No	They applied minimum film thickness formula to gear lubrication problems.

1970 Gu [70]	Thermal: Yes Transient: No Roughness: No	Modified mean-viscosity for the surface temperature rise determination.
1971 Vichard [71]	Thermal: No Transient: Yes Roughness: No	Squeeze-film effect is studied using the complete Reynolds equation.
1976 Wellauer, Holloway [72]	Thermal: No Transient: No Roughness: Yes	Gears operating in a EHL regime with λ greater than 2 run virtually without surface distress, and many gear drives operate at λ less than 0.7, which is mixed lubrication.
1980 Jackson, Rowe [73]	Experimental	The value of lubrication parameters can accurately be determined by direct measurement of the oil film thickness in an optical EHL apparatus.
1980 Wang, Cheng [74]	Thermal: No Transient: No Roughness: No Dynamic load: Yes	Dynamic load analysis is proposed which shows the dynamic load effect on lubrication without the squeeze effect.
1982 Sato [75]	Thermal: Yes Transient : No Roughness: No	The TEHL model is developed for a spur gear pair and the effect of the inlet temperature of the fluid is studied.

1984 Lin, Medley [76]	Thermal: No Transient: Yes Roughness: No	Effect of the modification to the contact geometry is studied.
1987 Tieu, Worden [77]	Thermal: No Transient: Yes Roughness: No Dynamic: Yes	However, the dynamic load was simulated by an arbitrary input either as a step input or a sine wave to cater for any of the above dynamic loads.
1991 Wu, Cheng [78]	Thermal: Yes Transient: Yes Roughness: Yes	The major power losses in spur gears owing to sliding and rolling friction have been analyzed by applying a simplified analytical friction model in the partial-EHL contacts where the friction is affected by both asperity interactions and hydrodynamic effects.
1995 Hua, Khonsari [79]	Thermal: No Transient: Yes Roughness: No	A parametric study was conducted to investigate effects of geometry factors on the lubrication behaviour of a gear transmission. Results show that the equivalent curvature radius of gear teeth plays an important role on EHL film formation.
1997 Larsson [80]	Thermal: No Transient: Yes Roughness: No	The multigrid method is applied.

1998 Scott, Hargreaves [81]	Thermal: No Transient: No Roughness: Yes	The work looks at the roughness profiles of gear tooth surfaces and attempts to put the subject of surface topography into context with EHL.
2003 Mihailidis, Panagiotidis [82]	Thermal: Yes Transient: Yes Roughness: No	A transient, TEHL model is presented that has been used to study the lubrication parameters at 250 contact points along the path of a contact.
2003 J. Tao, et al. [83]	Thermal: No Transient: Yes Roughness: Yes	The conclusion is made that the different fluid models considered lead to significantly different pressure and film thickness behaviour within the contact.
2004 Wang, et al. [84]	Thermal: Yes Transient: Yes Roughness: No	The thermal effect is considered with a TEHL model in which the energy equations are solved numerically.
2006 Sharif, Evans, Snidle [85]	Thermal: No Transient: Yes Roughness: No	A wear pattern prediction is made based upon a full EHL solution in which the detailed distribution of wear on the tooth surfaces during meshing is summed to determine the calculated wear per meshing cycle.

2007 Kumar, et al. [86]	Thermal: No Transient: Yes Roughness: No	The lubricant is assumed to be couple-stress fluid and the transient Reynolds equation for the compressible couple-stress fluid is derived using the Stokes theory. The EHL characteristics computed for couple-stress fluids are found to have strong dependence on couple-stress parameter.
2008 Akbarzadeh, Khonsari [87]	Thermal: Yes Transient: No Roughness: Yes	The load sharing concept is used for a statistical analysis of lubrication performance of a spur gear pair.
2009 Evans, Snidle, Sharif [88]	Thermal: No Transient: Yes Roughness: Yes	The paper discusses the effect of surface roughness when the EHL film thickness developed between the gear tooth surfaces is small compared to the heights of the roughness features.
2010 Brandão, Seabra, Castro [89, 90]	Thermal: No Transient: No Roughness: Yes	A numerical model for the prediction of surface initiated damage on gear tooth flanks is presented. This model hinges on a model of the mixed film lubrication regime and on the application of the Dang Van high-cycle multi-axial fatigue criterion.

2010 Li, Kahraman [91]	Thermal: No Transient: Yes Roughness: Yes	The reduced Reynolds technique is applied to deal with mixed lubrication line contacts.
2010 Wang, Yi [36]	Thermal: Yes Transient: Yes Roughness: No	The Ree-Eyring model is incorporated into the TEHL model.
2011 Li, Kahraman [92]	Thermal: No Transient: Yes Roughness: Yes	A non-linear vibratory model is used to study the effects of dynamic conditions.
2012 Anuradha, Kumar [93]	Thermal: Yes Transient: Yes Roughness: No	Carreau's shear-thinning model and Doolittle's free volume based pressure-viscosity relationship are adopted.
2012 Evans, et al. [94]	Thermal: No Transient: Yes Roughness: Yes	The mixed lubrication of gear contacts is calculated for a further fatigue failure prediction.
2012 Liu, et al. [5]	Thermal: No Transient: Yes Roughness: Yes	The reduced Reynolds technique is applied to show the coupled effects of roughness, speed and load.
2012 Liu, et al. [95]	Thermal: No Transient: Yes Roughness: No	The gear dynamic loads effect on lubrication performance is studied.

From the listed studies it is seen that, earlier studies consider Newtonian fluids, isothermal, smooth surface cases, while now people are trying to deal with non-Newtonian, thermal, rough surface case for spur gear pair lubrication problems.

However, until now a complete spur gear pair lubrication model which takes into account the thermal effect, non-Newtonian effect, surface topography effect, transient squeeze effect, and dynamic load effect, is yet to be developed. This work aims to develop this kind of model and each effect is studied in detail. The results are proposed by contact pressures, film profiles, frictions, temperature fields, etc. This work is believed to provide some valuable suggestions for spur gear pair lubrication engineering problems, and this approach can be extended to other gear type applications or bearings, amongst others.

Chapter 3 Contact Analysis Using Classical Approach

In this chapter, the classic dry contact theory and EHL theory are introduced. A dry contact model as well as a classical EHL model are developed and the numerical approaches are introduced. Fundamental equations of the EHL model such as the Reynolds equation, film thickness equation, force balance equation, viscosity-pressure-temperature equation and density-pressure-temperature equation of the fluid are introduced in detail. Typical EHL characteristics such as the inlet pressure build up and the outlet second pressure spike are described.

3.1. A Dry Contact Model

Physically, a classical dry contact problem can be described as such: given two solid bodies with known geometry pressed against each other with a force (or a pressure distribution) which caused deformations of the bodies. A theory of contact is required to predict the shape of the contact area and how it grows in size with increasing load, as well as the distribution of tractions, etc. Finally, it should enable the components of deformation and stress in bodies to be calculated in the vicinity of the contact region. Before the problem in elasticity can be formulated, a description of the geometry of the contact surfaces is necessary. With assumptions of parabolic surface profiles and linear elastic, frictionless materials, Hertz [8] proposed the first analytical solution for dry contact problems which laid the foundation for the subject of contact mechanics. Since then, the developments of contact theories mainly focus on eliminating assumptions made in the Hertz contact theory. Before giving the general dry contact model, Hertz analytical results are provided for the first insight of contact mechanisms.

3.1.1. Hertz Contact Theory

Hertz introduced the simplification that, for the purpose of calculating local deformations, each body can be regarded as an elastic half-space loaded over a small region of its plane surface. By this simplification, generally followed in contact stress theory, the highly concentrated contact stresses are treated separately from the general distribution of stress in the two bodies, which arises from their shape and the way in which they are supported. In order for this simplification to be reasonable, two conditions should be satisfied: the dimensions of the contact area must be small compared (a) with the dimensions of each body and (b) with the relative radii of curvature of surfaces. The first condition is necessary to ensure that the stress field calculated on the basis of a solid which is infinite in extent is not seriously influenced by the proximity of its boundaries to the highly stressed region. The second condition is to ensure firstly that the surfaces just outside the contact region approximate roughly to the plane surface of a half-space, and second that the strains in the contact region are sufficiently small to lie within the scope of the linear theory of elasticity. Hertz also assumed the surfaces to be frictionless so that only the normal pressure is transmitted between two bodies.

With those preparations, Hertz was able to give the analytical solution to classical dry contact problems. A line contact problem (a line contact problem is defined as two cylindrical bodies, with their axes lying parallel, pressed in contact by a force per unit length, which is the case assumed for a spur gear pair) can be simplified as Fig. 3.1 in which $R_{1,2}$ represents the contact radius of the solids, and $u_{1,2}$ represents the speed of the two solids, respectively. The coordinates are defined as follows: the x direction represents the direction of the rolling speed, for a lubrication case, it also represents the flow direction of the lubricant; the z

direction is the direction across the gap between the interacting surfaces (for a lubrication case, it represents the direction across the film); and the y direction is vertical to the $x-z$ plane. This coordinate set is used elsewhere in the work.

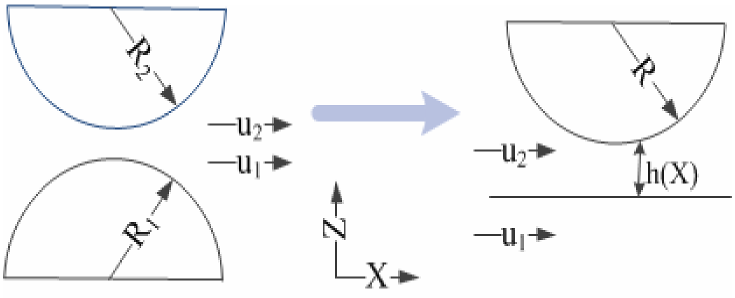

Fig. 3.1 Simplification of a line contact problem

For line contact problems, the maximum pressure occurred in the nominal contact region, also known as the Hertzian pressure, p_H, is expressed as

$$p_H = \sqrt{\frac{E^{'}F}{R\pi}} = \frac{4p_m}{\pi} = \frac{2F}{\pi b} \tag{3.1}$$

Where p_m is the mean contact pressure across the contact region. F is the load per unit width, and $E^{'}$ is the equivalent elastic modulus, which is derived from

$$\frac{2}{E^{'}} = \frac{1-v_1^2}{E_1} + \frac{1-v_2^2}{E_2} \tag{3.2}$$

Where v_1 and v_2 are the Poisson ratio of the two subjects, respectively, and E_1 and E_2 are the elastic modulus of the two subjects, respectively.

The reduced radius of curvature R is given by

$$\frac{1}{R} = \frac{1}{R_1} + \frac{1}{R_2} \tag{3.3}$$

With R_1 and R_2 are radii of the two subjects, respectively. The half contact width b is expressed as

$$b = \sqrt{\frac{8FR}{\pi E'}} \tag{3.4}$$

The pressure distribution within the Hertzian contact zone can be calculated with

$$p(x) = \frac{2F}{\pi b^2}\sqrt{b^2 - x^2} \tag{3.5}$$

The pressure falls to zero at the edge of the contact region.

By using the elastic mechanics theory, it is easy to find that at the contact interface the stress $\sigma_x = -p(x)$; outside the contact region all the stress components at the surface are zero. Along the z direction, the principal stresses are given by

$$u_s = u_1 - u_2 < 0 \tag{3.6}$$

$$\sigma_z = -\frac{p_H}{b}(b^2 + z^2)^{-1/2} \tag{3.7}$$

For plane strain, the third principal stress $\sigma_y = \nu(\sigma_x + \sigma_z)$.

Where σ_x, σ_y and σ_z are stresses along x, y and z direction, respectively.

The principal shear stress τ_1 therefore can be calculated by

$$\tau_1 = -\frac{p_H}{b}[z - z^2(b^2 + z^2)^{-1/2}] \tag{3.8}$$

The Hertz contact theory is introduced here is because (a) the theory is still the basis for surface contact strength standard for gears, bearings, etc., and (b) the Hertz contact parameters are chosen for the dimensionlessness of the following EHL model.

3.1.2. A General Dry Contact Model

In fact, most engineering contact problems are not Hertzian contact problems - for example, those cases in which surface topography cannot be neglected. Assuming a parabolical approximation of the two bodies with equal reduced radii of curvature in x direction, the gap between two surfaces can be expressed as

$$h(x,t) = h_0 + \frac{x^2}{2R} + rr(x,t) - \frac{4}{\pi E'} \int_{-\infty}^{+\infty} \ln|x - x'| p(x',t) dx' \qquad (3.9)$$

Where h_0 is a constant, R is the equivalent radius, $rr(x,t)$ represents the surface topography, x_0 is the distance where the displacement is zero and t is the time, $p(x',t)$ is the pressure at location x' and time t. For the smooth surface case, $rr(x,t) \equiv 0$.

When the surfaces are loaded, the gap h should remain non-negative. Neglecting adhesion this implies positive local pressure (in contact) or zero local pressure (no contact). p is determined by the equation $h = 0$ with the condition that $p \geq 0$. In mathematical terms, this lead to a complementarity problem that can be expressed as

$$\begin{cases} h(x) > 0, p(x) = 0, (non-contact) \\ h(x) = 0, p(x) > 0, (contact) \end{cases} \qquad (3.10)$$

The applied load per length is balanced by the integral over the contact pressure distribution

$$F = \int_{-\infty}^{+\infty} p(x,t) dx \qquad (3.11)$$

If no surface features are considered, this contact problem has been solved by Hertz analytically. However, many non-Hertzian contact problems do not permit analytical solutions in closed form. It has led to the development of various numerical methods such as the matrix inversion method [96], variational methods [97], and others. A non-Hertzian contact problem is, for example, the case if the shape of the undeformed surfaces differs from a paraboloide, or if the surfaces are not perfectly smooth. In the latter case their nominal shape may still be well approximated by paraboloides, but the roughness of the surface or its micro-geometry introduces a roughness term [2].

For a numerical solution it is convenient to introduce a dimensionless set of variables to reorganize the equations. A convenient choice is using the Hertzian contact parameters. Introducing:

$$\begin{cases} X = x/b \\ P = p/p_{\mathrm{H}} \\ H = hR/b^2 \\ T = tu_s/(2b) \end{cases} \tag{3.12}$$

Where x is the distance from the place where the maximum Hertzian pressure locates, b is the Hertz half width, p_H is the maximum Hertzian pressure, and R is the equivalent (reduced) radius.

Then the dimensionless gap equation reads

$$\begin{cases} H(X) > 0, P(X) = 0, (non-contact) \\ H(X) = 0, P(X) > 0, (contact) \end{cases} \tag{3.13}$$

with

$$H(X) = H_0 + \frac{X^2}{2} + RR(X,T) - \frac{1}{\pi}\int_{-\infty}^{+\infty} P(X',T)\ln|X - X'|dX' \tag{3.14}$$

The value of H_0 is determined by the force balance equation

$$\int_{-\infty}^{+\infty} P(X)dX = \frac{\pi}{2} \tag{3.15}$$

Where $RR(X,T) = rr \cdot R/b^2$. Mathematically speaking, the contact equations, the force balance equation and the inequality constraints lead to a linear complementarity problem. The problem can be discretized using an equal-spaced mesh size along X direction.

An approximation of the pressure profile by a piecewise constant function with value $P_j = P(X_j)$ in the region $X_j - h/2 \le X' \le X_j + h/2$ on a uniform grid with mesh size $h = (X_b - X_a)/n$, the elastic deformation in grid point i

$(X_i = X_a + ih)$ can be expressed as

$$d(X_i) = -\frac{1}{\pi}\sum_j K_{i,j}P_j \tag{3.16}$$

with the coefficients defined by

$$K_{i,j} = \int_{X_j-h/2}^{X_j+h/2} \ln\left|X_i - X'\right| dX' \tag{3.17}$$

These coefficients can be calculated analytically and finally they can be expressed as

$$\begin{aligned} K_{i,j} &= (X_i - X_j + h/2)(\ln|X_i - X_j + h/2| - 1) \\ &-(X_i - X_j - h/2)(\ln|X_i - X_j - h/2| - 1) \end{aligned} \tag{3.18}$$

Thus the discrete contact equation reads

$$\begin{cases} H_i > 0, P_i = 0, (non-contact) \\ H_i = 0, P_i > 0, (contact) \end{cases} \tag{3.19}$$

with

$$H_i = H_0 + \frac{X_i^2}{2} + RR_i - \sum_j K_{i,j}P_j \tag{3.20}$$

The discrete force balance equation reads

$$h\sum_i P_i = \pi/2 \tag{3.21}$$

The Jacobi or Gauss-Seidel relaxation scheme could be used for iteration of this system. In order to calculate fast, the triple Jacobi relaxation scheme, introduced in Ref. [2], is applied. As a first step, a simple Jacobi relaxation is studied. Given an initial pressure distribution $\overline{P}'$, a new approximation $\overline{P}$ can be obtained according to

$$\overline{P}_i = \overline{P}'_i + \varpi_1\delta_i \tag{3.22}$$

Where ϖ_1 is an under-relaxation coefficient. δ_i is solved from the requirement that the equation at the point X_i is satisfied after making this change. It is given by

$$\delta_i = r_i / K_{0,0} \tag{3.23}$$

Where r_i is the residual and for Jacobi relaxation changes already made to points previously relaxed are not taken into account and the residual is given by

$$r_i = -H_0 - RR_i - X_i^2 / 2 + \sum_{i'} K_{i,i'} \overline{P}'_{i'} = -H_i \tag{3.24}$$

Where K is the kernel and the expression can be found in Ref. [98]. The Jacobi relaxation is unstable for the contact problem. The reason for this is that the kernel K is non-zero for all values of $|i - i'|$. As a result, changing the value of the pressure $\overline{P}$ at a point X_i will affect the deformation and thus the gap $\overline{H}$ in all points of the domain. Moreover, at each point the changes applied to all points accumulate. As a result, for each point the positive effect of making the residual zero when relaxing that point may be outweighed by the accumulated negative effect in this point of the changes made in all other points. The residual then may become larger at the end of the sweep than it was before the sweep. Since it is related to the integrals in the equation, this kind of instability shows up as an amplification of low frequency error components. Distributive relaxation schemes may act better for this case. When relaxing the equation at a given point X_i, not only the value of the current approximation at that point is changed, but also the value of the current approximation in a few neighbouring points. A second order distribution scheme, also referred to as a triple change, is described as follows

$$\begin{cases} \overline{P}_{i-1} = \overline{P}'_{i-1} - \delta_i / 2 \\ \overline{P}_i = \overline{P}'_i + \delta_i \\ \overline{P}_{i+1} = \overline{P}'_{i+1} - \delta_i / 2 \end{cases} \tag{3.25}$$

Triple operation decays faster than the dipole one. However, in that case the equation reduces to the steady state $H(X) = 0$ and then dipole is the equivalent of tripole for the dry contact. When the updated pressure value is less than zero, it is set to zero to satisfy the compatibility condition.

Once the pressure is updated, the gap is updated accordingly. Then the force balance equation is used to adjust the value of H_0. This kind of iteration going on leads to final convergence of the dry contact problem very quickly, even for a rough surface problem.

3.2. An EHL Line Contact Model

For a concentrated contact, like a line contact or a point contact, even if sufficient lubricant is supplied to form a film separating the surfaces, the shape and thickness of the film will be strongly affected by the deformation of the contacting elements. Since the 1950s, the study of this film formation has evolved into a separate subject known as EHL. Currently, classical EHL theories have been developed completely and the main interests of researchers have been transferred to fluid rheology behaviours, thermal behaviours and mixed lubrication problems. Typically, an EHL model is made up of the Reynolds equation, the film thickness equation, the force balance equation and relations describing the viscosity-pressure behaviour and the density-pressure behaviour of the lubricant. Compared with the previous dry contact model, an EHL model adds the Reynolds equation to describe the fluid film formation.

A classical EHL model comprises an equation describing the flow of the fluid such as a Reynolds equation or a Navier-Stokes equation (in this work the Reynolds equation is applied), the film thickness equation (also refers to the elastic deformation equation), the force balance equation, and equations describing the viscosity-pressure-temperature and density-pressure-temperature relations.

3.2.1. The Reynolds Equation

The Reynolds equation, first proposed by Reynolds [99] in 1886, is a special kind of Navier-Stokes equation to describe (elasto)hydrodynamic lubrications. The Reynolds equation relates the pressure in the lubricant film to the geometry of the gap and the velocities of the moving surfaces. In the first place, the Reynolds equation was derived under those assumptions: constant viscosity, Newtonian lubricant, thin film geometry, negligible inertial, and negligible body forces, etc. It should be noted that the assumption of the Newtonian lubricant is not necessary. For a line contact case, the Reynolds equation with the Newtonian assumption reads

$$\frac{\partial}{\partial x}\left(\frac{\rho h^3}{\eta}\frac{\partial p}{\partial x}\right)=\underbrace{12u_r\frac{\partial(\rho h)}{\partial x}}_{wedge}+\underbrace{12\rho h\frac{\partial u_r}{\partial x}}_{stretch}+\underbrace{12\frac{\partial(\rho h)}{\partial t}}_{squeeze} \tag{3.26}$$

Where x represents the fluid flow direction, the rolling velocity is $u_r=(u_1+u_2)/2$, u_1 and u_2 are rolling velocity of the two surfaces, p is the fluid pressure, h is the film thickness, ρ is the density of the lubricant.

The boundary condition of the Reynolds equation reads

$$\begin{cases} p(x_a,t)=0 \\ p(x_{out},t)=\dfrac{\partial p}{\partial x}(x_{out},t)=0 \end{cases} \tag{3.27}$$

x_{out} is the position where the cavitation condition satisfies and it is a function of time. The cavitation condition can be treated directly by setting the negative pressure values to zero.

The three terms in the right hand side of Eq. 3.18 represent different effects that account for the pressure generation in the film and are commonly referred to as the wedge effect, the stretch effect and the squeeze effect, respectively. From the mathematic point of view, the Reynolds equation is a non-homogeneous partial differential equation, from which it is difficult to get its analytical solution.

In order to consider the non-Newtonian effects and the thermal effect on film formation, a generalized Reynolds equation proposed by Yang et al. [3] is preferable. A detailed derivation of the generalized equation can be found in Yang et al. [3]. The generalized Reynolds equation for an EHL line contact can be written as

$$\frac{\partial}{\partial x}((\frac{\rho}{\eta})_e h^3 \frac{\partial p}{\partial x}) = 12u_r \frac{\partial(\rho^* h)}{\partial x} + 12\frac{\partial(\rho_e h)}{\partial t} \tag{3.28}$$

Where

$$(\frac{\rho}{\eta})_e = 12(\frac{\eta_e \rho'_e}{\eta'_e} - \rho''_e) \tag{3.29}$$

$$\rho^* = \frac{\rho'_e \eta_e (u_b - u_a) + \rho_e u_a}{u_r} \tag{3.30}$$

$$\rho_e = \frac{1}{h}\int_0^h \rho dz \tag{3.31}$$

$$\rho'_e = \frac{1}{h^2}\int_0^h \rho \int_0^z \frac{1}{\eta^*} dz' dz \tag{3.32}$$

$$\rho''_e = \frac{1}{h^3}\int_0^h \rho \int_0^z \frac{z'}{\eta^*} dz' dz \tag{3.33}$$

$$\frac{1}{\eta_e} = \frac{1}{h}\int_0^h \frac{dz}{\eta^*} \tag{3.34}$$

$$\frac{1}{\eta'_e} = \frac{1}{h^2}\int_0^h \frac{zdz}{\eta^*} \tag{3.35}$$

This generalized equation considers the variation of viscosity and density along the direction across the film. It can incorporate most of the rheological laws found in the literature and is quite suitable for the complete solutions of the non-Newtonian thermal EHL problems.

It should be reminded that the fluid inertia force can be neglected for EHL line contacts or EHL point contacts. The modified Reynolds number for an EHL line contact is defined as

$$\mathrm{Re}^* = \frac{\rho_0 u_r b}{\eta_0}(\frac{b}{R})^2 \tag{3.36}$$

It is estimated that the order of magnitude of Re^* for an EHL line contact is no more than 0.0001 which means the fluid inertia force can be ignored in EHL studies.

3.2.2. Film Thickness Equation

The film thickness equation reads

$$h(x,t) = h_0 + \frac{x^2}{2R} + rr(x,t) - \frac{4}{\pi E'}\int_{-\infty}^{+\infty} \ln|x - x'| p(x',t)dx' \tag{3.37}$$

Its form is similar to the gap equation of the dry contact model.

3.2.3. Viscosity-Pressure Equations of Fluids

The approximately exponential increase of viscosity as the pressure goes up is one of the two dominant effects (the other is that the elastic deformation cannot be neglected) accounting for the film formation in nominal Hertz contact regions. The thermal effect on viscosity is sometimes neglected in part of investigations on EHL. In this case, the two most widely used viscosity-pressure relations are introduced: the exponential Barus equation and the Roelands equation. The isothermal Barus equation reads

$$\eta(p) = \eta_0 e^{\alpha p} \tag{3.38}$$

Where η_0 is the viscosity under ambient pressure, and α is the pressure-viscosity coefficient, typically its value is in the range $1\times10^{-8}Pa^{-1} < \alpha < 3\times10^{-8}Pa^{-1}$. In this work its value is defined as $\alpha = 2\times10^{-8}Pa^{-1}$. The Barus equation is applied extensively in early days owing to its simplicity. However, the predicted viscosities for pressures larger than approximately 0.1 GPa are too high. For heavy load cases, Roelands equation is preferable and reads

$$\eta(p) = \eta_0 \exp\{[\ln(\eta_0) + 9.67][-1 + (1 + p / p_0)^z]\} \qquad (3.39)$$

Where z is the pressure-viscosity index, typically in the range $z \in (0.5, 0.7)$. In this work $z = 0.68$ is applied. p_0 is a constant and in this work its value is chosen as $p_0 = 5.1 \times 10^9 Pa$.

Those two relations are acceptable for the prediction of film thickness, however, they greatly overestimated the friction and hence power loss in the lubricated conjunctions [26]. It is well known that the effective viscosity of most lubricants decreases substantially as the shear rate increases at constant pressure and temperature. This makes it necessary to consider the non-Newtonian fluid behaviour when calculating tractions within the nominal contact region. The non-Newtonian behaviour will be discussed in another section. When the thermal effect is taken into account, the thermal effect on viscosity of fluid should also be considered. If the thermal effect is taken into account, for the Barus relation, it becomes

$$\eta(p) = \eta_0 e^{\alpha p - \beta(T - T_0)} \qquad (3.40)$$

Where T is the temperature of the fluid and T_0 is the temperature at the ambient environment. β is the viscosity-temperature factor whose value is often chosen in the range $0.03 \sim 0.06 / K$. In this work it is fixed at $\beta = 0.048 / K$.

The Roelands viscosity-pressure-temperature relation reads

$$\eta(p,T) = \eta_0 \exp\{[\ln(\eta_0) + 9.67][-1 + (1 + p / p_0)^z (\frac{T - 138}{T_0 - 138})^{-s}]\} \qquad (3.41)$$

Where s is the viscosity-temperature factor.

It is worth noting that when the pressure drops to zero and the temperature goes to the ambient temperature T_0, the above two equations equal to each other. In this way, the relationship between z and α, as well as the relationship between s and β, can be derived as

$$z = \alpha / [5.1 \times 10^{-9} (\ln \eta_0 + 9.67)] \qquad (3.42)$$

$$s = \beta (T_0 - 138) / (\ln \eta_0 + 9.67) \qquad (3.43)$$

If not specified explicitly, the Roelands relation is applied anywhere in the thesis.

3.2.4. The Density-Pressure Equation

Generally, the compressibility of the lubricant under high pressures should not be neglected. One of the most cited relations is the one proposed by Dowson and Higginson [69], which reads

$$\rho(p) = \rho_0 \frac{0.59 \times 10^9 + 1.34 p}{0.59 \times 10^9 + p} \qquad (3.44)$$

Where ρ_0 is the density at the ambient pressure. This density-pressure relation is depicted in Fig. 3.2. From this figure it is seen that the compressibility of the lubricant is less than approximately 30%, which indicates that the effect of the compressibility of the lubricant on the film formation will be much smaller than the effect of the elastic deformation and the effect of the viscosity.

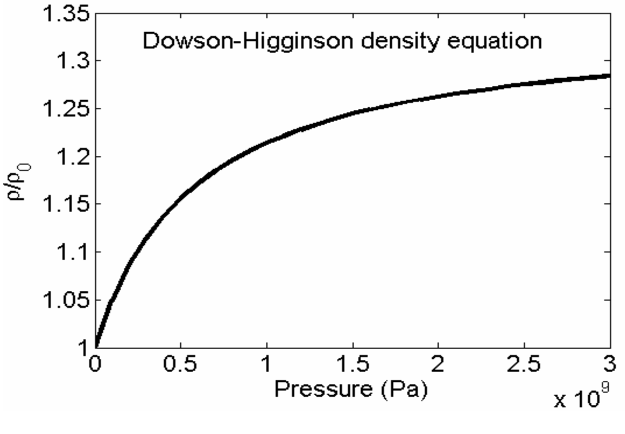

Fig. 3.2 Dowson-Higginson density-pressure relation

When the thermal effect on density is taken into account, the Dowson-Higginson density equation becomes

$$\rho(p,T)=\rho_0[1+\frac{0.6\times10^{-9}p}{1+1.7\times10^{-9}p}-0.00065(T-T_0)] \tag{3.45}$$

3.2.5. A Classic EHL Line Model

Together with the force balance equation - which is the same as the one used in the dry contact model - those pre-described equations form a classical EHL model. With an appropriate numerical method, the pressure and film thickness could be solved from those equations. Similar to the dry contact problem, it is much easier to solve if the model is dimensionless, for example using the Hertz parameters. Besides those used in dry contact problems, two additional dimensionless parameters are introduced:

$$\begin{cases}\bar{\rho}=\rho/\rho_0\\ \bar{\eta}=\eta/\eta_0\end{cases} \tag{3.46}$$

Where ρ and η are real density and viscosity of the lubricant, respectively, ρ_0 and η_0 are density and viscosity of the lubricant at atmospheric pressure, respectively.

The dimensionless Reynolds equation then reads

$$\frac{\partial}{\partial X}[\frac{\bar{\rho}H^3}{\bar{\eta}\lambda}\frac{\partial P}{\partial X}]-\frac{\partial(\bar{\rho}H)}{\partial X}-\frac{\partial(\bar{\rho}H)}{\partial T}=0 \tag{3.47}$$

With

$$\lambda=\frac{12\eta_0u_rR^2}{b^3p_h}=\frac{6\pi^2\eta_0u_rE'R}{8w^2} \tag{3.48}$$

The dimensionless Reynolds equation follows the cavitation condition $P\geq0$ and the boundary condition

$$P(X_a)=P(X_b)=0 \tag{3.49}$$

The dimensionless Roelands viscosity-pressure equation reads

$$\bar{\eta}(P) = \exp\{(\frac{\alpha p_0}{z})[-1 + (1 + \frac{P p_H}{p_0})^z]\} \tag{3.50}$$

The dimensionless Dowson-Higginson density-pressure equation reads

$$\bar{\rho}(P) = \frac{0.59 \times 10^9 + 1.34 P p_H}{0.59 \times 10^9 + P p_H} \tag{3.51}$$

The dimensionless film thickness equation can be expressed as

$$H(X) = H_0 + \frac{X^2}{2} + \underbrace{RR(X,T)}_{roughness} \underbrace{- \frac{1}{\pi} \int_{-\infty}^{+\infty} P(X',T) \ln|X - X'| dX'}_{deformation} \tag{3.52}$$

Where H_0 is the integration constant determined by the force balance condition, $RR(X,T)$ is the dimensionless surface feature geometry term. The solution is also subject to the condition of force balance, i.e. the integral over the pressure equals the externally applied contact load. The dimensionless form of this force balance equation for a line contact reads:

$$\int_{-\infty}^{+\infty} P(X) dX = \frac{\pi}{2} \tag{3.53}$$

Until now, a complete dimensionless EHL model has been developed. Once discretized, the next step is to seek an effective numerical method. Owing to the mathematical characteristic of the Reynolds equation, for the EHL model, a different relaxation scheme is suggested to be chosen compared with the distributive relaxation scheme used for the dry contact model. Venner et al. [100] proposed a hybrid relaxation scheme where in the Hertzian-contact region the simple Gauss-Seidel relaxation scheme is applied and in the far-away-Hertzian-contact region the dipole Jacobi relaxation scheme is applied. This hybrid relaxation scheme not only avoids the amplification of the low frequency error components, which may cause divergence, but also is good at reducing high frequency error components. This makes it a good "smoother" in the multigrid framework. In this section this hybrid relaxation scheme is applied for the EHL model, and for the Reduced Reynolds model will appear in the next chapter as well.

It should be also noted that three parameters are often used in the literature, to characterize a given contact. For the point contact problem, they are referred to as the Hamrock and Dowson parameters [101], defined as

$$\begin{cases} W = \dfrac{F}{E'R} \\ U = \dfrac{\eta_0 u_r}{E'R} \\ G = \alpha E' \end{cases} \tag{3.54}$$

And the associated dimensionless film thickness is defined as $H^{HD} = h / R$. The disadvantage of using these parameters is that it is not the minimum set of parameters. One reason mentioned in favour of these parameters is that they represent parameters that one generally varies independently in experiments, i.e. load, speed, and lubricant. However, this advantage does not outweigh the extra work needed in parametric studies. Also, in terms of these parameters the different asymptotic regimes are not so clearly defined. To present the results in design charts or survey diagrams, a convenient set of dimensionless variables for EHL problems was proposed by Blok and co-workers. For the line contact they were pointed out by Moes [102] and for the point contact by Moes and Bosma [103]. They are now often referred to as the Moes dimensionless parameters and for the line contact they are defined as

$$\begin{cases} M = \dfrac{F}{E'R^2}\left(\dfrac{2\eta_0 u_r}{E'R}\right)^{-3/4} = W(2U)^{-1/2} \\ L = \alpha E'\left(\dfrac{2\eta_0 u_r}{E'R}\right)^{1/4} = G(2U)^{1/4} \end{cases} \tag{3.55}$$

3.2.6. The Discretized Form and the Numerical Approach

One popular discretized form of the line contact problem is to make the Couette terms the second order and the Wedge term the first order, as follows

$$\frac{\varepsilon_{i-1/2}P_{i-1}-(\varepsilon_{i-1/2}+\varepsilon_{i+1/2})P_i+\varepsilon_{i+1/2}P_{i+1}}{\Delta X^2}+\frac{\overline{\rho}_iH_i-\overline{\rho}_{i-1}H_{i-1}}{\Delta X}+ \\ \frac{\overline{\rho}_iH_i-\overline{\rho}_{i-1}H_{i-1}}{\Delta T}=0 \tag{3.56}$$

Where

$$\varepsilon_i=\frac{\overline{\rho}_ih_i^3}{\overline{\eta}_i\lambda} \tag{3.57}$$

with

$$\lambda=\frac{6\eta_0u_sR^2}{b^3p_h} \tag{3.58}$$

$\varepsilon_{i-1/2}$ and $\varepsilon_{i+1/2}$ denote the value of ε at the intermediate locations $X=X_a+(i-1/2)\Delta X$ and $X=X_a+(i+1/2)\Delta X$, respectively. They can be expressed as

$$\begin{cases}\varepsilon_{i-1/2}=\dfrac{\varepsilon_{i-1}+\varepsilon_i}{2}\\[2ex]\varepsilon_{i+1/2}=\dfrac{\varepsilon_{i+1}+\varepsilon_i}{2}\end{cases} \tag{3.59}$$

For the force balance equation and the film thickness equation, there is no evident difference between previous works; they can be discretized as

$$\Delta X\sum_{j=0}^{n-1}\frac{P_j+P_{j+1}}{2}=\frac{\pi}{2} \tag{3.60}$$

$$H_i=H_{00}+X_i^2-\frac{1}{\pi}\sum_jK_{i,j}P_j \tag{3.61}$$

Where

$$K_{i,j}=(i-j+1/2)\Delta X(\ln(\Delta X\,|i-j+1/2|)-1) \\ -(i-j-1/2)\Delta X(\ln(\Delta X\,|i-j-1/2|)-1) \tag{3.62}$$

Fig. 3.3 shows an example for the kernal $K_{i,j}$ with $X \in (-4.5, 1.5)$, $nX = 257$. It is seen, however, that the influence factor does not go to zero for the 1d problem when $|i-j|$ goes to infinity. Strictly there should be a $\ln(|x-y|/x_0)$ where x_0 is the distance at which the elastic deformation is zero. However, when writing out the equation, the part $\int p(y)\ln(x_0)dy$ associated with this term integrated over the entire domain will be some constant that can be added to the integration constant that occurs anyway. This explains why, with increasing load for line contacts, the H_0 does not go to -1 as it does for the line contact problem, but to something like -0.56. So, if we do not enter the constant in the other constant, then we would have to specify this distance separately. This has been done, but physically is not particularly nice. The fact that it is controlled by force balance now is much more realistic. Details can be found in KL Johnson [104].

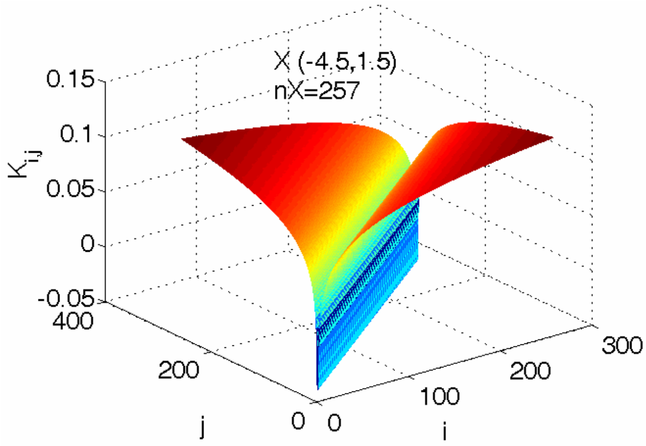

Fig. 3.3 The values of the kernel

In fact, the kernel K can be expressed as the function of the distance between two points and can be pre-stored in an array KK, such as shown in Fig. 3.4. This is very useful for the multi-dimensional problems like the point contact EHL problem, since the kernel is four-dimensional and will be hard to store in the original form.

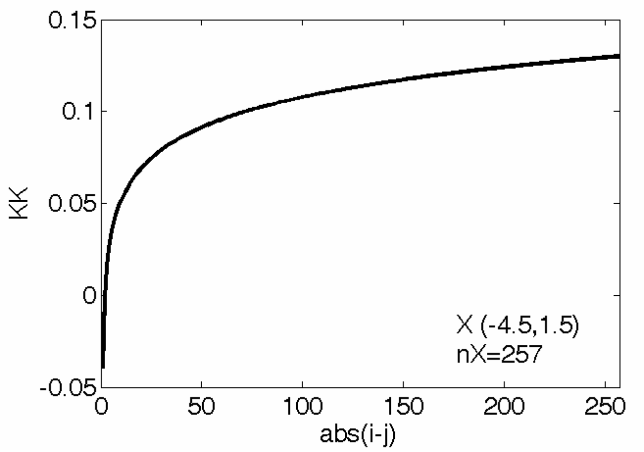

Fig. 3.4 The value of kernel as the distance varies

For the discretization problem, several relaxation approaches can be applied, such as the Jacobi dipole relaxation, the Newton-Raphson relaxation, and the Gauss-Seidel approach, etc. However, if only one relaxation is utilized, the convergence process may be not so satisfactory, especially for some special conditions (like a very heavy load condition or a very light load condition, for example). Venner [98] has applied the hybrid relaxation approach to suit a large variety of working conditions. The hybrid relaxation scheme, proposed by Venner [98], and used for solving the EHL model, is described as follows.

Look back to the steady state classical Reynolds equation in which the transient squeeze effect is not considered:

$$\frac{\partial}{\partial X}(\varepsilon\frac{\partial P}{\partial X})-\frac{\partial}{\partial X}(\bar{\rho}H)=0 \qquad (3.63)$$

Where $\varepsilon=\frac{\bar{\rho}H^3}{\bar{\eta}\lambda}$, $\lambda=\frac{12\eta_0 u_r R^2}{b^3 p_H}$.

We can see the coefficient ε decides the property of the equation. Owing to the exponential viscosity-pressure relation, the coefficient varies many orders of magnitude over the domain. In the inlet and outlet region, ε is very large, while in the centre area of Hertizian contact, region ε is very small.

When it is small enough, the Reynolds equation reduces to

$$\frac{\partial}{\partial X}(\overline{\rho} H) \approx 0 \tag{3.64}$$

Because the film thickness is given by an integral equation, this behaves like an integral problem. When ε is large enough, the Reynolds equation reduces to

$$\varepsilon \frac{\partial P^2}{\partial^2 X} \approx 0 \tag{3.65}$$

This looks like a Poisson problem: the differential aspects as represented by the second order derivative of the pressure determine the behaviour.

Understanding how to solve this model problem for large and small values of ε, respectively, forms the key to understanding how to construct an efficient solver for the complete EHL problem. It is believed that, when ε is large, the Gauss-Seidel relaxation is an efficient way to solve the problem. When ε is small, the distributive relaxation can take care of the stability problem. This is just the essence of the hybrid relaxation scheme proposed by Venner. This hybrid scheme is described in the following. In regions of large $\varepsilon / \Delta X^2$ new approximations to P_i read

$$\overline{\overline{P}}_i = \overline{P}_i + (\frac{\partial L_i}{\partial p_i})^{-1} r_i \tag{3.66}$$

Where r_i is the dynamic residual of the discrete Reynolds equation at the location X_i

$$\begin{gathered} r_i = -\frac{\varepsilon_{i-1/2}\overline{P}_{i-1} - (\varepsilon_{i-1/2} + \varepsilon_{i+1/2})\overline{P}'_i + \varepsilon_{i+1/2}\overline{P}'_{i+1}}{\Delta X^2} + \\ \frac{\overline{\rho}'_i \overline{H}'_i - \overline{\rho}'_{i-1} \overline{H}'_{i-1}}{\Delta X} + \frac{\overline{\rho}'_i \overline{H}'_i - \underline{\rho}_i \underline{H}_i}{\Delta \overline{t}} \end{gathered} \tag{3.67}$$

$$L_i = \frac{\varepsilon_{i-1/2}\overline{P}_{i-1} - (\varepsilon_{i-1/2} + \varepsilon_{i+1/2})\overline{P}'_i + \varepsilon_{i+1/2}\overline{P}'_{i+1}}{\Delta X^2} - \frac{\overline{\rho}'_i \overline{H}'_i - \overline{\rho}'_{i-1}\overline{H}'_{i-1}}{\Delta X} - \frac{\overline{\rho}'_i \overline{H}'_i - \underline{\rho}_i \underline{H}_i}{\Delta \bar{t}} \tag{3.68}$$

Recalling the expression of the film thickness H_i, the equation becomes

$$\frac{\partial L_i}{\partial P_i} \approx -\frac{\varepsilon_{i-1/2} + \varepsilon_{i+1/2}}{\Delta X^2} + \frac{1}{\pi}\frac{\overline{\rho}_i K_{i,i} - \overline{\rho}_{i-1} K_{i-1,i}}{\Delta X} + \frac{1}{\pi}\frac{\overline{\rho}_i K_{i,i}}{\Delta \bar{t}} \tag{3.69}$$

While in regions of small $\varepsilon / \Delta X^2$, the dipole change δ_i to be added to P_i and subtracted from P_{i-1} are calculated from

$$\delta_i = \left(\frac{\partial L_i}{\partial P_i} - \frac{\partial L_i}{\partial P_{i-1}}\right)^{-1} r_i \tag{3.70}$$

$$r_i = -\frac{\varepsilon_{i-1/2}\overline{P}'_{i-1} - (\varepsilon_{i-1/2} + \varepsilon_{i+1/2})\overline{P}'_i + \varepsilon_{i+1/2}\overline{P}'_{i+1}}{\Delta X^2} + \frac{\overline{\rho}'_i \overline{H}'_i - \overline{\rho}'_{i-1}\overline{H}'_{i-1}}{\Delta X} + \frac{\overline{\rho}'_i \overline{H}'_i - \underline{\rho}_i \underline{H}_i}{\Delta \bar{t}} \tag{3.71}$$

Since

$$\frac{\partial L_i}{\partial P_{i-1}} = \frac{\varepsilon_{i-1/2}}{\Delta X^2} + \frac{1}{\pi}\frac{\overline{\rho}'_i K_{i,i-1} - \overline{\rho}'_{i-1} K_{i,i}}{\Delta X} + \frac{1}{\pi}\frac{\overline{\rho}'_i K_{i,i-1}}{\Delta \bar{t}} \tag{3.72}$$

this leads to

$$\frac{\partial L_i}{\partial P_i} - \frac{\partial L_i}{\partial P_{i-1}} = -\frac{2\varepsilon_{i-1/2} + \varepsilon_{i+1/2}}{\Delta X^2} + \frac{(\overline{\rho}_i + \overline{\rho}_{i-1})}{\pi}\frac{K_{i,i} - K_{i-1,i}}{\Delta X} + \frac{1}{\pi}\frac{\overline{\rho}_i (K_{i,i} - K_{i-1,i})}{\Delta t} \tag{3.73}$$

It is worth noting that the dynamic residual r_i for the two relaxation schemes is slightly different because the one for the Gauss-Seidel relaxation scheme already incorporates the changes applied in the previous grid point. Fig. 3.5 shows the flowchart of this hybrid relaxation scheme.

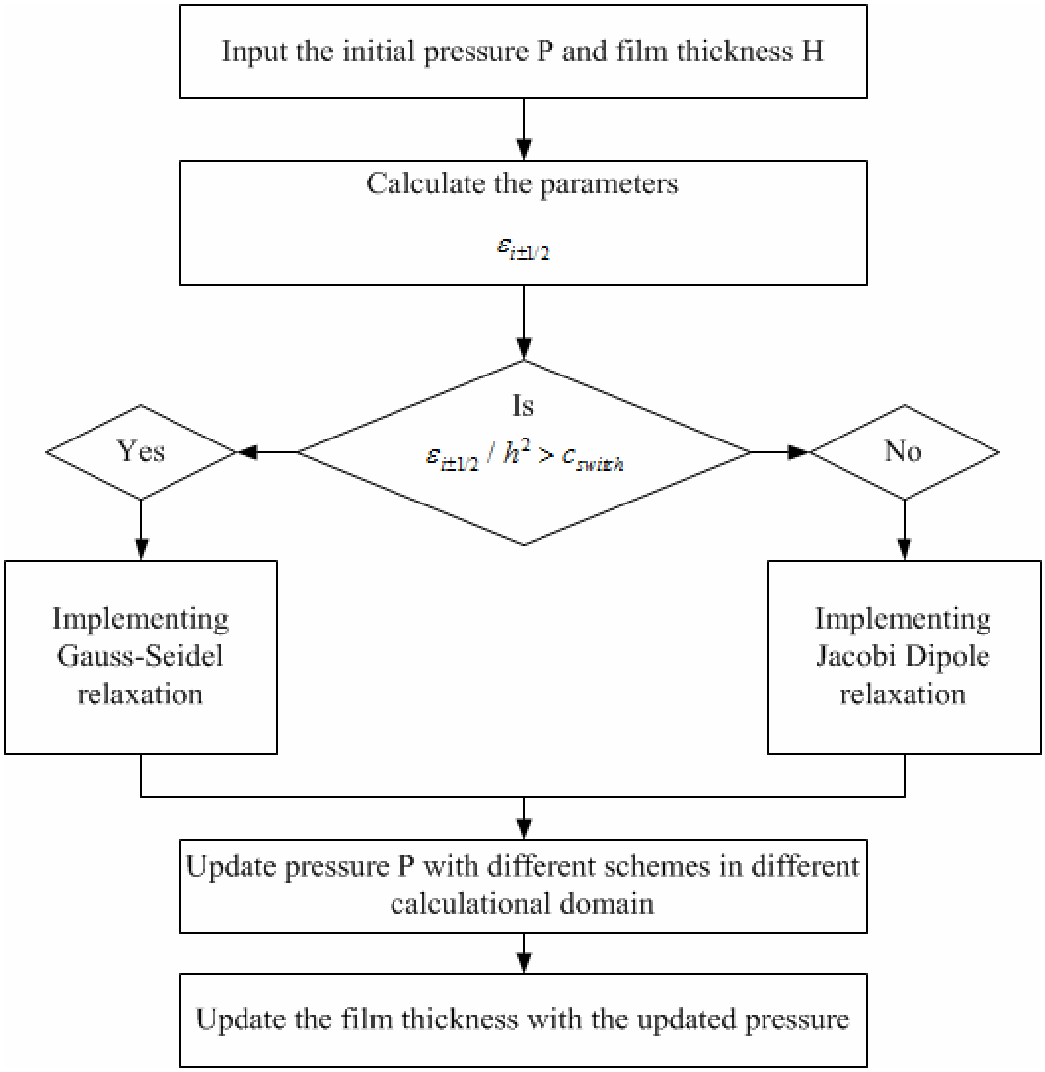

Fig. 3.5 Flowchart of the hybrid relaxation scheme proposed by Venner [98]

This hybrid relaxation scheme acts as an effective "smoother" in the multigrid framework. Combined with the hybrid relaxation scheme and the multigrid approach, convergence will be achieved very fast in a large regimes of operating conditions. Fig. 3.6 shows the way using the multigrid method can solve EHL problems.

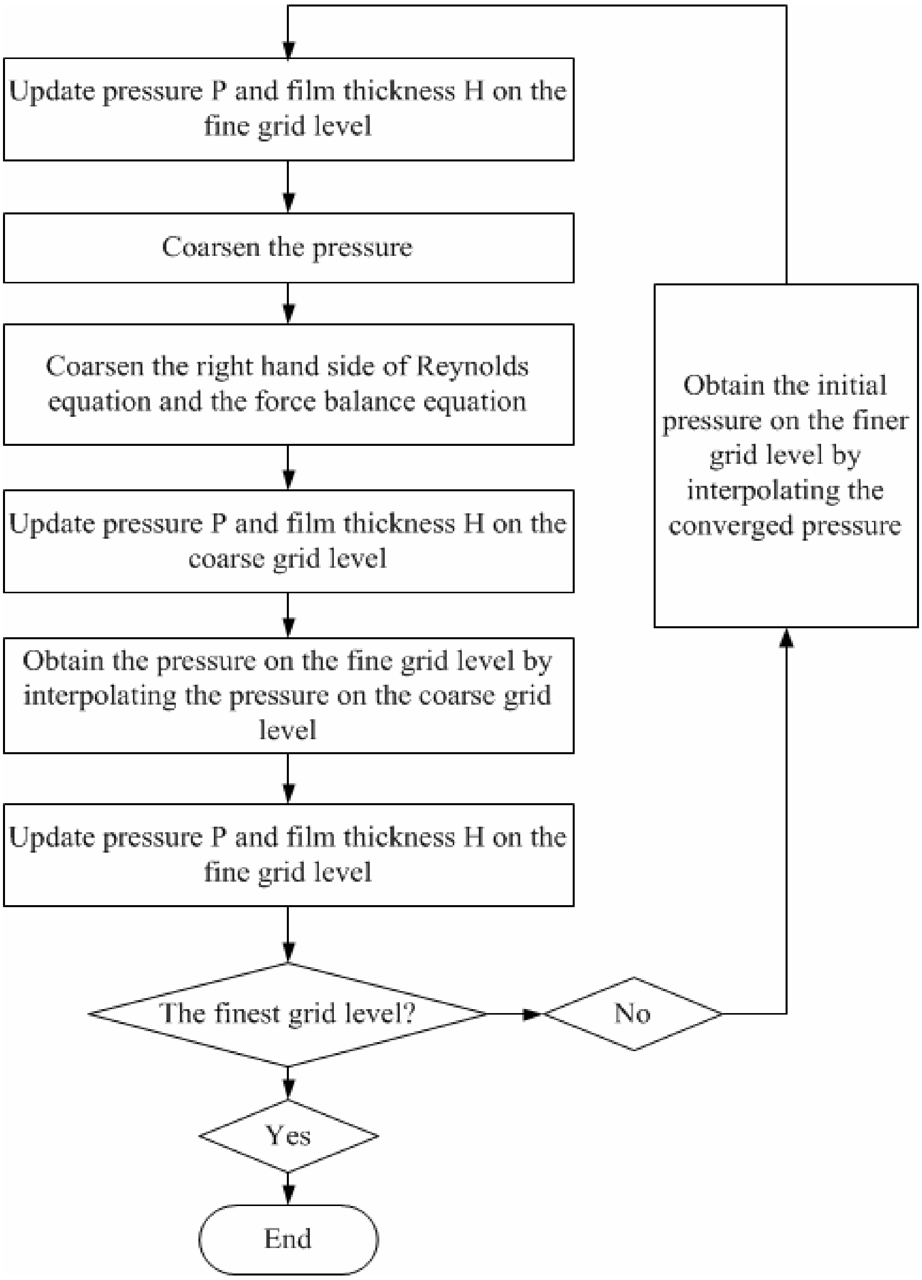

Fig. 3.6 Flowchart of the multigrid method solving EHL problems

The core idea of the multigrid method is that relaxations on different grid levels can help to eliminate all frequencies of error quickly, compared with a single grid level. The high frequency components of the error represent local behaviours, which result from the interactive coupling of the adjacent calculational nodes and are not closely related to boundary information or information of far-away nodes. On the other hand, the low frequency components of the error represent global behaviours. Some traditional iterative methods, like a Gauss-Seidel relaxation method or a Jacobi method with an under-relaxation factor, are effective to eliminate high frequency error components while having little effect on low frequency error components. When a traditional iterative method is applied, the error components with high frequency will be eliminated very quickly in the first several iterations. Since then the error represents a smooth behaviour - i.e. only low frequency components are exist. Solvers which can make the error smooth are referred to as smoothers. Given that the smoother can reduce errors of the frequency of the grid size, lower frequency errors can be eliminated by use of a coarser grid comparable to the order of the error. This approach can be extended to multiple levels. In this way, all kinds of frequency errors can be reduced quickly and convergence is achieved sooner. Details on implementing the multigrid method in dry contact and EHL problems can be found in Ref. [2]. Below are notes to remind readers to pay attention:

i. It should be realized that the multigrid method is just a way to speed up the convergence process. The elimination of error still relies on an appropriate smoother. If the high frequency components of the error decay faster than the low frequency components, then the iterative method is referred to as a smoother. In a multigrid process, the applied iterative method should be a smoother who can reduce the high frequency components of the error quickly. Error reduction can be evaluated by checking the iteration matrix and its eigenvalues [2] or conducting a local mode analysis, first proposed by Brandt [105].

ii. There are several ways to organize the coarse grid correction cycle, i.e. the V cycle, the W cycle, etc. Generally speaking there should be a limited number of iterations before transfer to a finer grid or a coarse one. Suppose ν_1 relaxation sweeps are carried out before they are transferred to a coarser grid and ν_2 relaxation sweeps carried out after they are transferred back from the coarser grid level, and ν_0 relaxation sweeps are conducted on the coarsest grid. If a coarse grid level is visited once before going back to a finer grid level, then the cycle is called V cycle, and noted with $V(\nu_1, \nu_2)$ cycle. On the other hand, if a coarse grid level is visited twice before going back to a finer grid level, the cycle is named W cycle, and noted with $W(\nu_1, \nu_2)$ cycle. It has been proven that W cycle holds a better convergence performance compared with V cycle, at least for the EHL problems where a global constraint - the force balance condition - exists. When a transient EHL problem (the transient effect should be taken into account in many cases, such as investigating a surface feature effect or a dynamic working condition effect on lubrication performance) is to be solved, an F cycle type is preferred because this kind of cycle could provide a first approximation with accuracy to the level of the truncation error for the next step. The only difference between the F cycle and others (like a V cycle or a W cycle) lies in the first approximation on the finest grid level. A more detailed description of the F cycle can be found in Ref. [106].

iii. When the cycle type is determined, the number of iterations - i.e. the pre-relaxation number ν_1, the post-relaxation number ν_2 and the relaxation number on the coarsest grid level ν_0 - should be determined as well. Fewer iterations will not eliminate all kinds of frequency components satisfactorily while more iterations will consume much more computer time without significant improvement of the accuracy. In order to find proper iteration numbers, the error reduction of the multigrid cycle should be evaluated. An accurate error reduction can be obtained with a two level analysis, which has been described by Brandt [107], Hemker [108], and others. This approach analyzes the effect of relaxations on the Fourier components of the error. The error reduction per cycle is given by the spectral radius of the two-level amplification matrix.

iv. Transfer operators, i.e. the restriction operator I_h^H and the prolongation operator I_H^h, are characterized by their orders. A rule of thumb is that the sum of the orders of the prolongation and of the restriction should at least be equal to the order of the differential equation solved [108]. When transferring the error to a coarser grid, the error is already smooth enough owing to the relaxations on a finer grid. In this case, a low order, say the first order, should be enough. For restriction operators, the most widely used are the injection ones and the full weighting ones. For prolongation operators, the most widely used are the linear (or multi-linear for multi-dimensional problems) ones. However, if multi-integration is used to calculate the elastic deformations, the order to treat the kernel should be higher owing to the character of the kernel, as explained by Brandt and Lubrecht [20]. The rougher the surface, the lower the order for multi-integration one should use to stay within discretization error. For detailed descriptions of the multi-integration on the elastic deformation calculation, or other applications such as the subsurface stress calculation, the reader can refer to Ref. [109, 110].

v. A basic EHL model, either a line contact problem or a point contact problem, can be written as a system of three main equations: the Reynolds equation, the film thickness equation, and the force balance equation. Those three equations form a nonlinear system with two basic unknowns - the pressure P and the film thickness H. Treating a nonlinear problem with the multigrid method is called the full approximation scheme (FAS). This implies that all three basic equations (the Reynolds equation, the film thickness equation and the force balance equation) should all be treated in the FAS scheme. Other equations appearing in EHL models, such as the density-pressure relation or the viscosity-pressure relation, can be implemented inside the relaxation scheme. Those equations do not need to be transferred between grids.

The multigrid iteration scheme may fail to converge for surfaces that are sufficiently rough to produce highly disconnected contact areas, although it does converge for smoother surfaces producing relatively simple contact areas. Thus, the applicability of the MG on rough surface EHL problems should be treated carefully.

3.3. Results and Discussions

3.3.1. Characteristics of EHL Solution

The EHL solution, as well as the dry contact solution are obtained for the case with the following parameters: $E' = 2\times10^{11}Pa$, $R = 1\times10^{-2}m$, $u_r = 1m/s$, $F = 1\times10^{5}N/m$, $sr = 1$. In the following work, if the value of the parameters E' and R are not explicitly specified, they are defined as identical to the ones used here. The dimensionless calculational domain is chosen as $X \in [-4.5, 1.5]$ and this domain is used elsewhere in this work except explicitly specified. Fig. 3.7 shows the difference between the EHL solution and the dry contact solution. The black solid line and the blue solid line represent the pressure distribution of the EHL solution and the dry contact solution, respectively, while the black dotted line and the blue dotted line represent the film thickness (or the gap height) of the EHL solution and the dry contact solution, respectively. For this smooth surface case, the dry contact solution is identical to the one obtained with the Hertzian contact theory. From Fig. 3.7 it is seen that there are several significant characteristics for an EHL solution; there is a pressure spike at the outlet zone of the Hertzian contact region; there is a gradually pressure built up at the inlet zone of the nominal contact zone; and for the Newtonian EHL, the film thickness is almost parallel with the Hertzian contact region, except there is a constriction at the outlet zone of the Hertzian contact region.

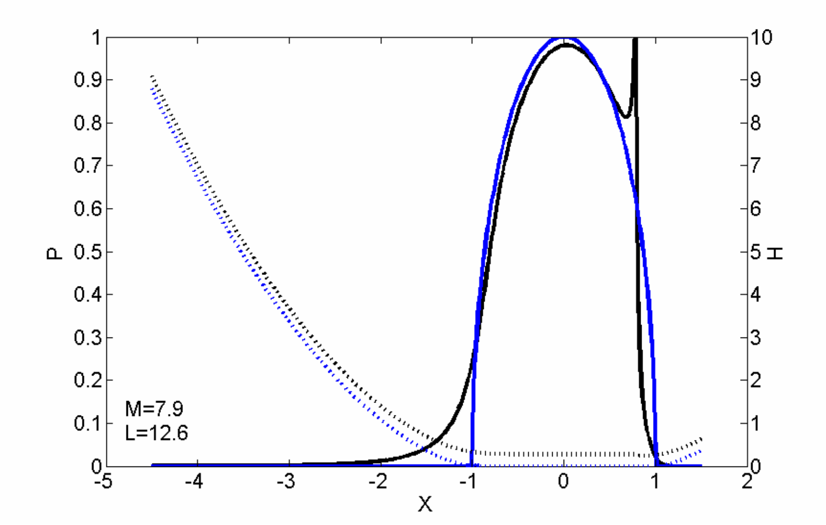

Fig. 3.7 Characteristics of a dimensionless EHL solution compared with dry contact solution

3.3.2. Effect of Calculation Domain and Mesh Density

Since for a light load case the calculation domain should be large enough to avoid any potential "numerical staving", the effect of the inlet zone on solutions is investigated. The light load case is chosen as: $F = 2\times 10^4 N/m$ and four calculation domains are studied: $X \in$[-4.5,1.5], [-6.5,1.5], [-8.5,1.5], and [-10.5,1.5]. As is seen from Fig. 3.8, variations of dimensionless pressure and film profile for those four domain cases are not quite remarkable which means it is fair to use [-4.5,1.5] for the light load cases studied in this thesis.

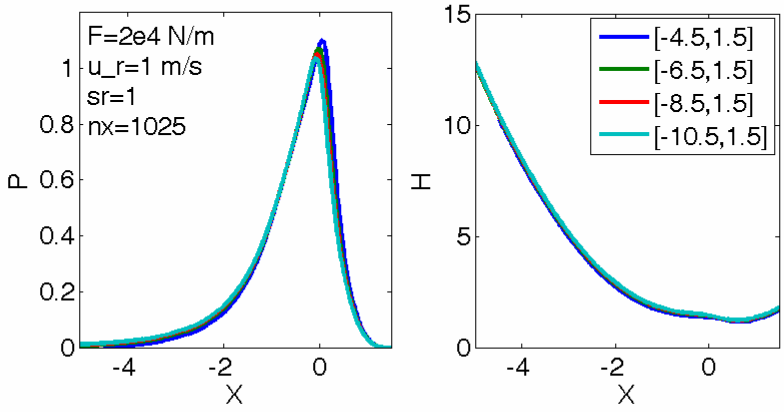

Fig. 3.8 Effect of calculation domain on pressure and film thickness

When the rolling speed is high, the "numerical staving" might also occur. In this work, a high speed case $u_r = 30 m/s$ is studied and the effect of calculation domain on this case is shown in Fig. 3.9. As is seen from Fig. 3.9, there is little variation of the pressure profile and the film profile for the four domains: $X \in$ [-4.5,1.5], [-6.5,1.5], [-8.5,1.5], and [-10.5,1.5]. $X \in$[-4.5,1.5] is enough for the speed regime studied in this work.

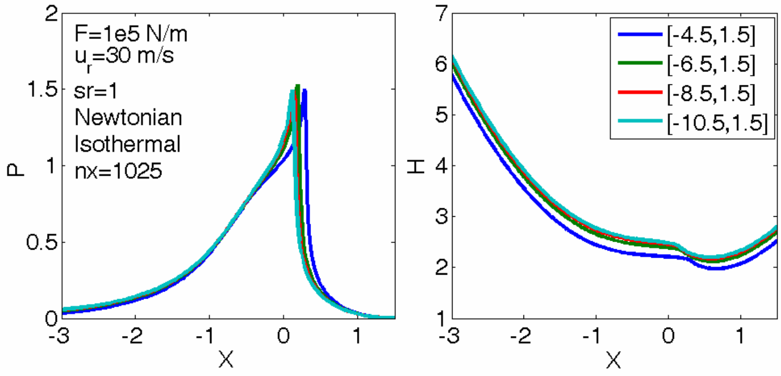

Fig. 3.9 Effect of calculation domain on pressure and film profile

Fig. 3.10 shows the effect of mesh density for the case $u_r = 1 m/s$, $F = 1 \times 10^5 N/m$, $sr = 1$. It is seen if attention is not paid to local, detailed information such as the location of the pressure spike - the mesh density with $nx = 1025$ is enough to represent accurate results. In the following work, if not explicitly specified, mesh density with $nx = 1025$ is used.

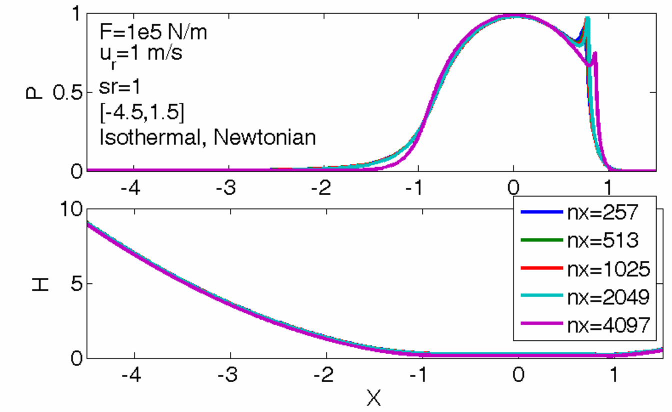

Fig. 3.10 Effect of mesh density on solution for the given case

3.4. Chapter Summary

A dry contact model and a classic EHL model are developed numerically in this chapter. Fundamental equations of the models are introduced. Typical characteristic behaviours of an EHL problem are described by comparison with the dry contact solution. The following conclusions can be made in this chapter:

- Compared with the dry contact solution, the EHL solution will show the pressure built up at the inlet zone and the second pressure spike and the film contraction at the outlet zone.
- For the working conditions studied - $F \in [2 \times 10^4 N/m, 3 \times 10^6 N/m]$ and $u_r \in [0.1m/s, 30m/s]$ - the calculation domain $X \in [-4.5, 1.5]$ used in this work is enough for avoiding "numerical starving". The mesh density chosen, $nx = 1025$, is enough for representing basic characteristic behaviours of solutions.

Chapter 4 Lubricant Non-Newtonian Behaviours

In this chapter, two non-Newtonian EHL models - the Ree-Eyring EHL model and the power-law EHL model - are developed to compare with the Newtonian model. The effects of non-Newtonian behaviours on pressure, film thickness, and shear stress distribution, amongst others, are studied. The influence of load, rolling speed and slide/roll ratio are shown for the Newtonian fluid, the Ree-Eyring fluid and the power-law fluid, respectively. The generalized Reynolds equation introduced in the previous chapter is used for considering those non-Newtonian fluid behaviours.

4.1. The Newtonian EHL Model

The classical Newtonian EHL model has already been described in the previous chapter. Here, in order to make a comparison with non-Newtonian models, essential formulae are given in terms of parameters of a generalized Reynolds equation. The way to calculate the shear stress and flow velocity for a Newtonian fluid is outlined below. For a Newtonian fluid, in terms of its constitutive equation, we have

$$u_b - u_a = \int_0^h \left(\frac{\tau_a}{\eta} + \frac{z}{\eta}\frac{\partial p}{\partial x}\right)dz = \tau_a \int_0^h \frac{1}{\eta}dz + \frac{\partial p}{\partial x}\int_0^h \frac{z}{\eta}dz \tag{4.1}$$

The shear stress on surface a, represented by τ_a, can then be calculated as

$$\tau_a = \frac{\eta_e(u_b - u_a)}{h} - \frac{\eta_e}{\eta'_e}\left(h\frac{\partial p}{\partial x}\right) \tag{4.2}$$

η_e and η'_e are parameters from the Yang-Wen generalized Reynolds equation and their expressions have been outlined previously.

The velocity of the film can be expressed as

$$u = u_a + \left(\int_0^z \frac{z'}{\eta^*}dz' - \frac{\eta_e}{\eta_e'}h\int_0^z \frac{1}{\eta^*}dz\right)\frac{\partial p}{\partial x} + \frac{\eta_e(u_b - u_a)}{h}\int_0^z \frac{1}{\eta^*}dz' \tag{4.3}$$

Introduce the dimensionless parameters

$X = x/b$, $P = p/p_{\mathrm{H}}$, $H = hR/b^2$, $Z = z/h$, $\bar{\rho} = \rho/\rho_0$, $\bar{\eta} = \eta/\eta_0$, $\bar{\tau} = \tau/p_H$,

$\bar{\tau}_a = \tau_a/p_H$, $\bar{\eta}^* = \eta^*/\eta_0$

We get the dimensionless form of τ_a for the Newtonian fluid

$$\bar{\tau}_a = \frac{(\bar{u}_b - \bar{u}_a)u_r - \dfrac{p_h \partial P}{\partial X}\dfrac{H^2 b^3}{R^2}\dfrac{1}{\eta_0 \bar{\eta}'_e}}{p_h H b^2/(R\bar{\eta}_e \eta_0)} \tag{4.4}$$

The dimensionless gradient of velocity of the Newtonian film is

$$\frac{\partial U}{\partial Z} = \frac{\partial(u/u_r)}{\partial(z/h)} = \frac{h}{u_r}\frac{\tau}{\eta} = \frac{h}{u_r}\frac{\tau_0 \bar{\tau}}{\eta_0 \bar{\eta}} = \frac{Hb^2 \tau_0}{R u_r \eta_0}\frac{\bar{\tau}}{\bar{\eta}} \tag{4.5}$$

4.1.1. Effect of Load with the Isothermal Model

The working condition is chosen as: $u_r = 1m/s$, $sr = 1$. Fig. 4.1 shows the effect of load on pressure and film profile for a Newtonian fluid. As the load increases, the pressure profile becomes close to the Hertzian solution. As the load increases, the second pressure spike gets smaller and closer to the outlet edge; meanwhile, the inlet zone gets smaller, as does the film thickness.

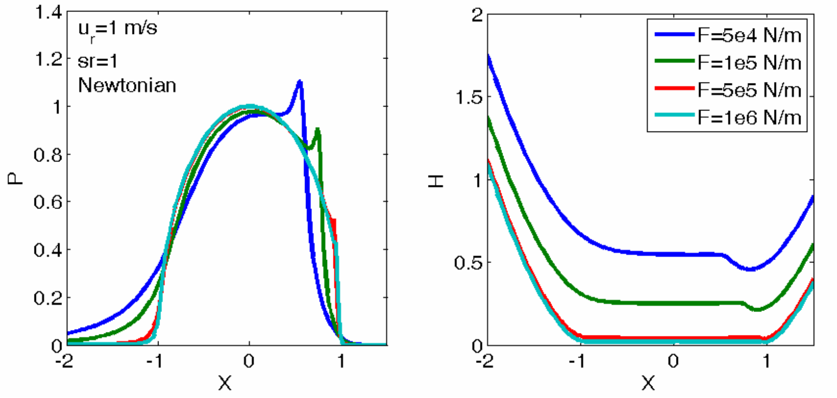

Fig. 4.1 Effect of load on pressure and film profile with the isothermal Newtonian model

Film thickness is one of the most popular parameters used in industry to evaluate the lubrication performance of gears, cams, bearings, etc. The effect of load on minimum film thickness is studied for the isothermal, Newtonian fluid. Fig. 4.2 shows the minimum film thickness within a large load regime for the case: $u_r = 1m/s$, $sr = 1$. As is seen, for both the numerical solutions and the Dowson-Higginson empirical results, the minimum film thickness varies exponentially with the load, approximately. The Dowson-Higginson formula [111] reads:

$$h_m = 2.65RU^{0.7}G^{0.54}W^{-0.13} \tag{4.6}$$

where R is the equivalent contact radius, U, G and W are the speed parameter, material parameter and load parameter, respectively. Those dimensionless parameters are already defined in the previous chapter. The exponential value of W used by Dowson and Higginson for this relation is -0.13, while others may choose a different exponential value.

For the load cases studied, the minimum film thicknesses are with the scale of sub-micrometres. This film thickness might have the same magnitude as the surface roughness for most gear tooth surfaces, which would be worth noticing because film failure may occur within the nominal contact zone for those sliding rough surface cases.

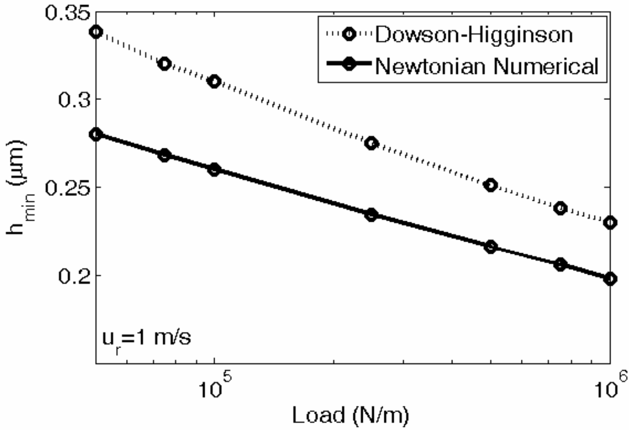

Fig. 4.2 Effect of load on minimum film thickness with the isothermal Newtonian model

Fig. 4.3 shows the load effect on the dimensionless shear stress on the interface surface a, $\bar{\tau}_a$, with the isothermal Newtonian model. It is seen that as the load increases, the value of $\bar{\tau}_a$ within the contact zone increases as well which would lead to a larger traction.

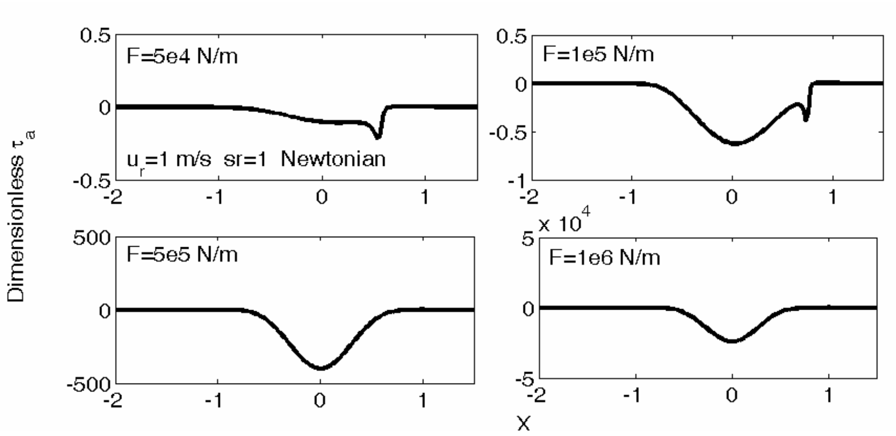

Fig. 4.3 Effect of load on $\bar{\tau}_a$ with the isothermal Newtonian model

The tangential force behaviour could be studied more clearly from a friction coefficient curve, as shown in Fig. 4.4. Fig. 4.4 shows the effect of load on friction coefficient for a Newtonian fluid under the isothermal condition. It shows that the friction coefficient value increases significantly with the load. When the load is high, the friction coefficient value obtained under the isothermal, Newtonian assumption exceeds unity, which is physically impossible. It shows clearly that in terms of friction coefficient, the isothermal Newtonian model is clearly not a good idea. The thermal effect, as well as the non-Newtonian effect, should be considered in a friction analysis because those factors affect the friction behaviour in a remarkable way, as is seen in the following sections.

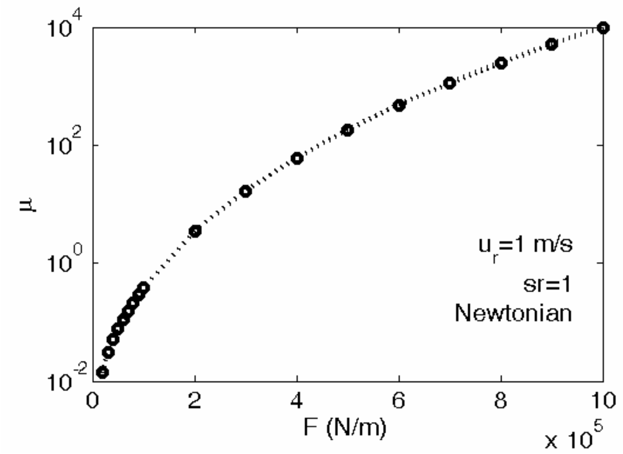

Fig. 4.4 Effect of load on friction coefficient with the isothermal Newtonian model

Fig. 4.5 shows the effect of load on the dimensionless viscosity of the film $\bar{\eta}$ with the isothermal Newtonian model. It is seen that, as the load increases, the value of $\bar{\eta}$ inside the contact zone increases. This increase of the viscosity is believed to be responsible for the increase of traction.

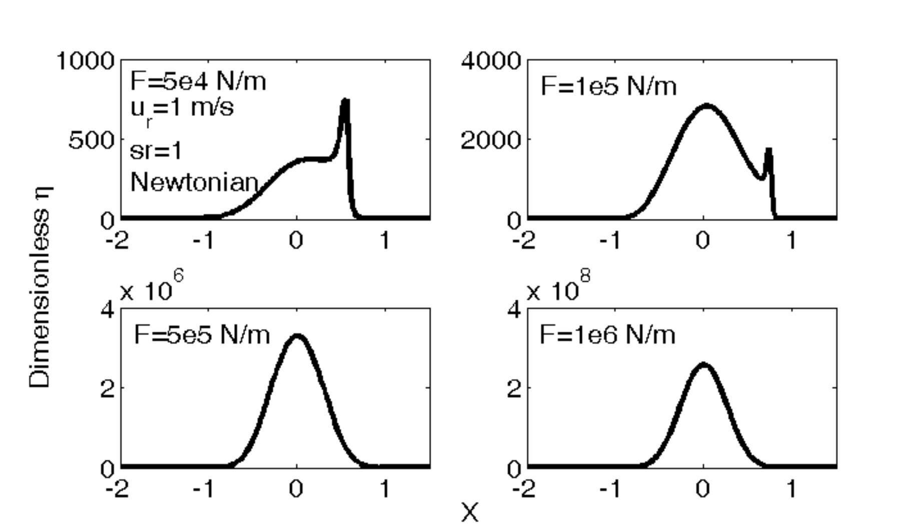

Fig. 4.5 Effect of load on $\bar{\eta}$ with the isothermal Newtonian model

Fig. 4.6 shows the effect of load on the velocity field of the film with the isothermal Newtonian model. It shows that the value of the velocity at the inlet zone within the film may become negative, which is referred to as the “inverse flow”. In order to study the load effect on velocity more clearly, information about the velocity distribution at the central layer of the film is given in Fig. 4.7. It is seen that, as the load increases, the “inverse flow” zone moves towards the central area of the nominal contact zone. The absolute maximum value of the velocity of the “inverse flow” zone does not change significantly when the load varies.

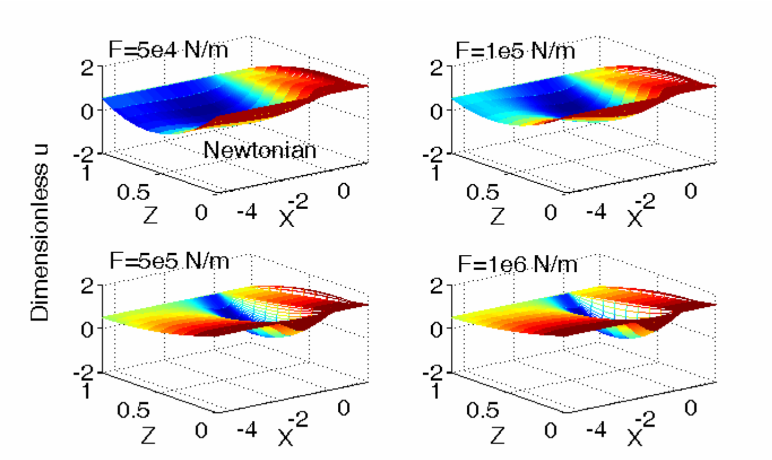

Fig. 4.6 Effect of load on velocity field of the film with the isothermal Newtonian model

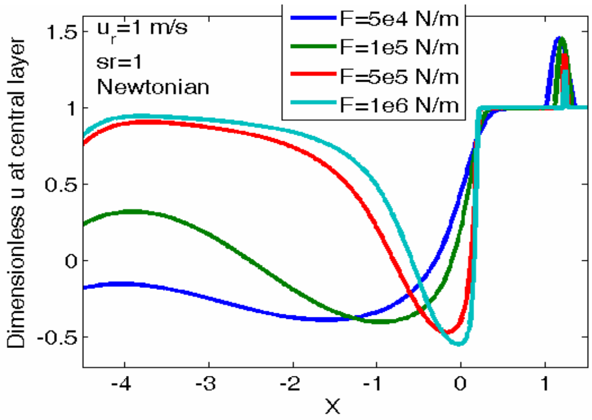

Fig. 4.7 Effect of load on distribution of $\overline{u}$ at the central layer of the film with the isothermal Newtonian model

4.1.2. Effect of Rolling Speed with the Isothermal Model

The effect of rolling speed with the isothermal Newtonian model is studied. Fig. 4.8

shows the effect of rolling speed on the pressure and film profile for a Newtonian fluid. It is seen that, as the rolling speed decreases, the pressure profile becomes close to the Hertzian solution. As the rolling speed decreases, the second pressure spike gets smaller and closer to the outlet edge; meanwhile, the inlet zone gets smaller, as does the film thickness.

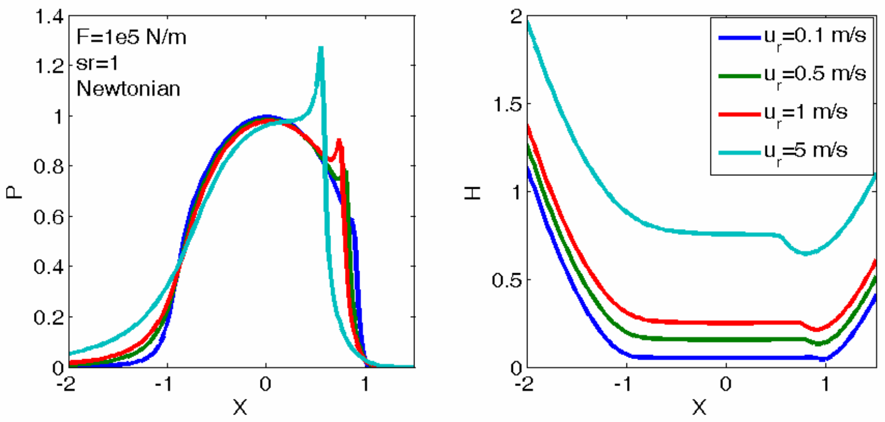

Fig. 4.8 Effect of rolling speed on pressure and film profile with the isothermal Newtonian model

The effect of rolling speed is also studied for the isothermal, Newtonian case. The effect of rolling speed on minimum film thickness is studied by showing the numerical results and their Dowson-Higginson counterparts. As is seen from Fig. 4.9, the minimum film thickness increases as the rolling speed goes up. At high speeds, the Dowson-Higginson formula overestimates the minimum film thickness slightly.

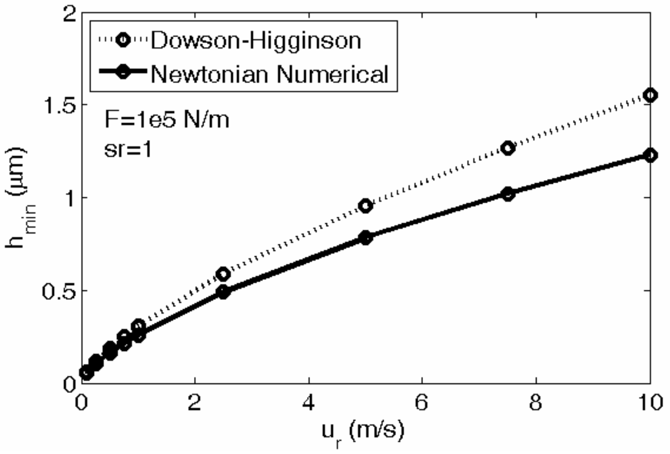

Fig. 4.9 Effect of rolling speed on minimum film thickness for an isothermal, Newtonian fluid

Although in the load effect section we conclude that it is not reasonable to predict friction with the isothermal Newtonian model, the effect of rolling speed on friction is still studied to help readers understand the relationship between rolling speed and the friction. Fig. 4.10 shows the effect of rolling speed on $\bar{\tau}_a$ with the isothermal Newtonian model. It is seen that as the rolling speed increases, the value of $\bar{\tau}_a$ within the contact zone increases as well which would lead to a larger traction.

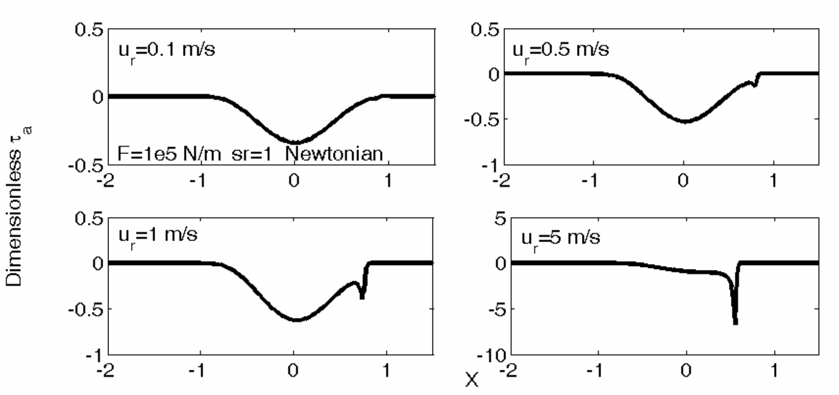

Fig. 4.10 Effect of rolling speed on $\bar{\tau}_a$ with the isothermal Newtonian model

Fig. 4.11 shows the effect of the rolling speed on the friction coefficient with the isothermal Newtonian model. It is seen that, as the rolling speed increases, the value of the friction coefficient increases almost linearly.

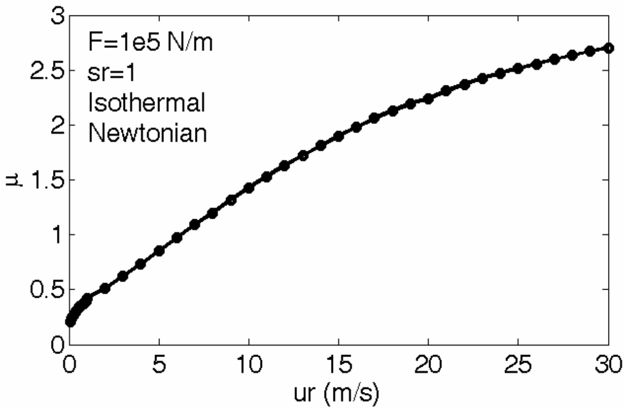

Fig. 4.11 Effect of rolling speed on friction coefficient with the isothermal Newtonian model

Fig. 4.12 shows the effect of the rolling speed on $\bar{\eta}$ with the isothermal Newtonian model. It is seen when the rolling speed is not high, as the rolling speed increases, the value of $\bar{\eta}$ does not change significantly; however, when the rolling speed is high, the second spike of the $\bar{\eta}$ profile is more evident.

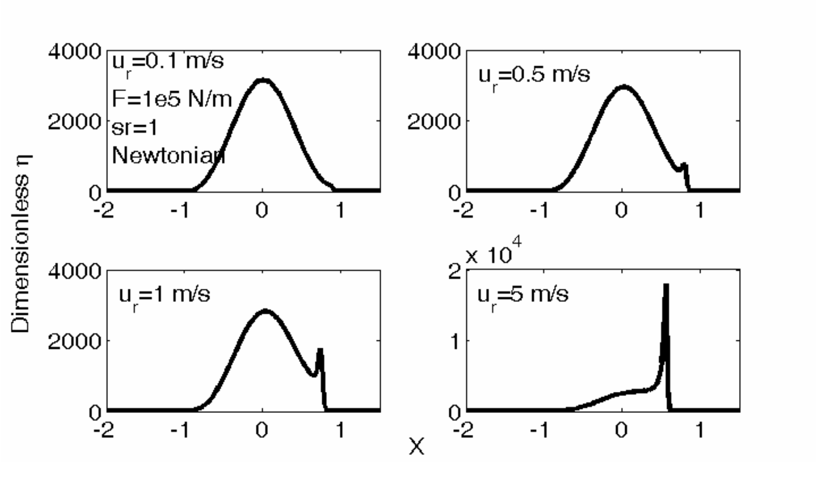

Fig. 4.12 Effect of rolling speed on $\bar{\eta}$ with the isothermal Newtonian model

Fig. 4.13 shows information on the distribution of $\bar{u}$ at the central layer of the film. It can be seen from Fig. 4.13 that, as the speed decreases, the "inverse flow" zone moves towards the central area of the nominal contact zone. The absolute maximum value of the velocity of the "inverse flow" zone does not change significantly when the rolling speed varies.

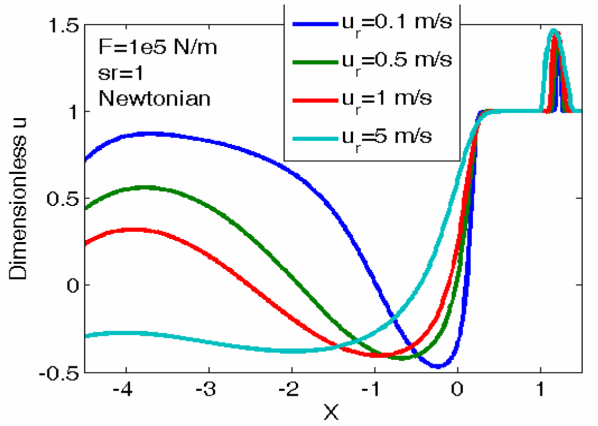

Fig. 4.13 Effect of rolling speed on distribution of $\bar{u}$ at the central layer of the film with the isothermal Newtonian model

4.1.3. Effect of Slide/Roll Ratio with the Isothermal Model

The effect of the slide/roll ratio with the isothermal Newtonian model is studied in this section. Fig. 4.14 shows the effect of the slide/roll ratio on the pressure and film profile for a Newtonian fluid. It is seen that for the working condition chosen, the slide/roll ratio has almost no effect on pressure and film profile at all.

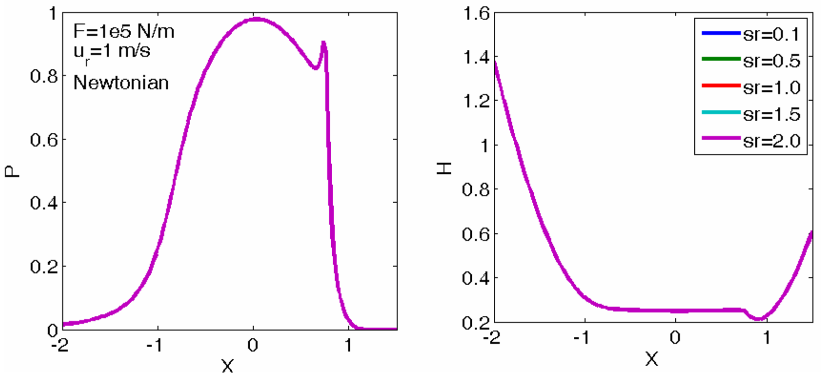

Fig. 4.14 Effect of slide/roll ratio on pressure and film profile with the isothermal Newtonian model

The effect of the slide/roll ratio on the minimum film thickness is studied and the result is shown in Fig. 4.15. It is seen that the slide/roll ratio has a very limited influence on the minimum film thickness for an isothermal, Newtonian fluid. The minor fluctuation of the minimum film thickness value as the slide/roll ratio varies is believed to be caused by the numerical convergence process.

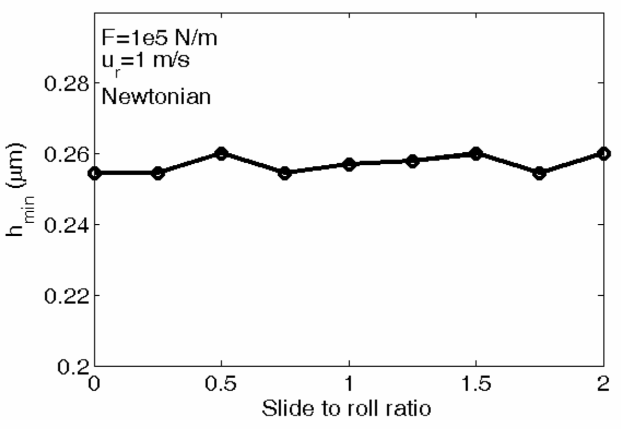

Fig. 4.15 Effect of slide/roll ratio on minimum film thickness for a Newtonian fluid

Fig. 4.16 shows the effect of the slide/roll ratio on $\bar{\tau}_a$. It is seen that as the slide/roll ratio increases, the value of $\bar{\tau}_a$ within the contact zone increases.

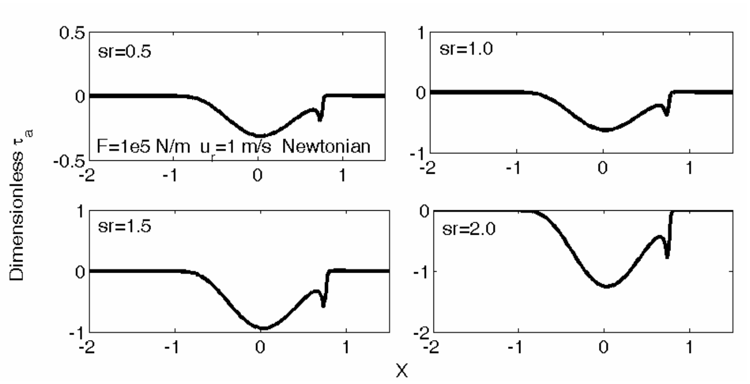

Fig. 4.16 Effect of slide/roll ratio on $\bar{\tau}_a$ with the isothermal Newtonian model

Fig. 4.17 shows the effect of the slide/roll ratio on the friction coefficient with the isothermal Newtonian model. It is seen that, the value of friction coefficient goes up linearly with the slide/roll ratio. This is easy to understand because the shear stress within the nominal contact zone is directly determined by the velocity difference between the two interacting solid surfaces.

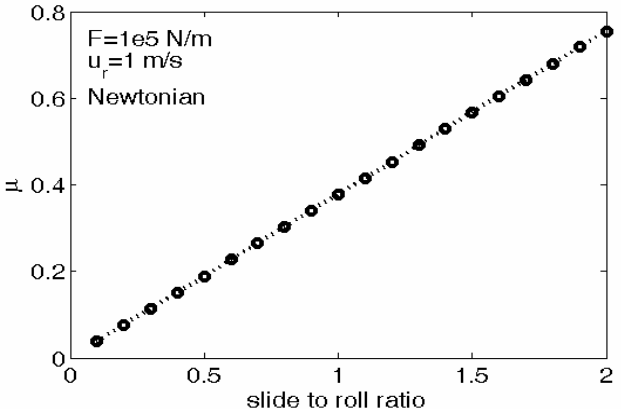

Fig. 4.17 Effect of slide/roll ratio on friction coefficient with the isothermal Newtonian model

Fig. 4.18 shows the effect of the slide/roll ratio on $\bar{\eta}$ for a Newtonian fluid. It is seen that the slide/roll ratio does not affect $\bar{\eta}$ at all for a Newtonian fluid.

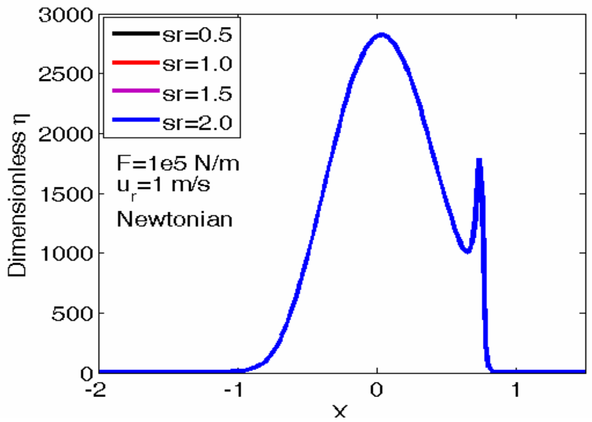

Fig. 4.18 Effect of slide/roll ratio on $\bar{\eta}$ with the isothermal Newtonian model

Fig. 4.19 shows the effect of the slide/roll ratio on the distribution of $\bar{u}$ at the central layer of the film. It is seen that the slide/roll ratio does not affect the velocity distribution in the film at all.

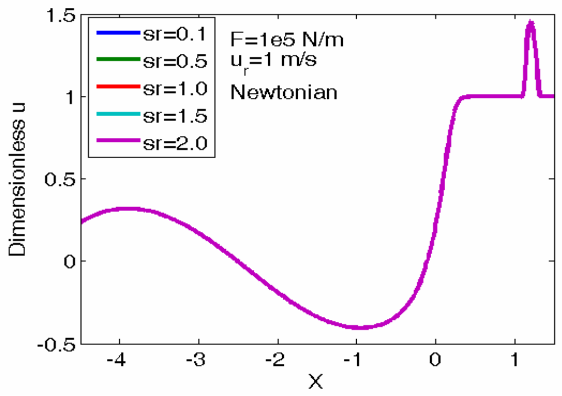

Fig. 4.19 Effect of slide/roll ratio on distribution of $\bar{u}$ at the central layer of the film with the isothermal Newtonian model

4.2. The Ree-Eyring EHL Model

4.2.1. Governing Equations

The constitutive equation of a Ree-Eyring fluid can be expressed as

$$\dot{\gamma} = \frac{\partial u}{\partial z} = \frac{\tau_0}{\eta} \sinh\left(\frac{\tau}{\tau_0}\right) \tag{4.7}$$

Where $\dot{\gamma}$ is the shear strain rate, τ_0 is the Eyring stress. If τ_0 goes to infinity, the constitutive equation becomes close to the Newtonian one because mathematically we have

$$\lim_{\tau_0 \to \infty} \frac{\sinh(\tau / \tau_0)}{\tau / \tau_0} = 1 \tag{4.8}$$

Regardless of whether a Newtonian fluid or a non-Newtonian fluid is assumed, the shear stress inside the film can always be expressed as

$$\tau = \tau_a + z \frac{\partial p}{\partial x} \tag{4.9}$$

Substituting this equation into the Ree-Eyring constitutive equation and integrating along the z direction (across the film) we get

$$\int_0^h \frac{\tau_0}{\eta}\sinh\left(\frac{\tau_a}{\tau_0}+\frac{z}{\tau_0}\frac{\partial p}{\partial x}\right)dz = u_b - u_a \tag{4.10}$$

It is important to remember the non-sliding condition, that is at $z = 0$, $u = u_a$ and at $z = h$, $u = u_b$, is used to get the above equation.

Since mathematically

$$\sinh(x+y) = \sinh x \cosh y + \cosh x \sinh y \tag{4.11}$$

Equation 4.10 can then be rewritten as

$$\sinh(\tau_a/\tau_0)F_1 + \cosh(\tau_a/\tau_0)F_2 = u_b - u_a \tag{4.12}$$

Where

$$\begin{cases} F_1 = \int_0^h \frac{\tau_0}{\eta}\cosh\left(\frac{z}{\tau_0}\frac{\partial p}{\partial x}\right)dz \\ F_2 = \int_0^h \frac{\tau_0}{\eta}\sinh\left(\frac{z}{\tau_0}\frac{\partial p}{\partial x}\right)dz \end{cases} \tag{4.13}$$

If $\partial p/\partial x$ and η are known, then for a given x, F_1 and F_2 can be calculated through numerical integration, which makes Eq. 4.12 with only one variable τ_a. τ_a can be solved analytically for the Ree-Eyring fluid

$$\tau_a = \tau_0 \ln\frac{(u_b-u_a)+\sqrt{(u_b-u_a)^2+(F_1^2+F_2^2)}}{F_1+F_2} \tag{4.14}$$

Once τ_a is calculated, the shear stress distribution τ across the film can be obtained using Eq. 4.9. Then the equivalent viscosity η^* can be solved as below

$$\eta^* = \eta(\tau/\tau_0)/\sinh(\tau/\tau_0) \tag{4.15}$$

The equivalent viscosity can be used in the generalized Reynolds equation for pressure updating.

Once the shear stress τ is solved, $\partial u/\partial z$ can be calculated using the fluid constitutive equation. The fluid velocity field can be expressed as

$$u = u_a + \int_0^z \frac{\partial u}{\partial z} dz' \tag{4.16}$$

And of course, for the Ree-Eyring fluid, the velocity could also be calculated using the parameters of the generalized Reynolds equation as

$$\begin{aligned} u = u_a &+ \left(\int_0^z \frac{z'dz'}{\eta^*} - \frac{\eta_e}{\eta_e'} \int_0^z \frac{dz'}{\eta^*}\right) \frac{\partial p}{\partial x} \\ &+ \frac{\eta_0 (u_b - u_a)}{h} \int_0^z \frac{dz'}{\eta^*} \end{aligned} \tag{4.17}$$

4.2.2. Dimensionless Equations

Beside the dimensionless parameters introduced in the Newtonian EHL model, additional parameters are introduced to describe the dimensionless Ree-Eyring EHL model:

$$\bar{\tau}_0 = \tau_0 / p_H \tag{4.18}$$

$$\begin{cases} \bar{F}_1 = F_1 \eta_0 R / (p_H b^2) \\ \bar{F}_2 = F_2 \eta_0 R / (p_H b^2) \end{cases} \tag{4.19}$$

$$CH = p_H b^2 / (\eta_0 u_r R) \tag{4.20}$$

The dimensionless shear stress on surface a is expressed as

$$\bar{\tau}_a = \bar{\tau}_0 \ln \frac{\sqrt{(u_a - u_b)^2 + CH^2 (\bar{F}_1^2 - \bar{F}_2^2)} - (u_a - u_b)}{CH(\bar{F}_1 + \bar{F}_2)} \tag{4.21}$$

The dimensionless velocity gradient can be expressed as

$$\frac{\partial \bar{u}}{\partial Z} = CH \cdot H \frac{\bar{\tau}_0}{\bar{\eta}} \sinh\left(\frac{\bar{\tau}}{\bar{\tau}_0}\right) \tag{4.22}$$

The dimensionless flow velocity then reads

$$\bar{u} = \bar{u}_a + \int_0^1 \frac{\partial \bar{u}}{\partial Z} dZ' \tag{4.23}$$

4.2.3. Results and Discussion

Fig. 4.20 shows the pressure and film profiles of the Newtonian-based solution and Ree-Eyring-based solution under the case $u_r = 1m/s$, $F = 1\times10^5 N/m$, $sr = 1$. The Eyring stress is chosen as $\tau_0 = 1\times10^7 Pa$ and unless it is specified explicitly this value is used elsewhere. It is seen that compared with the Newtonian solution, two main differences are shown for the Ree-Eyring results. The film profile is not as parallel as the Newtonian one within the Hertzian contact region, while the minimum film thickness at the outlet zone does not change significantly compared with the Newtonian value. In addition, the second pressure spike at the outlet zone is not as significant as the Newtonian one.

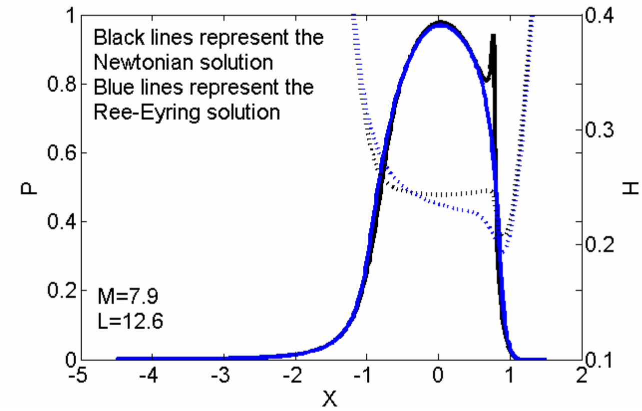

Fig. 4.20 Comparison of Newtonian-based solution and Ree-Eyring with $\tau_0 = 1\times10^7 Pa$ solution

4.2.3.1. Effect of Load with the Isothermal Ree-Eyring Model

The effect of the load for a Ree-Eyring fluid is studied with the following parameters: $u_r = 1m/s$, $sr = 1$. The minimum film thicknesses have been investigated by other researchers extensively and their numerical results are compared with empirical formulas such as the Dowson-Higginson formula [111] and the Moes formula, which can be found in Ref. [98]. In this work, more attention is paid to the tangential force bahaviour.

Fig. 4.21 shows the effect of load on the pressure profile and film profile with the isothermal Ree-Eyring model. For the pressure profile, the effect of load for a Ree-Eyring fluid is similar to the effect of load for a Newtonian fluid. That is, as the load increases, the second spike is less evident and the location of the second spike comes close to the outlet edge of the nominal contact zone; the inlet zone shrinks when the load increases. In terms of the film thickness, the effect of load for a Ree-Eyring fluid is also similar to the effect of load for a Newtonian fluid.

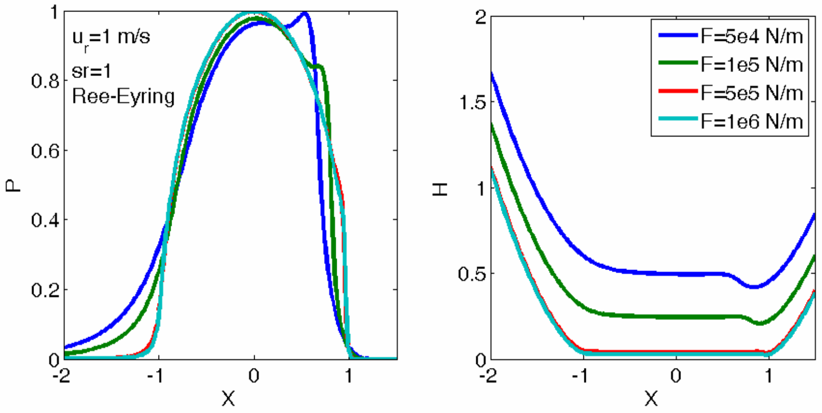

Fig. 4.21 Effect of load on pressure and film profile with the isothermal Ree-Eyring model

Fig. 4.22 shows the effect of load on the friction coefficient with the isothermal Ree-Eyring model. The x scale of the left subfigure is linear while the x scale of the right one is given in its logarithmic form. When the load is light, the value of the friction coefficient increases significantly. When the load is high and as the load keeps increasing, the value of the friction coefficient does not change too significantly. If the load is very high (such as $F > 1.5 \times 10^6 N/m$) and it keeps increasing, the friction coefficient will drop gradually.

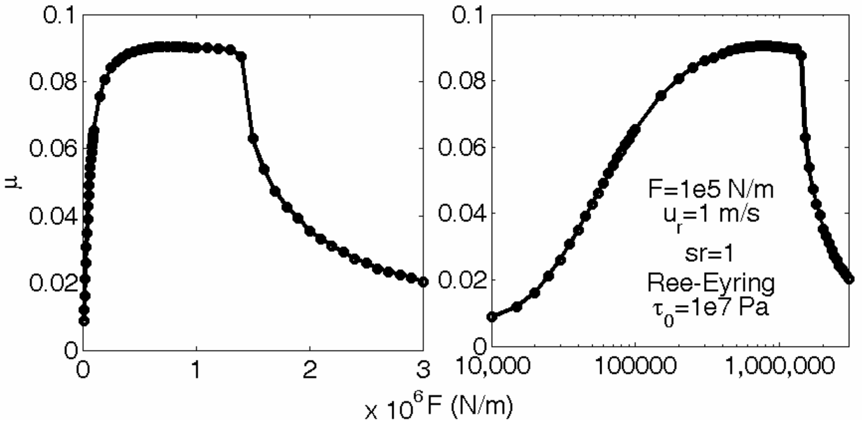

Fig. 4.22 Effect of load on friction coefficient with the isothermal Ree-Eyring model

Fig. 4.23 shows the effect of load on $\bar{u}$ at the central layer of the film with the isothermal Ree-Eyring model. It is seen that, the load affects the fluid velocity distribution of the inlet zone significantly. The fluid velocity in the nominal contact zone does not change significantly as the load changes. It is worth noting that for some cases shown in Fig. 4.23, the fluid velocity might become negative, which is referred to as "reverse flow". The reverse flow in the inlet zone will cause some numerical difficulty for thermal EHL solutions which will be discussed in the following thermal EHL chapter.

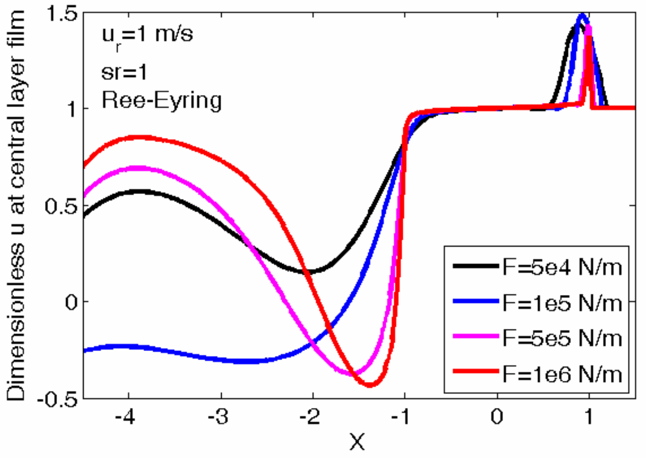

Fig. 4.23 Effect of load on $\bar{u}$ at the central layer of the film with the isothermal Ree-Eyring model

4.2.3.2. Effect of Rolling Speed with the Isothermal Ree-Eyring Model

Fig. 4.24 shows the effect of rolling speed on the pressure and film profile for an isothermal Ree-Eyring fluid. The trend is similar to the Newtonian one.

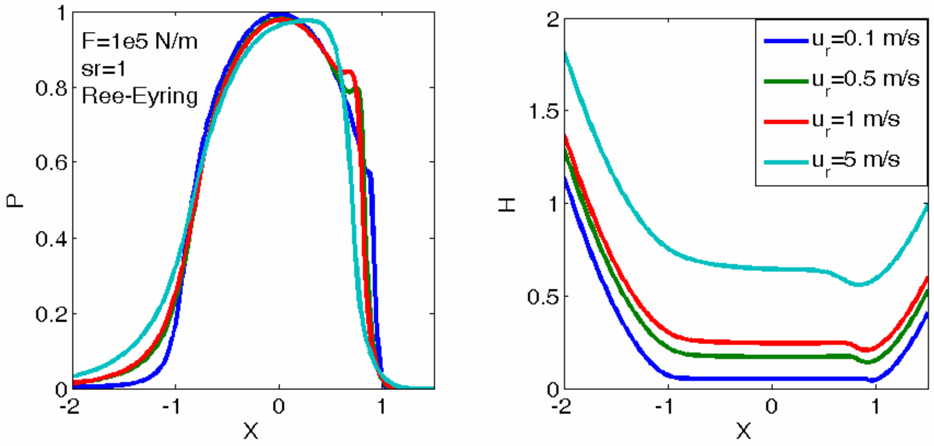

Fig. 4.24 Effect of rolling speed on pressure and film profile with a Ree-Eyring fluid with $\tau_0 = 1\times 10^7 Pa$

Fig. 4.25 shows the effect of rolling speed on $\overline{\tau}_a$ for a Ree-Eyring fluid. As the speed increases, the value of $\overline{\tau}_a$ inside the nominal contact zone increases first and if the speed keeps increasing, the value of $\overline{\tau}_a$ within the nominal contact zone does not change significantly.

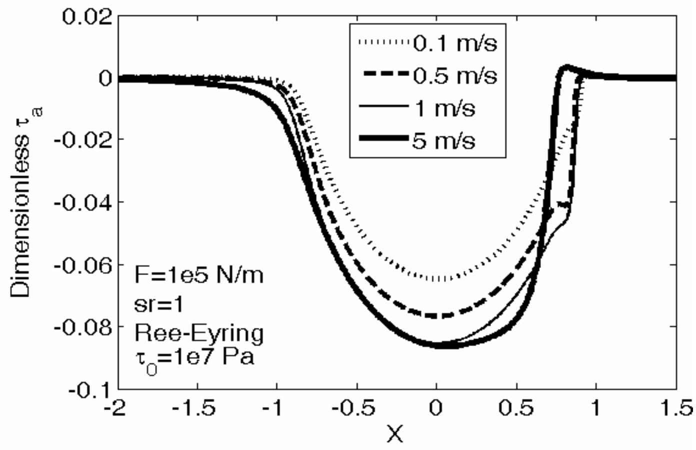

Fig. 4.25 Effect of rolling speed on dimensionless shear stress for a Ree-Eyring fluid

with $\tau_0 = 1 \times 10^7 Pa$

Fig. 4.26 shows the effect of rolling speed on the friction coefficient for a Ree-Eyring fluid. To help readers understand the trend, two scales of x are given: a linear scale on the left and a logarithmic scale on the right. It is seen that when the speed is not high, as the speed goes up, the value of the friction coefficient goes up significantly and if the speed goes up more, the value of the friction coefficient increases much more slowly.

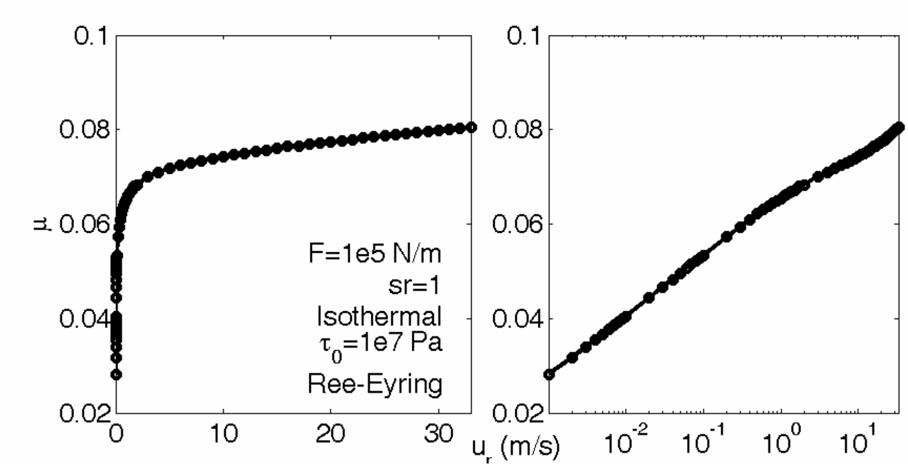

Fig. 4.26 Effect of rolling speed on friction coefficient for a Ree-Eyring fluid with $\tau_0 = 1 \times 10^7 Pa$

Fig. 4.27 shows the effect of rolling speed on $\bar{u}$ at the central layer of the film for a Ree-Eyring fluid. It is seen that, like the Newtonian solutions, the fluid velocity inside the nominal contact zone does not change significantly as the rolling speed changes. Reverse flow at the inlet zone still might occur under some speed conditions.

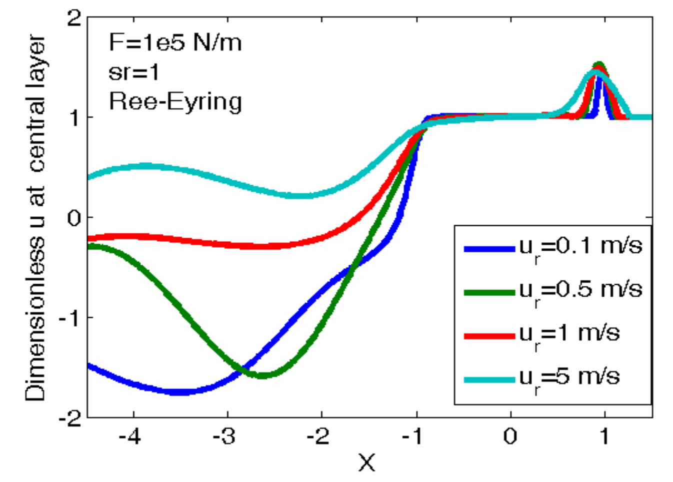

Fig. 4.27 Effect of rolling speed on $\bar{u}$ at central layer of the film for a Ree-Eyring fluid with $\tau_0 = 1 \times 10^7 Pa$

4.2.3.3. Effect of Slide/Roll Ratio with the Isothermal Ree-Eyring Model

The effects of the slide/roll ratio on the pressure profile, shear stress and friction coefficient are studied. Fig. 4.28 shows the effect of slide/roll ratio on pressure and film profile. For the pressure profile, the slide/roll ratio only affects the second spike at the outlet zone. While referred to the film profile, the slide/roll ratio does not affect the film thickness remarkably.

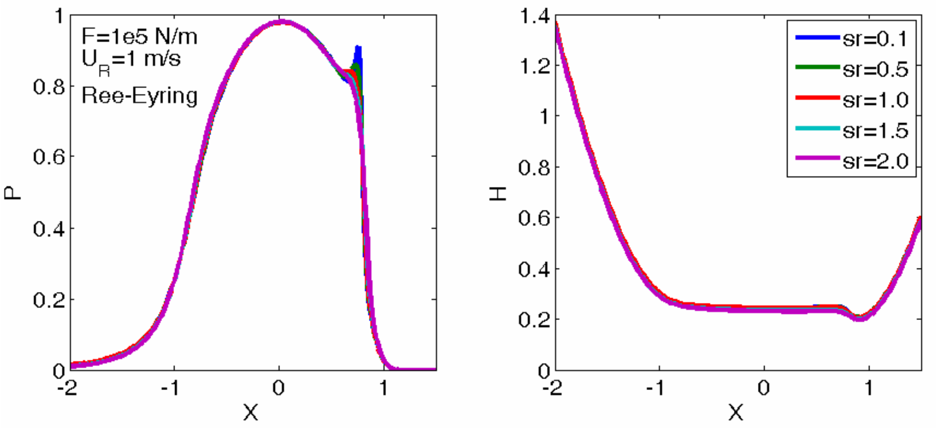

Fig. 4.28 Effect of slide/roll ratio on pressure and film profile with a Ree-Eyring fluid with $\tau_0 = 1 \times 10^7 Pa$

Fig. 4.29 shows the effect of the slide/roll ratio on $\overline{\tau_a}$ for a Ree-Eyring fluid. As is seen, the value of $\overline{\tau_a}$ within the nominal contact zone increases with the increasing slide/roll ratio. However, this trend is slower when the slide/roll ratio is high.

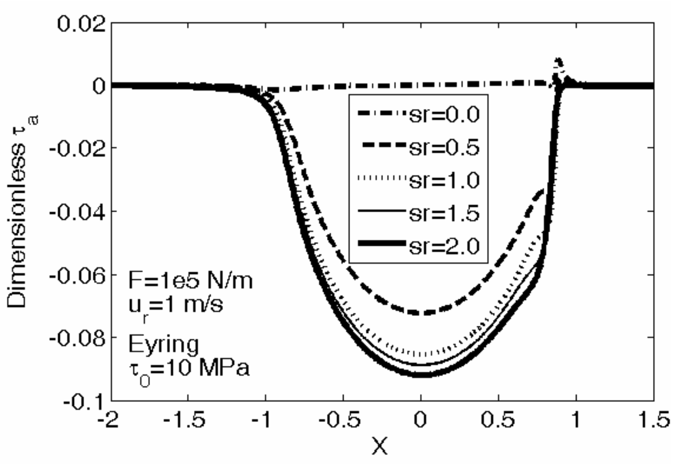

Fig. 4.29 Effect of slide/roll ratio on $\overline{\tau_a}$ for a Ree-Eyring fluid with $\tau_0 = 1 \times 10^7 Pa$

Fig. 4.30 shows the effect of the slide/roll ratio on the friction coefficient for a Ree-Eyring fluid. It is seen that the value of the friction coefficient goes up when the slide/roll ratio increases. However, this trend becomes slower when the slide/roll ratio is high.

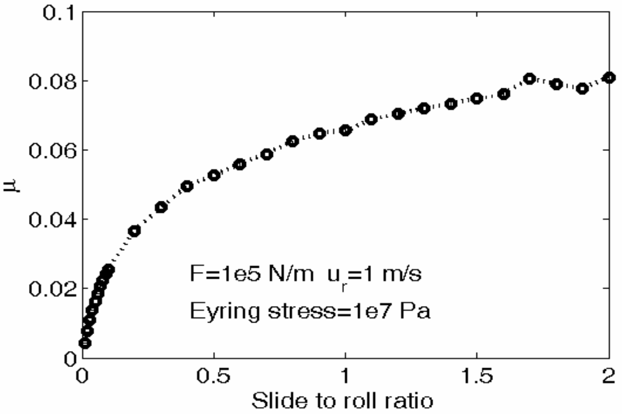

Fig. 4.30 Effect of slide/roll ratio on friction coefficient for a Ree-Eyring fluid with $\tau_0 = 1 \times 10^7 Pa$

Fig. 4.31 shows the effect of the slide/roll ratio on fluid velocity for a Ree-Eyring fluid. It shows that there is almost no difference on fluid velocity inside the nominal contact zone between different slide/roll ratio cases. However, the reverse flow might occur in some cases in the inlet zone.

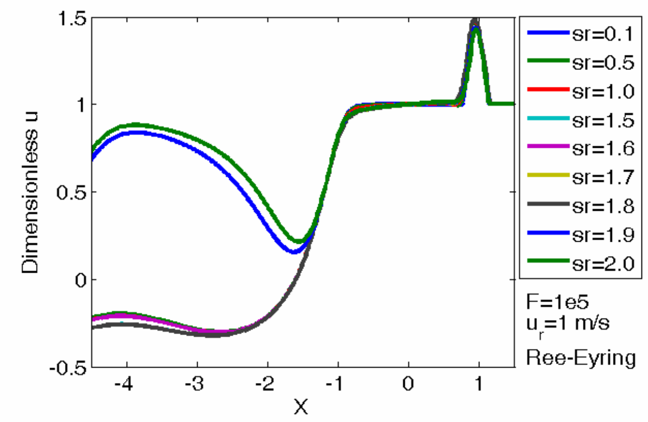

Fig. 4.31 Effect of slide/roll ratio on $\bar{u}$ for a Ree-Eyring fluid with $\tau_0 = 1\times10^7 Pa$

4.2.3.4. Effect of Eyring Stress with the Isothermal Ree-Eyring Model

In principle, the use of a shear thinning non-Newtonian lubricant formulation allows the calculation of realistic values of fluid traction. For the Ree-Eyring fluid, the main difficulty in applying the analysis is the choice of the Eyring stress value for the lubricant [112]. Wang et al. [113] use 2 MPa, Bou-Chakra et al. [114] use 2.6 MPa, Britton et al. [112] use 3-4 MPa, Jacod et al. [115] use 4 MPa, Chang and Zhao [116] use 5-50 MPa, Morales-Espejel et al. [117] use 8 MPa, Olver and Spikes [118] use 9 MPa, Kumar et al. [119] use 10 MPa, Sottomayor et al. [120] use 18.06 MPa, Wang and Yi [36] use 18.7 MPa.

Fig. 4.32 shows the effect of the characteristic Eyring stress on the pressure and film profile for the working case described in the figure. It is seen that Eyring stress affects the second pressure spikes at the outlet zone significantly, while its effect on the film profile is much less.

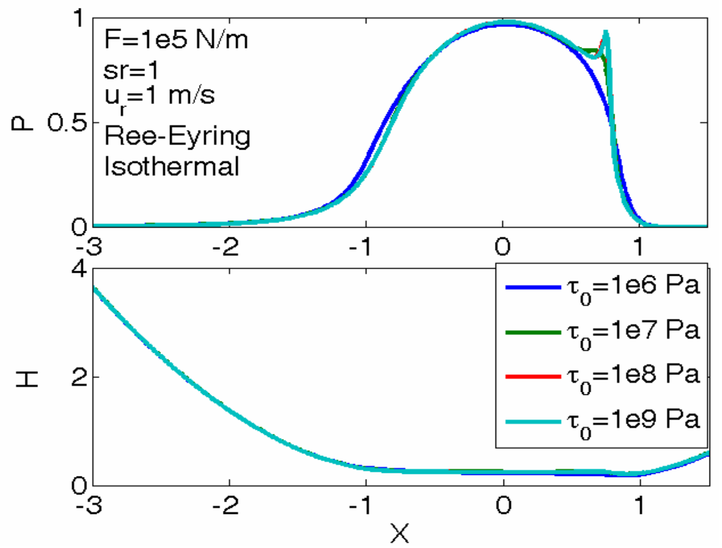

Fig. 4.32 Effect of Eyring stress on pressure and film profile

Fig. 4.33 shows the effect of Eyring stress on fluid viscosity. The upper subfigures represent the viscosity distribution across the film, while the lower subfigures represent the viscosity at the central layer of the film. In lower subfigures the dashed lines represent the original Newtonian viscosity, while the solid lines represent the viscosity obtained using the Ree-Eyring assumption. Fig. 4.33 (a) and (e) correspond to $\tau_0 = 1 \times 10^6 Pa$, (b) and (f) correspond to $\tau_0 = 1 \times 10^7 Pa$, (c) and (g) correspond to $\tau_0 = 1 \times 10^8 Pa$, while (d) and (h) correspond to $\tau_0 = 1 \times 10^9 Pa$. It is seen that the viscosities of a Ree-Eyring fluid are smaller than their Newtonian counterparts. As the Eyring stress decreases, the viscosities decrease significantly. When the Eyring stress is high, such as $\tau_0 = 1 \times 10^9 Pa$ shown in Fig. 4.33 (h), the difference between the Ree-Eyring solution and the Newtonian one is negligible.

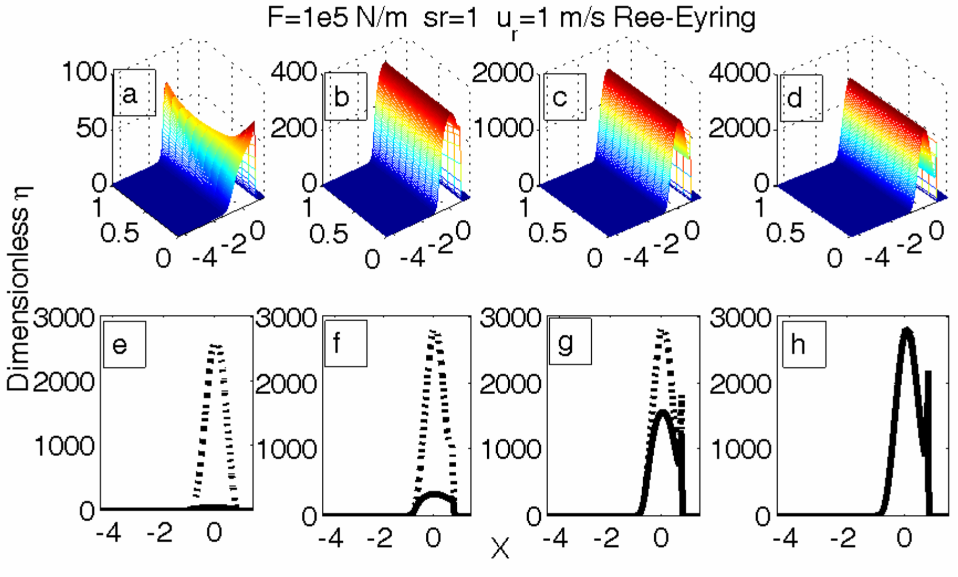

Fig. 4.33 Effect of Eyring stress on viscosity with the isothermal Ree-Eyring model

Figs. 4.34 and 4.35 show the traction on the interface and the friction coefficient, respectively, with the isothermal Ree-Eyring model. It is seen from Fig. 4.35 that when the Eyring stress is not high, the friction coefficient increases as the Eyring stress goes up. When the Eyring stress is between the value $\tau_0 = 1\times 10^7 Pa$ and the value $\tau_0 = 1\times 10^9 Pa$, the increase of the friction coefficient is rapid. However, when the Eyring stress is above $\tau_0 = 1\times 10^9 Pa$, the friction coefficient almost does not change, since the solutions are quite similar to the Newtonian solution.

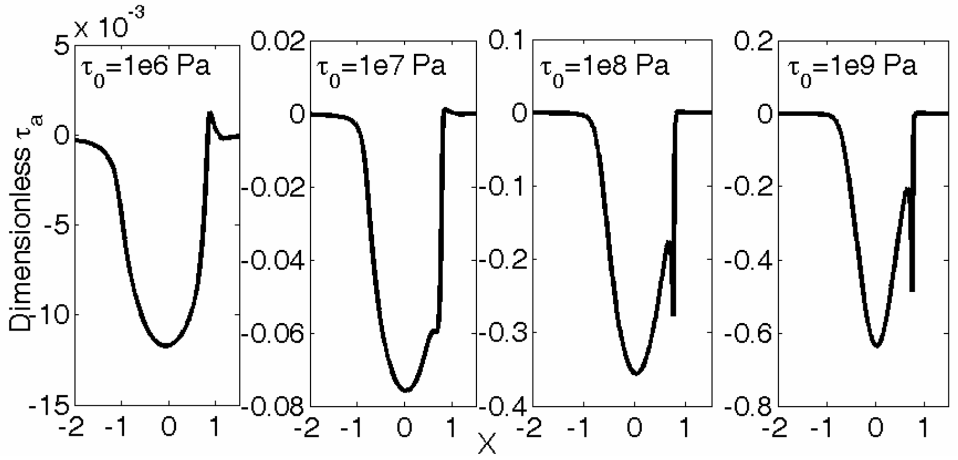

Fig. 4.34 Effect of Eyring stress on shear stress with the isothermal Ree-Eyring

model

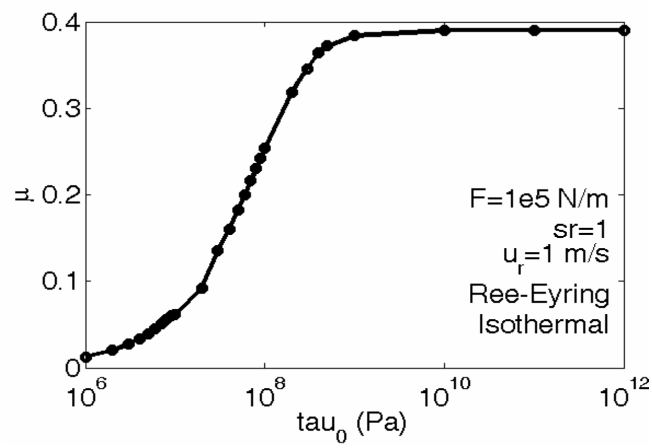

Fig. 4.35 Effect of Eyring stress on friction coefficient with the isothermal Ree-Eyring model

It is seen from the previous analysis that the characteristic Eyring stress should be chosen carefully, since it may affect the pressure spikes, viscosities, traction distribution and the friction coefficient significantly.

4.3. The Power-Law EHL Model

4.3.1. Governing Equations

It is somewhat difficult to calculate τ_a for a power-law fluid because its value should be determined iteratively. In the following the derivation of the expression of τ_a for the power law fluid is given.

The constitutive equation of a power-law fluid reads

$$\tau = m\left|\frac{\partial u}{\partial z}\right|^{n-1}\frac{\partial u}{\partial z} = \tau_a + z\frac{\partial p}{\partial x} \tag{4.24}$$

Where m is the viscosity index and n is the flow index. Fluids with $n > 1$, $n = 1$, and $n < 1$ correspond to a dilatant fluid, Newtonian fluid, and pseudoplastic fluid, respectively.

The viscosity index m should be a function of the pressure and the temperature. If the Roelands equation is applied, m can be expressed as

$$m = m_0 \exp\{(\ln m_0 + 9.67)[(1 + 5.1\times 10^{-9} p)^{z_0} - 1]\} \qquad (4.25)$$

Where m_0 is the viscosity index at ambient pressure and ambient temperature. When $n = 1$, we have $m_0 = \eta_0$. However, for cases with $n \neq 1$, we still assume $m_0 = \eta_0$ owing to the lack of relevant empirical data. z_0 is the pressure-viscosity index and it is chosen as $z_0 = 0.6$.

Substitute Eq. 4.25 into Eq. 4.24, and τ_a can finally be expressed as

$$\tau_a = -\frac{u_a - u_b + \dfrac{\partial p}{\partial x}\displaystyle\int_0^h m^{-1/n}\left|\tau_a + z\frac{\partial p}{\partial x}\right|^{(1-n)/n} z dz}{\displaystyle\int_0^h m^{-1/n}\left|\tau_a + z\frac{\partial p}{\partial x}\right|^{(1-n)/n} dz} \qquad (4.26)$$

τ_a appears at both sides of this equation and it should be calculated iteratively - usually for each updated pressures, dozens of iterations of τ_a are required to satisfy the convergence criteria. It is seen that the calculation of τ_a of the power-law fluid is more complex than that of the Ree-Eyring fluid, which can be calculated analytically.

Once the shear stress field is obtained, the equivalent viscosity of a power-law fluid can be calculated using

$$\eta^* = m^{1/n} |\tau|^{(n-1)/n} \qquad (4.27)$$

4.3.2. Dimensionless Equations

Introducing new parameters:

$$\bar{m} = m / m_0 \tag{4.28}$$

The expression of $\bar{\tau}_a$ for a power-law fluid can be calculated as

$$\bar{\tau}_a = -\frac{\dfrac{u_a - u_b}{p_H} + \dfrac{p_H^{(1-n)/n} dP}{bdX}\displaystyle\int_0^1 (\bar{m}\mathrm{m}_0)^{-1/n}\left|\bar{\tau}_a + ZH\frac{b}{R}\frac{dP}{dX}\right|^{(1-n)/n} ZH^2\frac{b^4}{R^2}dZ}{p_H^{(1-2n)/n}\displaystyle\int_0^1 (\bar{m}\mathrm{m}_0)^{-1/n}\left|\bar{\tau}_a + ZH\frac{b}{R}\frac{dP}{dX}\right|^{(1-n)/n} H\frac{b^2}{R}dZ} \tag{4.29}$$

If $n = 1$ the expression of $\bar{\tau}_a$ is simplified to

$$\bar{\tau}_a = -\frac{\dfrac{u_a - u_b}{p_H} + \dfrac{dP}{bdX}\displaystyle\int_0^1 (\bar{m}\mathrm{m}_0)^{-1} ZH^2\frac{b^4}{R^2}dZ}{p_H^{-1}\displaystyle\int_0^1 (\bar{m}\mathrm{m}_0)^{-1} H\frac{b^2}{R}dZ} \tag{4.30}$$

which corresponds to the Newtonian one.

4.3.3. Results and Discussion

4.3.3.1. Effect of Power-Law Index with the Isothermal Power-Law Model

Fig. 4.36 shows the effect of the power-law index n on the pressure and film profile for a power-law fluid. It is seen that as n increases, the second pressure spike becomes weaker, and the film becomes thinner.

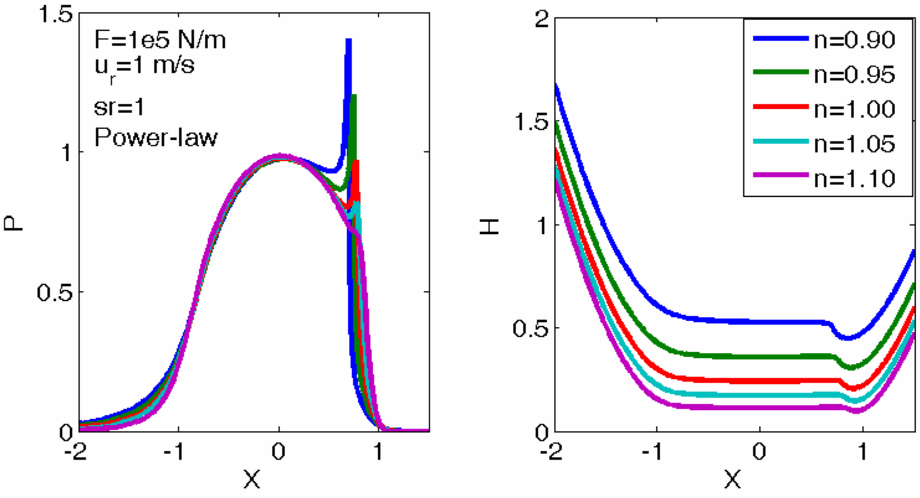

Fig. 4.36 Effect of power-law index on pressure and film profile with the isothermal power-law model

Fig. 4.37 shows the effect of the index on shear stress distribution with the isothermal power-law model. It is seen that as the index increases, the absolute value of shear stress within the nominal contact zone decreases. For the cases $n = 0.90$ and $n = 0.95$, the predicted value of the friction coefficient exceeds unity, which is physically impossible. Special attention should be paid when attempting to use the power-law model for traction studies.

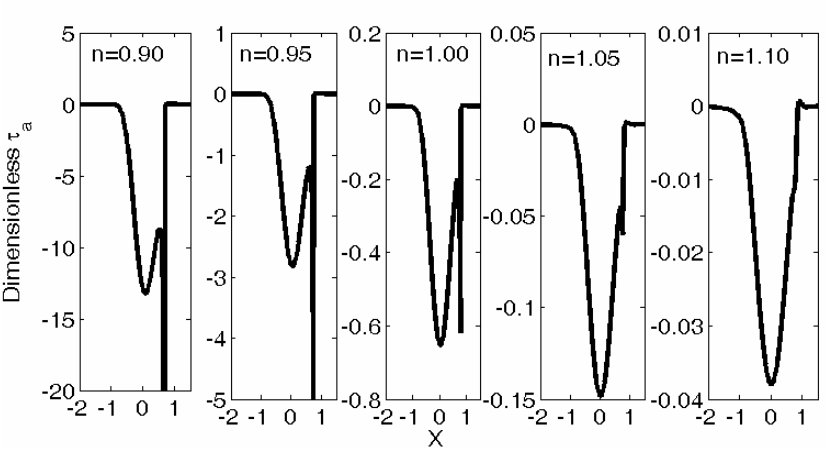

Fig. 4.37 Effect of the index on shear stress distribution with the isothermal power-law model

4.3.3.2. Effect of Load with the Isothermal Power-Law Model

Fig. 4.38 shows the effect of load on the pressure and film profile for a $n = 1.05$ power-law fluid. It is seen that, as the load increases, the pressure profile becomes similar to the Hertzian contact solution. As the load increases, the film thickness becomes lower. These conclusions are similar to those with a Newtonian fluid or a Ree-Eyring fluid.

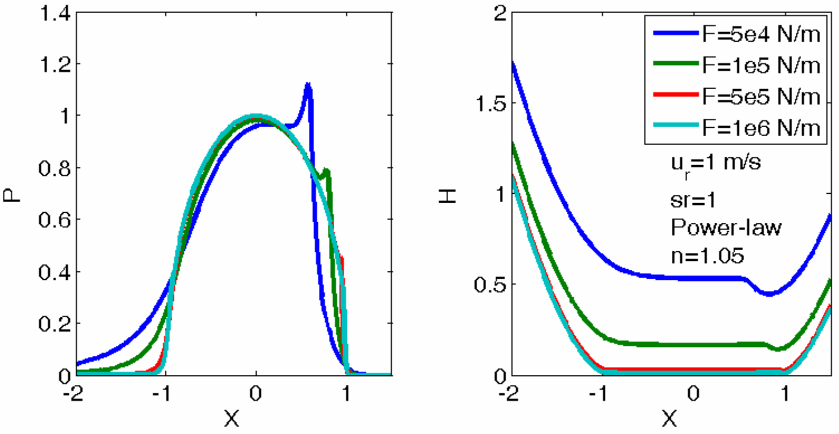

Fig. 4.38 Effect of load on pressure and film profile for a power-law fluid with $n = 1.05$

Fig. 4.39 shows the effect of load on $\bar{\tau}_a$ for a $n = 1.05$ power-law fluid. It shows that, for a power-law fluid with $n = 1.05$, as the load increases, the absolute value of $\bar{\tau}_a$ within the nominal contact zone increases, which would lead to a higher friction coefficient value. Fig. 4.40 shows the variation of friction coefficient along the load. The value of the friction coefficient increases exponentially as the load increases.

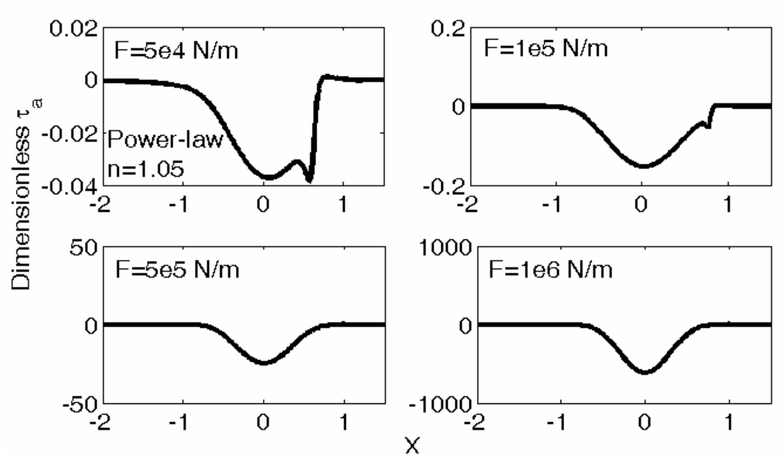

Fig. 4.39 Effect of load on dimensionless shear stress for a power-law fluid with $n = 1.05$

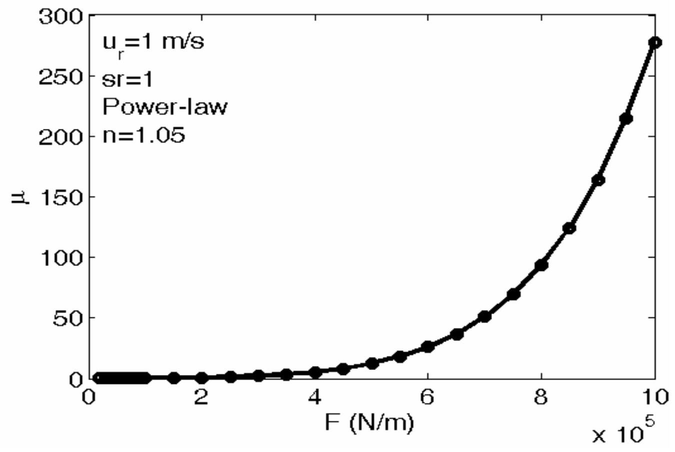

Fig. 4.40 Effect of load on friction coefficient for a power-law fluid with $n = 1.05$

Fig. 4.41 shows the three-dimensional velocity field of the film for different load cases with the power law fluid. In order to see the effect of load on velocity distribution more clearly, a two-dimensional velocity distribution at the central layer of the film is extracted from Fig. 4.41 and is shown in Fig. 4.42.

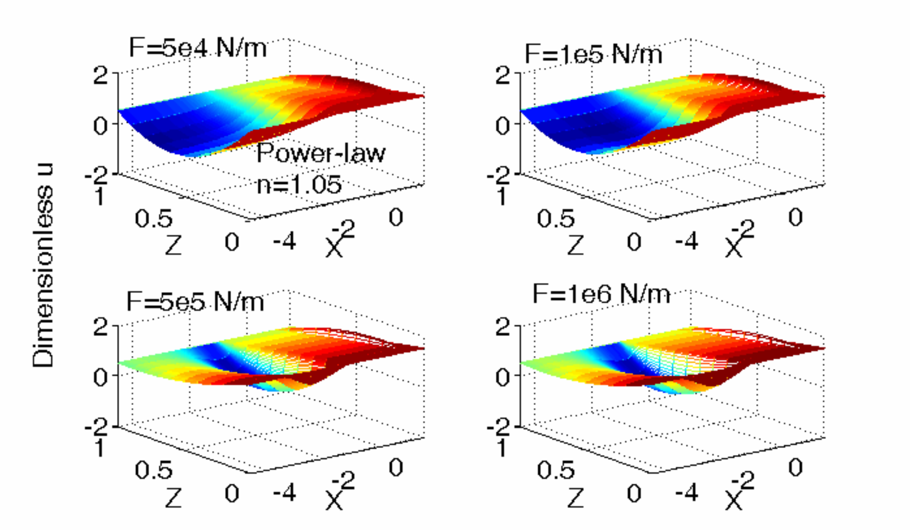

Fig. 4.41 Effect of load on velocity field within the film for a power-law fluid with $n = 1.05$

It is seen from Fig. 4.42 that the load affects the velocity field at the inlet zone of the nominal contact area significantly while it affects little within the nominal contact area. At the outlet zone the velocity also varies slightly between different load cases.

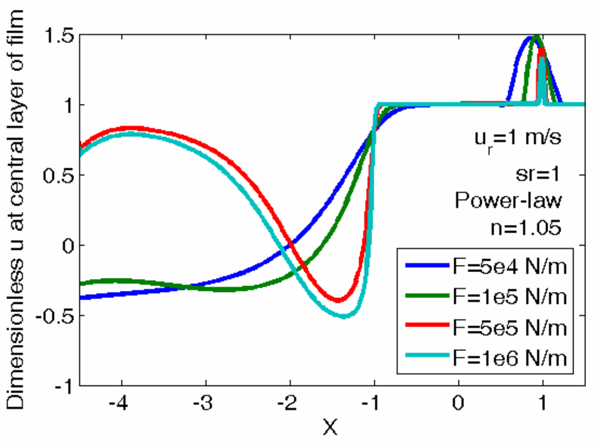

Fig. 4.42 Effect of load on velocity field at central layer of the film for a power-law fluid with $n = 1.05$

4.3.3.3. Effect of Rolling Speed with the Isothermal Power-Law Model

Fig. 4.43 shows the effect of rolling speed on the pressure and film profile for a $n = 1.05$ power-law fluid. It is seen that, as the rolling speed goes up, the pressure profile deviates from the Hertzian contact solution; that is, both the inlet zone and the second pressure spike are getting larger. As the rolling speed increases, the film thickness also increases.

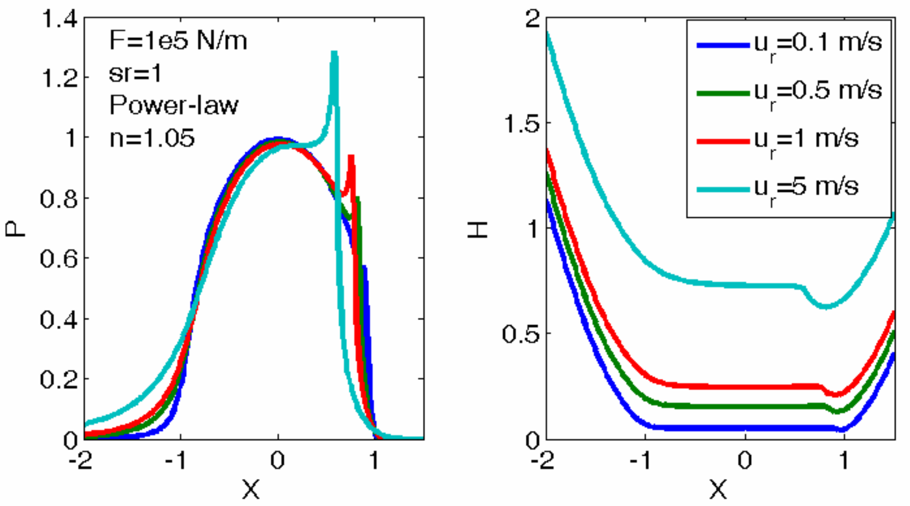

Fig. 4.43 Effect of rolling speed on pressure and film profile for a power-law fluid

with $n = 1.05$

Fig. 4.44 shows the effect of rolling speed on $\bar{\tau}_a$ for this power-law fluid. As the rolling speed increases, the absolute value of $\bar{\tau}_a$ within the nominal contact zone increases, which would lead to a larger friction coefficient value. The spike at the outlet zone also gets bigger when the speed increases.

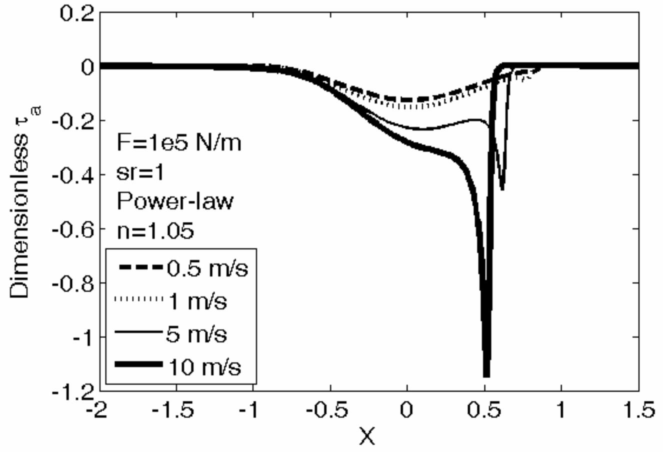

Fig. 4.44 Effect of rolling speed on dimensionless shear stress for a power-law fluid with $n = 1.05$

Fig. 4.45 shows the effect on the friction coefficient. As the speed increases, the value of the friction coefficient increases almost linearly.

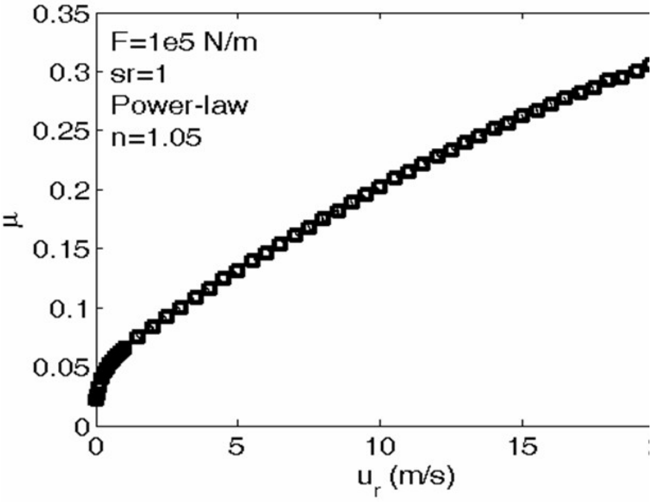

Fig. 4.45 Effect of rolling speed on friction coefficient for a power-law fluid with $n = 1.05$

Fig. 4.46 shows the effect on velocity distribution at the central layer of the film for this power-law fluid. It is seen that, the rolling speed also affects the velocity field at the inlet zone but affects little within the nominal contact zone. The velocity at the outlet zone also is affected by the rolling speed.

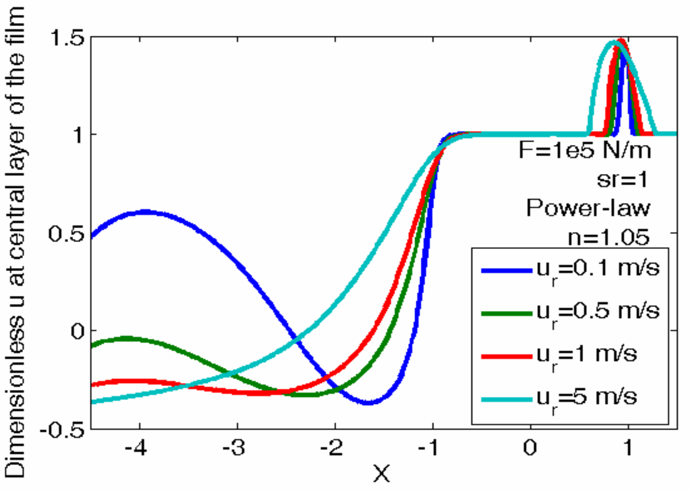

Fig. 4.46 Effect on velocity distribution at the central layer of the film for a power-law fluid with $n = 1.05$

4.3.3.4. Effect of Slide/Roll Ratio with the Isothermal Power-Law Model

Fig. 4.47 shows the effect of the slide/roll ratio on the pressure and film profile for the $n = 1.05$ power-law fluid. It is seen that the slide/roll ratio does not affect the pressure and film profile at all for a power-law fluid.

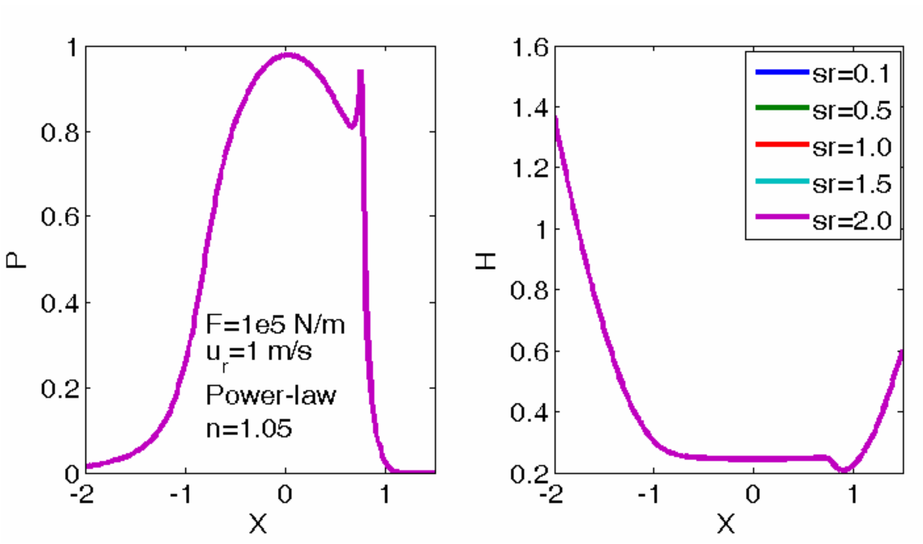

Fig. 4.47 Effect of slide/roll ratio on pressure and film profile for a power-law fluid with $n = 1.05$

Figs. 4.48 and 4.49 show the effect of the slide/roll ratio on the shear stress distribution and on the friction coefficient for a power-law fluid with $n = 1.05$, respectively. It is seen that as the slide/roll ratio increases, the absolute value of $\bar{\tau}_a$ within the nominal contact zone increases, which would lead to a larger friction coefficient value, as is seen from Fig. 4.49. For the power-law fluid with $n = 1.05$, the friction coefficient varies almost linearly with the slide/roll ratio. As mentioned before, the Newtonian one also holds this linear relationship between the slide/roll ratio and the friction coefficient.

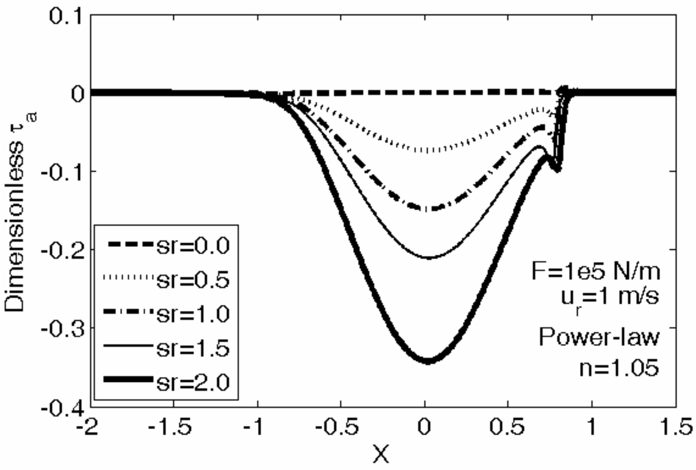

Fig. 4.48 Effect of slide/roll ratio on dimensionless shear stress for a power-law fluid with $n = 1.05$

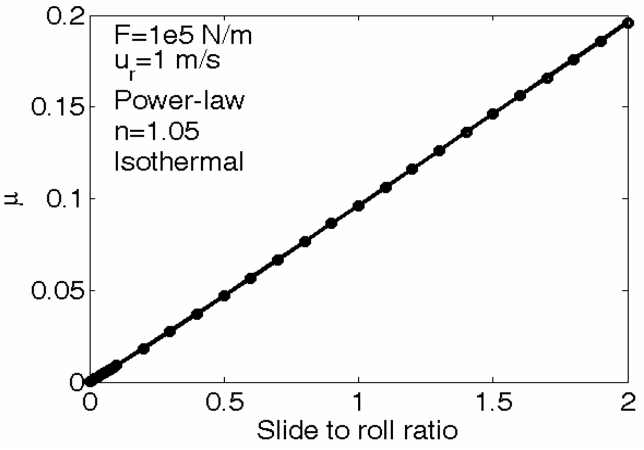

Fig. 4.49 Effect of load on friction coefficient for a power-law fluid with $n = 1.05$

Fig. 4.50 shows the effect on velocity distribution at the central layer of the film. It is seen that there is no effect on velocity distribution for the slide/roll ratio parameter at all for a power-law fluid.

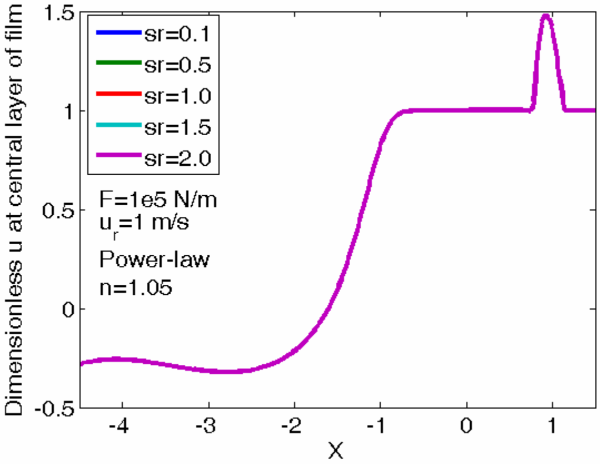

Fig. 4.50 Effect of slide/roll ratio on velocity field within the film for a power-law fluid with $n = 1.05$

4.4. Chapter Summary

In this chapter, two non-Newtonian models, the Ree-Eyring model and the power-law model, are incorporated in the lubrication model by using the generalized Reynolds equation. The following conclusions can be made in this chapter:

- For the Ree-Eyring fluid, the minimum film thickness within the nominal contact zone does not change significantly from the Newtonian solution. However, for a power-law fluid, the minimum film thickness changes significantly with the power-law index n. The second pressure spikes for the Ree-Eyring solution, as well as the power-law solution with $n > 1$, are much more alleviated than the Newtonian solution owing to the decrease of the equivalent viscosity within the nominal contact zone.
- Compared with the Newtonian solution, the Ree-Eyring solution gives a lower fluid viscosity which will cause a lower friction coefficient when the same working condition is considered. Similar conclusions can be made for the power-law fluid with $n > 1$.
- For the Newtonian fluid, the Ree-Eyring fluid, and the power-law fluid with $n = 1.05$, as the load increases, the pressure profile becomes similar to the Hertzian contact solution. As the load increases, the film thickness becomes lower. For the Newtonian fluid and the power-law fluid with $n = 1.05$, the friction coefficient value increases significantly with the load. For the Ree-Eyring fluid, when the load is light, the value of the friction coefficient increases significantly. When the load is high and as it keeps increasing, the value of the friction coefficient does not change too considerably at first; if it keeps increasing, the friction coefficient will drop gradually.
- For the Newtonian fluid, the Ree-Eyring fluid, and the power-law fluid with $n = 1.05$, as the rolling speed goes up, the pressure profile deviates from the Hertzian

contact solution: that is, the inlet zone is getting larger and the second pressure spike is getting bigger as well. As the rolling speed increases, the film thickness increases. For the Newtonian fluid, as the rolling speed increases, the value of the friction coefficient increases almost linearly. For the Ree-Eyring fluid, when the speed is not high, as the speed goes up, the value of the friction coefficient goes up significantly and if the speed continues to increase, the value of the friction coefficient increases much more slowly. The friction coefficient is almost linear with the logarithmic form of rolling speed, while for the power-law fluid with $n = 1.05$, as the speed increases, the value of the friction coefficient increases almost linearly;

- As for the effect of slide to roll ratio on pressure and film profile, there is almost no difference on pressure and film profile for the Newtonian one and the power-law with $n = 1.05$. For the Ree-Eyring fluid, the slide to roll ratio affect the second pressure spikes while it has a very limited influence on the other part of the pressure profile and the whole film profile. For the Newtonian fluid and the power-law fluid with $n = 1.05$, the value of friction coefficient goes up linearly with the slide to roll ratio. For the Ree-Eyring fluid, the value of friction coefficient goes up when the slide to roll ratio increases. However, this trend becomes slower when the slide to roll ratio is high.

Chapter 5 Rough Surface EHL and Mixed Lubrication

In this chapter, rough surface EHL problems and mixed lubrication problems are studied. Ultra thin film problems are handled using the Hu-Zhu unified approach [4]. Numerical cases are given with this type of deterministic model.

5.1. Reduced Reynolds Technique for Line Contacts

Zhu and Hu [4] presented a unified approach that is capable of simulating the entire transition from the full film, mixed, down to boundary lubrication. The Reduced Reynolds technique has been proven to be robust with no convergence problem when handling rough engineering surfaces under severe operating conditions [121]. To understand the Reduced Reynolds technique, we should look again at the classical Reynolds equation

$$\frac{\partial}{\partial x}\left(\frac{\rho h^3}{\eta}\frac{\partial p}{\partial x}\right) = 12u_r\frac{\partial(\rho h)}{\partial x} + 12\frac{\partial(\rho h)}{\partial t} \tag{5.1}$$

The Reynolds equation implies the balance of fluid flow. The first term on the left-hand side of Eq. 5.1 represents the lubricant flow owing to the hydrodynamic pressure, while the other two terms represent the flow caused by surface motion. The essence of the Reduced Reynolds techniques lies in that when the film thickness becomes zero - the regions where two surfaces are in direct contact - the pressure flow vanishes, and a reduced Reynolds equation still applies to the direct-contact regions:

At $h = 0$

$$u_r\frac{\partial(\rho h)}{\partial x} + \frac{\partial(\rho h)}{\partial t} = 0 \tag{5.2}$$

When solving the Reynolds equation, a very small value - e.g. ε=0.00001 - is used as a criterion for checking if $h = 0$. When the dimensionless film thickness is less than ε, it is considered that the film thickness is practically zero, and the pressure flow term in the Reynolds equation should be turned off. In this way, a unified Reynolds model can be used to describe the mixed lubrication problems and both hydrodynamic and contact pressures can be obtained through the same iteration loop without requiring boundary conditions between the hydrodynamic and contact regions. This technique was first proposed by Hu and Zhu [4] for point contact problems, and in this chapter it is used for line contact problems.

5.2. Numerical Cases with Wavinesses

Sinusoidal waviness is considered to show the effects of amplitude and wavelength of the waviness on pressure, film profile, traction, etc. If the steady-state condition is considered, the form of the dimensionless waviness expression reads

$$RR = Amp \cdot \cos(2\pi x / Wav) \tag{5.3}$$

where Amp is the dimensionless amplitude and Wav is the dimensionless wavelength. This term will be added to the film thickness equation. Fig. 5.1 shows some of the dimensionless waviness terms studied in this work. The effect of amplitude and wavelength on pressure, film thickness, friction, etc., are studied.

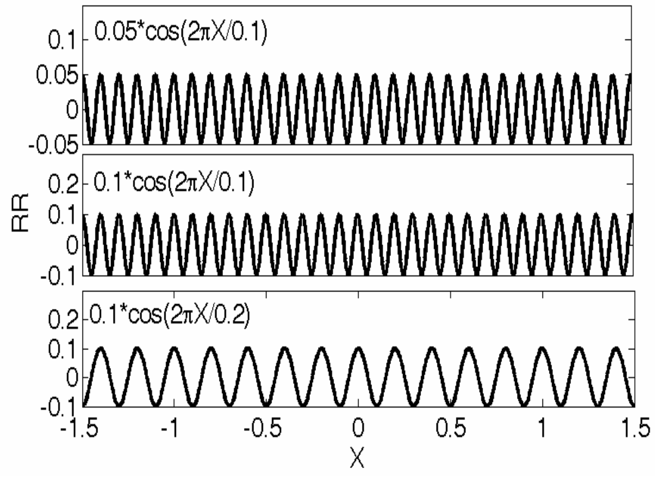

Fig. 5.1 Three dimensionless wavinesses studied

5.2.1. Effect of Amplitude

The effect of amplitude is studied first for the cases with working condition $F = 1\times10^5 N/m$, $u_r = 1m/s$ and $sr = 1$. Fig. 5.2 shows the pressure profiles and film profiles for an isothermal, Newtonian case. It is seen that for a Newtonian isothermal case, the waviness causes relevant fluctuation on pressure and film thickness within the nominal contact zone. The larger the amplitude, the more evident the fluctuations on pressure profile and film profile. The wavelengths of the fluctuations are in accordance with the original waviness profile.

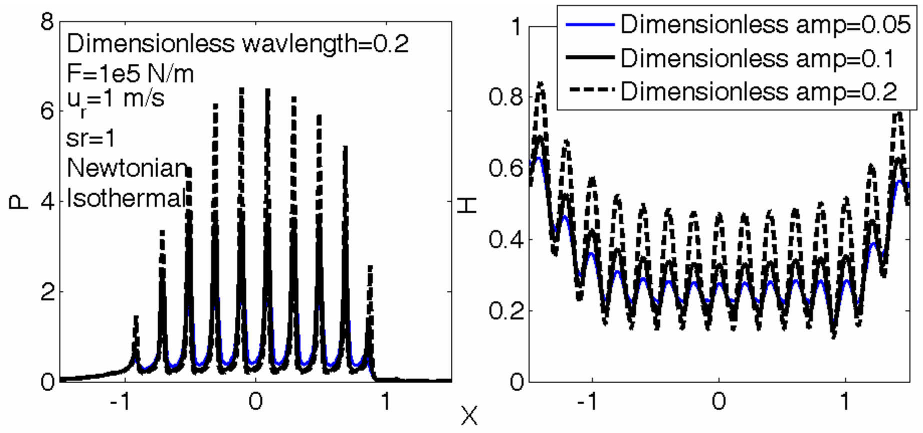

Fig. 5.2 Effect of amplitude on pressure and film profile for a Newtonian, isothermal fluid with dimensionless wavelength $Wav = 0.2$

Fig. 5.3 and 5.4 show solutions for a Ree-Eyring fluid and a power-law fluid with $n = 1.05$, respectively. It is seen that the larger the amplitude, the more evident the fluctuations on pressure profile and film profile. However, comparing the Ree-Eyring solution and the power-law solution with the Newtonian one, the pressure fluctuation amplitudes are far smaller.

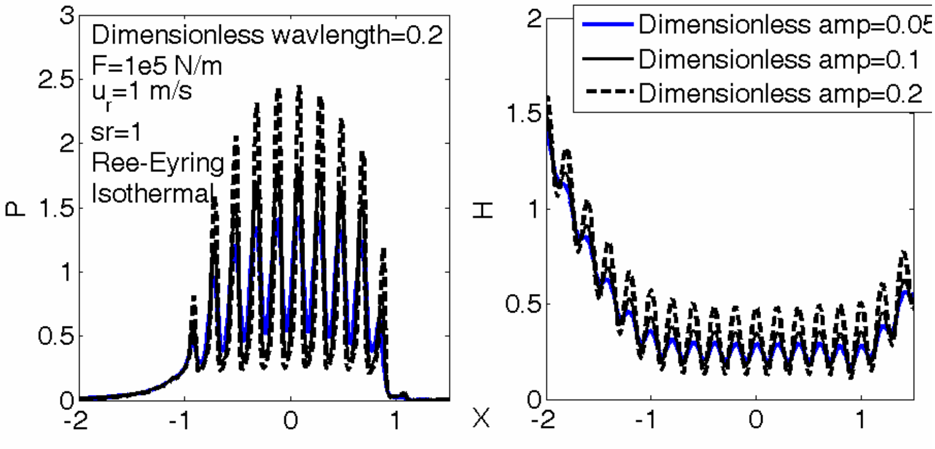

Fig. 5.3 Effect of amplitude on pressure and film profile for a Ree-Eyring, isothermal fluid with dimensionless wavelength $Wav = 0.2$

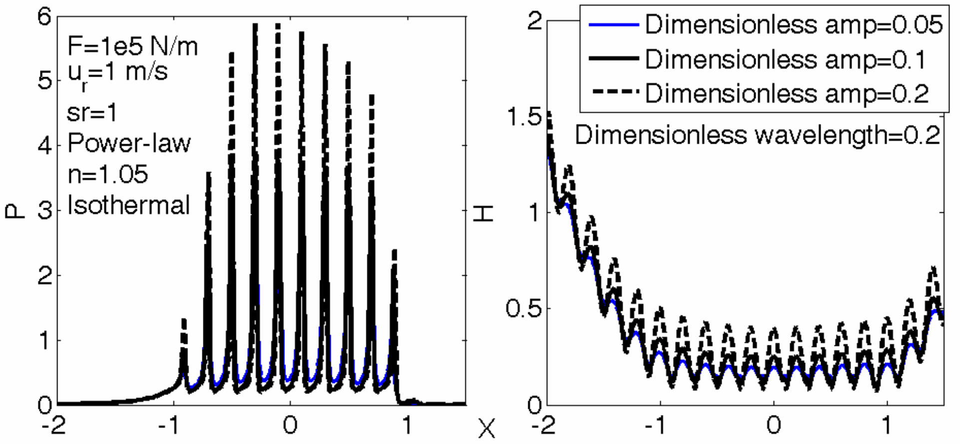

Fig. 5.4 Effect of amplitude on pressure and film profile for a power-law n=1.05, isothermal fluid with dimensionless wavelength $Wav = 0.2$

Fig. 5.5 shows the effect of amplitude on the dimensionless traction $\bar{\tau}_a$ for the Newtonian, Ree-Eyring, a power-law $n = 1.05$, and isothermal fluid with $Wav = 0.2$. Subfigures 5.5a, 5.5b, and 5.5c represent the Newtonian solution, 5.5d, 5.5e, and 5.5f represent the Ree-Eyring solution, while 5.5g, 5.5h, and 5.5i represent the power-law solution. It is seen that for the Newtonian and the power-law solutions, the waviness causes rapid peaks on $\bar{\tau}_a$ at local nominal contact areas. For the

Ree-Eyring solution, the fluctuation of $\overline{\tau}_a$ within the nominal contact region has a regular pattern according to the original waviness.

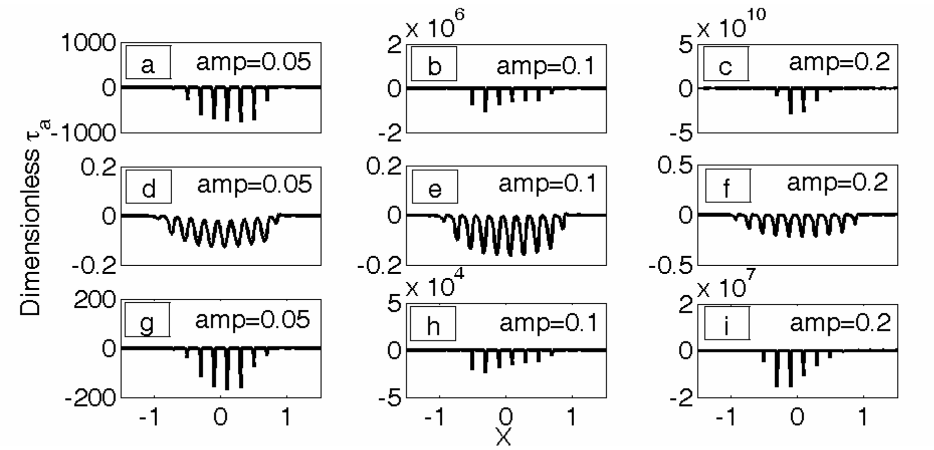

Fig. 5.5 Effect of amplitude on traction for a Newtonian, Ree-Eyring, a power-law n=1.05, isothermal fluid with dimensionless wavelength $Wav = 0.2$

Figs. 5.6 to 5.8 show the effect of amplitude on the friction coefficient for the Newtonian, Ree-Eyring, and power-law fluid, respectively. For the Newtonian solution and the power-law solution, the friction coefficient increases rapidly as the amplitude of the waviness goes up. Even though the power-law fluid values are lower than their Newtonian counterparts, they are still too large to be physically meaningful. It is interesting to see from Fig. 5.7 that for the Ree-Eyring fluid, with $Wav = 0.2$, as the amplitude of waviness increases, the friction coefficient first decreases a little and then increases constantly when the amplitude is larger than $Amp = 0.05$. This phenomenon is interesting because it implies that a carefully controlled artificial surface roughness pattern with a small amplitude may lead to a less frictional power loss. In order to assure this conclusion, another two cases with $Wav = 0.1$ and $Wav = 0.05$ are studied using the Ree-Eyring assumption, the results of which are shown in Figs. 5.9 and 5.10, respectively.

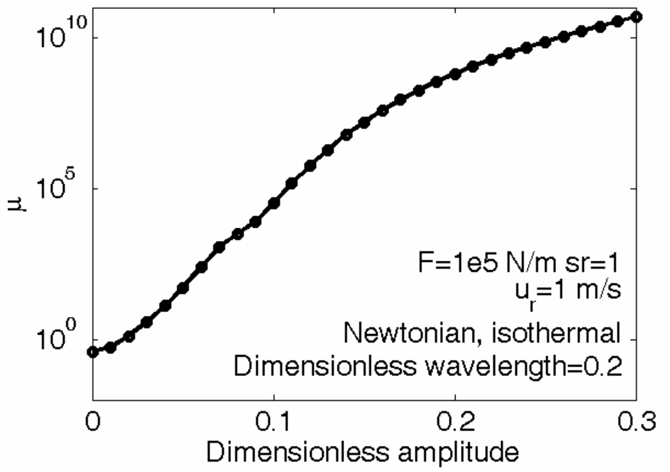

Fig. 5.6 Effect of amplitude on friction coefficient for a Newtonian fluid with dimensionless wavelength $Wav = 0.2$

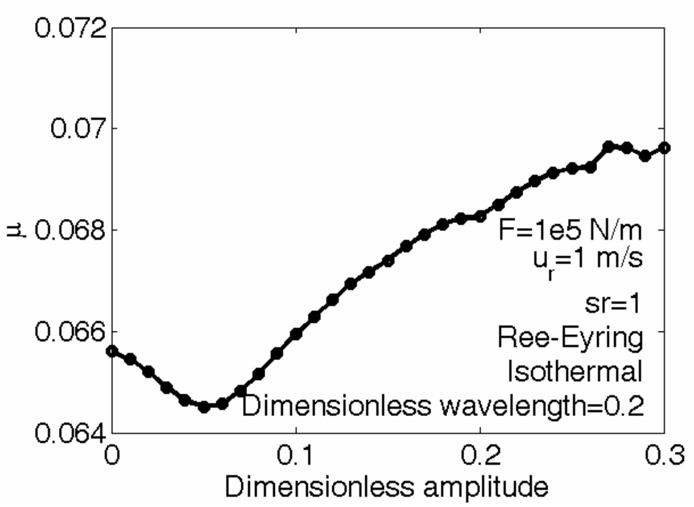

Fig. 5.7 Effect of amplitude on friction coefficient for a Ree-Eyring fluid with dimensionless wavelength $Wav = 0.2$

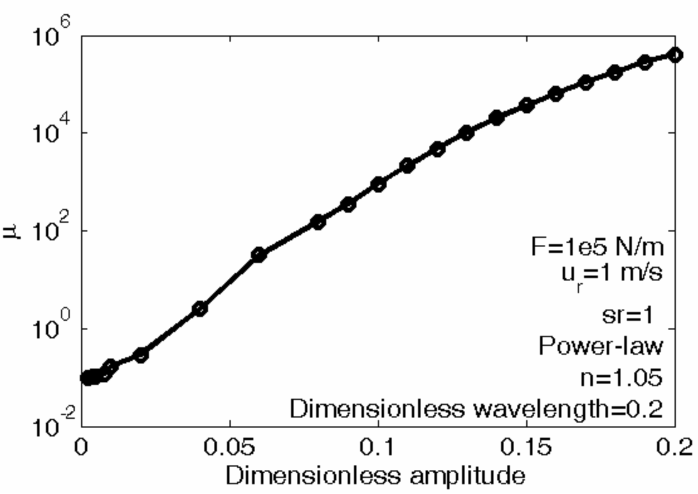

Fig. 5.8 Effect of amplitude on friction coefficient for a Power-law fluid with $n = 1.05$ with dimensionless wavelength $Wav = 0.2$

It is seen from Figs. 5.7, 5.9 and 5.10 that at a small-amplitude range, as the amplitude of waviness increases, the friction coefficient will not increase, and sometimes a small amplitude will reduce the friction coefficient. For the cases where $Wav = 0.2$ and $Wav = 0.1$, the turning points also differ from each other. This means if artificial surface roughness is applied which is trying to decrease the friction, special attention should be paid to the amplitude of the waviness.

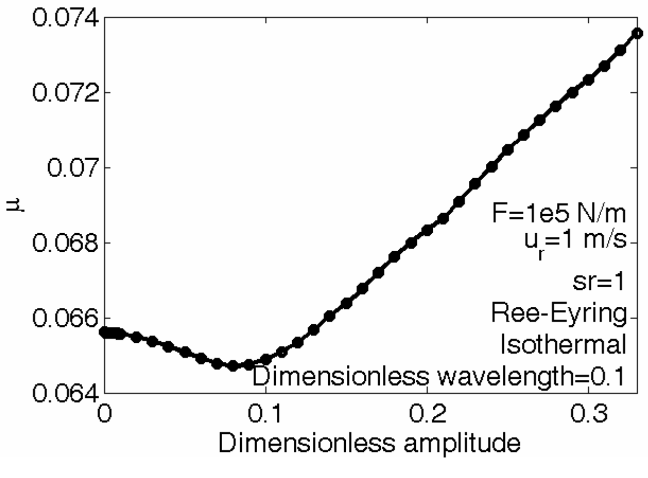

Fig. 5.9 Effect of amplitude on friction coefficient for a Ree-Eyring fluid with dimensionless wavelength $Wav = 0.1$

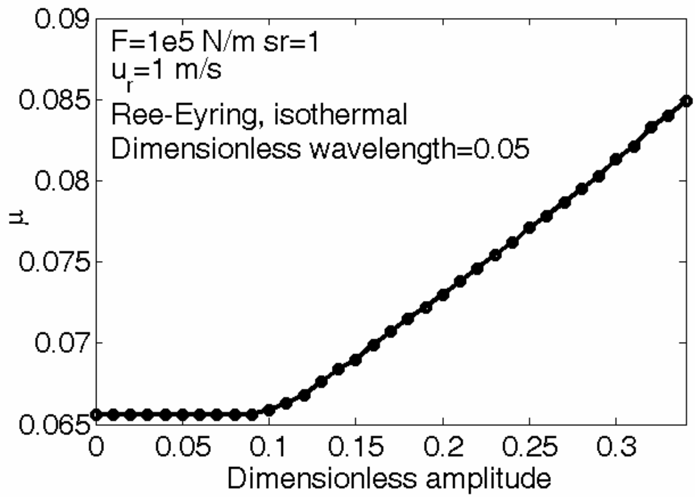

Fig. 5.10 Effect of amplitude on friction coefficient for a Ree-Eyring fluid with dimensionless wavelength $Wav = 0.05$

5.2.2. Effect of Wavelength

The effect of wavelength is studied for the working condition $F = 1\times10^5 N/m$, $u_r = 1m/s$ and $sr = 1$. Fig. 5.11 shows the effect of wavelength on pressure and film profile for a Newtonian, isothermal fluid with the dimensionless roughness amplitude $Amp = 0.2$. It is seen that as the wavelength increases, the amplitude of the pressure fluctuation becomes a little more remarkable. The minimum film thickness does not vary greatly with the wavelength of wavinesses.

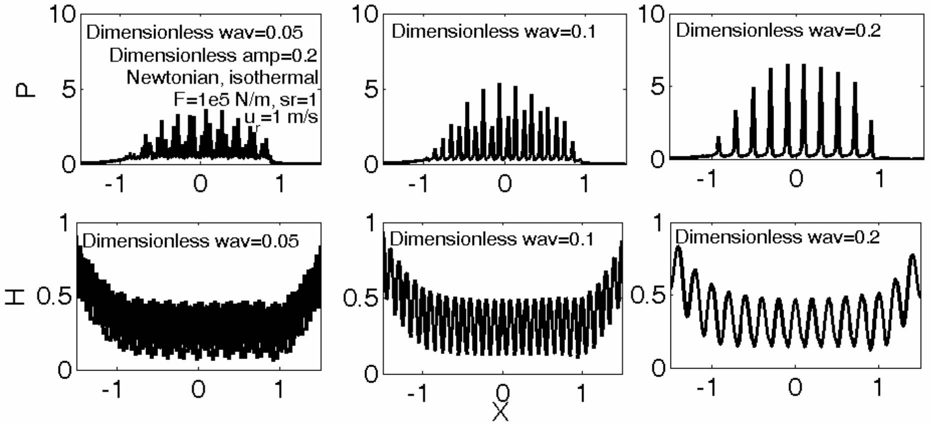

Fig. 5.11 Effect of wavelength on pressure and film profile for a Newtonian,

isothermal fluid with dimensionless roughness amplitude $Amp = 0.2$

Figs. 5.12 and 13 show the pressure and film profile for the Ree-Eyring fluid and the power-law fluid with $n = 1.05$. Just like the Newtonian solution, as the wavelength increases, the amplitude of the pressure fluctuation might become more remarkable.

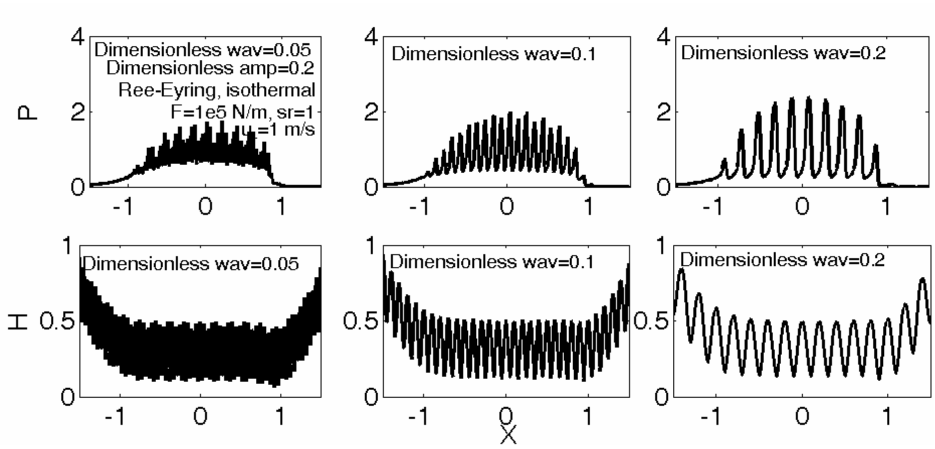

Fig. 5.12 Effect of wavelength on pressure and film profile for a Ree-Eyring, isothermal fluid with dimensionless roughness amplitude $Amp = 0.2$

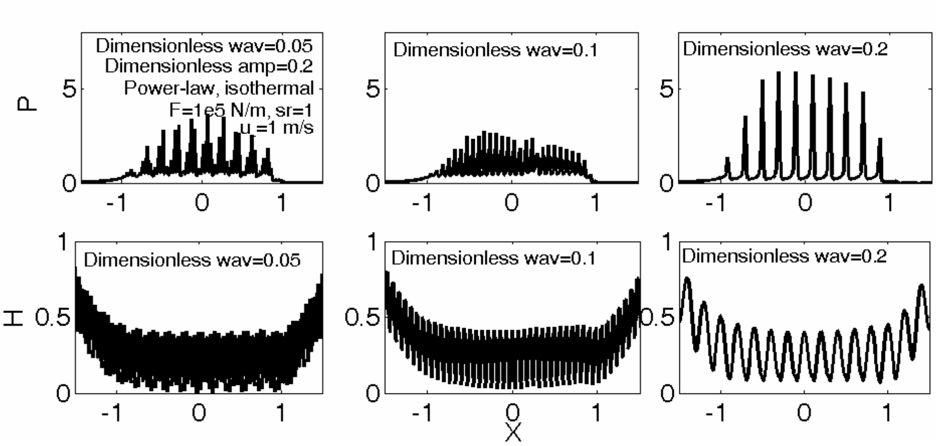

Fig. 5.13 Effect of wavelength on pressure and film profile for a power-law n=1.05, isothermal fluid with dimensionless roughness amplitude $Amp = 0.2$

Figs. 5.14 to 5.16 show the effects of wavelength on the friction coefficient for the three fluids. From the three figures It is seen that when the wavelength is small, such as smaller than $Wav = 0.05$, the trend of the friction coefficient along the wavelength is unstable. This is probably caused by the fact that the mesh density used is not enough to represent such high-frequency components of the waviness. For the Newtonian solution and the power-law solution, when the wavelength is above $Wav = 0.05$, the friction coefficient first increases and then decreases as the wavelength increases. The peak of the friction coefficient curves occur at around $Wav = 0.2$ for both fluids. For the Ree-Eyring fluid, when the wavelength is above $Wav = 0.05$, the friction coefficient first decreases rapidly and then increases gradually as the wavelength goes up.

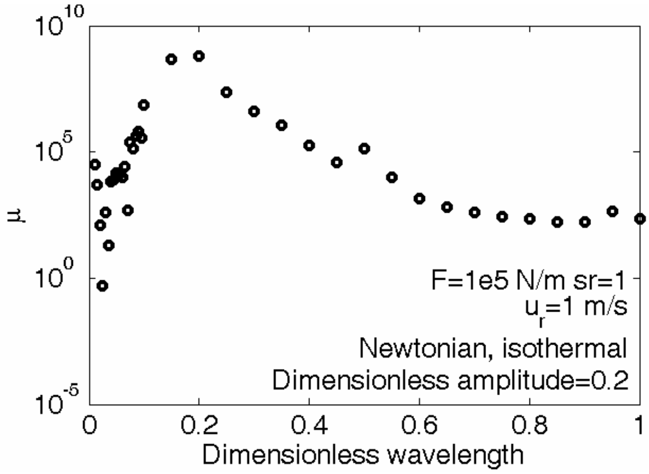

Fig. 5.14 Effect of wavelength on friction coefficient for a Newtonian, isothermal fluid with dimensionless roughness amplitude $Amp = 0.2$

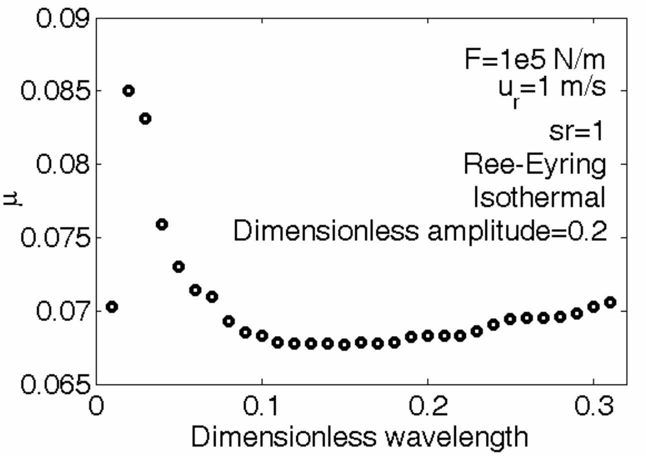

Fig. 5.15 Effect of wavelength on friction coefficient for a Ree-Eyring, isothermal fluid with dimensionless roughness amplitude $Amp = 0.2$

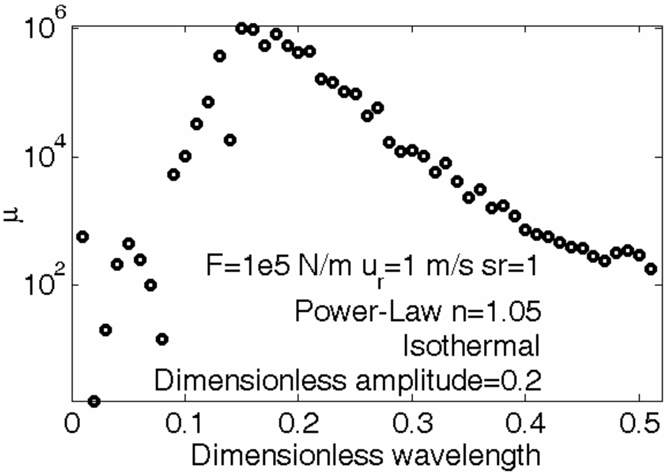

Fig. 5.16 Effect of wavelength on friction coefficient for a power-law n=1.05, isothermal fluid with dimensionless roughness amplitude $Amp = 0.2$

Fig. 5.17 shows solutions for the Ree-Eyring fluid with the dimensionless roughness amplitude $Amp = 0.05$. It is seen that there is no evident trend for the friction coefficient prediction when the wavelength changes.

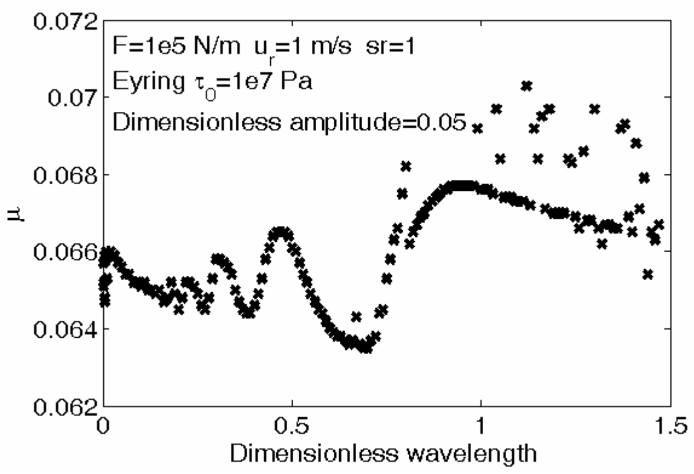

Fig. 5.17 Effect of wavelength on friction coefficient for a Ree-Eyring, isothermal fluid with dimensionless roughness amplitude $Amp = 0.05$

Fig. 5.18 shows the effect of wavelength on the friction coefficient for a power-law with $n = 1.05$, isothermal fluid and with a dimensionless roughness amplitude $Amp = 0.05$. It also shows that the friction coefficient first increases and then decreases as the wavelength increases.

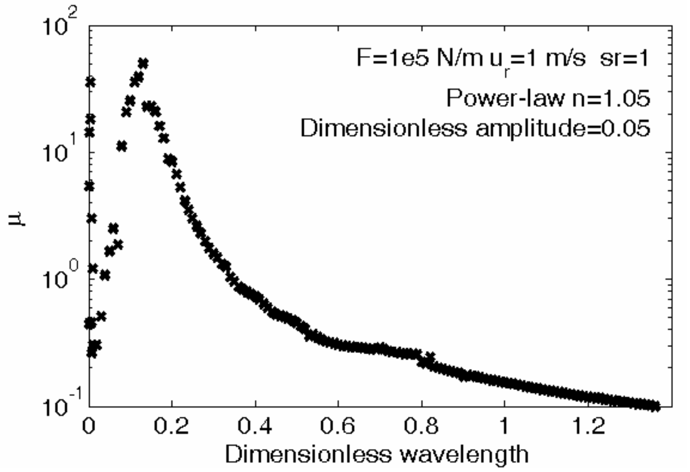

Fig. 5.18 Effect of wavelength on friction coefficient for a power-law with $n = 1.05$, isothermal fluid with dimensionless roughness amplitude $Amp = 0.05$

5.3. Numerical Cases with Digitalized Roughness

5.3.1. Comparison Between Dry Contact Model, Newtonian EHL Model and Eyring EHL Model

The case studied is still used here: $u_r = 1m/s$, $F = 1\times10^5 N/m$, $sr = 1$. Only the surface topography term RR is changed. The surface roughnesses are generated randomly and follow the Gaussian distribution. Fig. 5.19 shows the steady state dimensionless pressure and the film profile of a rough surface with the dimensionless RMS $\overline{R}_q = 0.2$, under dry contact, Newtonian fluid or Ree-Eyring fluid, respectively. Under dry contact condition, the surface roughness has significant effects on pressure ripples. The highest pressure within the nominal Hertzian contact region can reach more than fifteen times the maximum Hertzian pressure. Gaps exist within the nominal Hertzian contact region which means that the surface roughnesses are not flattened completely within the nominal contact area. The pressure ripples are alleviated significantly if lubrication is considered between contacting surfaces. With a roughness value of $\overline{R}_q = 0.2$, the film thickness within the whole calculation domain is always above zero and never reaches the limiting threshold value of ε=0.00001 defined in the Reduced Reynolds model. If the Ree-Eyring behaviour is considered, the pressure fluctuation is alleviated further.

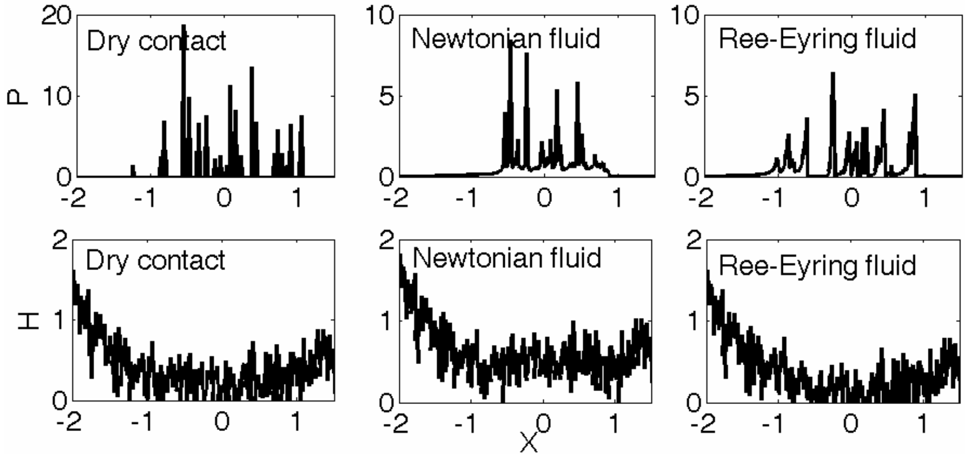

Fig. 5.19 Pressure and film profile with $\overline{R}_q = 0.2$ under dry contact condition, Newtonian fluid, and Ree-Eyring fluid, respectively

5.3.2. Steady-State Solutions and Transient Solutions

Fig. 5.20 shows the pressure distribution at different moments: $\bar{t} = 0$, $\bar{t} = 5\Delta\bar{t}$ and $\bar{t} = 10\Delta\bar{t}$. The dimensionless time interval $\Delta\bar{t}$ is chosen to be $\Delta\bar{t} = \Delta X$. The pressure distribution displays a shifting which is caused by surface topography. Fig. 5.21 shows the film profile at those three moments. The three film distributions also display a shifting with time.

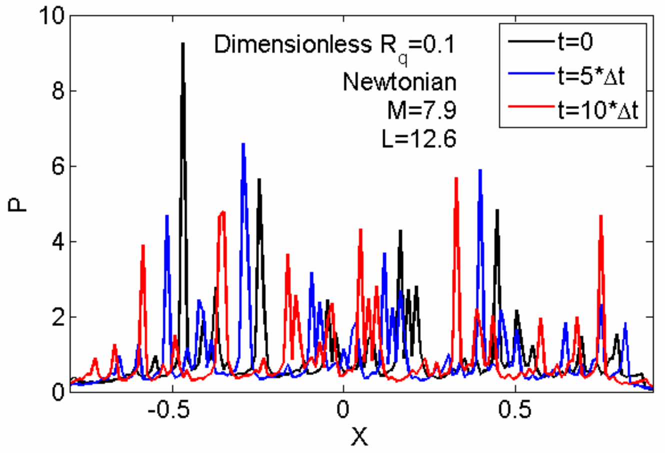

Fig. 5.20 Pressure distribution at three chosen moments with a Newtonian fluid

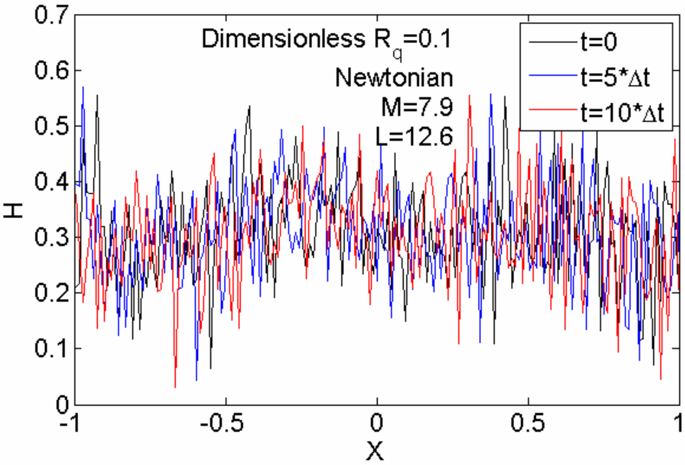

Fig. 5.21 Film profile at three chosen moments with a Newtonian fluid

5.3.3. Effect of RMS Value of Surface Roughness

In this section, the isothermal Ree-Eyring EHL model is used to study the effect of the RMS value of surface roughness. A smooth surface and four surface roughnesses, as shown in Fig. 5.22, are chosen to make a comparison. Fig. 5.23 shows the effect of the RMS value on pressure and film profile with a Ree-Eyring fluid. It is seen as the RMS value increases, the fluctuation of both the pressure and the film thickness become more evident. The maximum pressure may exceeds five times of the maximum Hertzian pressure in the case that $\overline{R}_q = 0.2$. In the case of $\overline{R}_q = 0.15$ and $\overline{R}_q = 0.2$, the film thickness may drop almost to zero, which means "asperity contact" may occur within the nominal contact zone.

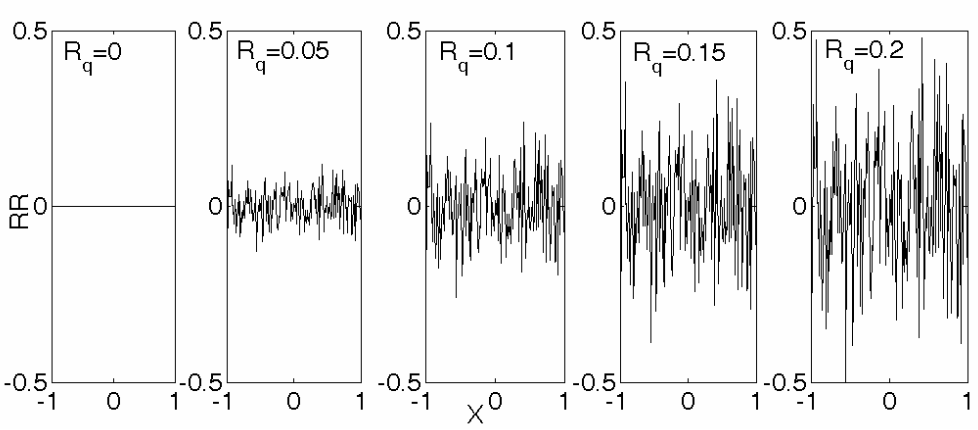

Fig. 5.22 Dimensionless surface roughness with different RMS values

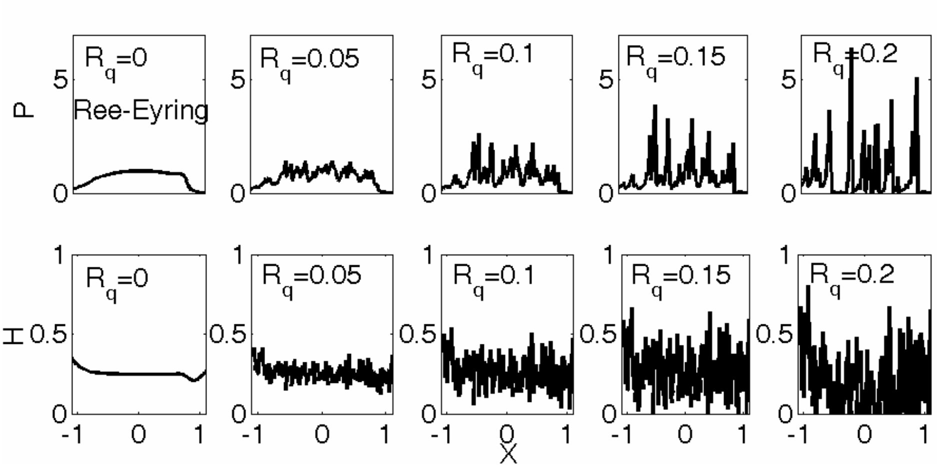

Fig. 5.23 Effect of RMS value on pressure and film profile using a Ree-Eyring fluid with $\tau_0=1\times10^7Pa$

Fig. 5.24 shows the effect of the RMS value on the pressure and film profile for a dry contact. Compared with Fig. 5.23, it is seen that the fluid between contacting surfaces could alleviate the pressure fluctuation within the nominal contact zone if surface roughness is considered. For the dry contact case with $\overline{R}_q = 0.2$, the maximum pressure within the nominal contact zone can reach as high as almost twenty times the Hertzian maximum pressure, while for the Ree-Eyring fluid case, the maximum pressure within the nominal contact zone only reaches six times the Hertzian maximum pressure.

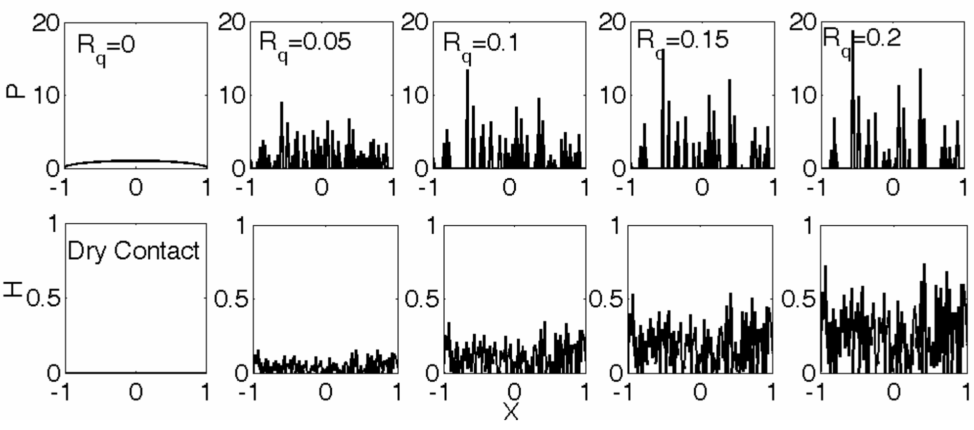

Fig. 5.24 Effect of RMS value on pressure and film profile for a dry contact

The effect of the RMS value on the friction coefficient with a Ree-Eyring fluid is also studied. Fig. 5.25 shows the effect of the RMS value on the friction coefficient for the Ree-Eyring fluid. It is seen that when the RMS value is large, say $\overline{R}_q > 0.15$, the friction coefficient starts fluctuating as the RMS value keeps increasing. While the value is small, the friction coefficient will at first decrease, and then go up as the RMS value increases. This phenomenon is similar to the one found when evaluating the effects of the amplitude of a regular sinusoidal waviness on the friction coefficient using a Ree-Eyring fluid in a previous section. This indicates that a controlled surface pattern with small RMS value may be helpful for reducing the friction.

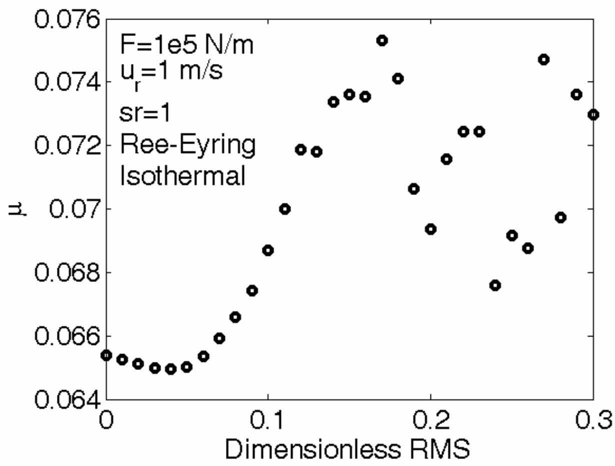

Fig. 5.25 Effect of RMS value on friction coefficient for a Ree-Eyring fluid

As a comparison, the Newtonian-based friction coefficient prediction is also given in Fig. 5.26. It is seen if the Newtonian fluid is assumed, the friction coefficient will generally increase as the RMS value of the roughness increases. The Newtonian-based friction coefficient is still lacking of physical meaning owing to their values being too large.

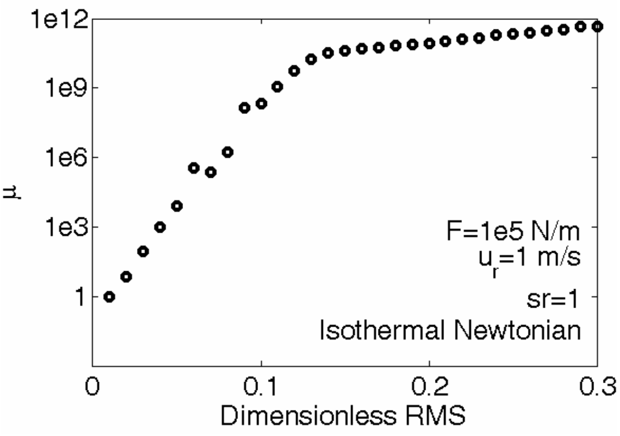

Fig. 5.26 Effect of RMS value on friction coefficient for a Newtonian fluid

5.4. Chapter Summary

A rough surface is considered in this chapter in two ways: first with the regular sinusoidal waviness, and second with the randomly generated roughness following Gaussian distribution. The surface roughness term is added to the film thickness equation. The Reduced Reynolds equation technique is applied to deal with local ultra-thin film situations. The following conclusions can be made:

- With the regular waviness, the larger the amplitude of the waviness, the more evident the fluctuations, which have the same frequency as the original waviness, on the pressure profile and film profile. For the Newtonian solution and the power-law solution, the friction coefficient increases rapidly as the amplitude of the waviness goes up. Even though the power-law fluid friction coefficient values are lower than their Newtonian counterparts, they are still too large to be physically meaningful. For the Ree-Eyring fluid, as the amplitude of waviness increases, the friction coefficient at first decreases slightly or stays constant, and when the amplitude is high the friction coefficient increases gradually as the amplitude keeps increasing.
- For the Newtonian solution and the power-law solution, when the wavelength is above a certain level - e.g. $Wav = 0.05$ in the studies - the friction coefficient first

increases and then decreases as the wavelength increases. However, for the Ree-Eyring fluid, the relationship between the friction coefficient and the wavelength of the waviness depends on the amplitude of the waviness. A more detailed analysis of the waviness wavelength effect is yet to be studied.

- If the digitalized roughness is considered, as the RMS value increases, the fluctuation of both the pressure and the film thickness become more evident. The maximum pressure within the nominal contact zone may exceed several times that of the maximum Hertzian pressure, and the minimum film thickness within the nominal contact zone may drop almost to zero locally which leads to the "mixed lubrication" situation.

Chapter 6 A Thermal EHL Model

In this chapter, TEHL models considering different fluid rheology models are developed. The generalized Reynolds equation proposed by Yang and Wen [3] is used, within which it is easy to incorporate the thermal effect. This method has been applied by Yang and co-workers for starved EHL analysis [122], the size effect of roller pairs [123], the thermal conductivity effects of contacting surfaces [124], and vibration effects [125], amongst others.

Compared with point contact problems, solving temperature distribution for line contact problems is easier for the following reasons:

i. The y direction, which is normal to the flow direction and the direction across the film, does not need to be considered which decreases the computational cost significantly.

ii. The type of energy equation describing the fluid and the solids is the same.

iii. The temperature at the boundary in x direction does not to be calculated again for a line contact, which means the forms of those differential equations are identical and can be treated in a single way.

6.1. A TEHL Model with Energy Equations

6.1.1. Energy Equation

The fluid will generate heat owing to the viscous shearing and compression which would cause the rising of temperature. Meanwhile, the heat generated would dissipate owing to the convection effect and the conduct effect. These effects lead to a steady state of temperature distribution once the thermal balance is achieved. The temperature field then can be determined by solving energy equations of solids and the film.

The energy equation for the film is with a complicated form and the dimensionless process of this equation is necessary to reproduce here, which stems from Ref. [126].

If no transient effect is taken into account, the energy equation for the fluid can be written as

$$\underbrace{c[\rho u\frac{\partial T}{\partial x}-\frac{\partial}{\partial x}\int_0^z \rho udz'\frac{\partial T}{\partial z}]}_{HeatConvection}+\underbrace{\frac{T}{\rho}\frac{\partial \rho}{\partial T}\frac{u\partial p}{\partial x}}_{CompressionHeat} = \underbrace{k\frac{\partial^2 T}{\partial z^2}}_{HeatConduction}+\underbrace{\eta(\frac{\partial u}{\partial z})^2}_{ViscousHeat} \quad (6.1)$$

Where c is specific heat of the fluid ($J/(kgK)$), ρ is the density of the fluid (kg/m^3), k is the thermal conductivity of the fluid ($W/(mK)$). T is the temperature (K), and u is the velocity of the fluid along the flow direction.

The first term on the left side of Eq. 6.1 represents the heat transfer by convection. The first term of the convection heat transfer can be expressed as

$$c\rho u\frac{\partial T}{\partial x}=cT_0\rho_0\frac{u_r}{b}\overline{\rho u}(\frac{\partial \overline{T}}{\partial X}-\frac{Z}{H}\frac{\partial H}{\partial X}\frac{\partial \overline{T}}{\partial Z}) \quad (6.2)$$

if the dimensionless parameter $\overline{T}$ is defined as

$$\overline{T}=T/T_0 \quad (6.3)$$

While the second term of the convection heat transfer reads

$$-c\frac{\partial}{\partial x}\int_0^z \rho udz'\frac{\partial T}{\partial z}=-cT_0\rho_0\frac{u_r}{b}[\frac{\partial}{\partial X}(H\int_0^Z \overline{\rho u}dZ')\frac{1}{H}\frac{\partial \overline{T}}{\partial Z}- \\ \overline{\rho u}\frac{Z}{H}\frac{\partial H}{\partial X}\frac{\partial \overline{T}}{\partial Z}] \quad (6.4)$$

When deriving the above equation the following differential relation is used

$$\frac{\partial}{\partial Z}\int_0^Z \overline{\rho u}HdZ'=\overline{\rho u}H \quad (6.5)$$

The total convection heat transfer term then reads

$$Term=cT_0\rho_0\frac{u_r}{b}(\overline{\rho u}\frac{\partial \overline{T}}{\partial X}+\overline{q}\frac{\partial \overline{T}}{\partial Z}) \quad (6.6)$$

In which

$$\bar{q} = -\frac{1}{H}\frac{\partial}{\partial X}(H\int_0^Z \rho u dZ') \tag{6.7}$$

6.1.2. Calculation Scheme

The temperature domain is divided into three sub-domains including the film region and the two solid regions. At constant load and constant surface velocities, when thermal equilibrium has been reached, the temperature field is time-independent. Therefore, the energy equation for the film region can be written as

$$\begin{aligned} &c\left(\rho\frac{\partial T}{\partial t} + \rho u\frac{\partial T}{\partial x} + \rho w\frac{\partial T}{\partial z}\right) = k\frac{\partial^2 T}{\partial z^2} \\ &-\frac{T}{\rho}\frac{\partial \rho}{\partial T}(\frac{\partial p}{\partial t} + u\frac{\partial p}{\partial x}) + \tau\frac{\partial u}{\partial z} \end{aligned} \tag{6.8}$$

Where c is specific heat of the fluid ($J/(kgK)$), ρ is the density of the fluid (kg/m^3), k is the thermal conductivity of the fluid ($W/(mK)$), T is the temperature (K), and u is the velocity of the fluid along the flow direction. It is noted that the velocity at the bottom interface is u_a and at the upper interface is u_b. The term ρw could be eliminated with the continuity equation

$$\frac{\partial \rho}{\partial t} + \frac{\partial(\rho u)}{\partial x} + \frac{\partial(\rho w)}{\partial z} = 0 \tag{6.9}$$

Hence

$$\rho w = -\frac{\partial}{\partial t}\int_0^z \rho dz' - \frac{\partial}{\partial x}\int_0^z \rho u dz' \tag{6.10}$$

The thermal conductivity relation can be taken as a fixed parameter [3], or a varying one [127]. Based upon experimental data of lubricants, the pressure dependence of the thermal conductivity can be written as

$$k = k_0(0.75 + 0.25\sqrt{1 + 2\times 10^{-8} p}) \tag{6.11}$$

Where k_0 is the thermal conductivity at ambient pressure.

For di-(2-ethyl-hexyl)-sebacate [128], it can be expressed as

$k = k_0(0.56 + 0.44\sqrt{1 + 2\times10^{-8} p})$ for mineral oils [129]. Fig. 6.1 shows the variation of thermal conductivity along pressure. In this work the thermal conductivity is taken as a constant value.

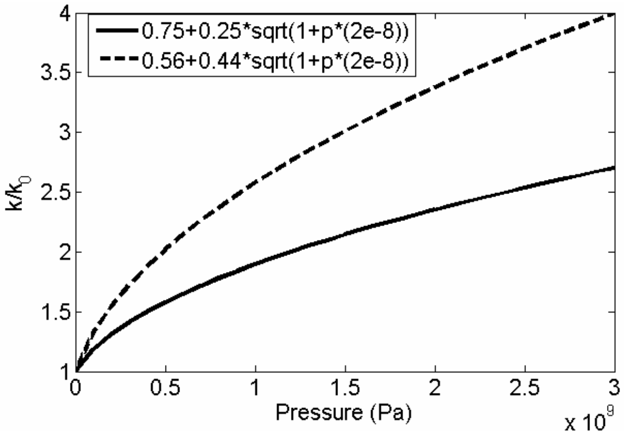

Fig. 6.1 Two thermal conductivity relations

The energy equations for the two solids are

$$\begin{cases} \mathrm{c}_a \rho_a (\dfrac{\partial T}{\partial t} + u_a \dfrac{\partial T}{\partial x}) = k_a \dfrac{\partial^2 T}{\partial z_a^2} \\ \mathrm{c}_b \rho_b (\dfrac{\partial T}{\partial t} + u_b \dfrac{\partial T}{\partial x}) = k_b \dfrac{\partial^2 T}{\partial z_b^2} \end{cases} \tag{6.12}$$

Where $\mathrm{c}_i (i = a, b)$, $\rho_i (i = a, b)$ and $k_i (i = a, b)$ are specific heat, densities and thermal conductivities of the solids. Directions of z_a and z_b are the same as the direction of z defined in an isothermal THL model. Equation 6.12 is generated by assuming that the moving solids are fluids. This equation is a simplified form of the energy equation given before. Equation 6.12 is used for predicting the temperature field inside the solid bodies. The temperature of the solid and that of the film should be the same at the interface. This heat flux continuity condition reads

$$\begin{cases} k\left.\dfrac{\partial T}{\partial z}\right|_{z=0} = k_a \left.\dfrac{\partial T}{\partial z_a}\right|_{z_a=0} \\ k\left.\dfrac{\partial T}{\partial z}\right|_{z=h} = k_b \left.\dfrac{\partial T}{\partial z_b}\right|_{z_b=0} \end{cases} \tag{6.13}$$

The domain is given by $x_b \le x \le x_a$, $0 \le z \le h$, $-d \le z_a \le 0$ and $0 \le z_b \le d$. d is the thickness of the thermal layers in the bodies and is often given by $d / b = 3.15$ [122] because this distance inside the solids is considered to be far away enough from the surfaces and the temperatures there are assumed to be the temperature of the environment.

The temperature boundary condition at the upstream of the film is

$$T(0, z, t) = T_0 \tag{6.14}$$

when $u(0, z, t) \ge 0$.

At the counter flow area in the upstream of the film, there is no need to set the boundary condition, which is the same situation at the downstream of the film. For solids a and b, the temperature boundary conditions along z_a and z_b direction are

$$\begin{cases} T\big|_{z_a=-d} = T_0 \\ T\big|_{z_b=d} = T_0 \end{cases} \tag{6.15}$$

Similar to the boundary condition of the film, there is no need to set a boundary condition for energy equations of solids at the downstream $x = x_b$, while at the upstream $x = x_a$, the boundary condition for Eq. 6.13 is not necessary, which could be chosen as $T = T_0$ or $\partial T / \partial z = 0$.

It is worth noting that those thermal equations were also applied in the exit cavitation region. Since in the cavitation region the film is not continuous, the solved temperature in this region is not accurate. Fortunately this inaccuracy has no effect on the solution in the full film region [122].

Additionally, if the quasi-steady state is considered, the transient energy equations of the contact bodies do not need to be solved [125]. Thus the quasi-steady state surface conditions become

$$\begin{cases} T_a(x,t) = T_0 + \dfrac{k}{\sqrt{\pi c_a \rho_a k_a u_{a0}}} \displaystyle\int_{x_b}^{x} \left.\dfrac{\partial T}{\partial z}\right|_{z=0} \dfrac{dx'}{\sqrt{x-x'}} \\ T_b(x,t) = T_0 - \dfrac{k}{\sqrt{\pi c_b \rho_b k_b u_{b0}}} \displaystyle\int_{x_b}^{x} \left.\dfrac{\partial T}{\partial z}\right|_{z=h} \dfrac{dx'}{\sqrt{x-x'}} \end{cases} \tag{6.16}$$

Where c_a, c_b are specific heats of the two solids ($J/(kgK)$), ρ_a, ρ_b are densities of the two solids (kg/m^3), k_a, k_b are thermal conductivities of the two solids ($W/(mK)$), respectively.

The approach applied for TEHL problems here is that proposed by Yang et al. [47]. Fig. 6.2 shows the flow chart of the TEHL calculation process.

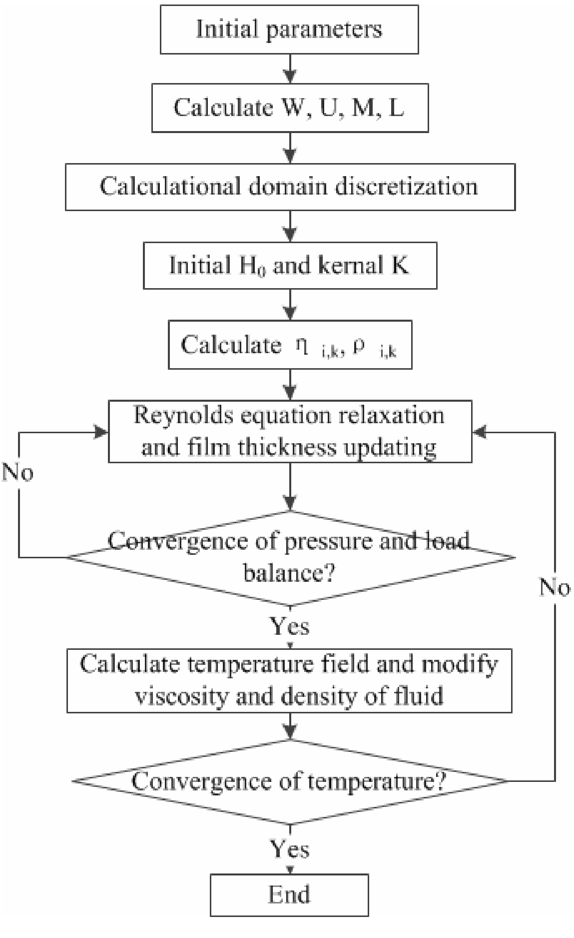

Fig. 6.2 Flow chart of the TEHL model solving process

6.1.3. Dimensionless Scheme

Define the following parameters

$$P_\gamma = c\eta_0 / k \tag{6.17}$$

$$E_c = u_r^2 / (cT_0) \tag{6.18}$$

$$Y_t = cbp_H / (u_r k) \tag{6.19}$$

The dimensionless energy equation of the film is derived as

$$\begin{aligned} & P_\gamma R_e^*(\bar{\rho}\frac{\partial \bar{T}}{\partial \bar{t}} + \bar{\rho}\bar{u}\frac{\partial \bar{T}}{\partial X} - \frac{\bar{q}}{H}\frac{\partial \bar{T}}{\partial Z}) - \frac{1}{H^2}\frac{\partial^2 \bar{T}}{\partial Z^2} = \\ & -E_c Y_t (\frac{k_0}{b})^2 \frac{\bar{T}}{\bar{\rho}}\frac{\partial \bar{\rho}}{\partial \bar{T}}(\frac{\partial P}{\partial \bar{t}} + \bar{u}\frac{\partial P}{\partial X}) \end{aligned} \tag{6.20}$$

Where

$$\bar{q} = \frac{\partial}{\partial \bar{t}}(H\int_0^Z \bar{\rho} dZ') + \frac{\partial}{\partial X}(H\int_0^Z \bar{\rho}\bar{u} dZ') \tag{6.21}$$

Energy equations for solids could be dimensionlessed with the following set of dimensionless parameters, as defined by Yang [126]:

$$\begin{cases} CN_a = bUc_a\rho_a / k_a \\ CN_b = bUc_b\rho_b / k_b \end{cases} \tag{6.22}$$

Then the dimensionless energy equations of solids are

$$\begin{cases} CN_a(\frac{\partial \bar{T}}{\partial \bar{t}} + \bar{U}_a\frac{\partial \bar{T}}{\partial X}) - \frac{\partial^2 T}{\partial Z_a^2} = 0 \\ CN_b(\frac{\partial \bar{T}}{\partial \bar{t}} + \bar{U}_b\frac{\partial \bar{T}}{\partial X}) - \frac{\partial^2 T}{\partial Z_b^2} = 0 \end{cases} \tag{6.23}$$

The dimensionless continuity heat flux equations at the interfaces are

$$\begin{cases} \dfrac{CM_a}{\overline{h}} \dfrac{\partial \overline{T}}{\partial Z}\bigg|_{Z=0} = \dfrac{\partial \overline{T}}{\partial Z_a}\bigg|_{Z_a=0} \\ \dfrac{CM_b}{\overline{h}} \dfrac{\partial \overline{T}}{\partial Z}\bigg|_{Z=1} = \dfrac{\partial \overline{T}}{\partial Z_b}\bigg|_{Z_b=0} \end{cases} \tag{6.24}$$

Where

$$\begin{cases} CM_a = \dfrac{k}{k_a} \dfrac{R}{b} \\ CM_b = \dfrac{k}{k_b} \dfrac{R}{b} \end{cases} \tag{6.25}$$

It is clear that once dimensionlessed, the calculation domain of the temperature field becomes rectangular with no relation to time or film shape. The boundary condition of the temperature domain is $\overline{T} = 1$ at four boundaries $X = X_a$, $X = X_b$, $Z = 0$ or $Z = 1$.

6.1.4. Discretization and Differential Scheme

6.1.4.1. Grid Discretization

In order to get differential equations, a discretized scheme should be chosen. Along the x direction, the discretization scheme for pressure and film thickness, etc., applied in a thermal EHL model, is identical to the isothermal EHL model. The discretization along z direction is determined like this: the grid used along z direction is set to be equally spaced within the film while it is unequally spaced within the solid bodies, as shown in Fig. 6.3. In z direction there are 21 points set in total, of which 11 points are located equally within the film and 5 points are located within each solid.

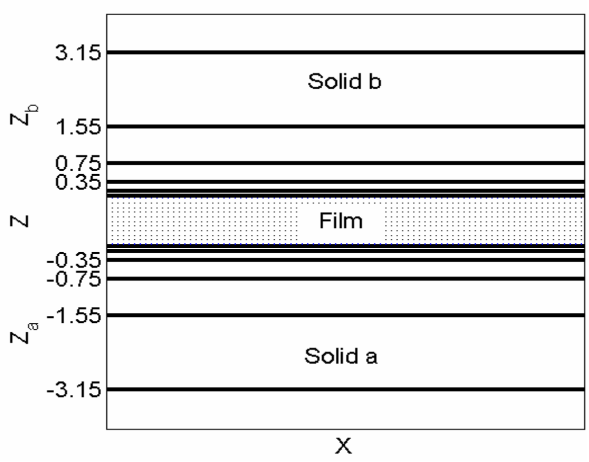

Fig. 6.3 Configuration of Z_a, Z, Z_b for the temperature field

6.1.4.2. Differential Schemes of the Temperature

Since the heat conduction along x direction is neglected in the energy equation, the temperature of a point bears no business to the ones downstream. Therefore, an appropriate differential scheme of $\partial \overline{T} / \partial X$ inside the film can be expressed as

$$\left.\frac{\partial \overline{T}}{\partial X}\right|_{i,k} = \begin{cases} \dfrac{\overline{T}_{i,k} - \overline{T}_{i-1,k}}{\Delta X}, & \overline{u}_{i,k} \geq 0 \\ \dfrac{\overline{T}_{i+1,k} - \overline{T}_{i,k}}{\Delta X}, & \overline{u}_{i,k} < 0 \end{cases} \tag{6.26}$$

In the z direction, a central differential scheme is often applied

$$\begin{cases} \left.\dfrac{\partial \overline{T}}{\partial Z}\right|_{i,k} = \dfrac{\overline{T}_{i,k+1} - \overline{T}_{i,k-1}}{2\Delta Z} \\ \left.\dfrac{\partial^2 \overline{T}}{\partial Z^2}\right|_{i,k} = \dfrac{\overline{T}_{i,k+1} - 2\overline{T}_{i,k} + \overline{T}_{i,k-1}}{\Delta Z^2} \end{cases} \tag{6.27}$$

Differential equations at the interface should be determined according to the continuity condition of heat flux. Differential schemes for the temperature prediction inside solids are often chosen as a central differential one.

The discretization terms used in this work are listed as follows:

$$\left(\frac{\partial^2 \overline{T}}{\partial {Z_a}^2}\right)_{i,j} = A_{j,j-1}T_{i,j-1} + A_{j,j}T_{i,j} + A_{j,j+1}T_{i,j+1}(j=-5,-4,...,-1) \quad (6.28)$$

$$\left(\frac{\partial^2 \overline{T}}{\partial Z^2}\right)_{i,j} = \frac{(T_{i,j-1} - 2T_{i,j} + T_{i,j+1})}{\Delta Z^2}(j=1,2,...,9) \quad (6.29)$$

$$\left(\frac{\partial^2 \overline{T}}{\partial {Z_b}^2}\right)_{i,j} = B_{j,j-1}T_{i,j-1} + B_{j,j}T_{i,j} + B_{j,j+1}T_{i,j+1}(j=11,12,...,15) \quad (6.30)$$

$$\left(\frac{\partial \overline{T}}{\partial Z_a}\right)_{i,j} = \frac{\overline{T}_{i,j} - \overline{T}_{i,j-1}}{\Delta Z_a}(j=0) \quad (6.31)$$

$$\left(\frac{\partial \overline{T}}{\partial Z}\right)_{i,j} = \frac{\overline{T}_{i,j+1} - \overline{T}_{i,j}}{\Delta Z}(j=0) \quad (6.32)$$

$$\left(\frac{\partial \overline{T}}{\partial Z}\right)_{i,j} = \frac{\overline{T}_{i,j+1} - \overline{T}_{i,j-1}}{2\Delta Z}(j=1,2,...,9) \quad (6.33)$$

$$\left(\frac{\partial \overline{T}}{\partial Z}\right)_{i,j} = \frac{\overline{T}_{i,j} - \overline{T}_{i,j-1}}{\Delta Z}(j=10) \quad (6.34)$$

$$\left(\frac{\partial \overline{T}}{\partial Z_b}\right)_{i,j} = \frac{\overline{T}_{i,j+1} - \overline{T}_{i,j}}{\Delta Z_b}(j=10) \quad (6.35)$$

$$\left(\frac{\partial \overline{T}}{\partial X}\right)_{i,j} = \frac{\overline{T}_{i,j} - \overline{T}_{i-1,j}}{\Delta X}(j=-5,-4,...,-1;11,12,...,15; \\ j=1,2,...,9 if \overline{u}_{i,j} \geq 0) \quad (6.36)$$

$$\left(\frac{\partial \overline{T}}{\partial X}\right)_{i,j} = \frac{\overline{T}_{i+1,j} - \overline{T}_{i,j}}{\Delta X}(j=1,2,...,9 if \overline{u}_{i,j} < 0) \quad (6.37)$$

$$\left(\frac{\partial \overline{T}}{\partial \overline{t}}\right)_{i,j} = \frac{\overline{\overline{T}}_{i,j} - \overline{T}_{i,j}}{\Delta \overline{t}} \quad (6.38)$$

Where $\Delta Z_a = (Z_a)_0 - (Z_a)_{-1}$, $\Delta Z_b = (Z_b)_{11} - (Z_b)_{10}$, $\Delta Z = 0.1$. $\overline{\overline{T}}_{i,j}$ means the previous value of $T_{i,j}$ at time $\overline{t} - \Delta\overline{t}$.

The new differential coefficients are

$$\begin{cases} A_{j,j-1} = 2/\{[(Z_a)_{j-1} - (Z_a)_j][(Z_a)_{j-1} - (Z_a)_{j+1}]\} \\ A_{j,j} = 2/\{[(Z_a)_j - (Z_a)_{j-1}][(Z_a)_j - (Z_a)_{j+1}]\} \\ A_{j,j+1} = 2/\{[(Z_a)_{j+1} - (Z_a)_{j-1}][(Z_a)_{j+1} - (Z_a)_j]\} \end{cases} \tag{6.39}$$

$$\begin{cases} B_{j,j-1} = 2/\{[(Z_b)_{j-1} - (Z_b)_j][(Z_b)_{j-1} - (Z_b)_{j+1}]\} \\ B_{j,j} = 2/\{[(Z_b)_j - (Z_b)_{j-1}][(Z_b)_j - (Z_b)_{j+1}]\} \\ B_{j,j+1} = 2/\{[(Z_b)_{j+1} - (Z_b)_{j-1}][(Z_b)_{j+1} - (Z_b)_j]\} \end{cases} \tag{6.40}$$

Using those discretization forms and those coefficients, six differential equations are derived to describe different regions for the temperature prediction.

When the speed is slow and load is light, the inverse flow zone is small, while when the speed is high or the load is heavy, the inverse flow zone becomes bigger and the terminating point of this zone moves towards the nominal contact centre. The inverse flow phenomenon introduces two difficulties for TEHL solving. First, since the fluid flows in an inverse way, the temperature distribution at the inlet boundary will be unknown; second, it may make the solving process of energy equations being instability. Fig. 6.4 shows the boundary conditions for the temperature calculation. The inverse flow zone is treated separately.

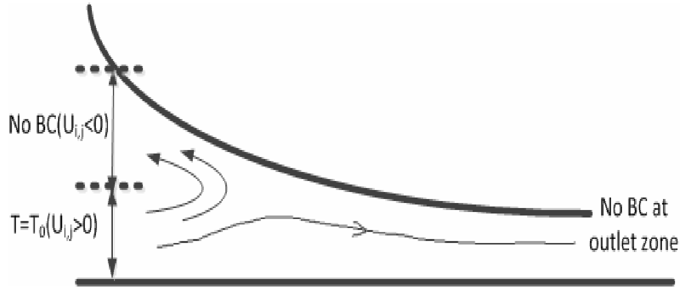

Fig. 6.4 Boundary conditions for temperature calculation

- For the points inside the solid a:

$$\begin{aligned} &-A_{j,j-1}\overline{T}_{i,j-1} + \left(\frac{CN_a}{\Delta t} + \frac{CN_a\overline{u}_a}{\Delta X} - A_{j,j}\right)\overline{T}_{i,j} - A_{j,j+1}\overline{T}_{i,j+1} = \\ &\frac{CN_a}{\Delta t}\overset{\square}{T}_{i,j} + \frac{CN_a\overline{u}_a}{\Delta X}\overline{T}_{i-1,j}(j = -5,-4,...,-1) \end{aligned} \tag{6.41}$$

- For the points on the interface between solid a and the film:

$$\frac{\bar{T}_{i,j-1}}{\Delta Z_a} - \left(\frac{CM_a}{H\Delta Z} + \frac{1}{\Delta Z_a}\right)\bar{T}_{i,j} + \frac{CM_a}{H\Delta Z}\bar{T}_{i,j+1} = 0(j=0) \tag{6.42}$$

- For the points inside the film:

$$\begin{aligned}
&-\left[\frac{1}{(H_i\Delta Z)^2} - \frac{CS_1 Q_{i,j}}{2H_i\Delta Z}\right]\bar{T}_{i,j-1} + \left[\frac{CS_1\bar{\rho}_{i,j}}{\Delta \bar{t}} + \frac{CS_1\bar{\rho}_{i,j}\bar{u}_{i,j}}{\Delta X} + \right. \\
&\left.\frac{2}{(H_i\Delta Z)^2}\right]\bar{T}_{i,j} - \left[\frac{1}{(H_i\Delta Z)^2} + \frac{CS_1 Q_{i,j}}{2H_i\Delta Z}\right]\bar{T}_{i,j+1} = \\
&\frac{CS_3}{H_i}\bar{\tau}_{i,j}\left(\frac{\partial\bar{u}}{\partial Z}\right)_{i,j} + \frac{CS_1\bar{\rho}_{i,j}}{\Delta \bar{t}}\overset{\square}{\bar{T}}_{i,j} + \frac{CS_1\bar{\rho}_{i,j}\bar{u}_{i,j}}{\Delta X}\bar{T}_{i-1,j} + \\
&\frac{CS_2}{\bar{\rho}_{i,j}}\left[\left(\frac{\partial P}{\partial \bar{t}}\right)_i + \bar{u}_{i,j}\left(\frac{\partial P}{\partial X}\right)_i\right]\bar{T}_{i,j}(j=1,2,\ldots,9 if \bar{u}_{i,j} \geq 0)
\end{aligned} \tag{6.43}$$

- While for the points inside the film with $\bar{u}_{i,j} < 0$

$$\begin{aligned}
&-\left[\frac{1}{(H_i\Delta Z)^2} - \frac{CS_1 Q_{i,j}}{2H_i\Delta Z}\right]\bar{T}_{i,j-1} + \left[\frac{CS_1\bar{\rho}_{i,j}}{\Delta \bar{t}} - \right. \\
&\left.\frac{CS_1\bar{\rho}_{i,j}\bar{u}_{i,j}}{\Delta X} + \frac{2}{(H_i\Delta Z)^2}\right]\bar{T}_{i,j} - \left[\frac{1}{(H_i\Delta Z)^2} + \frac{CS_1 Q_{i,j}}{2H_i\Delta Z}\right]\bar{T}_{i,j+1} \\
&= \frac{CS_3}{H_i}\bar{\tau}_{i,j}\left(\frac{\partial\bar{u}}{\partial Z}\right)_{i,j} + \frac{CS_1\bar{\rho}_{i,j}}{\Delta \bar{t}}\overset{\square}{\bar{T}}_{i,j} - \frac{CS_1\bar{\rho}_{i,j}\bar{u}_{i,j}}{\Delta X}\bar{T}_{i+1,j} - \\
&\frac{CS_2}{\bar{\rho}_{i,j}}\left[\left(\frac{\partial P}{\partial \bar{t}}\right)_i + \bar{u}_{i,j}\left(\frac{\partial P}{\partial X}\right)_i\right]\bar{T}_{i,j}
\end{aligned} \tag{6.44}$$

- For the points on the interface between solid b and the film:

$$\frac{CM_b}{H_i\Delta Z}\bar{T}_{i,j-1} - \left(\frac{CM_b}{H_i\Delta Z} + \frac{1}{\Delta Z_b}\right)\bar{T}_{i,j} + \frac{\bar{T}_{i,j+1}}{\Delta Z_b} = 0 \tag{6.45}$$

- For the points inside the solid b $(j = 11,12,\ldots,15)$

$$\begin{aligned}
&-B_{j,j-1}\bar{T}_{i,j-1} + \left(\frac{CN_b}{\Delta \bar{t}} + \frac{CN_b\bar{u}_b}{\Delta X} - B_{j,j}\right)\bar{T}_{i,j} - \\
&B_{j,j+1}\bar{T}_{i,j+1} = \frac{CN_b}{\Delta \bar{t}}\overset{\square}{\bar{T}}_{i,j} + \frac{CN_b\bar{u}_b}{\Delta X}\bar{T}_{i-1,j}
\end{aligned} \tag{6.46}$$

Where

$$\begin{cases} CS_1 = P_T \operatorname{Re}^* \\ CS_2 = \overline{C}_3 EcYt(b/R)^2 \\ CS_3 = EcYt(b/R) \end{cases} \qquad (6.47)$$

Where $\overline{C}_3 = 0.00065T_0$.

The temperature terms on the right hand side of those equations are treated as the old ones, while the terms on the left hand side of the equations are handled as unknowns.

6.1.4.3. Matrix Solving

The coefficient matrix of the set of equations can be written as a 21×21 tridiagonal matrix which is a diagonally dominant matrix. Hence, this set of equations (21 equations for a X_i) can be solved efficiently with the chasing method. Equation 6.47 is the system of equations for temperature prediction at X_i. Once the equations for X_i are solved, solutions for X_{i+1} can be solved similarly until the temperature field is calculated completely.

$$\begin{bmatrix} A_{-5,-5} & A_{-5,-4} & & & & \\ A_{-4,-5} & A_{-4,-4} & A_{-4,-3} & & & \\ & \cdot & \cdot & \cdot & & \\ & & \cdot & \cdot & \cdot & \\ & & & A_{14,13} & A_{14,14} & A_{14,15} \\ & & & & A_{15,14} & A_{15,15} \end{bmatrix} \begin{Bmatrix} \overline{T}_{-5} \\ \overline{T}_{-4} \\ \cdot \\ \cdot \\ \overline{T}_{14} \\ \overline{T}_{15} \end{Bmatrix} = \begin{Bmatrix} b_{-5} \\ b_{-4} \\ \cdot \\ \cdot \\ b_{14} \\ b_{15} \end{Bmatrix} \qquad (6.48)$$

Fig. 6.5 shows the calculation flow chart of the temperature field.

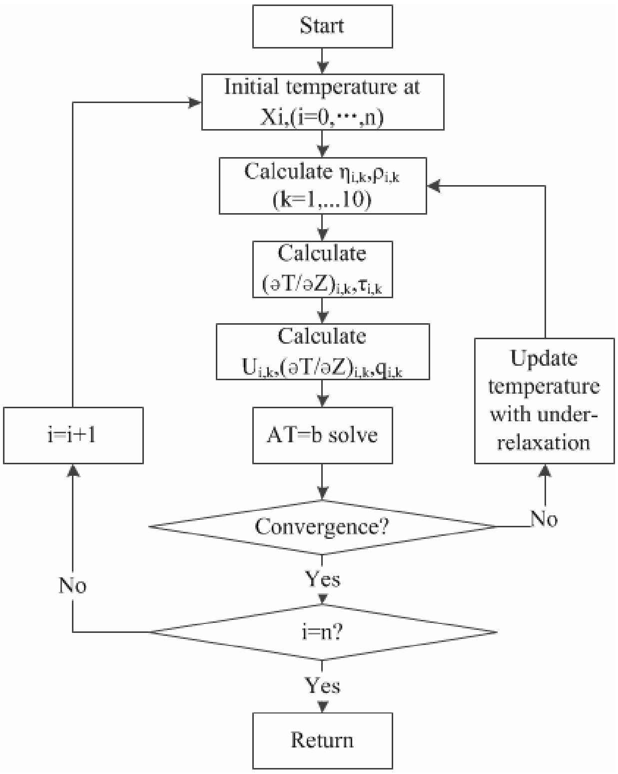

Fig. 6.5 Calculation flow chart of the temperature field

In order to guarantee the numerical stability in the iteration process, the new temperature distribution can act as the initial values for the next time with an under-relaxation factor such as $w_T = 0.2 - 0.4$.

$$\overline{T}_{i,j} = \overline{T}'_{i,j} + \varpi_T(\overline{T}''_{i,j} - \overline{T}'_{i,j}) \qquad (6.49)$$

As found by Yang [126], in the first several relaxation loops, values less than 1 may occur for the updated dimensionless temperature which is physically unreasonable. It is fair to let those values equal 1 immediately when they are discovered. A convergence check is performed after all X_i are scanned. The convergence criterion is defined as

$$\sum_{j=1}^{20} \left| \overline{T}^{k}_{i,j} - \overline{T}'^{k-1}_{i,j} \right| / \sum_{j=1}^{20} \left| \overline{T}^{k}_{i,j} \right| \leq 0.0001 (i = 0, \ldots, n) \qquad (6.50)$$

Once the temperature is converged, the density and viscosity of the fluid can be updated which are used in the pressure updating process. This outside iteration needs to be done with just several iterations. It is much easier to get a converged solution for the temperature field than for the pressure field. If the multigrid method is not used, the pressure may need more than thousands of iterations to converge, while the temperature will probably converge within several iterations.

6.2. Numerical Cases

Numerical cases are provided to help readers gain some understanding about thermal effects. The parameters used in this case are chosen as follows:

$T_0 = 300K$, $\eta_0 = 0.08Pas$, $c = 2000J/kgK$, $k = 0.14W/mK$, $\rho_0 = 870kg/m^3$, $\rho_{a,b} = 7850kg/m^3$, $c_{a,b} = 470J/kgK$, $k_{a,b} = 46W/mK$.

Fig. 6.6 shows the distribution of $\bar{\eta}$ for a Newtonian fluid under thermal conditions. It is seen that the profile of $\bar{\eta}$ varies along z direction for the thermal solution while it keeps constant along z direction for the isothermal case. The values of $\bar{\eta}$ for the thermal case are smaller than the values for the isothermal case. This indicates that the thermal effect would reduce the equivalent viscosity of the fluid.

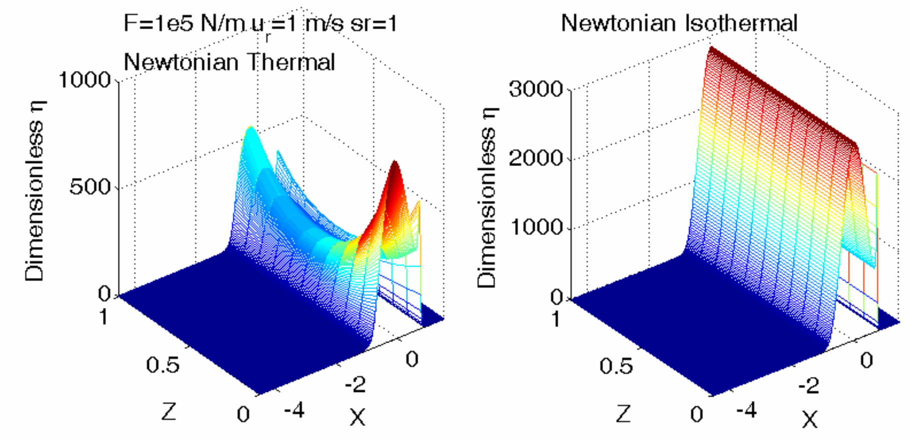

Fig. 6.6 Comparison of $\bar{\eta}$ for the isothermal solution and the thermal solution with a Newtonian fluid

Fig. 6.7 shows the distribution of $\bar{\tau}$ for the isothermal solution and the thermal solution. It is seen that for both cases, the $\bar{\tau}$ profile along z direction doesn't change significantly, which indicates that the frictional behaviour can be studied simply by just checking the traction on the interface $\bar{\tau}_a$. For the given conditions, the values of the shear stress reduce remarkably if the thermal effect is considered. The thermal effect on frictional behaviour is studied in detail later.

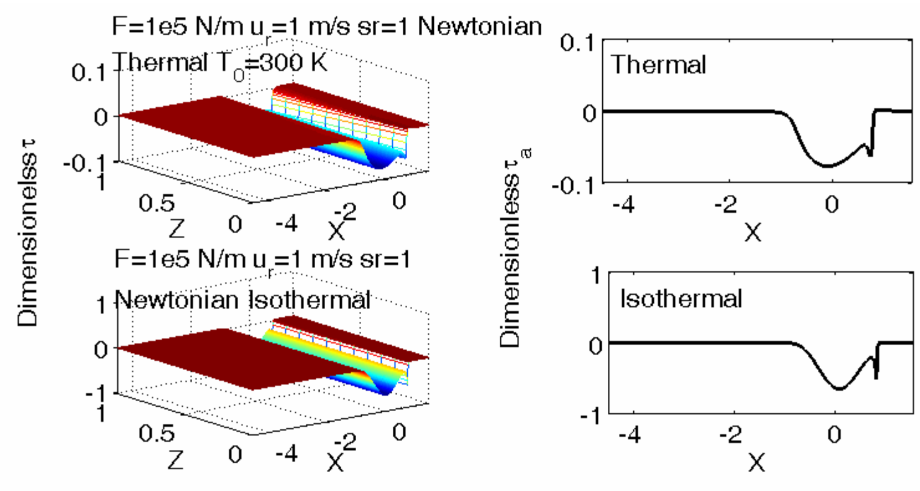

Fig. 6.7 Comparison of $\bar{\tau}$ for the isothermal solution and the thermal solution with a Newtonian fluid

Fig. 6.8 shows the comparison of the distribution of the dimensionless flow velocity $\bar{u}$. Thermal action does not have a significant effect on the velocity field of the fluid.

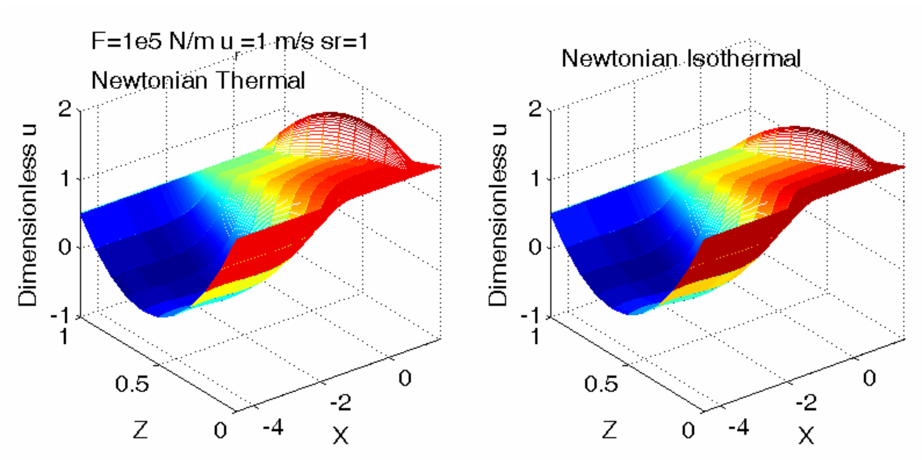

Fig. 6.8 Comparison of $\bar{u}$ for the isothermal solution and the thermal solution with a Newtonian fluid

Fig. 6.9 shows the details of the $\bar{u}$ distribution. Three positions across the film - surface a , the centre in the film, and surface b - are chosen. For both positions, there is only a slight variation of the $\bar{u}$ profile between the isothermal solution and the thermal solution. At the surface nearby, the values of $\bar{u}$ at the inlet zone are above zero, while in the centre area across the film, the values of $\bar{u}$ at the inlet zone fall to negative values for the chosen working condition.

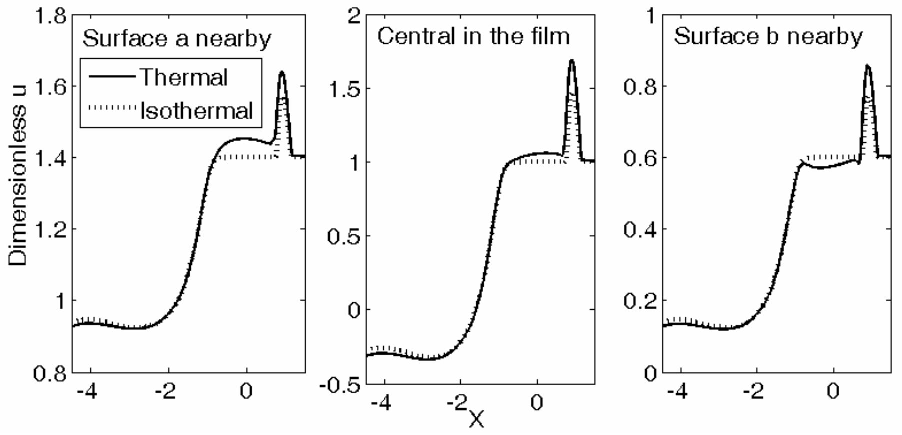

Fig. 6.9 Distribution of $\bar{u}$ at three layers across the film

Fig. 6.10 shows the pressure profile and the film profile. It shows that the profile of the pressure varies only slightly when comparing the thermal solution to the isothermal solution. In terms of pressure, only the amplitude and location of the second pressure spike vary when the thermal effect is considered under this working condition. The minimum film thickness and the average film thickness of the thermal solution change only slightly compared with the isothermal solution. This can be explained as follows: the thermal effect on film thickness can be neglected because the film thickness is mainly dominated by the lubricant entraining action in the inlet zone where the gap is still large and the effects of thermal behaviours are still limited in most cases [26].

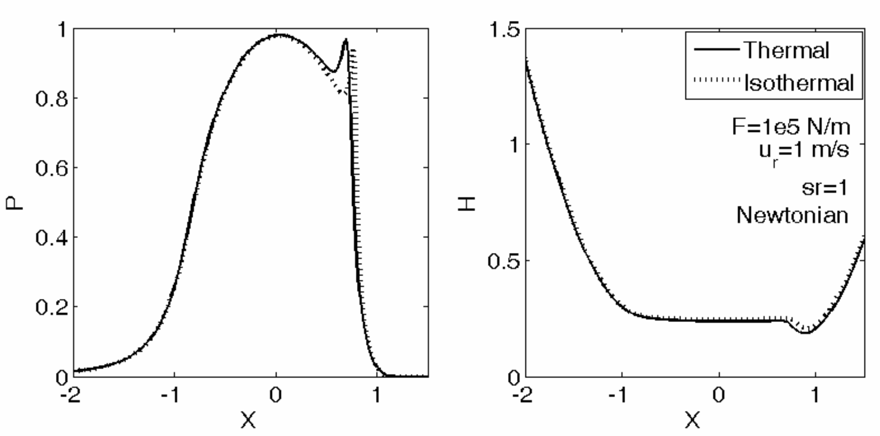

Fig. 6.10 Comparison of P and H for the isothermal solution and the thermal solution with a Newtonian fluid

Fig. 6.11 shows the temperature distribution for the Newtonian thermal case. It is seen that the temperature at the outlet zone is higher than the one in the inlet zone. Within the nominal contact zone, similar to the pressure profile, the temperature profile also has a second spike at the outlet zone. Along the z direction across the film, the highest temperature occurs at the central layer of the film.

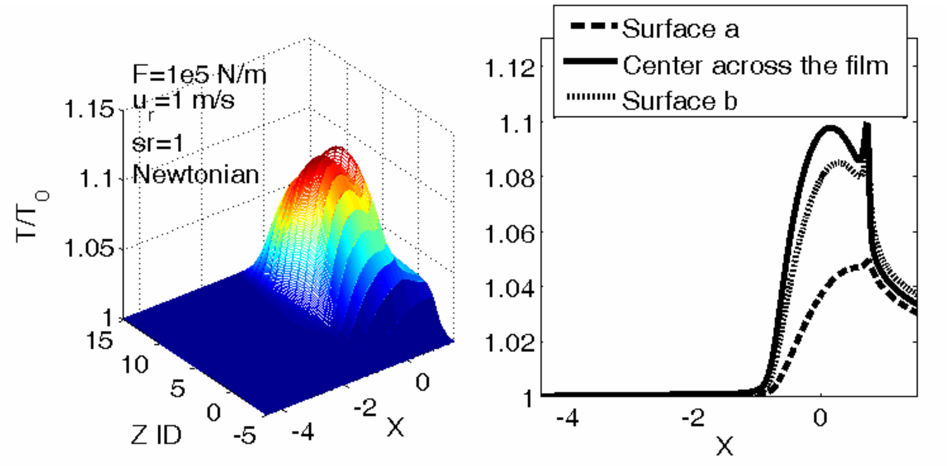

Fig. 6.11 Temperature field for the Newtonian thermal case

6.2.1. Effect of Load Under Thermal Condition

6.2.1.1. The Newtonian Fluid

The effect of load for a Newtonian thermal EHL model is studied. Fig. 6.12 shows the friction coefficient for different load cases. It is seen that for the working condition selected, there is almost no difference between the isothermal friction coefficient values and their thermal counterparts. The friction coefficient still increases almost exponentially as the load increases.

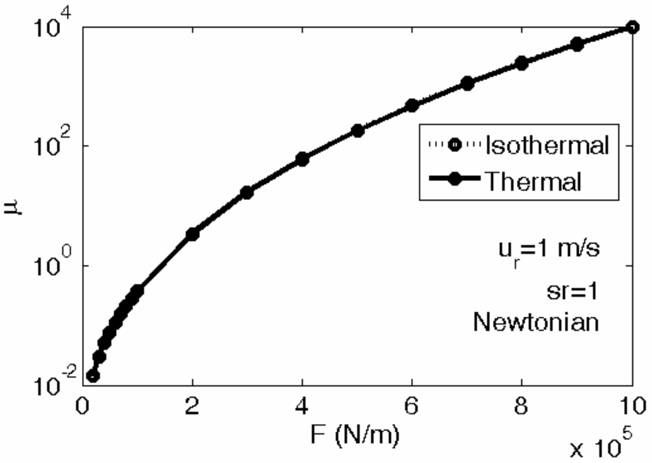

Fig. 6.12 Variation of μ with load for a Newtonian fluid

Fig. 6.13 shows the distribution of dimensionless temperature $\overline{T}$ for a Newtonian fluid. The right side subfigures show the temperature at the central layer of the film. It is seen that, under the working condition studied - $u_r = 1m/s$, $sr = 1$ - the temperature does not change significantly as the load increases.

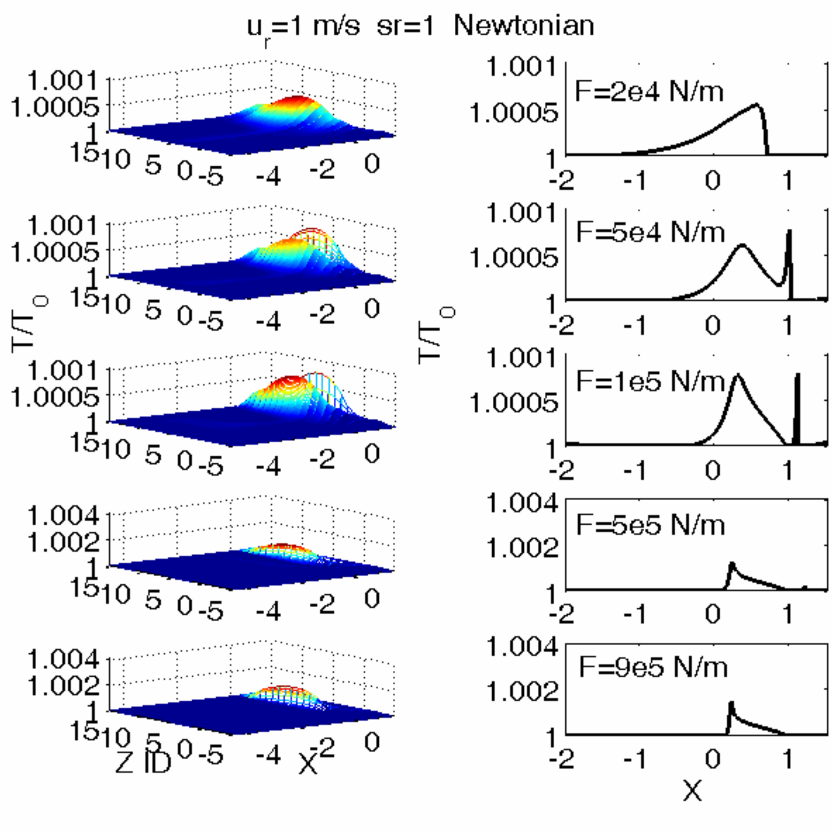

Fig. 6.13 Temperature field for a Newtonian fluid

Fig. 6. 14 shows a comparison of the pressure and film profiles of isothermal and thermal solutions. It is seen that for this case, there is almost no difference between isothermal and thermal solutions for all five load sets.

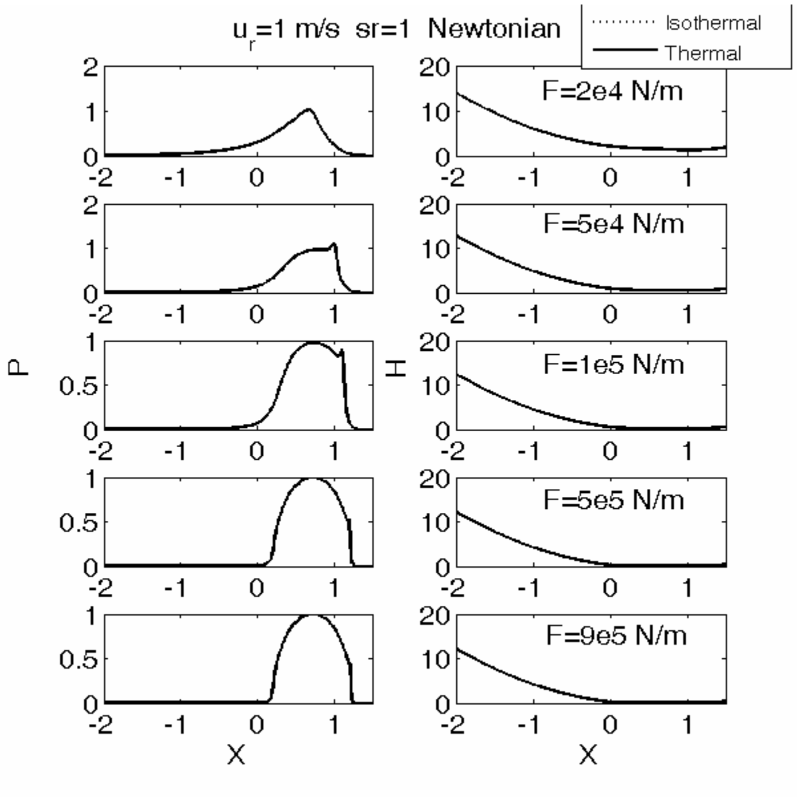

Fig. 6.14 Pressure and film profiles for a Newtonian fluid under thermal and isothermal conditions

6.2.1.2. The Ree-Eyring Fluid

Fig. 6.15 shows the distribution of $\bar{\tau}_a$ for five different load cases: $F = 2\times10^4$, 5×10^4, 1×10^5, 5×10^5 and $9\times10^5 N/m$ with a Ree-Eyring fluid. It is seen that as the load increases, the shear stress within the nominal contact area increases, and the difference between the distribution of $\bar{\tau}_a$ of the thermal solution and the isothermal solution becomes evident, which indicates that, for a Ree-Eyring fluid, the thermal effect on traction is more remarkable when the load is heavy. Fig. 6.16 shows the friction coefficient for different load cases. It is seen that, compared with the isothermal solutions, the friction coefficient is smaller for the thermal solutions, which is caused by the decrease of equivalent viscosity. The thermal effect is more remarkable for the heavier load. When the load is heavy and if the load continues to increase, the friction coefficient drops slightly.

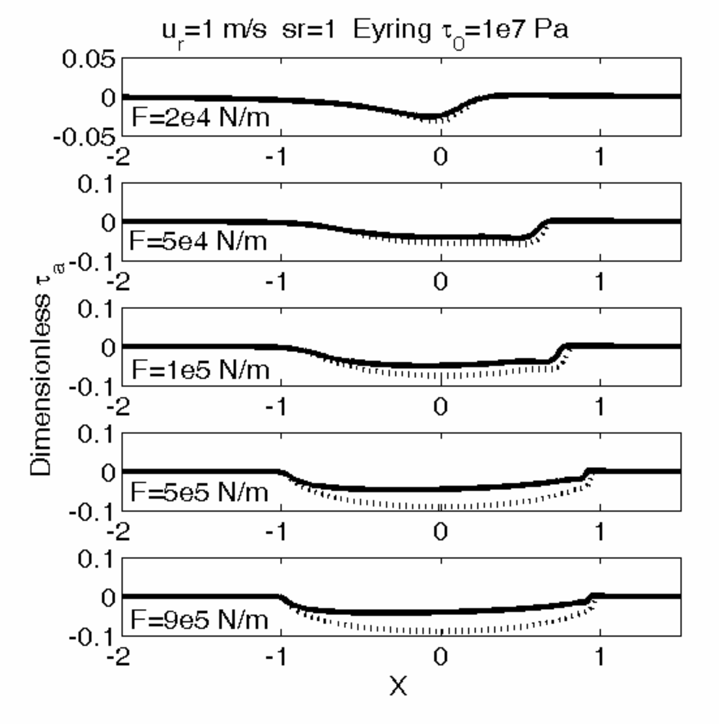

Fig. 6.15 Distribution of $\bar{\tau}_a$ for five load cases for a Ree-Eyring fluid

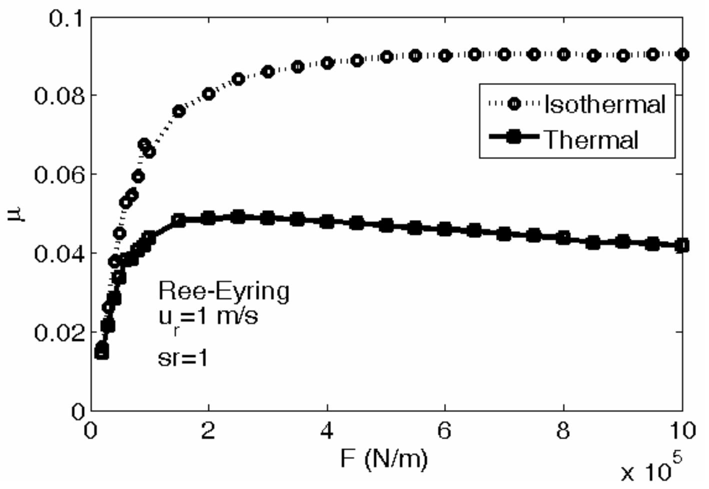

Fig. 6.16 Variation of μ with load for a Ree-Eyring fluid

Fig. 6.17 shows the distributions of temperature for those load cases. As the load increases, the temperature rise is more evident.

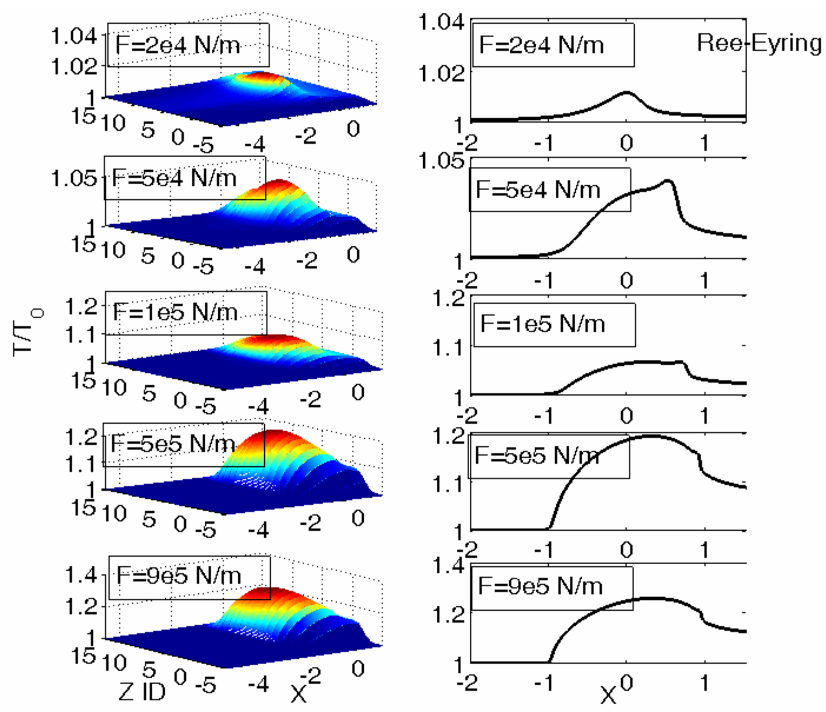

Fig. 6.17 Distributions of temperature for a Ree-Eyring fluid

Fig. 6.18 shows a comparison of pressure and film profiles between isothermal solutions and thermal solutions for those load cases. It can been seen that for the given working condition, thermal action doesn’t change the pressure profile and the film profile significantly for all the chosen load conditions.

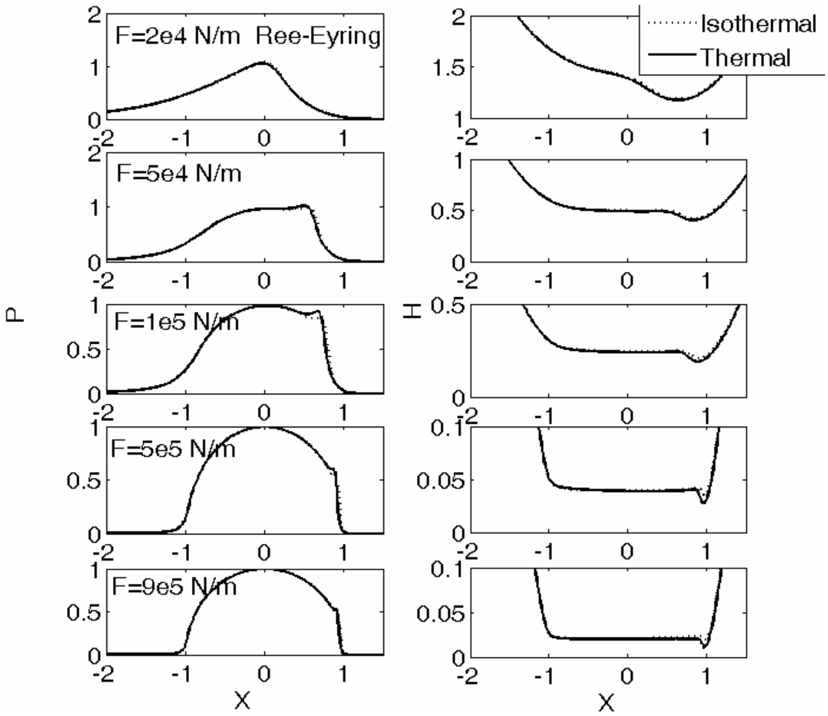

Fig. 6.18 Pressure profile and film thickness for a Ree-Eyring fluid

6.2.2. Effect of Roll Velocity Under Thermal Condition

6.2.2.1. The Newtonian Fluid

Fig. 6.19 shows the variation of the friction coefficient along a rolling speed for a Newtonian fluid. It is seen that as the speed goes up, the friction coefficient of the thermal solution reduces more remarkably. For the isothermal solutions, the value of the friction coefficient increases as the speed goes up; however, for the thermal solutions, the value of the friction coefficient first increases and then decreases as the rolling speed increases.

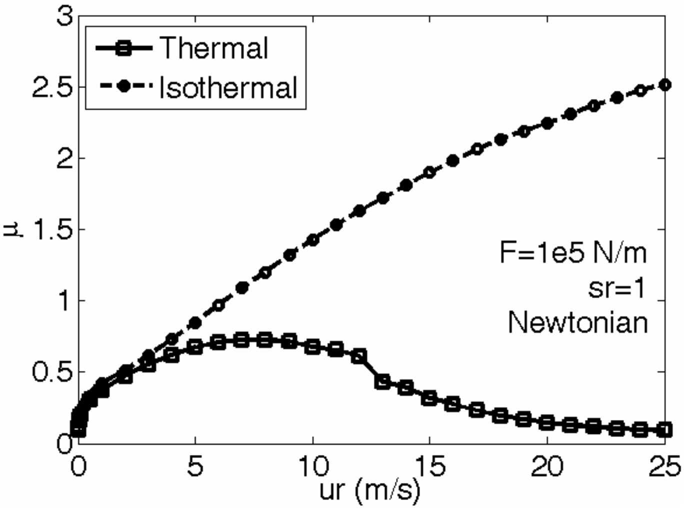

Fig. 6.19 Variation of friction coefficient with rolling speed for a Newtonian fluid

Fig. 6.20 shows the distribution of temperature for five speed cases: $u_r = 0.1$, 0.5, 1, 5 and $10 m/s$. As the speed goes up, the temperature at the nominal contact zone rises.

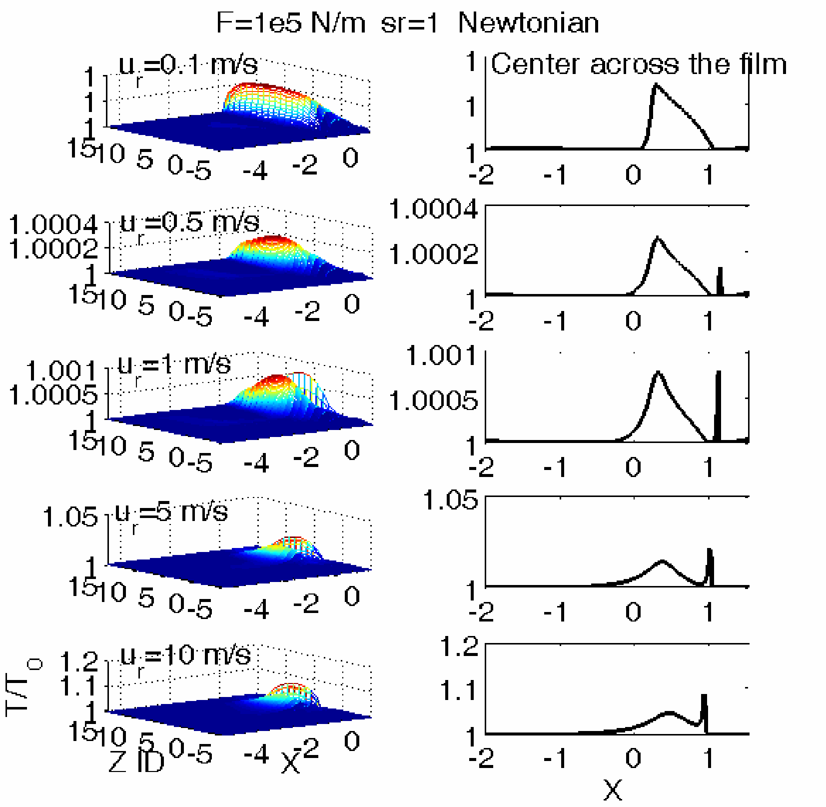

Fig. 6.20 Temperature field with different rolling speed for a Newtonian fluid

Fig. 6.21 shows comparisons of pressure and film profile between the isothermal solutions and thermal solutions. The differences between the two solutions for all the chosen speed cases can be neglected. It can be concluded that the thermal effect does not affect the pressure profile and the film thickness for the given working conditions.

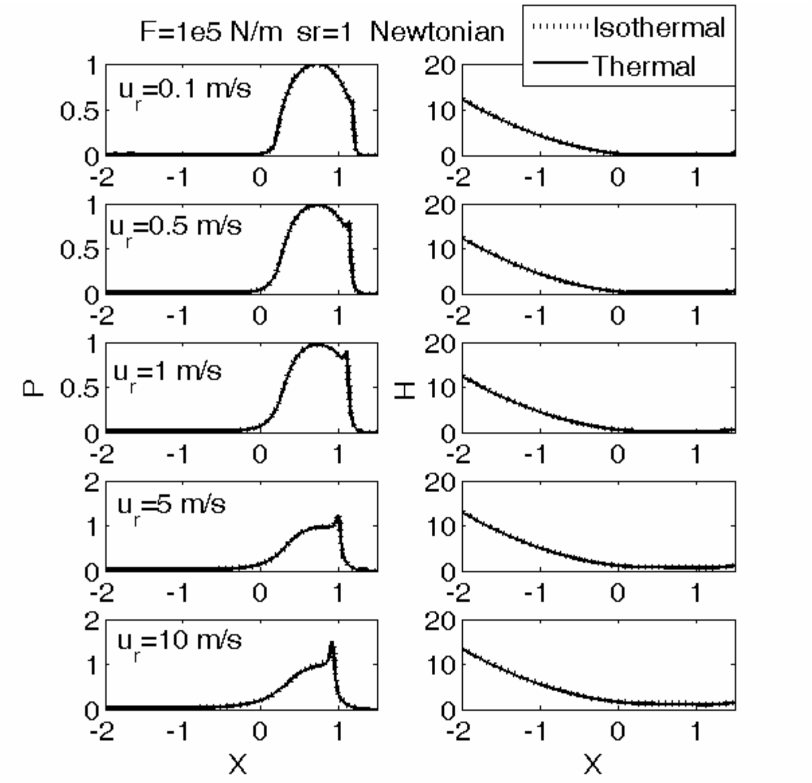

Fig. 6.21 Pressure and film profile for a Newtonian fluid

6.2.2.2. The Ree-Eyring fluid

In this section the Ree-Eyring fluid is studied. Fig. 6.22 shows the distribution of $\bar{\tau}_a$ for the Ree-Eyring fluid with different rolling speeds. It shows that as the rolling speed increases, the value of $\bar{\tau}_a$ for the thermal cases decreases more significantly compared with the one for isothermal cases. This means that at a high rolling speed, the thermal effect should not be neglected.

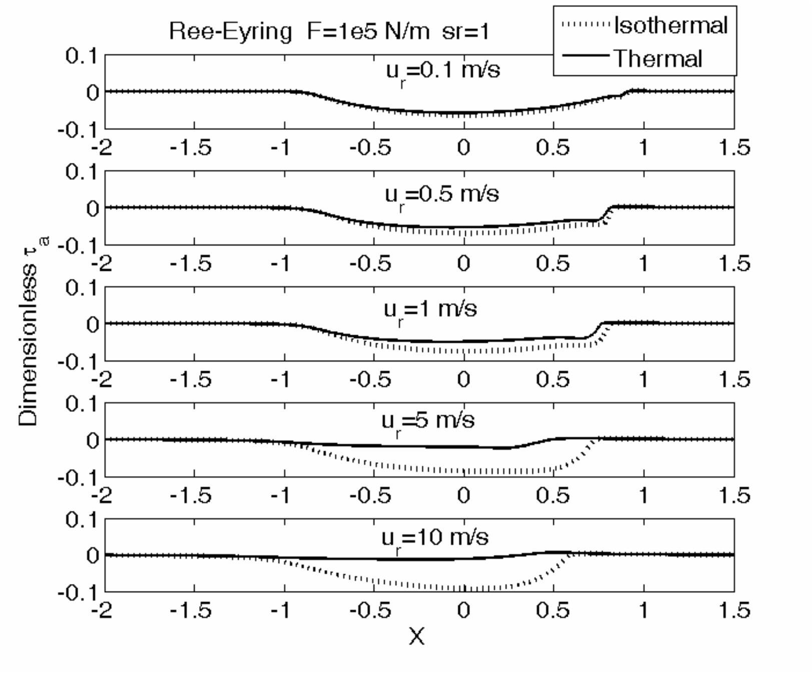

Fig. 6.22 Distribution of $\bar{\tau}_a$ with different rolling speed for a Ree-Eyring fluid

Fig. 6.23 shows the variation of friction coefficient with different rolling speed for isothermal cases and thermal cases. For thermal solutions, the value of the friction coefficient first increases and then decreases as the rolling speed increases. At higher speeds, the thermal effect on the friction coefficient for the Ree-Eyring fluid is more remarkable.

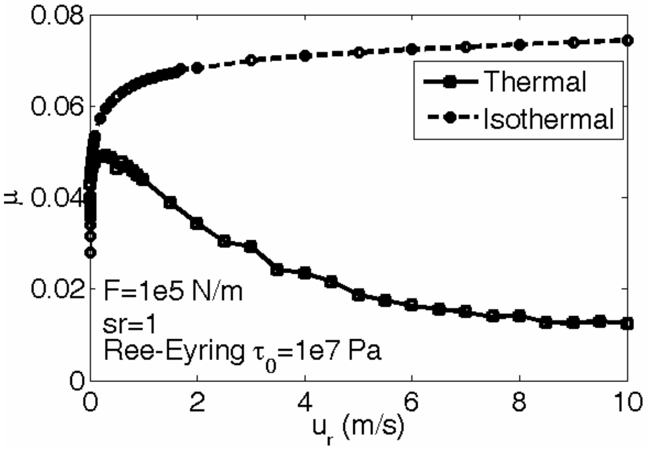

Fig. 6.23 Variation of friction coefficient for the Ree-Eyring fluid under isothermal and thermal conditions

Fig. 6.24 shows the effect of the rolling speed on the temperature distribution at the central layer of the film within the contact area. It is seen that, as speed increases, the temperature within the film rises. This is easy to understand, since if the slide/roll ratio is constant, the sliding velocity increases as the rolling speed increases. The sliding action between interacting surfaces is responsible for the temperature rise.

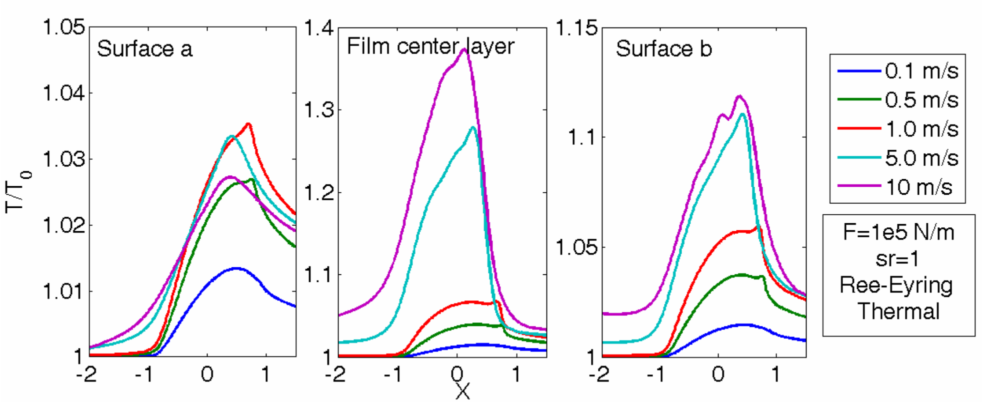

Fig. 6.24 Effect of rolling speed on temperature field for the Ree-Eyring fluid under thermal conditions

Fig. 6.25 shows a comparison of pressure and film profile between thermal solutions and isothermal solutions for a Ree-Eyring fluid. It also shows that for the Ree-Eyring fluid, the thermal effect does not significantly influence the pressure and the film thickness.

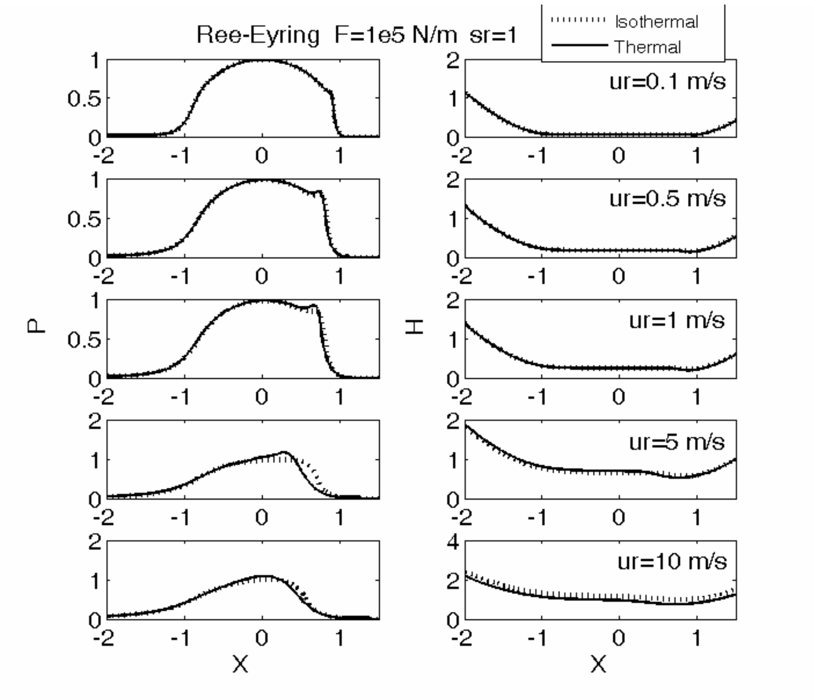

Fig. 6.25 Pressure and film profile with different rolling speed for a Ree-Eyring fluid under isothermal and thermal conditions

6.2.3. Effect of Slide/Roll Ratio Under Thermal Condition

6.2.3.1. The Newtonian Fluid

The effect of the slide/roll ratio for a Newtonian fluid is studied in this section. Fig. 6.26 shows that for the given cases, there is no evident deviation between isothermal solutions and thermal solutions at the whole slide-to-roll ratio range. The friction coefficient increases linearly as the slide/roll ratio increases.

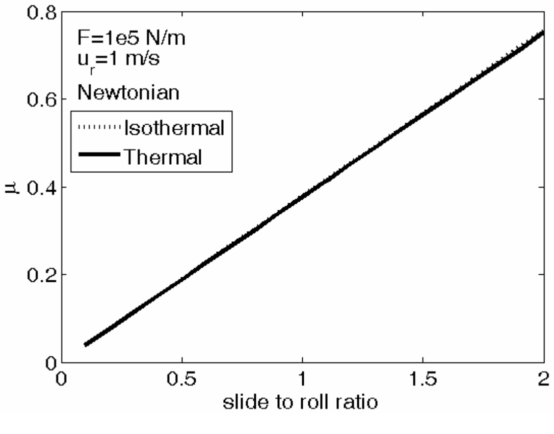

Fig. 6.26 Variation of friction coefficient with slide/roll ratio for a Newtonian fluid

under isothermal and thermal conditions

Fig. 6.27 shows the temperature field of the film and solids at different cases. As the slide/roll ratio increases, the temperature rise within the nominal contact zone increases as well.

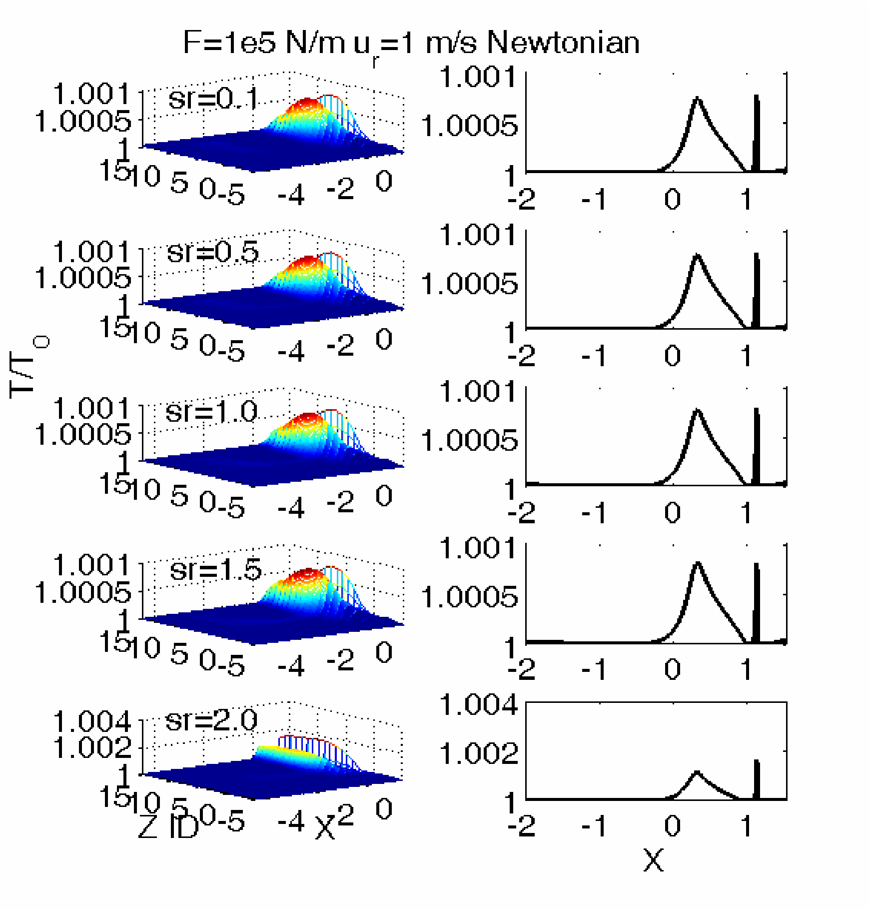

Fig. 6.27 Temperature field with different slide/roll ratio for a Newtonian fluid under thermal conditions

6.2.3.2. The Ree-Eyring Fluid

The Ree-Eyring fluid is considered in this section. Fig. 6.28 shows the distribution of $\bar{\tau}_a$ with five slide/roll ratio cases: $sr = 0.1$, 0.5, 1.0, 1.5 and 2.0. It is seen that as the slide/roll ratio increases, the distribution of $\bar{\tau}_a$ deviates more significantly for the thermal solution compared with the isothermal solution.

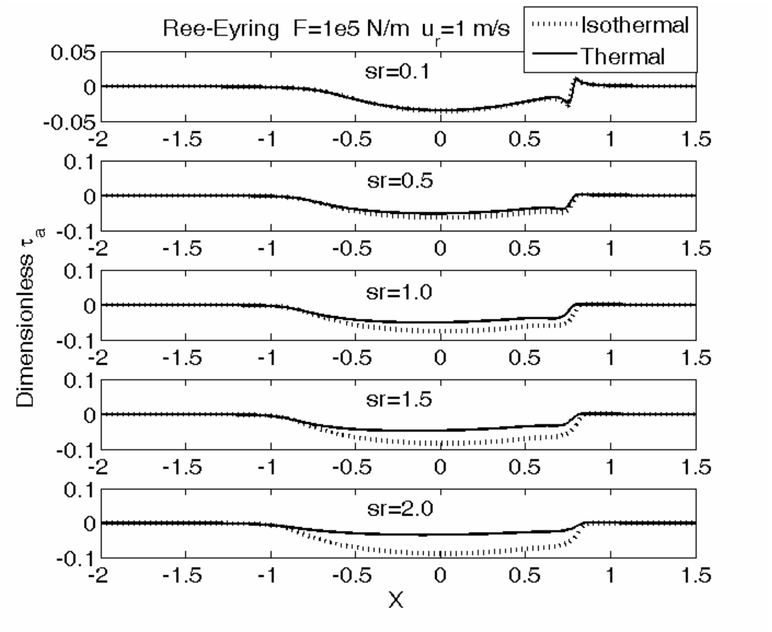

Fig. 6.28 Distribution of $\bar{\tau}_a$ with different slide/roll ratio for a Ree-Eyring fluid

Fig. 6. 29 shows the variation of the friction coefficient for both isothermal cases and thermal cases with different slide/roll ratios. It is seen that for thermal solutions, as the slide/roll ratio increases, the value of the friction coefficient first increases and then decreases. This means that the thermal effect in high slide/roll ratio cases is more remarkable.

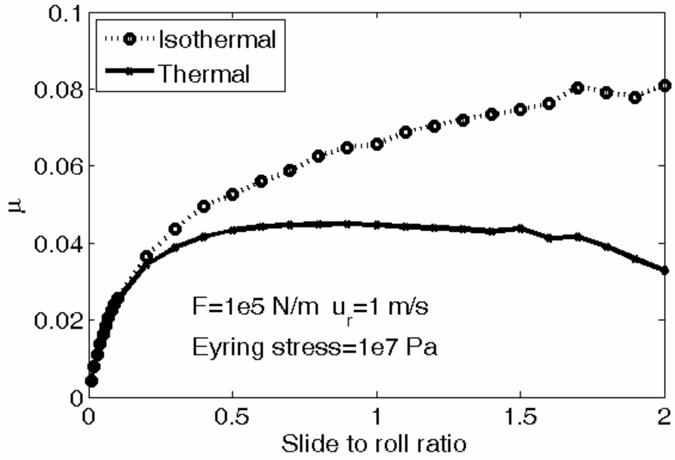

Fig. 6.29 Variation of friction coefficient with different slide/roll ratios for a Ree-Eyring fluid under isothermal and thermal conditions

Fig. 6.30 shows a comparison of pressure and film profile of isothermal solutions and thermal solutions. It shows that the thermal effect still has a very limited effect on the pressure and film profile for a Ree-Eyring fluid for the given cases.

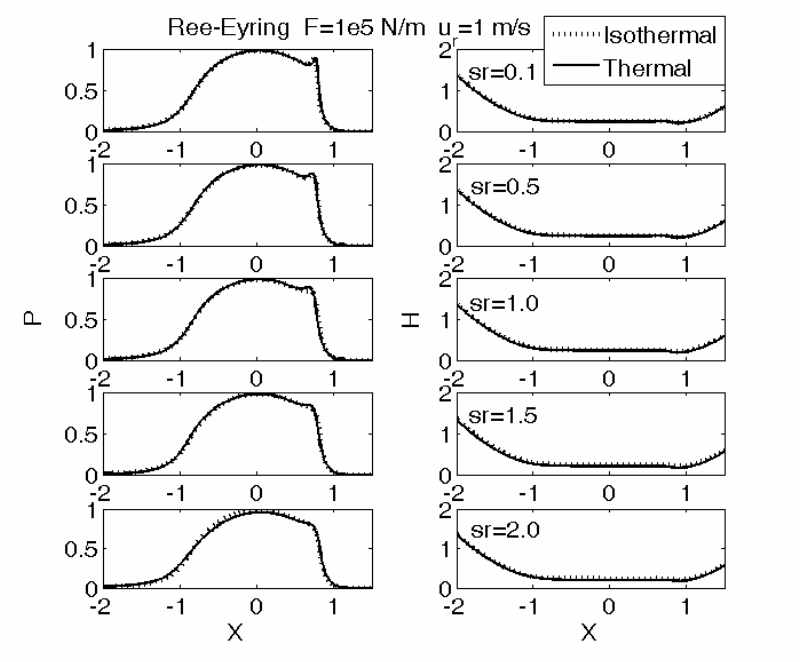

Fig. 6.30 Pressure and film profile with different slide/roll ratio for a Ree-Eyring fluid under isothermal and thermal conditions

Fig. 6.31 shows the temperature field for those slide/roll ratio cases. As the slide/roll ratio increases, the temperature at the nominal contact zone rises as well.

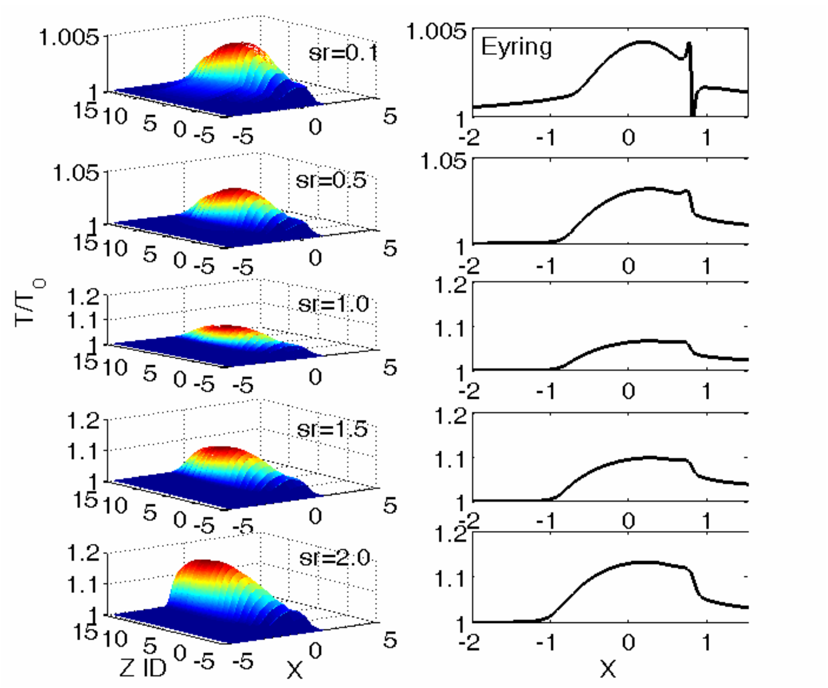

Fig. 6.31 Temperature field with different slide/roll ratios for a Ree-Eyring fluid

6.3. Chapter Summary

The thermal effect is studied in this chapter and a thermal EHL model is developed by numerically solving energy equations for the solids and the film. The following conclusions can be made in this chapter:

- TEHL results with a Newtonian fluid still overestimate the friction coefficient between contacting surfaces.
- For the Ree-Eyring fluid, compared with the isothermal solutions, the friction coefficients are smaller for the thermal solutions if the working condition is the same. This is caused by the decrease of equivalent viscosity within the nominal contact zone.
- Referring to the load effect, for the Ree-Eyring fluid, as the load increases, the temperature rise is more evident. When the load is heavy and if the load continues to increase, the friction coefficient drops slightly, which means that the thermal effect is more evident for heavier loads.

- Referring to the rolling speed effect, for the Ree-Eyring fluid, the value of the friction coefficient for the TEHL model first increases and then decreases as the rolling speed increases. This means that the thermal effect in high rolling speed cases would be more significant owing to the high sliding speed.
- Referring to the slide to roll ratio effect, for the Ree-Eyring fluid, the value of the friction coefficient of the TEHL model first increases and then decreases as the slide to roll ratio increases. This means that the thermal effect in high slide to roll ratio cases would be more significant owing to the high sliding speed.

Chapter 7 A Spur Gear Pair Application with Quasi-Steady Loads

In this chapter, a spur gear pair lubrication analysis is proposed based on quasi-steady loads assumption. Pressure distributions, film profiles, and temperature fields are calculated along the LOA. The information along the LOA indicates the lubrication performance of the gear pair in a complete meshing period. The quasi-static load is assumed along the LOA, which means the dynamic load effect is not considered in this chapter. The dynamic load effect will be discussed in a later chapter in which a system dynamic model is developed for predicting the dynamic loads along the LOA.

It is acceptable to assume that spur gears are 2-dimensional. The contact between the gear teeth can be represented by two circular cylinders of radii rotating with the same angular velocities as the wheels themselves [130]. Indeed, this assumption forms the basis of the two-disk machine that has been used extensively and effectively.

7.1. Gear Geometry and Kinematics

Gear contacts experience a number of time-varying contact parameters:

i. The radii of curvature of the contact tooth surfaces vary periodically. When a tooth of the pinion initiates the contact with its mating tooth, it has the lowest radius of curvature $R_1 = R_{1\min}$. As the meshing process continues, R_1 increased until reaching its maximum value at the tip. Conversely, the radius of curvature of the wheel gradually decreases as the gear drive engages.

ii. The tangential velocities of those interacting tooth surfaces vary as well. For any contact position below the pitch point of the driving gear, the tangential velocity of the pinion is smaller than that of the wheel, i.e. $u_1 < u_2$, which makes the sliding velocity negative $u_s = u_1 - u_2 < 0$. At the pitch point, the tangential velocities of those two surfaces are identical and there is no sliding at all when engaging at this position. As the gear drive engages, the tangential velocity of the pinion is higher than the one of the wheel which makes the sliding velocity positive $u_s > 0$. The equivalent rolling velocity $u_r = (u_1 + u_2)/2$ also varies along the LOA.

iii. Even if the torque is constant, the normal load taken by a single gear pair is not constant owing to the change of number of gear pairs that engage simultaneously. The intentional tooth profile modifications and unavoidable manufacturing errors and assembly errors also affect the load distribution along the LOA. More importantly, the dynamic effect of a gear drive system on the normal load should be emphasized, especially at certain speeds. This aspect will be described in another chapter. In this chapter, the solutions are obtained by ignoring the dynamic load effect, the profile modification and the errors caused by manufacturing and assembling. The load per unit width is assumed that when two tooth pairs are simultaneously engaged, the load carried by a single gear pair varies from one third to two thirds of the load per unit width when only one pair is engaged. This implies that at the LPSTC point and HPSTC point, a sudden load change exists. A similar method of dealing with the load distribution is also used by Larsson [80] , Wang et al. [84], and Li and Kahraman [91].

Essential formulae for gear contact parameters calculation can be found in any gear design manuals and standards. The LOA is discretized into points. The number of discretized points along the LOA should not be too small. A small time step size should be used to capture the transient effects caused by the squeeze effects and the variation of working conditions (such as sudden load change).

The geoemtry equations for external spur gears are given in the following according to the information sheet AGMA 908-B89. All angles are given in terms of radians, unless otherwise specified. The following variables must be made dimensionless by dividing with the normal module m_n, or multiplying with the normal diametral pitch p_{nd}, because the equations are derived in terms of unity normal module ($m_n = 1$) or unity normal diametral pitch.

The standard (reference) pitch radius for the pinion R_{1p} reads

$$R_{1p} = n_1 / (2\cos\varphi) \tag{7.1}$$

Where φ is the standard helix angle, for spur gear pairs, its value is zero. N_1 is the teeth number of the pinion. The standard pitch radius for the wheel R_{2p} reads

$$R_{2p} = R_{1p} i_g \tag{7.2}$$

Where i_g is the gear ratio.

The standard transverse pressure angle ϕ is

$$\phi = \tan^{-1}(\tan\phi_n / \cos\varphi) \tag{7.3}$$

Where ϕ_n is the standard normal pressure angle.

The pinion base radius R_{b1}

$$\begin{cases} R_{b1} = R_1 \cos\phi \\ R_{b2} = R_{b1} i_g \end{cases} \tag{7.4}$$

Operating transverse pressure angle ϕ_r

$$\phi_r = \cos^{-1}(\frac{R_{b1} + R_{b2}}{c}) \tag{7.5}$$

Where c is the operating centre distance.

The transverse base pitch p_b reads

$$p_b = 2\pi R_{b1} / n_1 \tag{7.6}$$

The normal base pitch p_n is

$$p_n = \pi \cos\phi_n \tag{7.7}$$

The base helix angle φ_b

$$\varphi_b = \cos^{-1}(p_n / p_b) \tag{7.8}$$

Fig. 7.1 shows the LOA in the transverse plane. The lengths c_1 through c_6 are derived in the following way:

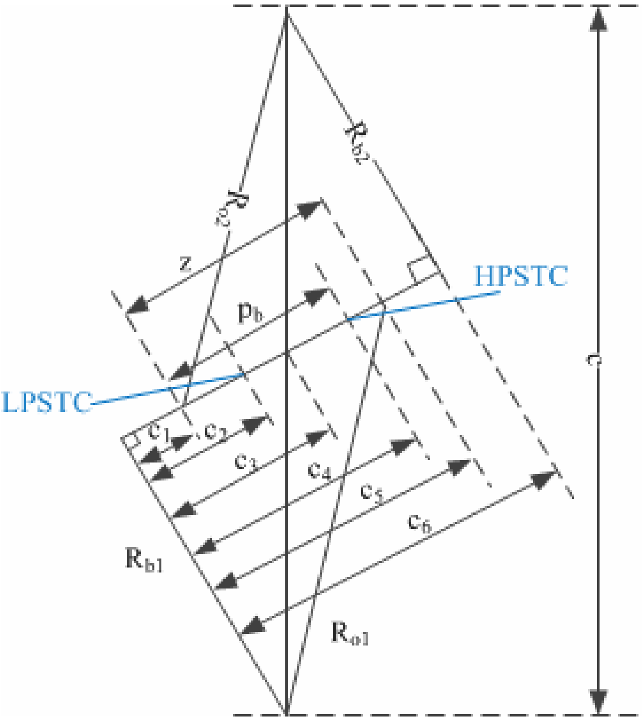

Fig. 7.1 Transverse plane view of the LOA

Sixth distance along LOA c_6

$$c_6 = c \sin\phi_r \tag{7.9}$$

First distance along LOA c_1

$$c_1 = c_6 - \sqrt{R_{o2}^2 - R_{b2}^2} \tag{7.10}$$

Where R_{o2} is the addendum radius of the wheel.

Third distance along LOA c_3

$$c_3 = c_6 / (i_g + 1) \tag{7.11}$$

Fourth distance along LOA c_4

$$c_4 = c_1 + p_b \tag{7.12}$$

Fifth distance along LOA c_5

$$c_5 = \sqrt{R_{o1}^2 - R_{b1}^2} \tag{7.13}$$

Where R_{o1} is the addendum radius of the pinion.

Second distance along LOA c_2

$$c_2 = c_5 - p_b \tag{7.14}$$

Active length of LOA z is then

$$z = c_5 - c_1 \tag{7.15}$$

Distance c_2 locates the lowest point of single tooth contact (LPSTC) and distance c_4 locates the highest point of single tooth contact (HPSTC).

The equivalent radii for the pinion and the gear at any meshing point can be determined with

$$\begin{cases} R_1 = R_{1p} \sin\phi + \xi \\ R_2 = R_{2p} \sin\phi - \xi \end{cases} \tag{7.16}$$

Where ξ means the distance from the current engaging point to the pitch point along the LOA. The equivalent comprehensive radius R can be expressed as

$$R = \frac{R_1 R_2}{R_1 + R_2} \tag{7.17}$$

The tangential velocities of the pinion and the wheel are

$$\begin{cases} u_1 = \pi n_1 R_1 / 30 \\ u_2 = \pi n_2 R_2 / 30 \end{cases} \tag{7.18}$$

with unit m / s. The rolling speed u_r and the sliding speed u_s can be expressed as

$$\begin{cases} u_r = (u_1 + u_2)/2 \\ u_s = |u_1 - u_2| \end{cases} \tag{7.19}$$

7.2. Contact Parameters of the Gear Pair Sample

The parameters of the gear pair sample used in this work are listed in table 7.1. Since the effects of the load and the speed will be studied, the input speed and the load per unit width for single gear engage are allocated several values. Those gear parameters can be used to give dimensionless working condition parameters, i.e. the set of Dowson dimensionless parameters W, U and G, or the set of Moes' dimensionless parameters M and L [131], which act as input data for lubrication models.

For an involute spur gear set the tooth contact occurs along the LOA. A typical spur gear set has a contact ratio of $1 \le i_c \le 2$ and therefore, for the finite section along the LOA within a mesh cycle, only one pair of teeth is carrying the full load. The transition points where the contact shifts from one pair of teeth to two pairs are critical for gear strength calculations. The lowest point of single tooth contact (LPSTC) is defined as the location where is the smallest diameter on a spur gear at which a single tooth of one gear is in contact with its mating gear. Typically, the gear's contact stress is calculated with the load applied at this point. The HPSTC is the largest diameter on a spur gear at which a single tooth of one gear is in contact with the mating gear. Typically a gear's bending stress is determined by the load applied at this point.

Table 7.1 Gear geometry parameters

Number of pinion teeth	$N_1 = 28$

Gear ratio	$i_g = 3$
Module	$m = 0.003175m$
Pinion pitch radius	$R_{1p} = 0.0445m$
Gear width	$B = 0.1m$
Pressure angle	$\phi = 20^\circ$

Fig. 7.2 shows some of parameters of the gear pair sample using the data listed in Table 7.1 with the case $T_1 = 100Nm$, $n_1 = 300r/\min$. It is seen that for the gear drive with a transmission ratio $i_g = 3$, the radius of the wheel is always higher than that of the pinion. As the mesh process continues, the radius of the pinion increases while that of the wheel decreases. The rolling speed of the pinion increases and that of the wheel decreases. The crossing point of the two rolling speed lines is located at the pitch point where the sliding speed is absolutely zero if no manufacture or assembly error is considered. There is a sudden change of the contact width and the Hertzian maximum pressure at LPSTC and HPSTC. Specifically, at the LPSTC, the contact width and the Hertzian maximum pressure suddenly increase, while at the HPSTC those two parameters suddenly decrease, owing to the sudden load jumping assumed at those locations.

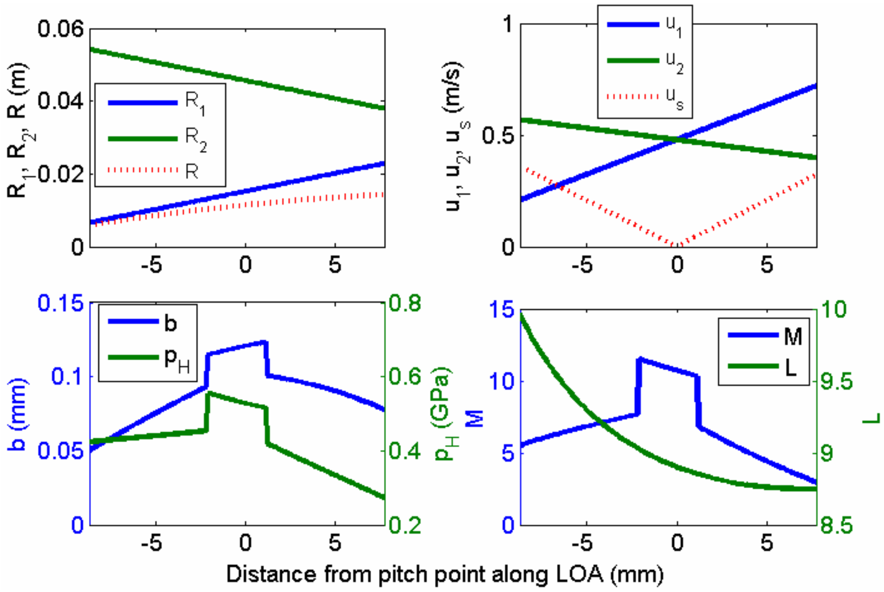

Fig. 7.2 Variations of gear parameters along LOA

The load carried per unit width F can be related to the input torque T_1 using the following equation

$$F = T_1 / (Br_{b1}) \tag{7.20}$$

Where r_{b1} represents the base radius of the pinion. Fig. 7.3 shows the comparison of the load per unit width F of three torque cases, while Figs. 7.4 and 7.5 show the comparison of the contact width and Hertzian maximum pressure, and Moes parameters for the three torque cases. Fig. 7.6 shows the comparison of M and L with different speeds. It is seen that with different speeds, both the value of M and L vary.

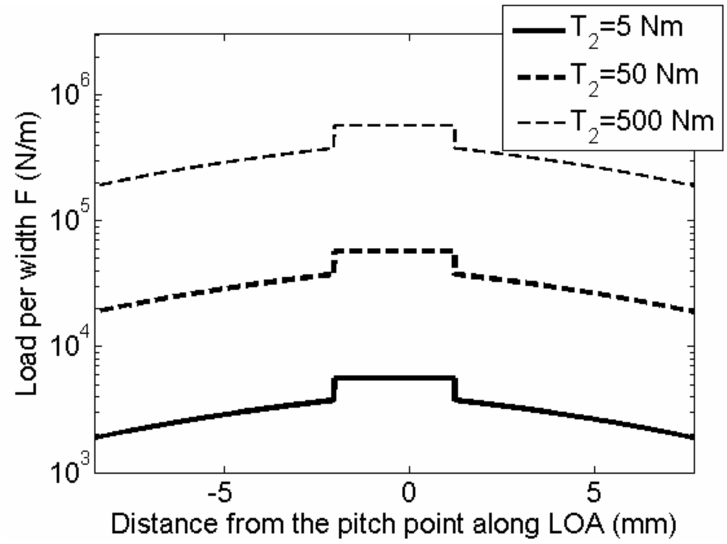

Fig. 7.3 Variation of F with different torques

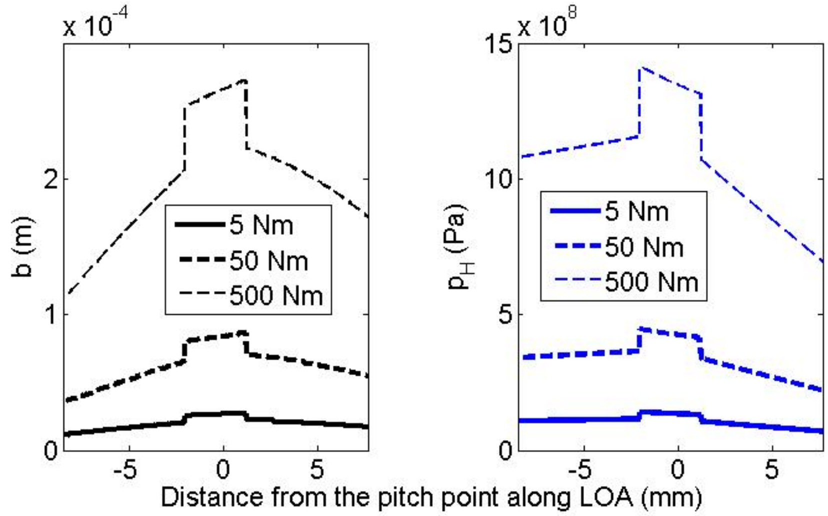

Fig. 7.4 Variation of b and p_H with different torques

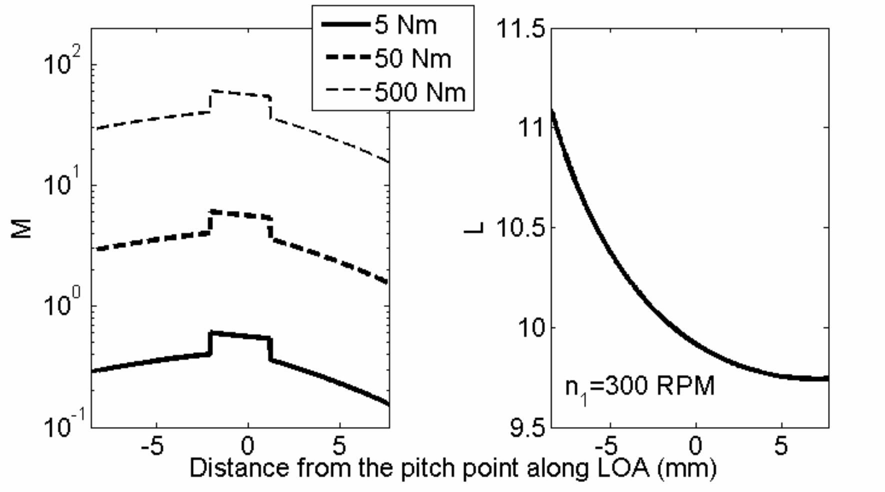

Fig. 7.5 Variation of M and L with different torques

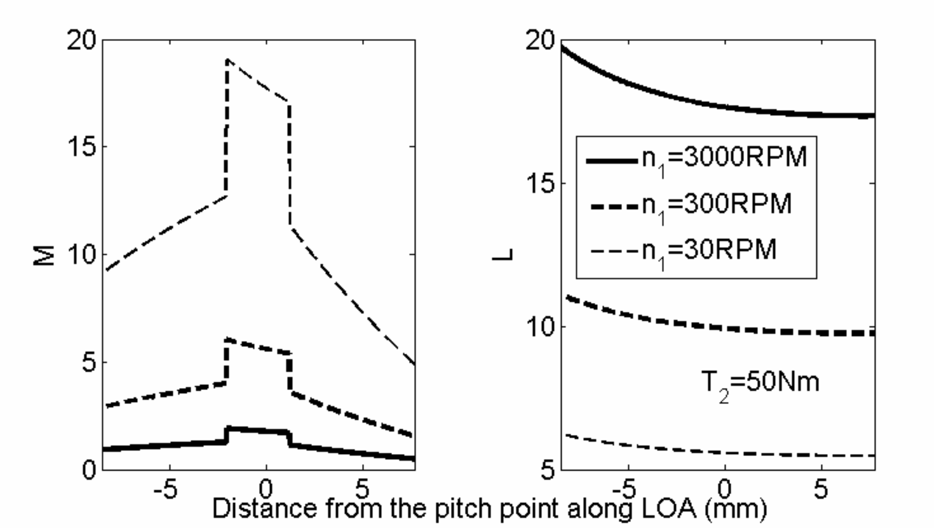

Fig. 7.6 Variation of M and L with different speeds

7.3. Lubrication Solutions for Spur Gear Pairs

Fig. 7.7 shows the comparison of the steady-state solution and the transient solution. The steady-state solution does not consider the transient squeeze effect in the Reynolds equation. It shows that the transient squeeze effect causes an opposite sudden fluctuation at LPSTC and HPSTC point while a sudden load change occurs. In the following work, if not specified explicitly, the transient solutions are given.

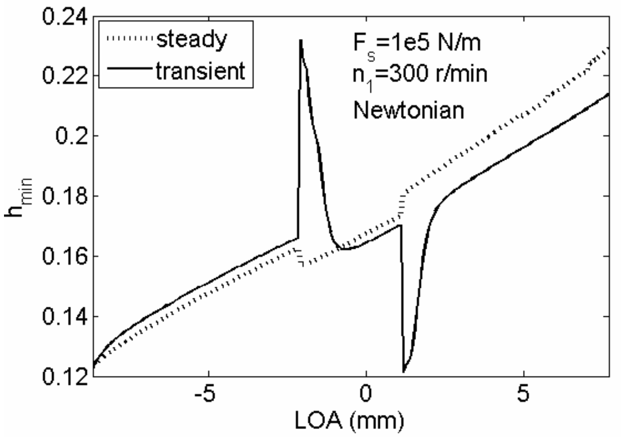

Fig. 7.7 Comparison between transient solution and steady solution

In order to show the effect of the mesh density of time interval on solutions, the minimum film thickness variations with different mesh densities are predicted with the case $F_s = 1e5Nm$, $n_1 = 300r/\min$. F_s represents the load per unit width when only one gear pair is carrying a load. The case $F_s = 1e5Nm$ means the input torque is $T_1 = F_s r_{b1} B \approx 83.6Nm$. Fig. 7.8 shows the minimum film thickness along the LOA with different mesh densities for this situation. It shows for cases with $nt = 257$, 513, and 1025, the differences are not evident in all the ranges along the LOA. In this work, if not explicitly specified, the mesh density is chosen as $nt = 257$.

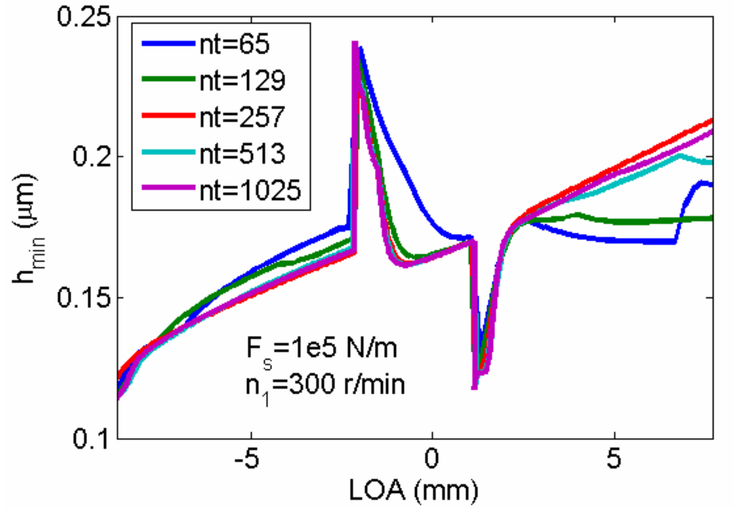

Fig. 7.8 Effect of mesh density of time interval on minimum film thickness

Fig. 7.9 shows the comparison of minimum film thickness between the Newtonian solution and the Ree-Eyring solution for this case. It shows that under this condition, there is little difference in the minimum film thickness along the LOA for those two fluids. In the following work, if not explicitly specified, the Ree-Eyring behaviour is assumed for the fluid. Fig. 7.9 also shows that the film thickness is small at the recess point, as well as at the HPSTC point if the transient squeeze effect is considered. The sudden load drop at HPSTC causes the sudden film thickness drop by the transient squeeze effect.

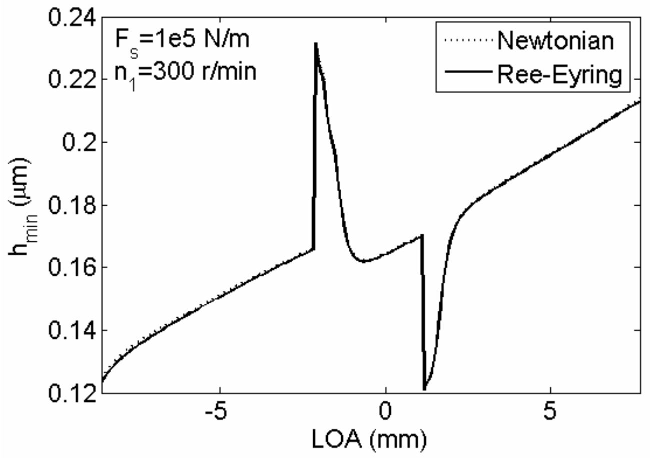

Fig. 7.9 Minimum film thicknesses along the LOA for the Newtonian solution and the Ree-Eyring solution

7.3.1. Pressure, Film and Temperature in a Meshing Period

The pressure and film profile along the LOA are studied in detail for the case $F_s = 1e5Nm$, $n_1 = 300r/\min$. Figs. 7.10 and 7.11 show the pressure profile and the film profile of five locations: the approach point, LPSTC, the pitch point, HPSTC, and the recess point, respectively. Fig. 7.11 shows that the film at the recess point is thicker than the others. Minimum film thickness occurs at the approach point among those five cases which can be also represented by Fig. 7.9. This means the lubrication condition at the approach point requires special attentions owing to the thinnest film.

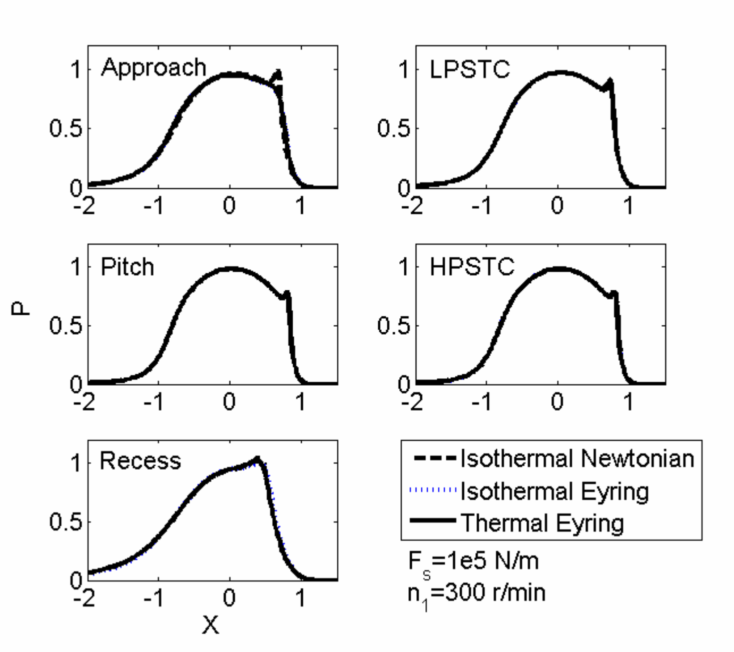

Fig. 7.10 Pressure distribution within a meshing period

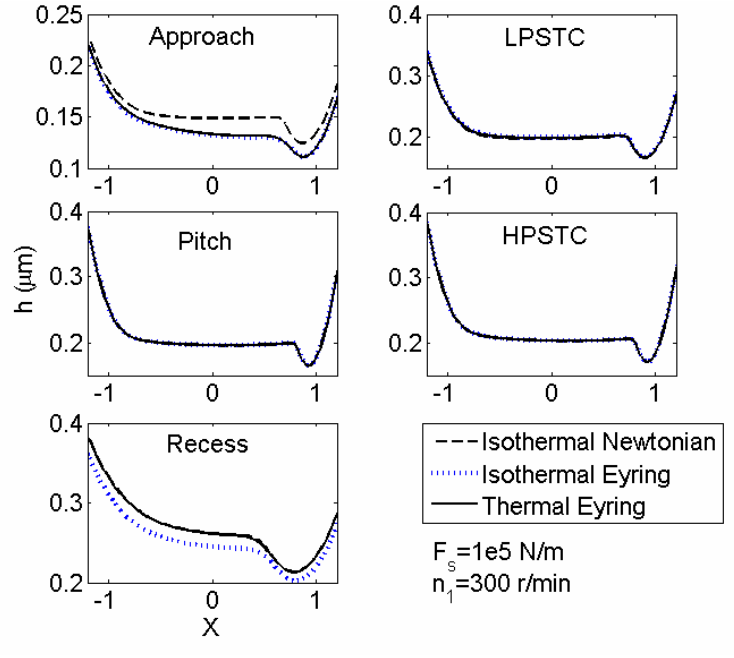

Fig. 7.11 Film profile within a meshing period

Temperature fields are also obtained using the developed thermal Ree-Eyring EHL model. Fig. 7.12 shows the dimensionless pressure distributions at the five characteristic mesh points under the working condition: $F_s = 1e5N/m$,

$n_1 = 300r/\min$. Fig. 7.13 shows the comparison of the temperature distribution of those five cases at the interfaces of solids and the central layer of the film. It is seen that the maximum temperature rise occurs at the approach point while the minimum temperature rise occurs at the pitch point owing to the zero slide/roll ratio. Along the LOA, not only the minimum film thickness but also the maximum temperature rise occurs at the approach point. This means special attention should be paid to this meshing position, under the operating conditions considered.

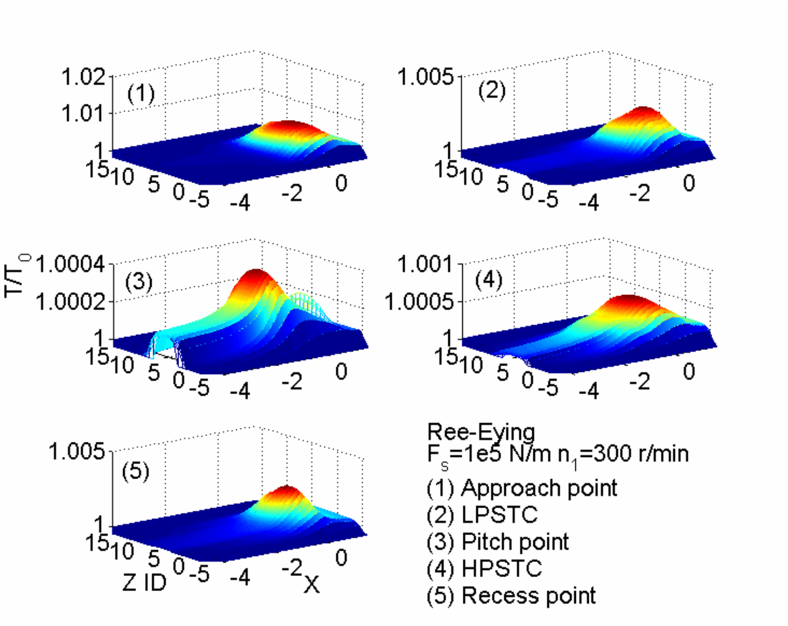

Fig. 7.12 Temperature field with the given case

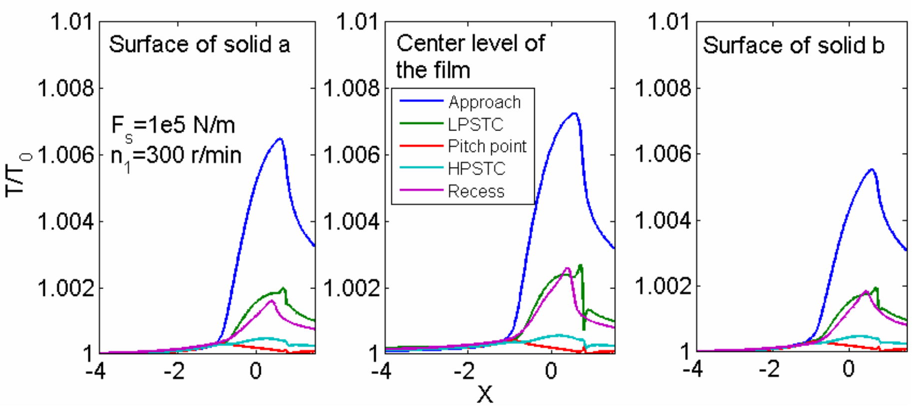

Fig. 7.13 Comparison of temperature distribution with different meshing locations

7.3.2. Effect of Speed

Fig. 7.14 shows the effect of the pinion speed on the minimum film thickness with $F_s = 1\times10^5 N/m$. As the speed goes up, the minimum film thickness increases as well. This is true and can be explained by the empirical formula given by Dowson and Higginson [111]. For all those cases, film thickness fluctuation occurs at LPSTC and HPSTC. Film thicknesses under those conditions mainly have an order of sub-micrometres.

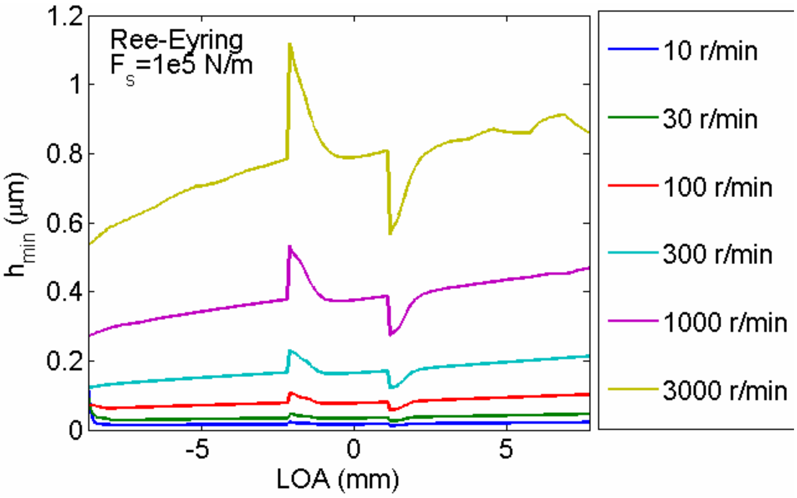

Fig. 7.14 Effect of rotation speed on minimum film thickness

Fig. 7.15 shows the pressure distribution in a meshing period at four speed cases. It is seen that, for the four cases, the load changes abruptly when the number of simultaneously engaging gear pair(s) varies at the HPSTC and LPSTC. The higher the speed, the more evident the inlet zone pressure build up.

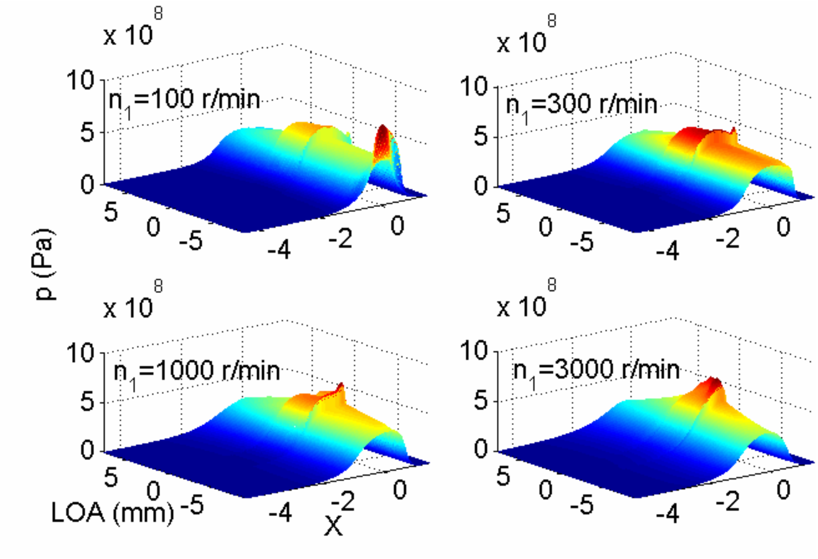

Fig. 7.15 Effect of speed on pressure distribution within a meshing period

Fig. 7.16 shows the dimensionless pressure distributions at the five characteristic mesh points under the working condition: $F_s = 1e5N/m$, $n_1 = 3000r/\min$. Compared with results shown in Fig. 7.12, It is seen that the temperature rise increases as the pinion speed goes up.

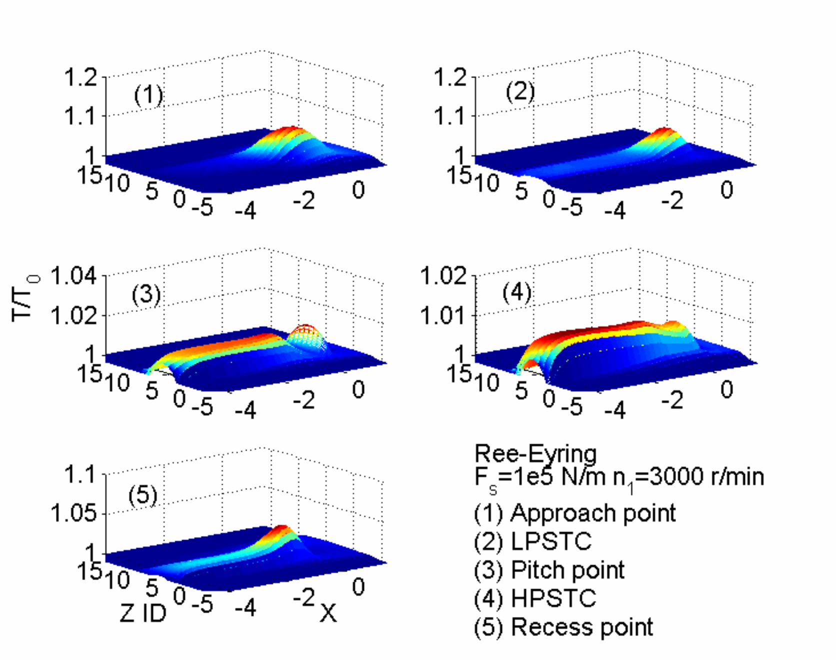

Fig. 7.16 Temperature field with $F_s = 1e5N/m$, $n_1 = 3000r/\min$

7.3.3. Effect of Load

Fig. 7.17 shows the effect of the load on the minimum film thickness with $n_1 = 300 r / \min$. Compared with the speed effect, the load effect on the minimum film thickness is weaker. This could also be explained with the empirical Dowson-Higginson formula.

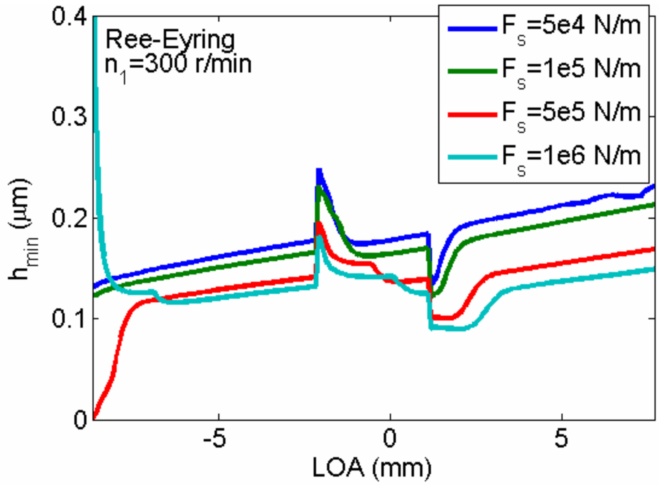

Fig. 7.17 Effect of load on minimum film thickness within a mesh period

Fig. 7.18 shows the pressure distribution in a meshing period at four load cases. It is seen that, for the four cases, the load changes abruptly when the number of simultaneously engaging gear pair(s) varies at the HPSTC and LPSTC. The lighter the load, the more remarkable the second pressure spikes and the inlet zone pressure build up. At heavy load cases, the pressure distribution along the LOA can be approximately estimated by the Hertzian theory. Those conclusions are in accordance with previous studies [130].

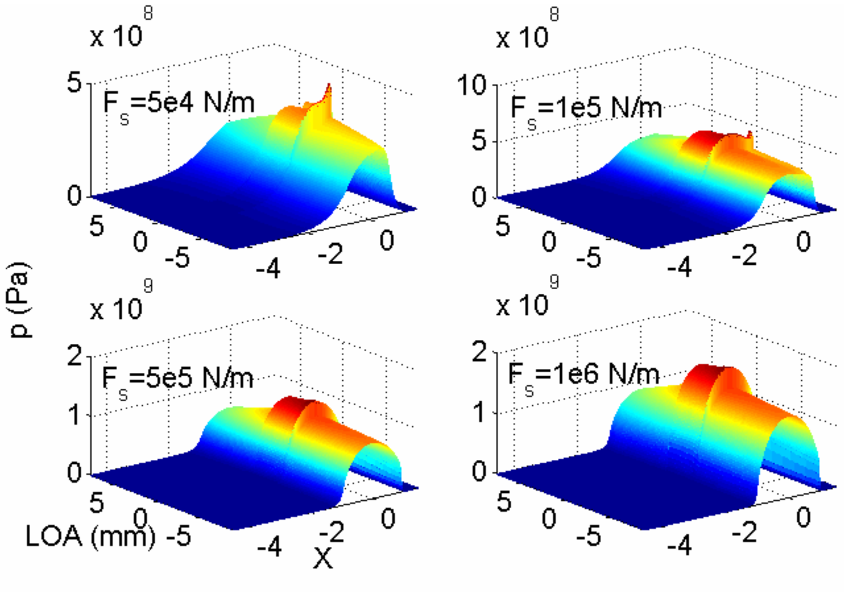

Fig. 7.18 Effect of load on pressure distribution within a meshing period

Fig. 7.19 shows the dimensionless temperature distributions at the five characteristic mesh points under the working condition: $F_s = 5e4N/m$, $n_1 = 300r/\min$. Compared with the results shown in Fig. 7.12, It is seen that the temperature rise decreases as the pinion torque decreases.

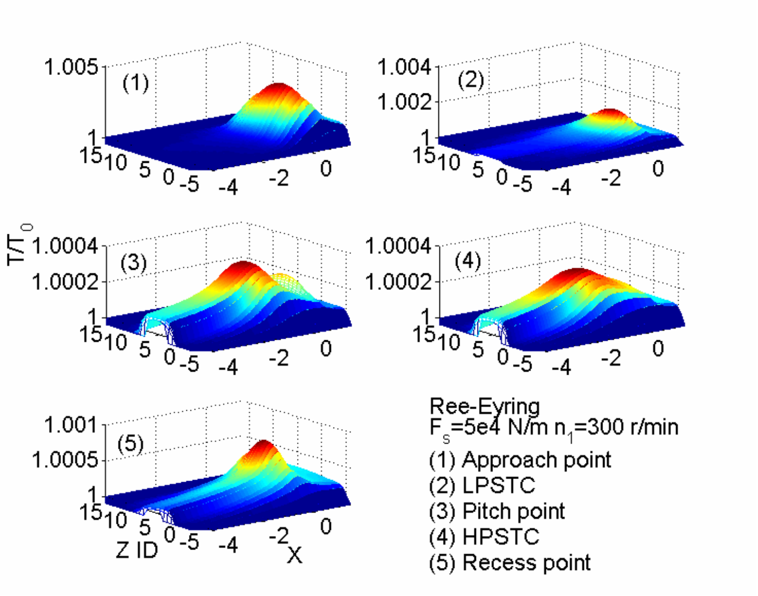

Fig. 7.19 Temperature field with $F_s = 5e4N/m$, $n_1 = 300r/\min$

7.3.4. Effect of Surface Roughness

Figs. 7.20 to 7.24 show the effect of the RMS value of surface roughness on the pressure profile for the approach point, LPSTC, the pitch point, and HPSTC, the recess point, respectively, under the working condition $F_s = 1e5N/m$, $n_1 = 3000r/\min$. It is seen that the selected surface roughnesses - $\overline{R}_q = 0.1$, 0.2, 0.3 - do not cause big fluctuations at the approach point or at the recess point, while significant pressure fluctuations occur at the other three points. However, since the Ree-Eyring fluid is chosen, the maximum pressure within the nominal contact zone only slightly larger than the Hertzian maximum pressure.

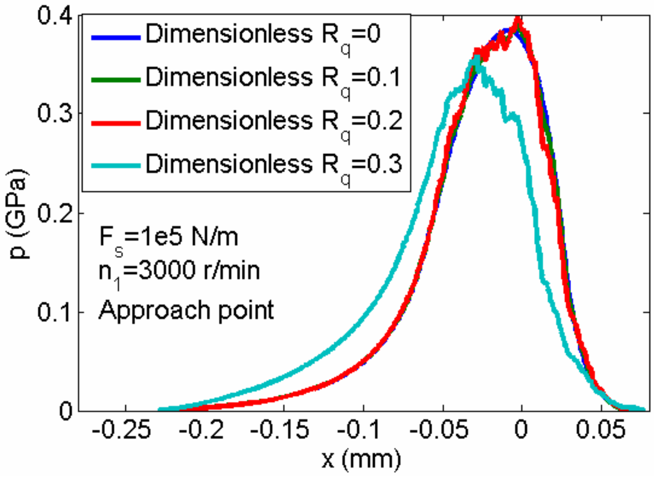

Fig. 7.20 Pressure profile at the approach point with different roughnesses

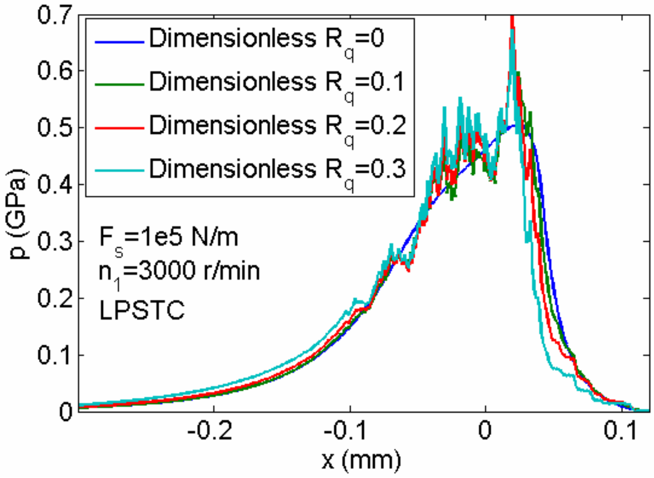

Fig. 7.21 Pressure profile at LPSTC with different roughnesses

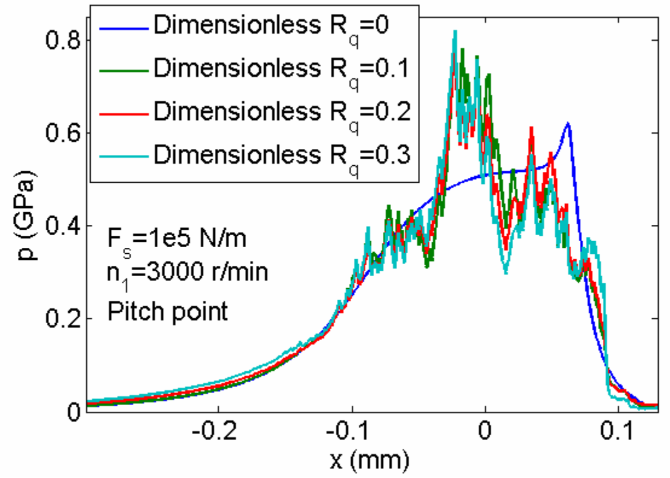

Fig. 7.22 Pressure profile at the pitch point with different roughnesses

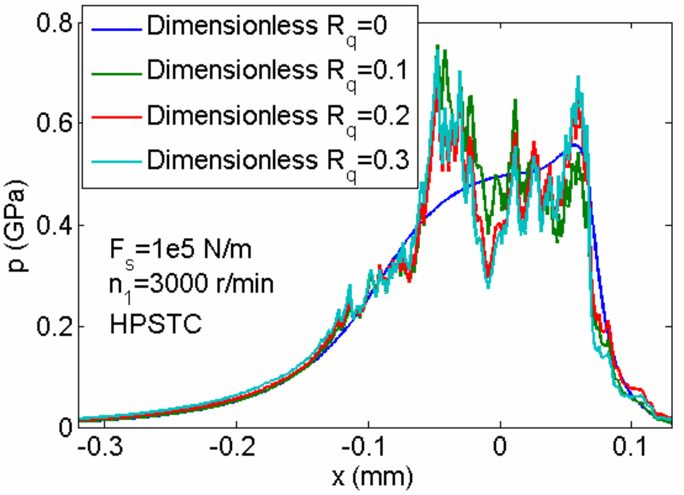

Fig. 7.23 Pressure profile at HPSTC with different roughnesses

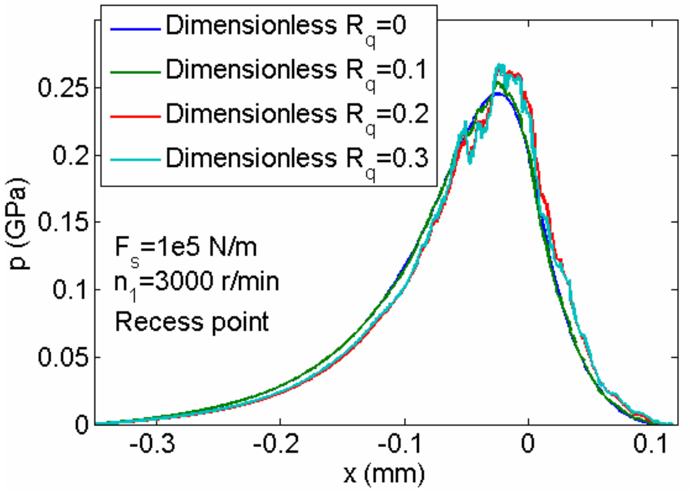

Fig. 7.24 Pressure profile at the recess point with different roughnesses

For comparison, dry contact solutions are provided here for the cases. Fig. 7.25 shows the dimensionless pressure profile during the meshing period, while Fig. 7.26 shows the pressure fluctuation at the approach, pitch and recess points, respectively. It is seen as the RMS value increases, for the dry contact, the pressure fluctuation becomes significant. The maximum pressure within the nominal contact zone may be as high as twenty times that of the Hertzian contact pressure. Compared with the Ree-Eyring fluid results, we clearly see that the lubricant between engaging tooth surfaces could alleviate the pressure fluctuation effectively.

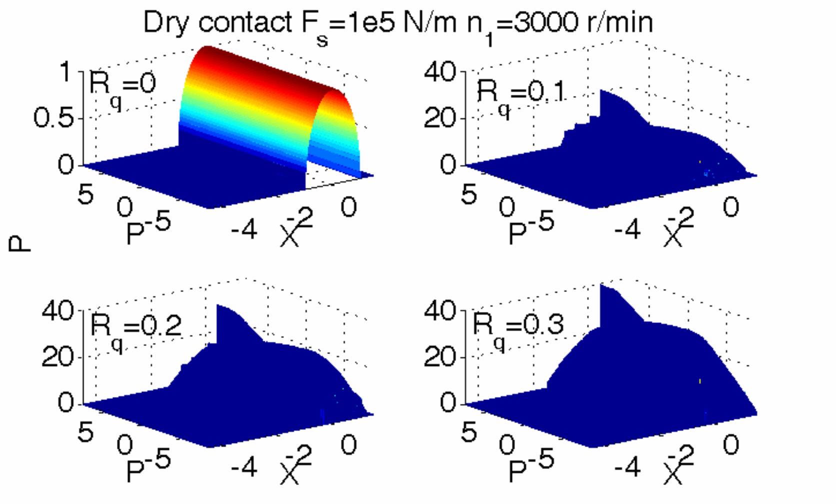

Fig. 7.25 Pressure distribution for dry contacts with different RMS values

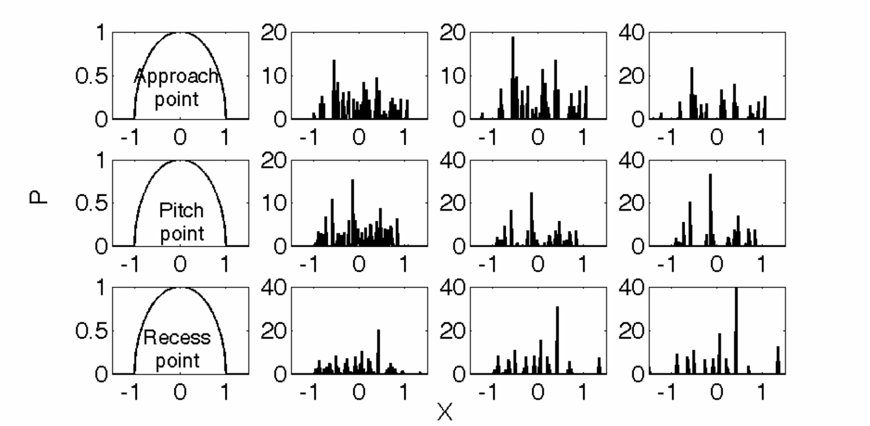

Fig. 7.26 Pressure distribution at the approach point, pitch point and recess point (from left to right, subfigures represent the results for $\overline{R}_q = 0$ 0.1, 0.2, 0.3, respectively)

Figs. 7.27 to 7.31 show the effect of the RMS value of surface roughness on the film profile for the approach point, LPSTC, the pitch point, HPSTC, the recess point, respectively. Film profile fluctuations caused by roughness are shown from those film profile figures. With the surface roughnesses applied under the given working conditions, no asperity contact occurs at all those locations along the LOA.

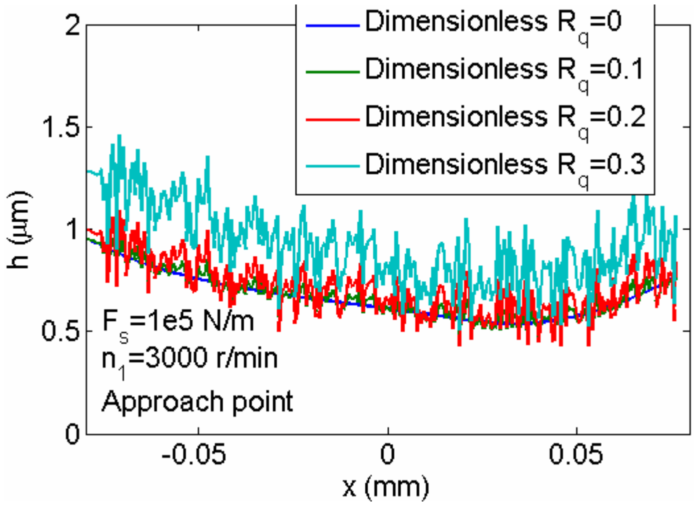

Fig. 7.27 Film profile at the approach point with different roughnesses

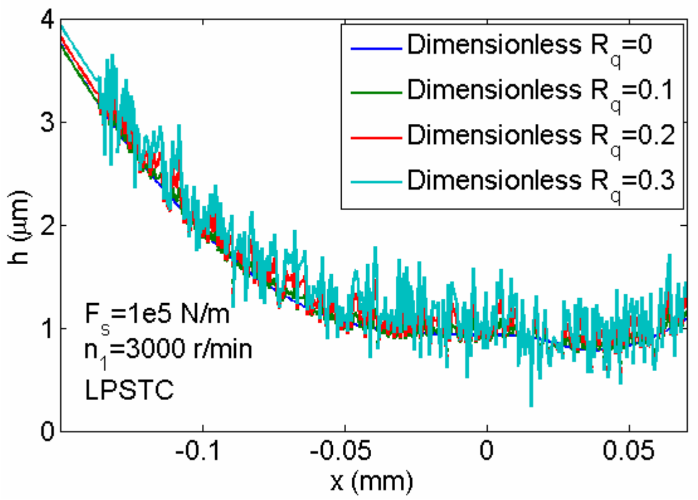

Fig. 7.28 Film profile at LPSTC with different roughnesses

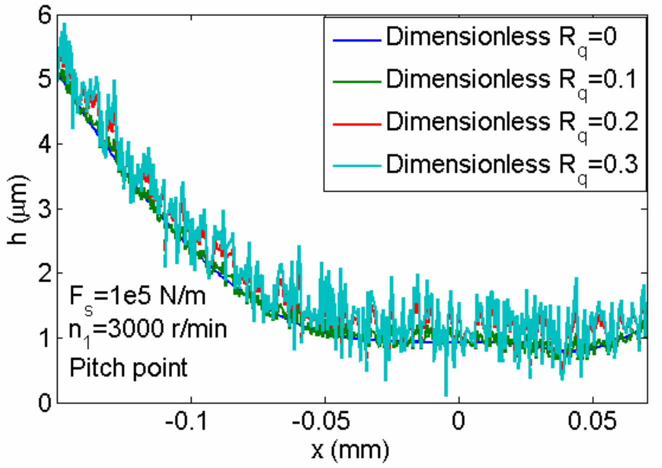

Fig. 7.29 Film profile at the pitch point with different roughnesses

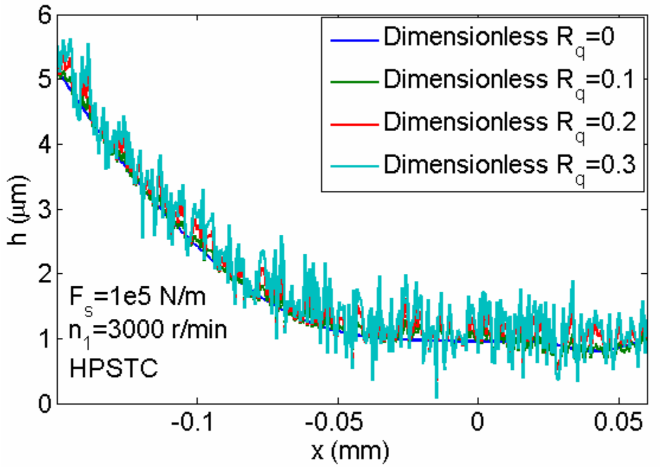

Fig. 7.30 Film profile at HPSTC with different roughnesses

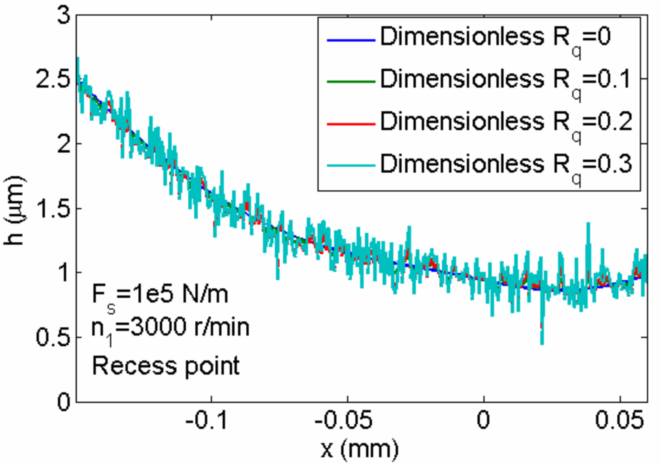

Fig. 7.31 Film profile at the recess point with different roughnesses

A more detailed study of surface roughness effect on gear lubrication performance can be found in Ref. [5], published by the author and coworkers.

7.4. Chapter Summary

A spur gear pair application is studied for its lubrication performance evaluation with quasi-steady loads. The quasi-steady load distribution along the LOA represents a sudden load change at the LPSTC and HPSTC owing to the sudden change of the number of simultaneously engaging gear pairs. For the given gear pair sample, the effect of load and speed on minimum thickness, pressure distribution etc. are investigated. The following conclusions can be made:

- The transient squeeze effect causes an opposite sudden fluctuation at the LPSTC and HPSTC points where a sudden load change occurs.
- Along the LOA, the thinnest film thickness occurs at the approach point. The maximum temperature rise occurs at the approach point while the minimum temperature rise occurs at the pitch point owing to the zero slide to roll ratio. Along the LOA, not only the minimum film thickness but also the maximum temperature rise occurs at the approach point. This means special attention should be paid to this meshing position, under the operating conditions considered.
- Lubricated with the Ree-Eyring fluid, the maximum pressure within the nominal contact zone is only slightly larger than the Hertzian maximum pressure.
- For the surface roughness applied, no asperity contact occurs at all those locations along the LOA.

Chapter 8 Dynamic Load Effects on Spur Gear Pair Lubrication Performance

As well as the lubrication and contact performance, the dynamic performance of a gear drive system is investigated extensively in academia and industry for the following reasons. One is that the vibration and the noise are directly determined by its dynamic behaviour. The second reason is the durability concern. The force and stress may be amplified significantly under dynamic conditions, which make it necessary to take dynamic effects into account in the design of gear drives [132]. In this chapter, the dynamic loads' effect on the lubricated contact performance of a spur gear pair is studied by using a classic lumped mass-spring gear model, which takes the mesh stiffness variation as the only excitation. The dynamic loads are calculated using a numerical time-step integration scheme and act as the input load data of lubrication models developed in previous chapters. In this way, the spur gear speed effect on lubrication performance can be studied in a more comprehensive way since the indirect effect on dynamic loads is also taken into account. The main work of this chapter has been published by the author and coworkers [7].

8.1. Gear Dynamic Load

Currently there are two main ways to calculate gear dynamic loads: one is the finite element method, and one is the lumped mass-spring model. In this chapter the later approach is applied. More detailed information about this approach can be found in Ref. [132].

8.1.1. The SDOF Dynamic Model

A two-degree-of-freedom semi-definite model of the spur gear pair with rotary inertias I_1 and I_2 for the pinion and the wheel, respectively, is considered, as shown in Fig. 8.1. The shafts and bearings are assumed to be rigid. The gear backlash and manufacturing error are neglected here. This makes the time-varying mesh stiffness the only excitation for the dynamic system. The time-varying mesh stiffness, caused by the alternating engagement of single and double pairs of teeth, is believed to be the most important factor determining the dynamic behaviour of the gear pair as a type of parametric vibration [133]. The equations of motion of the spur gear pair can be written as

$$\begin{cases} I_1\ddot{\theta}_1 + C(r_{b1}\dot{\theta}_1 - r_{b2}\dot{\theta}_2)r_{b1} + k(t)f(r_{b1}\theta_1 - r_{b2}\theta_2)r_{b1} = T_1 \\ I_2\ddot{\theta}_2 - C(r_{b1}\dot{\theta}_1 - r_{b2}\dot{\theta}_2)r_{b2} - k(t)f(r_{b1}\theta_1 - r_{b2}\theta_2)r_{b2} = -T_2 \end{cases} \tag{8.1}$$

where θ_1 and θ_2 represent the rotation angle of the pinion and the wheel, respectively. T_1 and T_2 are the torque on the pinion and the wheel, respectively. r_{b1} and r_{b2} are the base circle radius of the two gears. $k(t)$ represents the time-varying mesh stiffness. The damping ratio c is often determined empirically owing to the lack of measurement data and proper models. In this work the value 0.1 is allocated to the damping ratio, as the same one used by Ozuguwen and Houser [134] and Atanasiu et al. [135].

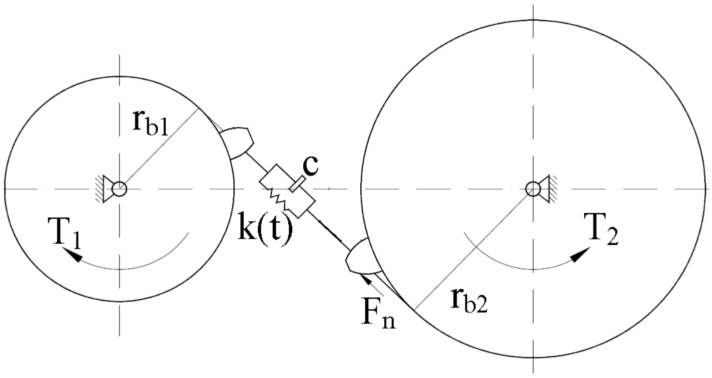

Fig. 8.1 Spur gear pair dynamic model with mesh stiffness variation as the only excitation source

Introducing the variable $x = r_{b1}\theta_1 - r_{b2}\theta_2$, the rigid body mode that would occur for the semi-definite two-DOF model will be eliminated and a definite SDOF model is derived as

$$m_e \ddot{x} + c\dot{x} + k(t)f(x) = (T_1 + T_f)/r_{b1} \tag{8.2}$$

where m_e is the equivalent mass and is expressed as

$$m_e = I_1 I_2 / (I_1 r_{b2}^2 + I_2 r_{b1}^2) \tag{8.3}$$

where I_1 and I_2 are the rotation inertia of the pinion and the wheel, respectively. r_{b1} and r_{b2} are the base radius of the pinion and the wheel, respectively.

The variable x, representing the relative displacement along the direction of the LOA, is often referred to as the dynamic transmission error (DTE). It should be noted that in the proposed model the manufacturing error is not considered, which leads to a zero static unloaded transmission error.

8.1.2. Mesh Stiffness

In fact, the fluid may affect the contact mesh stiffness of engaging gear pairs, however, little work has been done in this field. In this work, the effect of the film on the mesh stiffness is not taken into account. The mesh stiffness is calculated with dry contact assumption. The mesh stiffness can be calculated with several approaches. Early work to model the meshing stiffness was based on a mechanics of materials approach. Later, the finite element approach is extensively used to get the mesh stiffness. In this work the mesh stiffness is calculated using the potential energy method, which was first proposed by Yang and Lin [136], and further modified by Tian [137]. Yang and Lin pointed out that the total potential energy stored in the meshing gear system included three parts: the Hertzian energy, the bending energy and the axial compressive energy, which can be used to get the Hertzian contact stiffness, the bending stiffness and the axial compressive stiffness, respectively. Tian further considered the shear energy. In this work the effect of the Hertzian energy, bending energy, axial compressive energy, and shear energy are all taken into account.

8.1.2.1. Hertzian Contact Stiffness

According to the Hertzian law, the elastic compression of two isotropic elastic bodies can be approximated by two paraboloids in the vicinity of the contact. The Hertzian contact stiffness of a pair of meshing teeth made of the same material is a constant along the LOA which can be expressed as

$$k_h = \frac{\pi EB}{4(1-\nu^2)} \tag{8.4}$$

Where E is the Young's modulus of the gear material, B is the width of a tooth. When the tooth width decreases, the Hertzian contact stiffness will decrease as well.

8.1.2.2. Bending, Shear and Axial Compressive Contact Stiffness

The contact force is exerted along the LOA direction for an involute gear pair which can be decomposed into two components: one is parallel to the $\overline{O_1O_2}$ direction F_a and F_b, which is perpendicular to F_a. The bending effect of F_a can be considered by calculating the torque M_1 caused by this force. M_1, together with F_b, result in a bending deflection. F_a will also cause axial compressive strain. The detailed description of those mesh stiffnesses can be found in Ref. [137].

8.1.2.3. Total Mesh Stiffness

The effective stiffness k_e for a pair of teeth can be obtained by

$$\frac{1}{k_e} = \frac{1}{k_h} + \frac{1}{k_{b1}} + \frac{1}{k_{b2}} + \frac{1}{k_{a1}} + \frac{1}{k_{a2}} \tag{8.5}$$

where k_{b1}, k_{b2}, k_{a1}, and k_{a2} are the bending stiffness, shear and axial compressive stiffness of the pinion and the wheel, respectively.

Fig. 8.2 shows the calculated mesh stiffness using the gear pair sample given in Chapter 7. Also shown in this figure is its frequency spectrum. The mesh stiffness excitation exhibits a mesh frequency component and its super-harmonic frequency components. The mean component of the gear mesh stiffness is $\bar{k} = 3.25 \times 10^8 N/m$, which is used to calculate the natural frequency of the linear system once the equivalent mass and the damping ratio are known. Compared with the gear mesh stiffness, the lubricant stiffness is too large [92] and it is reasonable to ignore the effect of the lubricant stiffness in this work. The first two harmonic resonances of the excitation are significant, compared with the remaining ones.

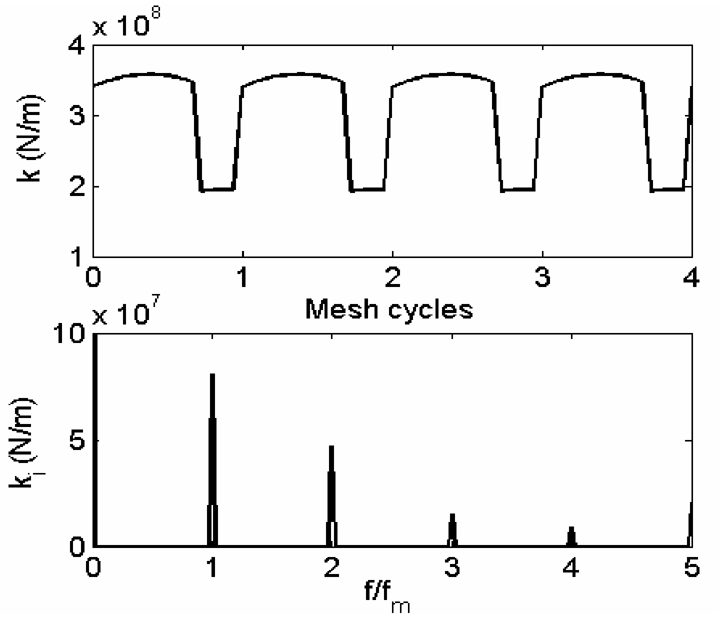

Fig. 8.2 Gear mesh stiffness time history and the frequency spectrum

8.1.2.4. Effect on Dynamic Factor

The mesh stiffness is believed to be a periodic function with the mesh frequency [134], hence sometimes it is convenient to rewrite the mesh stiffness function in its Fourier series form as

$$k(t) = k_m + \sum_{i=1}^{n} (a_i \cos(i\varpi_m t) + b_i \sin(i\varpi_m t)) \qquad (8.6)$$

where $\bar{k}$ is the average mesh stiffness in a mesh cycle and ϖ_m represents the mesh angular frequency. In this work n is chosen as 3, and the coefficients are given in table 8.1.

Table 8.1 Fourier series coefficients

i	a_i	b_i
1	-4.215e7	6.921e7
2	2.43e7	4.026e7
3	1.541e7	-1.304e6

Fig. 8.3 shows the mesh stiffness and its Fourier series and their dynamic factor results under the working condition $T_1 = 100Nm$, $n_1 = 4533r/\min$. It shows the Fourier series expansion can depict the original values very well and the effect on the dynamic response is not evident. Since the numerical time-step integration scheme can deal with numerical mesh stiffness, the direct numerical mesh stiffness is applied in the following calculations.

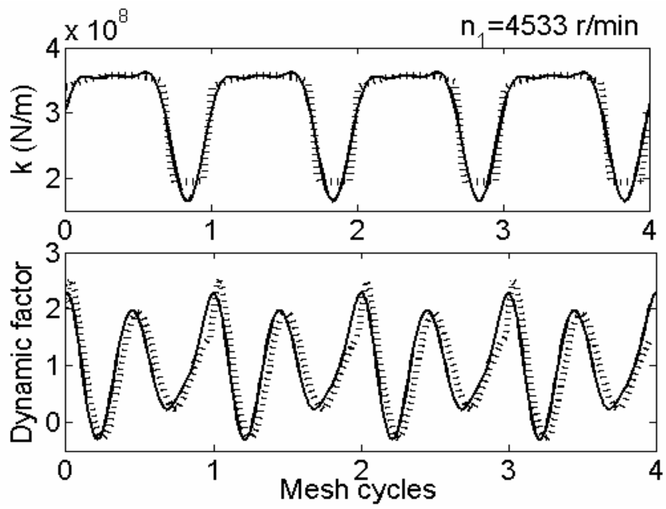

Fig. 8.3 Comparison of the numerical mesh stiffness and its Fourier series expansion (dashed lines represent the direct numerical mesh stiffness while solid lines represent the Fourier series expansion)

8.1.3. Quasi-steady Load Distribution

In this work, the quasi-static tooth force is obtained through a finite element contact analysis using Abaqus. The non-linear finite element method has been used in determining gear contact stress [138] and transmission error [139], by one of the authors. The finite element model is shown in Fig. 8.4. The mesh around the interacting tooth surface is refined owing to the small contact width which is in the order of sub-millimetres. In comparison with the deformable-body model used by Parker et al. [140] and Tamminana et al. [141], this mesh-refined model would give reasonable results of the individual tooth force without using an additional semi-analytical deformation model in the near field within the contact zone, which makes the calculation of the quasi-steady tooth force easier if a powerful workstation is available. The pinion is given a rotation speed while a torque is applied on the wheel, both in the centre shafts of the gears. By recording the contact force for a single gear pair, for instance the one noted with the bold black line in Fig. 8.4, the quasi-steady tooth force in a mesh cycle would be available.

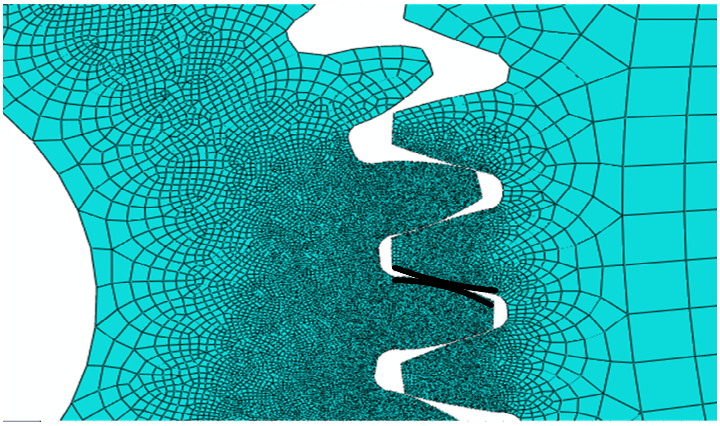

Fig. 8.4 Finite element model for the quasi-steady tooth force calculation

8.1.4. Dynamic Load and Dynamic Factor

The dynamic factor, defined as the ratio of the dynamic mesh force to the static mesh force, is used to get the dynamic tooth load, if the quasi-steady tooth load distribution is known. This way of calculating dynamic single tooth load is also used by Tamminana et al. [141] and Li et al. [92].

8.2. Effects of Dynamic Loads

The SDOF dynamic model could be solved numerically by the aid of the ODE toolbox provided in Matlab - for instance, the ode45 function, which applies a variable-step-size Runge-Kutta method. With the displacement response and the velocity response, the dynamic tooth force and the dynamic factor could be calculated. By multiplying the dynamic factor with the quasi-steady tooth load, the individual dynamic tooth force could be obtained, which will be used as the input load data for the lubrication model.

Fig. 8.5 shows the RMS value of the DTE which reveals one primary resonance peak caused by the first harmonic of the mesh stiffness excitation as well as one super-harmonic resonance caused by the second harmonic terms of the mesh stiffness excitation. This means that if the case with the resonance pinion speed $n_1 = 30\sqrt{k / m_e} / (\pi z_1) \approx 9067 rpm$ or the second super-harmonic resonance pinion speed $n_1 = 30\sqrt{k / m_e} / (2\pi z_1) \approx 4533 rpm$ is given, the dynamic response would vary significantly. From the view of noise and vibration performance, researchers have already shown that special attention should be paid to those resonance situations. This work will describe the effect of those critical situations from the view of lubrication and contact performance.

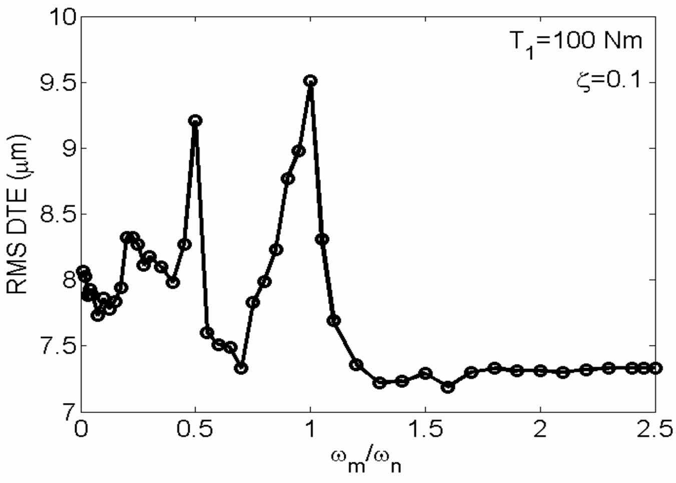

Fig. 8.5 RMS value of DTE as a function of gear mesh frequency

8.2.1. Effect on Minimum Film Thickness

With the assumption of the steady load distribution, it has been found that the speed has a significant effect on the minimum film thickness, which could be seen from the Dowson-Higginson minimum film thickness formula [111]. This formula, developed almost half a century ago, is believed to have a very high accuracy. As a consequence, their film thickness prediction is still used by designers and engineers all over the world. Moreover, researchers all over the world use the same equation as a reference for their numerical EHL development [142]. Some other formulae [143] may differ slightly in the coefficients, but they all indicate that the speed parameter U affects more than the load parameter W upon the minimum film thickness. However, the speed will affect the lubrication performance of the spur gear pair through another means (rotation speeds), especially those within the resonance regions. The speed will also have a significant influence on dynamic load owing to the internal and external excitations (thus the load parameter W is a function of the speed parameter U), which further affects the lubrication performance. In this work the speed effect on lubrication performance is investigated by considering those two paths.

When the quasi-steady loads are assumed, the thermal effect and the Ree-Eyring fluid effect are investigated. Fig. 8.6 shows the minimum film thickness along LOA under the quasi-steady load assumption for two speed cases, i.e. $n_1 = 300r/\min$ and $n_1 = 4533r/\min$. It is seen that for the two speed cases, the thermal effect and the non-Newtonian effect on the minimum film thickness are not too obvious. This could be explained by the fact that non-Newtonian effects as well as thermal effects are limited to influence the conditions of the entraining region which dominates the film thickness [26]. In the following section, if not explicitly specified, the solutions of the Ree-Eyring thermal model are given.

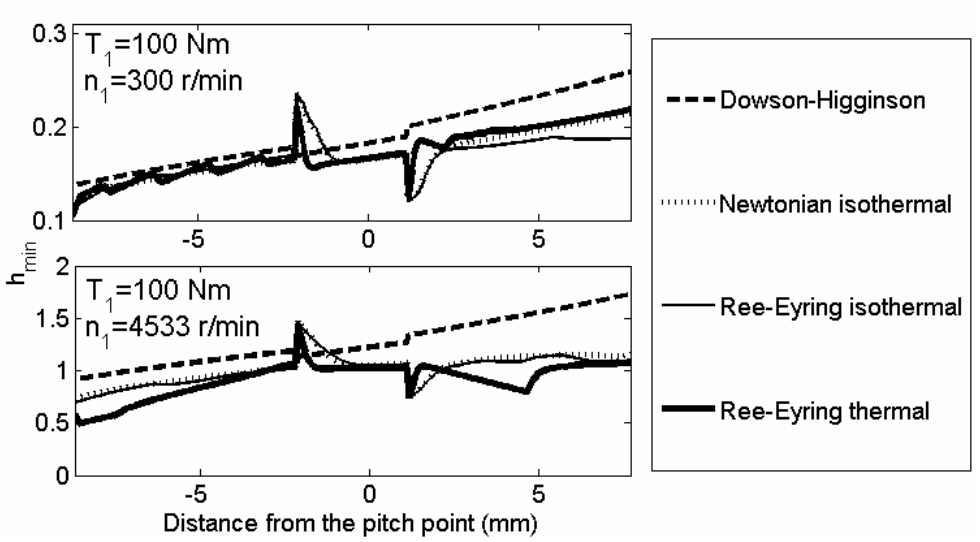

Fig. 8.6 Minimum film thickness variation with quasi-steady load assumption

A pinion rotation speed range between $n_1 = (100 \sim 9067) rpm$, which covers the most common operating conditions occurred in practical engineering, is chosen to investigate the effect of rotation speed on lubrication performances of the gear pair. With the constant input torque $T_1 = 100 Nm$, twelve speed cases are chosen: $n_1 = 100$, 300, 600, 900, 1133, 1813, 2267, 3000, 4533, 6000, 7500, 9067r/min. It should be repeated that $n_1 = 4533 r/\min$ represents the second super-harmonic resonance while n_1=9067r/min represents the main resonance frequency. Fig. 8.7 shows the dynamic factor response under those selected operating cases in four mesh cycles. Fig. 8.8 shows the dynamic tooth force in a mesh cycle. At high speeds, especially those with resonance frequencies, the dynamic load effect is significant. It is worth noting that owing to the large variation of DTE at cases of $n_1 = 4533$, 7500, and $n_1 = 9067 r/\min$, the dynamic factor may drop nearly to zero (or even below zero). The approach treating the nearly-zero (or negative) tooth force is chosen to be as the same as that used by Li and Kahraman [92]. That is, whenever the tooth force reaches zero, a very small positive loading value of 10 N was applied artificially.

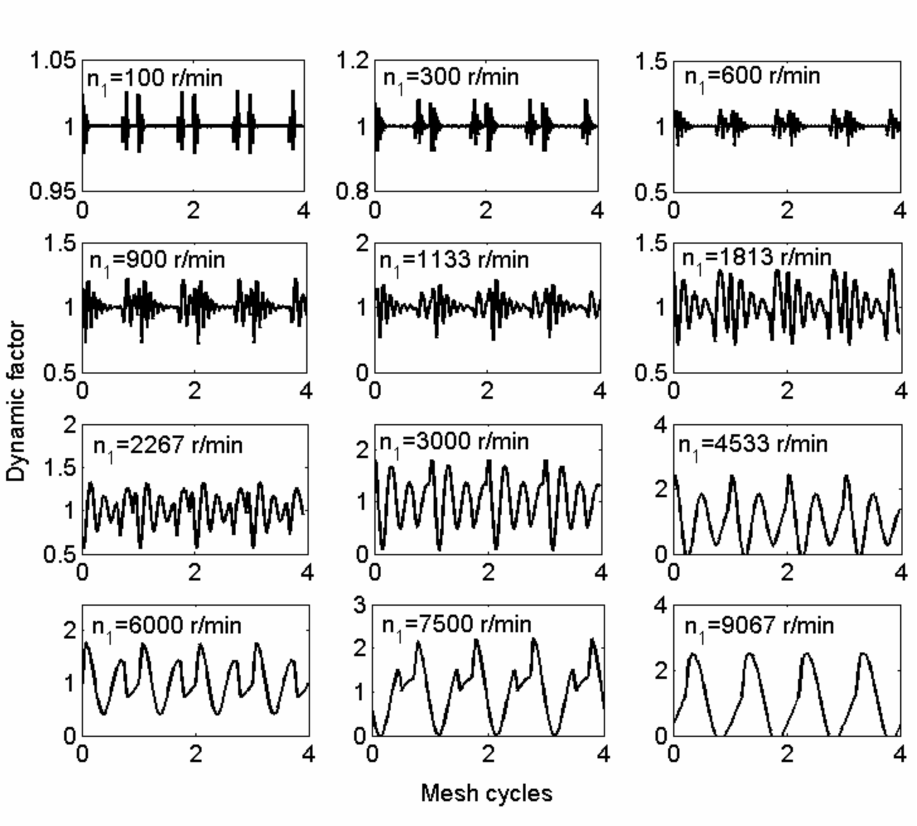

Fig. 8.7 Dynamic factors for selected speed cases

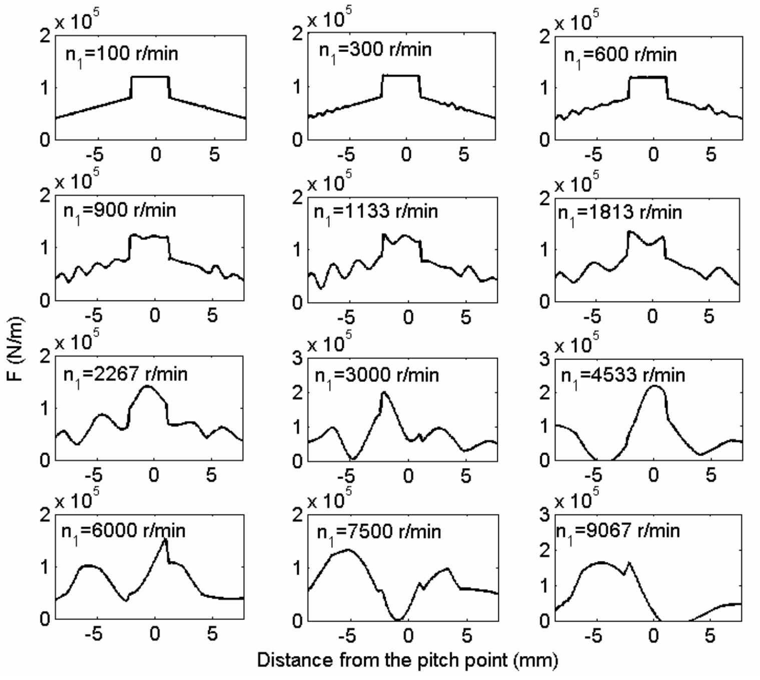

Fig. 8.8 Dynamic tooth forces in a mesh cycle for selected speed cases

Fig. 8.9 shows the minimum film thickness variation along the LOA under quasi-steady cases. Comparing the transient solution to the values obtained using the Dowson-Higginson minimum film thickness formula, it is seen that the sudden load change which occurred at the LPSTC and HPSTC point will cause significant film thickness fluctuations. Specifically, the sudden load drop occurred at the LPSTC point causes a transient increase of the minimum film thickness, while the sudden load increase causes a transient drop of the minimum film thickness. As the speed goes up, the deviation between the Dowson-Higginson values and the transient numerical values are getting bigger which implies that attention should be paid when evaluating the minimum film thickness for a high-speed situation using a simple Dowson-Higginson empirical formula, because it may overestimate the minimum film thickness at high speeds.

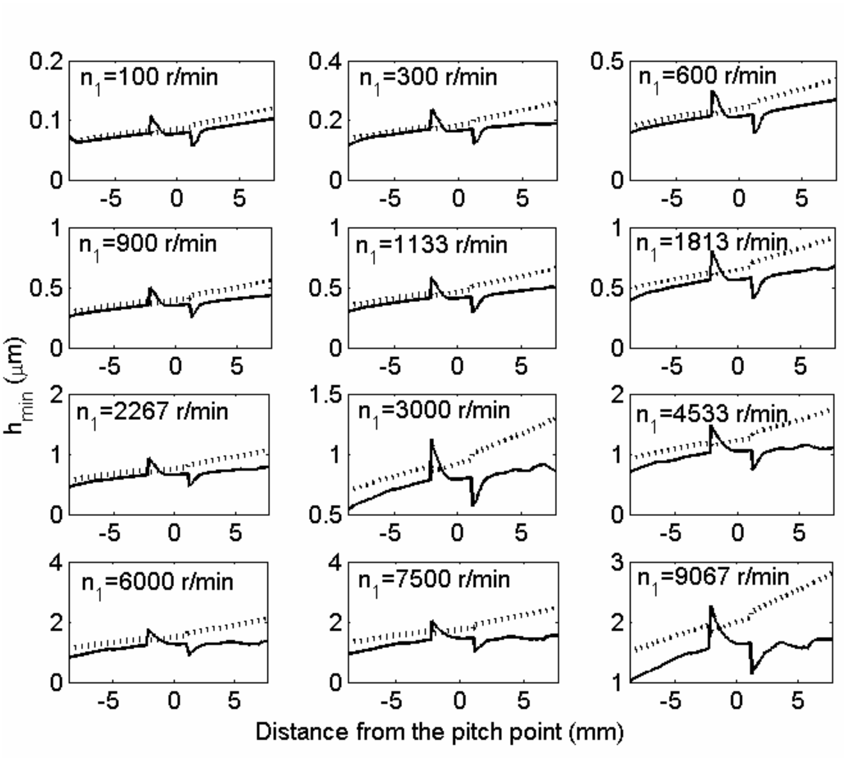

Fig. 8.9 Minimum film thickness with quasi-steady load (dashed lines represent empirical Dowson-Higginson solutions while solid lines represent the numerical solutions)

Fig. 8.10 shows the minimum film thickness results by taking the dynamic load into account. For cases where the dynamic factor does not deviate too much from unity, the minimum film thickness distribution would look like the quasi-steady solutions. However, special attention should be paid to cases where the dynamic factor varies significantly, such as $n_1 = 4533$, 7500, and $n_1 = 9067 r / \min$. According to the Dowson-Higginson formula, the minimum film thickness will increase when the dynamic factor (equivalently the dynamic force) drops. However, once the dynamic tooth force drops to nearly zero, the minimum film thickness will first drop significantly as well. In the cases $n_1 = 4533$, 7500, and $n_1 = 9067 r / \min$, the sudden drop of film thickness may lead to ultra-thin film situations during gear meshing. Combined with the surface roughness effect [5, 144] (which is not considered in this work), the lubrication condition would face a serious challenge at those high-speed cases which are close to resonance frequencies. It can be concluded that for gears, increasing the speed does not always increase the minimum film thickness since the vibration condition of the gear system might be harmful to the lubrication performance.

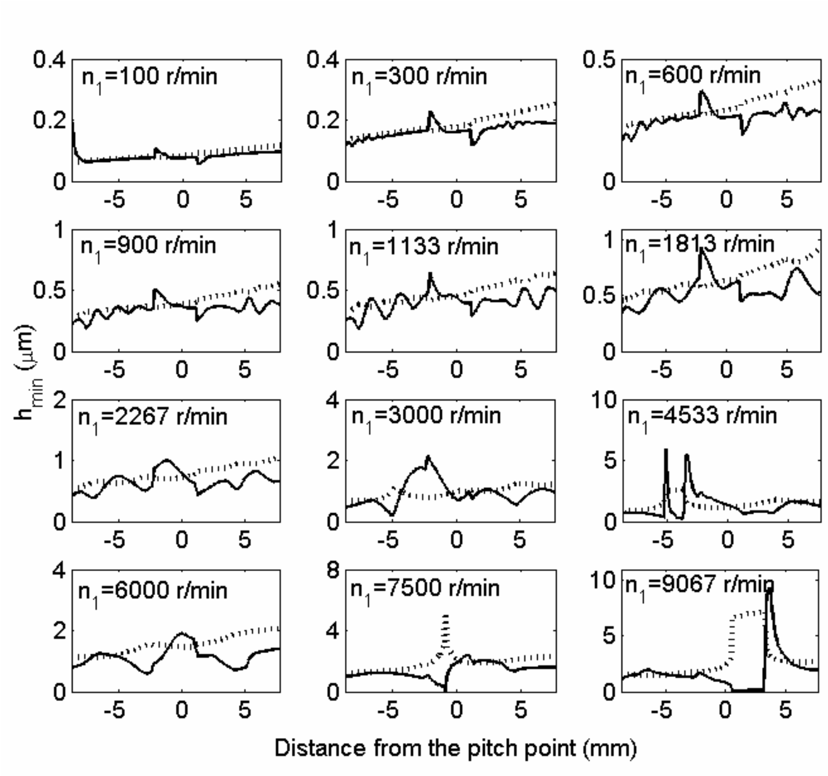

Fig. 8.10 Minimum film thickness with dynamic load (dashed lines represent empirical Dowson-Higginson solutions while solid lines represent the numerical solutions)

8.2.2. Effect on Pressure Distribution

The case of $n_1 = 4533 r/\min$ is chosen here to study the effect of dynamic loads on pressure distribution. Fig. 8.11 shows comparison of the pressure distribution in a mesh cycle between quasi-steady load solutions and dynamic load solutions under a Ree-Eyring isothermal assumption. It is seen that the dynamic load causes significant fluctuation of pressure distribution in a mesh cycle. In areas where the dynamic load is small, the pressure is also very low, while at areas where the dynamic load is high, the pressure is high. The amplification factor of the maximum pressure is proportional to the amplification factor of the load.

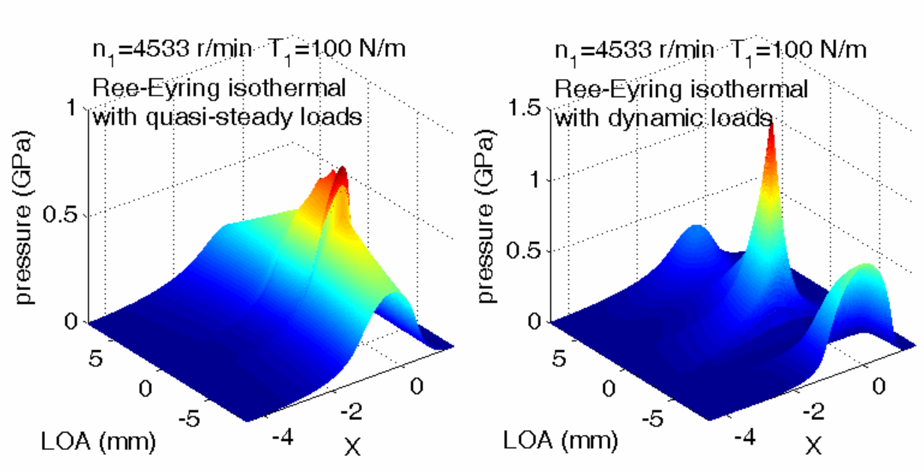

Fig. 8.11 Dimensionless pressure distributions with quasi-steady loads and dynamic loads

8.2.3. Effect on Temperature

The effect of dynamic loads on the temperature distribution is studied for the case of $n_1 = 4533 r/\min$. Fig. 8.13 shows the temperature distribution at locations (a-f) shown in Fig. 8.12. For both the quasi-steady loads and the dynamic loads, the temperature rises inside the film are higher than the ones inside the solids. When dynamic loads are considered, the temperatures inside the film at points (b) and (c) are higher than the ones with quasi-steady loads assumptions, as also shown in Fig. 8.14. However, as time goes on, the temperature field at point (d) with the dynamic loads assumption drops close to the one with the quasi-steady loads assumption. Fig. 8.14 shows that for the quasi-steady load case, the variation of maximum temperature rise in a mesh cycle corresponds to the slide-to-roll ratio which drops nearly to zero at the pitch point and then goes up. Fig. 8.14 also shows that the dynamic loads do affect the temperature rise of the film.

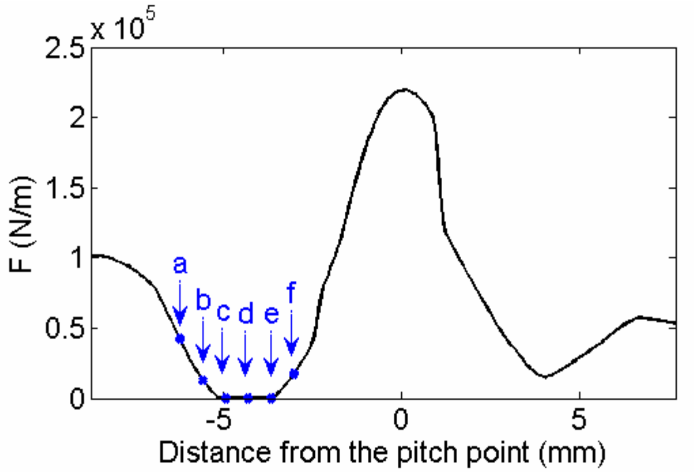

Fig. 8.12 Dynamic tooth force with $n_1 = 4533 r/\min$

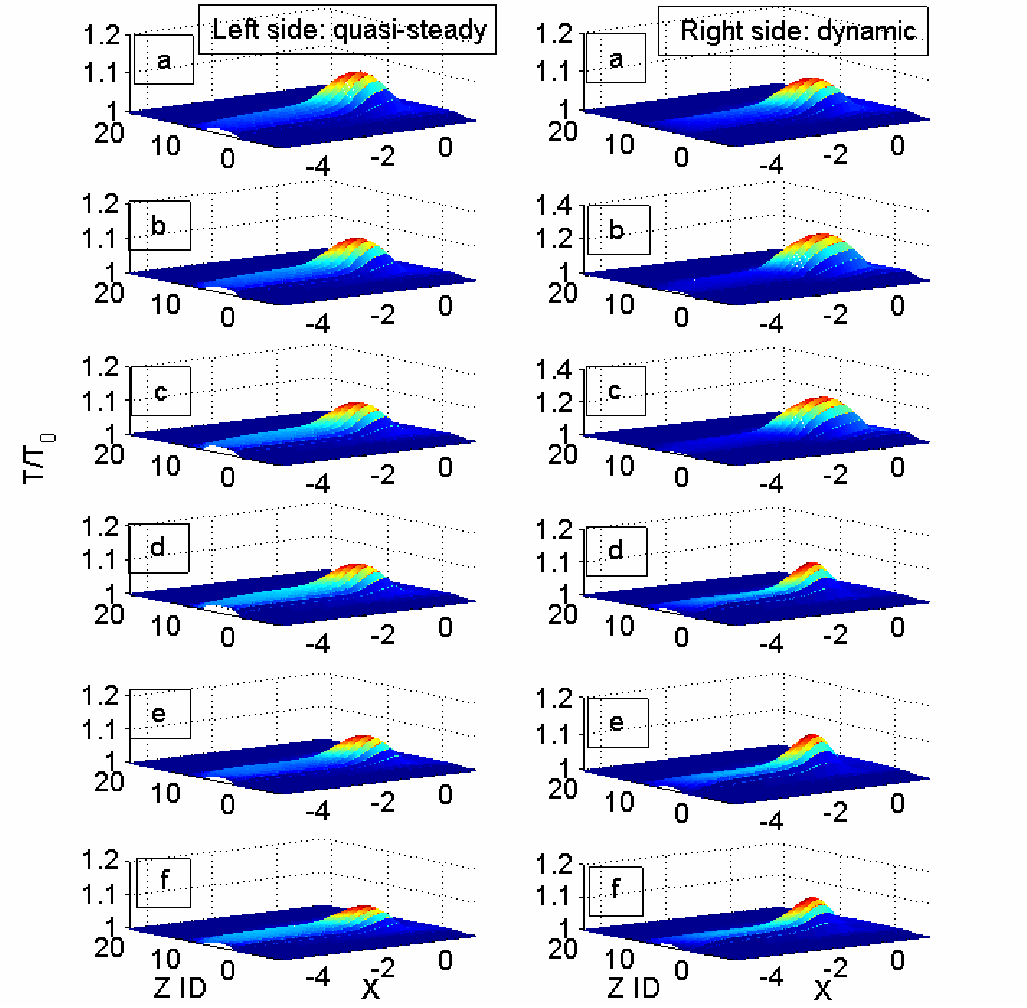

Fig. 8.13 Temperature distributions at the nearly-zero dynamic load area

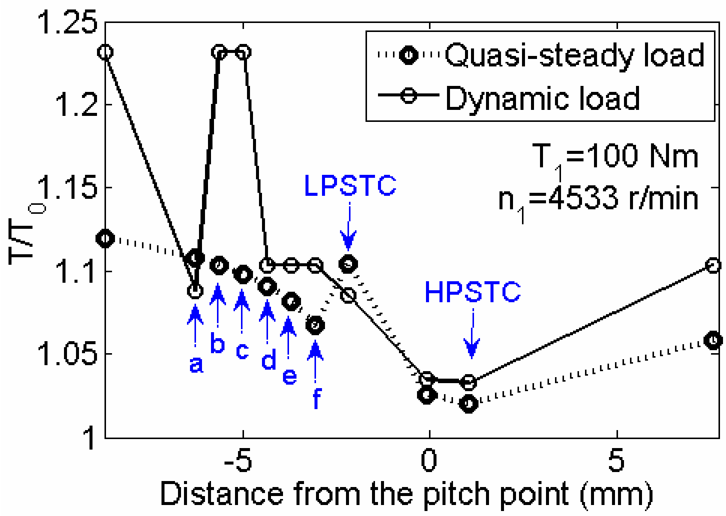

Fig. 8.14 Maximum temperatures along LOA for the case of $n_1 = 4533 r / \min$

8.3. Chapter Summary

A thermal elastohydrodynamic lubrication line contact model, which could handle ultra-thin film conditions, is developed to study the effects of speed on the lubrication performance of a spur gear pair, by taking into account the dynamic loads which are calculated using a classic mass-spring model. The speed effect on lubrication performance is studied comprehensively through its direct influence on lubrication and an indirect influence by affecting the dynamic loads of the gear pair. The following conclusions can be drawn:

- Special attention should be paid to using empirical formulae such as the Dowson-Higginson formula to evaluate the film thickness of a gear pair under high-speeds, especially within the resonance regions. Increasing the speed could not always increase the minimum film thickness since the vibration condition of the gear system might be harmful to the lubrication performance.
- The dynamic load might be intermittent in high-speed cases which are close to the resonance frequency or super-harmonic frequencies. At the transient intermittent phase of the dynamic load, a significant film thickness drop is observed.

- For the quasi-steady load case, the variation of maximum temperature rise in a mesh cycle corresponds to the slide-to-roll ratio which drops nearly to zero at the pitch point and then goes up. The dynamic loads affects the temperature rise of the film. The coupled effect of the dynamic loads, slide-to-roll ratio, fluid properties, etc. on temperature rise is yet to be studied.
- The lubricated contact performance of a spur gear drive should be evaluated together with its dynamic performance since the dynamic behaviour has a significant impact on the lubricated contact performance through dynamic loads. However, in this work, the effect of lubricated contact behaviour on the dynamic performance is not considered (for example, the lubrication condition affects the contact stiffness and the damping which further affect the dynamic behaviour.). A coupled tribology-dynamic model is yet to be developed for a more complete working performance evaluation of gear drives.
- In this work, the variation of meshing stiffness is taken as the exclusive excitation of the dynamic system. However, the gear clearance, the friction between engaging gear pairs and other factors such as the assembly error and the manufacturing error affect the dynamic load as well. A further study on the effects of friction excitation and gear backlash on spur gear lubrication performance can be found in Ref. [6], published by the author and coworkers.

Chapter 9 A Tribological Model for Normal Contact Stiffness Prediction

A tribological model for the normal contact stiffness prediction of a spur gear pair is proposed. Pressure distribution and compliance within the nominal contact zone are calculated at each engaging point along the LOA using a deterministic dry contact model and an EHL model which is able to deal with ultra-thin conditions - caused by surface roughness - aided by the Reduced Reynolds technique. Three methods for normal contact stiffness calculation are proposed and the results are compared with two existing analytical methods. The effects of surface roughness, load and speed on normal contact stiffness are discussed under dry contacts and EHL contacts.

9.1. Gear Contact Stiffness

As an internal excitation, the varying mesh stiffness of gear pairs, particularly owing to the different number of tooth pairs in contact, causes noise and vibration of gear systems [145]. Generally speaking, the mesh stiffness of gear pairs consists of contact stiffness, stiffness as a result of bending and traction, and stiffness caused by the deformation of the tooth roots. As an essential part of mesh stiffness, the contact stiffness which represents the deformations of the engaging tooth plays an important role in the dynamic behaviour of gear systems.

Researchers have conducted studies on the contact stiffness of interacting surfaces decades ago. Pharr et al. [146] studied the relationship between contact stiffness, contact area, and elastic modulus during indentation. Rabe et al. [147] presented a technique to measure the contact stiffness and the Young's modulus of sample surfaces quantitatively, with a resolution of approximately 20 nm, exploiting the contact resonance frequencies of standard cantilevers used in atomic force microscopy. Li and Bhushan [148] presented a review of nanoindentation continuous stiffness measurement technique and its applications. Królikowski and Szczepek [149] utilized the ultrasonic method for the prediction of contact parameters such as the real contact area and the contact stiffness. Sherif [150] discussed the parameters affecting the contact stiffness of nominally flat surfaces. It is found that when considering the theory of Greenwood and Williamson [151] (GW model), the contact stiffness is dependent upon the standard deviation of height distribution of asperities, the effective radius of curvature of asperities and the density of asperities per unit area. When considering the theory of Onions and Archard [152] (OA model), the contact stiffness is dependent upon the correlation distance, the apparent area of contact, and the standard deviation of height distribution of asperities. It is also found that the standard deviation in both models strongly affects the value of the contact stiffness, and the GW model underestimates the contact stiffness when it is compared with the OA model. Recently, finite element methods have been extensively used for contact stiffness calculation [153-155] owing to the popularity of commercial finite element packages.

The previous review implies that there are currently two ways commonly used for contact stiffness prediction: one is based on the GW model, which considers the surface roughness with limited statistical parameters, and the other one is based on the finite element method. Though the former one statistically represents rough surface effects, it cannot capture the local detailed information at asperity contacts level, which is believed to be essential for the understanding of surface contact fatigue mechanisms. The latter one mainly relies on commercial finite element packages which are not currently able to take surface roughness into account easily. Deterministic models in the finite difference frame are commonly used in rough surface contact and lubrication problems [2]. However, researchers mainly focus on pressure, compliance distribution, film thickness and traction, among other things. Less attention is paid to the contact stiffness calculation based on deterministic contact models. In this work, the deterministic method is used for the normal contact stiffness studies of a spur gear pair.

Based on Hertzian contact solution, some analytical formulae have been proposed for the contact stiffness calculation. However, this type only takes macro-parameters, such as the macro geometry of the surfaces and the elastic modulus of materials, for example, into account while micro-parameters such as roughness are neglected. Even though the Majumdar-Bhushan fractal model [156] can be used for micro-parameter analysis, the approach could not capture detailed information within the nominal contact zone.

With the procedure of Lundberg [157], the local compliance owing to contact stresses is expressed as

$$\delta_c = \frac{1.275}{E^{0.9} B^{0.8} F_c^{0.1}} \tag{9.1}$$

where δ_c is the contact elastic deformation, E is the elastic modulus of the gear material, B is the tooth width and F_c is the total tooth force and for spur gear pairs it is calculated as

$$F_c = FB \tag{9.2}$$

where F is the tooth force for the line contacts with unit N/m.

Then the normal contact stiffness is expressed as

$$k_c = F_c / \delta_c \tag{9.3}$$

From a result derived by Yang and Sun [158], the stiffness of the Hertzian contact of meshing teeth is a constant along the LOA independent both to the position of contact and the depth of interpenetration which is given by [159]

$$k_c = \frac{\pi E B}{4(1-\nu^2)} \tag{9.4}$$

where E, B, ν represent the Young's modulus, tooth width and Poisson's ratio, respectively. Those two contact stiffness formulae will be discussed and compared with proposed numerical methods.

The proposed lubrication model mentioned in previous chapters provides a way to calculate the normal contact stiffness using the detailed local information inside the nominal contact zone. This chapter tries to discuss the effect of lubrication, load, speed and surface roughness on normal contact stiffness for a spur gear pair. In this work isothermal conditions are assumed.

9.2. Methods for Normal Contact Stiffness Prediction

Three methods, named Methods A, B and C, are proposed to calculate the normal contact stiffness with the predicted pressure distribution and the elastic deformation. They are introduced below.

Method A: since the discretized models require many nodes spaced within the nominal Hertzian contact zone, each node pair is considered as a small spring. The total normal contact stiffness is the sum of stiffnesses of those small springs.

$$k_c = B\sum_{i=0}^{n_d}\frac{F_i}{d_i} \tag{9.5}$$

Where B is the tooth width, n_d is the number of node pairs where the elastic deformation $d > 0$. F_i is the local load applied on the node pair and is expressed as

$$F_i = \frac{p_i}{\sum_{i=1}^{n_d} p_i}F \tag{9.6}$$

d_i and p_i are the elastic deformation and pressure at the node pair i. F is the total tooth force at the specific engaging location.

Method B: the normal contact stiffness with Method B is defined as the ratio of the total tooth force and the maximum elastic deformation within the nominal Hertzian contact zone.

$$k_c = B\frac{F}{d_{\max}} \tag{9.7}$$

Method C: this Method is similar to Method B with the difference that the mean elastic deformation within the nominal Hertzian contact zone is applied, instead of the maximum one.

$$k_c = B\frac{F}{d_m} \tag{9.8}$$

The mean elastic deformation d_m is defined as

$$d_m = \frac{\sum_{i=1}^{n_d} d_i}{n_d} \tag{9.9}$$

It is noticed that these three methods capture the detailed local information inside the nominal Hertzian contact zone, which provide more physically-meaningful insights on the normal contact stiffness of rough surface contacts.

9.3. Results and Discussions

9.3.1. Methods Comparison

First, the proposed three methods are compared with the Yang-Lin analytical solution [159] and the Lundberg solution [157]. If not explicitly specified, the working conditions are taken as $F = 1\times10^6 N/m$, $n_1 = 300r/\min$ and tooth surfaces are assumed smooth. Under dry and EHL contact, a comparison of normal contact stiffness along the LOA using those methods is shown in Fig. 9.1. It is seen that the Lundberg formula far overestimates the normal contact stiffness, while the Yang-Lin formula gives the result with the same order of magnitude of the three proposed methods. For the dry contacts, the normal contact stiffness keeps constant in a meshing period, while for the EHL contacts the normal contact stiffness varies slightly, especially at the HPSTC and the LPSTC point. For the given working conditions, the normal contact stiffnesses under EHL contact only slightly differ from their dry-contact counterparts. It has been extensively known that with lubrication, the pressure distribution and the traction within the nominal Hertzian contact zone varies with their counterparts under dry contacts [69]. However, with reference to the elastic deformation, the EHL result remains almost the same with the dry contact result if the surfaces are smooth. When we recall the definition of the contact stiffness, the slightly differences of normal contact stiffness between the EHL result and the dry contact result for smooth surface cases are easily established.

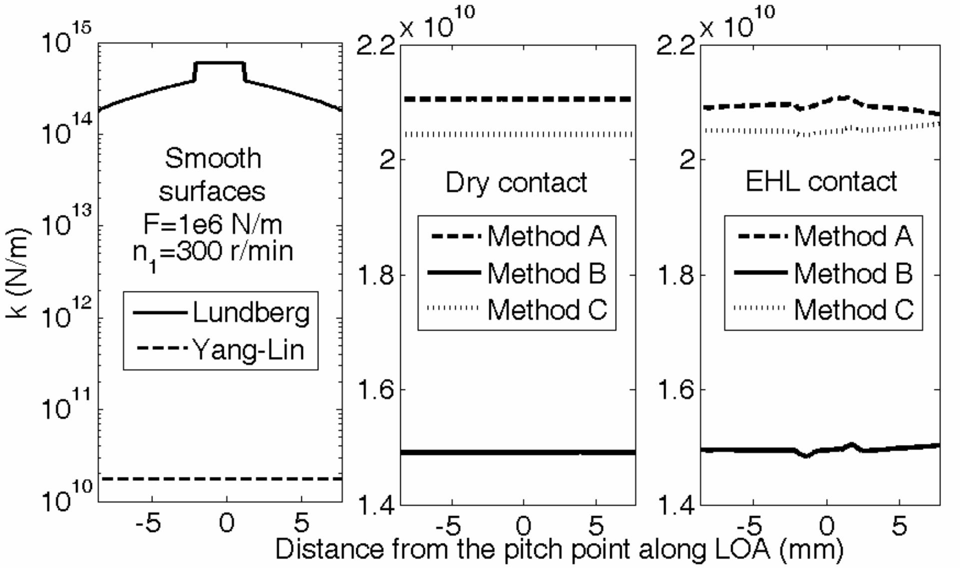

Fig. 9.1 Comparison of methods for normal contact stiffness calculation

The effects of tooth surface roughness, applied load, and speed, on normal contact stiffness are studied under both the dry contacts and the Newtonian EHL contacts.

9.3.2. Effect of Roughnesses

Fig. 9.2 shows the contact stiffness along the LOA with different surface roughness , i.e. $\overline{R}_q = 0$, 0.1, 0.2 and 0.3, under dry contacts using Method C. It is seen that if surfaces are smooth the contact stiffness in a meshing period does not vary.

However, if roughnesses are present, the contact stiffness in different meshing positions varies. It is clearer if a mean contact stiffness in a whole meshing period is defined to show the effects of roughness on contact stiffness. The mean contact stiffness in a whole meshing period can be defined as

$$k_m = \sum_{i=1}^{n_T} k_i / n_T \tag{9.10}$$

where k_i is the instantaneous normal contact stiffness at a specific moment during the meshing process.

Fig. 9.3 shows the effect of roughness on the mean normal contact stiffness during a whole meshing period under dry contacts. The contact stiffness in a meshing period varies when the surface roughness exists. It is seen that under dry contacts, for Methods A and B, as the surfaces gets rougher, the mean normal contact stiffness decreases, while for Method C the mean normal contact stiffness increases.

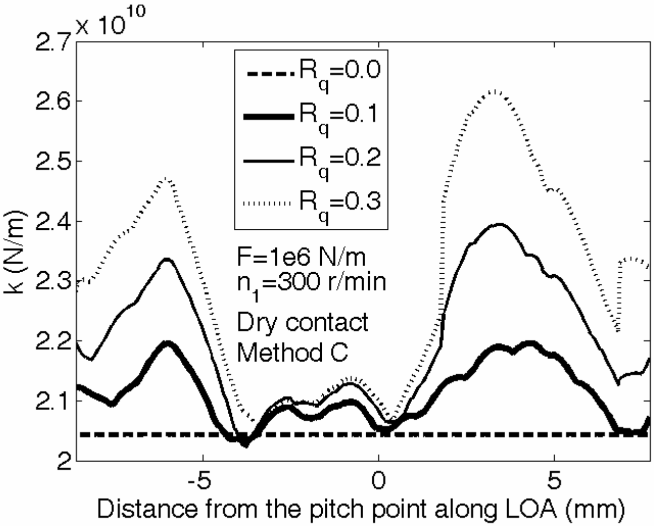

Fig. 9.2 Effect of surface roughness on contact stiffness under dry contacts

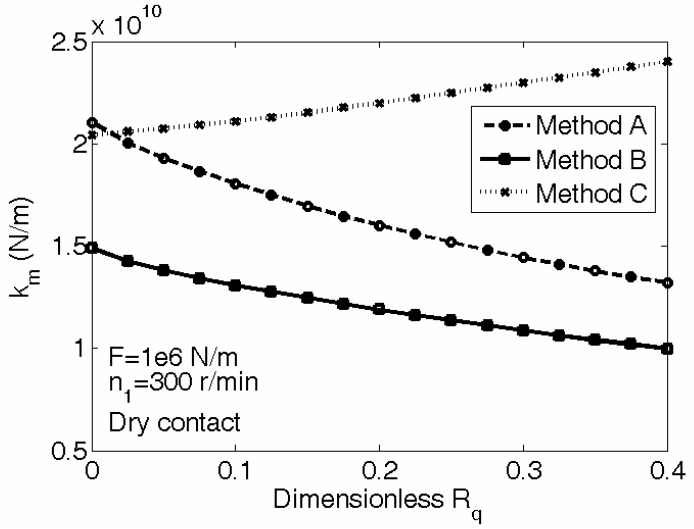

Fig. 9.3 Mean contact stiffness along LOA as surface roughness increases under dry contacts

In the following, the effect of roughness on normal contact stiffness is discussed under EHL conditions. Fig. 9.4 shows the contact stiffness along the LOA with different surface roughness under Newtonian EHL contacts using Method C, while Fig. 9.5 shows the mean contact stiffness variation as roughness changes. It also shows that surface roughness causes variation of normal contact stiffness as the gear pair is in the meshing process. Under EHL contacts, for Methods A and B, as the surfaces get rougher, the mean normal contact stiffness decreases, while for Method C, the mean normal contact stiffness increases. This trend is similar to the dry contact results.

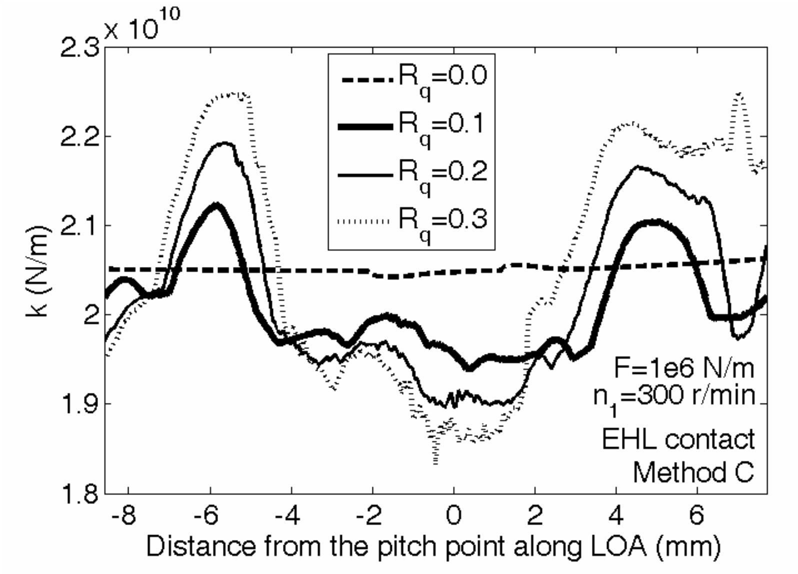

Fig. 9.4 Effect of surface roughness on contact stiffness under EHL contacts

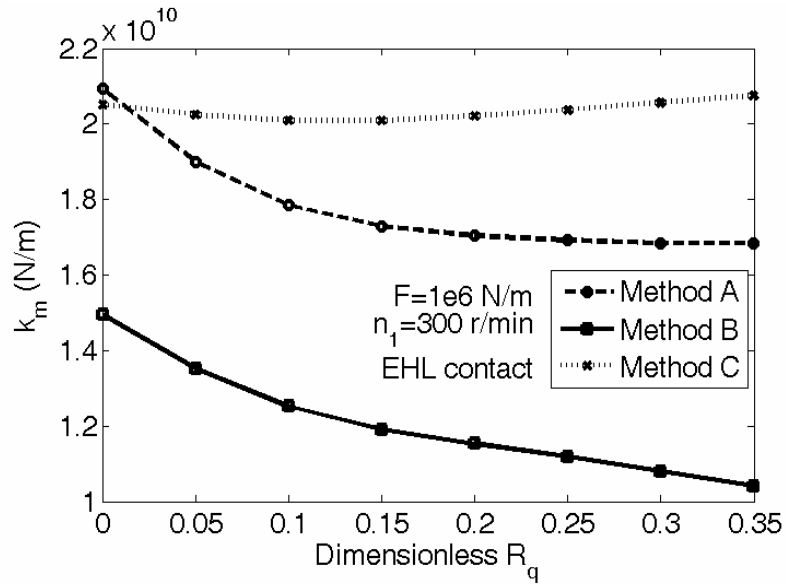

Fig. 9.5 Mean contact stiffness along the LOA as surface roughness increases under EHL contacts

9.3.3. Effect of Load

According to Kiekbusch et al. [155], the contact stiffness varies as the applied torque changes. The effect of load is studied under both dry contacts and EHL contacts. Several load cases, which covers three orders of magnitude, are chosen to study the effect of load on normal contact stiffness.

For the dry contacts, it is found that the load does not affect the normal contact stiffness if the same surface roughness is assumed. However, for the EHL contacts, the normal contact stiffness varies as the load changes, as is seen in Fig. 9.6. For Method C, as the load increases the variation of normal contact stiffness along the LOA is alleviated.

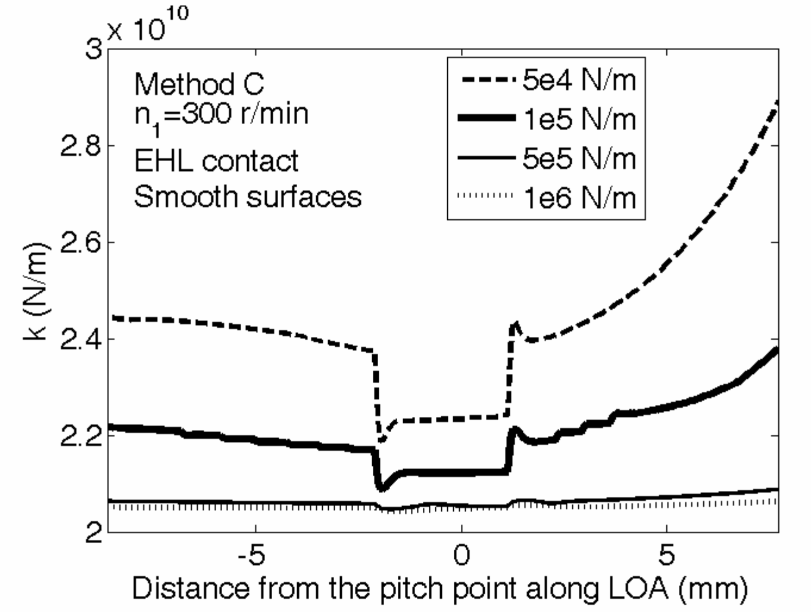

Fig. 9.6 Effect of load on normal contact stiffness under EHL contacts

Fig. 9.7 shows the variation of mean contact stiffness as the load changes under EHL contacts using the three Methods. It is seen that for the three Methods, when the load is relatively light, as the load increases the mean contact stiffness drops significantly. While the load is moderate, as the load increases, the mean contact stiffness drops much more slowly. For Method B, when the load is not light, the mean contact stiffness almost keeps constant as the load increases.

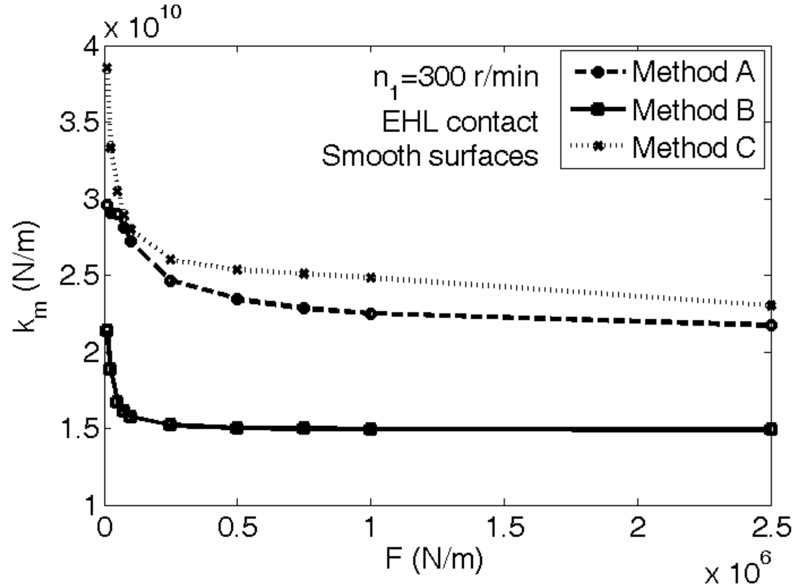

Fig. 9.7 Variation of mean contact stiffness along LOA as load increases under EHL contacts

9.3.4. Effect of Speed

The effect of speed on normal contact stiffness is also studied. For the dry contacts, speed also does not affect the normal contact stiffness at all. Meanwhile, for the EHL contacts, speed affects the normal contact stiffness as is seen in Fig. 9.8. As the speed increases for Method C the variation of normal contact stiffness along the LOA becomes evident. Fig. 9.9 shows the mean contact stiffness with the three methods. As the speed increases, for Methods A and B, the mean contact stiffness decreases, while for Method C, the mean contact stiffness increases.

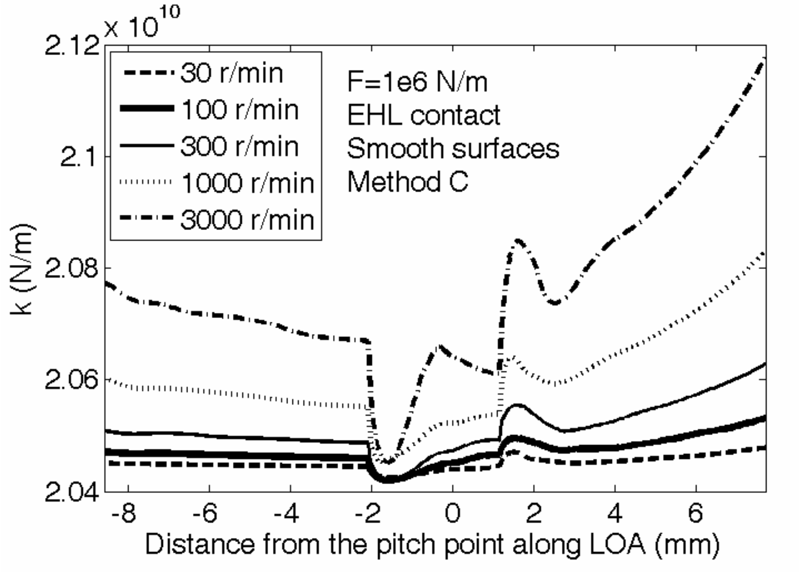

Fig. 9.8 Effect of speed on normal contact stiffness under EHL contacts

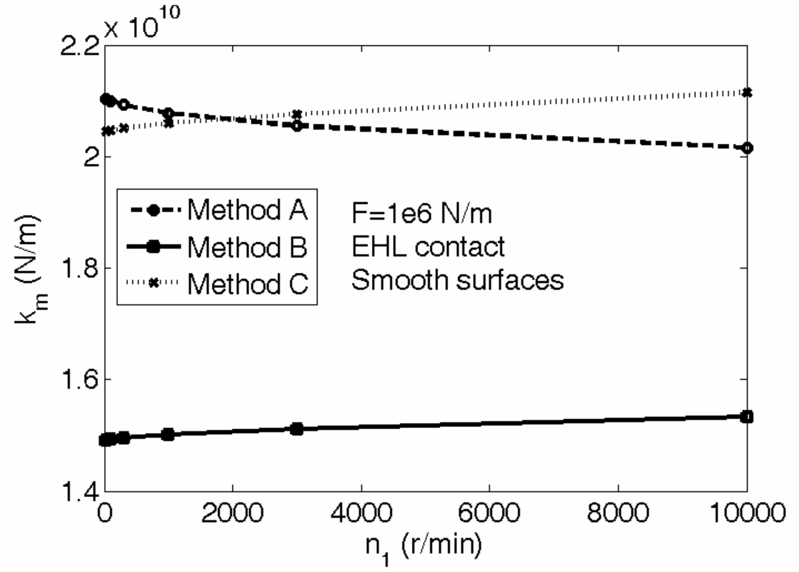

Fig. 9.9 Variation of mean contact stiffness along the LOA as speed increases under EHL contacts

9.4. Chapter Summary

The proposed model is used for a normal contact stiffness prediction of a spur gear pair. Three methods for normal stiffness calculation are proposed and compared with two existing analytical formulae. The following conclusions are drawn:

The Lundberg contact stiffness formula overestimates the normal contact stiffness, while the Yang-Lin formula gives the result with a reasonable order of magnitude. For the given gear pair sample, in most working condition cases the predicted value with Method A is between the value with Method C (higher) and the one with Method B (lower).

If surfaces are smooth, the EHL-based normal contact stiffness only very slightly differs from the dry-contact-based one.

Surface roughness causes fluctuation of contact stiffness in the meshing period. Both for dry contacts and EHL contacts, as the surfaces get rougher, for Methods A and B, the mean normal contact stiffness decreases, while for Method C, the mean normal contact stiffness increases.

Under dry contacts, the normal contact stiffness keeps constant as the load or speed varies. Under EHL contacts, the normal contact stiffness varies as the load or speed changes. For the three proposed methods, when the load is relatively light, as the load increases, the mean contact stiffness drops significantly. While the load is moderate, as the load increases, the mean contact stiffness drops much more slowly. As the speed increases, for Methods A and B, the mean contact stiffness decreases while for Method C, the mean contact stiffness increases when EHL contacts are assumed.

The study on normal contact stiffness has laid a foundation for a further advanced modelling of mesh stiffness of gear pairs and is able to throw some light on tangential contact stiffness studies. The proposed methodology provides a potential way for an advanced tribo-dynamic model of gear pairs, which is believed to provide a more comprehensive evaluation of total working performance of gear pairs, both tribologically and dynamically.

Chapter 10 Conclusions and Future Work

In this work a comprehensive spur gear lubrication analysis is made by considering the thermal effect, non-Newtonian effects, rough surface effects, transient squeeze effects, and dynamic load effects. First, the modern elastohydrodynamic lubrication theory is studied and relevant numerical approaches are introduced. The non-Newtonian fluid effect is discussed with a Ree-Eyring fluid model and a power-law fluid model. The thermal effect is studied by solving energy equations of interacting solids and the film numerically with the sequential sweeping technique. The rough surface effect is studied by directly adding the surface topography term to the film thickness equation, which makes the approach a deterministic model. The reduced Reynolds equation technique is applied to deal with any potential "asperity contacts" or any ultra-thin film situations. Those situations can be caused because of the surface roughness or the dynamic load effect. This approach allows us to capture local information about pressure, traction, film thickness, etc., within the nominal contact zone. The influence of working conditions - including load, rolling speed and the slide/roll ratio - are discussed with those models (Newtonian or non-Newtonian fluids, isothermal or thermal conditions). Then, a spur gear pair lubrication analysis is conducted using the developed modern EHL model with the quasi-steady load assumption. Notices about its lubrication performance are given in an attempt to provide some guidance for engineering practice. Finally, the dynamic load effect is incorporated into the spur gear pair lubrication analysis, since the excitations owing to the varying mesh stiffness, for example, cause significant dynamic behaviour for the spur gear system, especially under some critical rotation speeds. The dynamic load is calculated using a two degree-of-freedom lumped parameter system dynamic model in which the varying mesh stiffness is considered as the excitation. The dynamic model is solved using the Runge-Kutta method with the aid of Matlab. The consequences of dynamic load effects on pressure distribution and film thickness in the whole mesh period are discussed. In the last chapter, normal contact stiffness of the spur gear pair is predicted using the proposed deterministic dry contact and EHL models. Towards the three objectives presented in the Introduction Section, conclusions have been made as follows.

In terms of the first objective - that is, a study of the effect of working conditions, thermal conditions, non-Newtonian behaviours and surface topography on pressure, film thickness and friction coefficient of a line contact problem, the following conclusions are established:

i. The Newtonian fluid model and the power-law fluid model with a fixed power-law index are not suitable for friction prediction even though they can give reasonable film thickness results. Ree-Eyring fluid models give reasonable friction coefficient values whose range are in accordance with those existing experimental results.

ii. For the Ree-Eyring fluid, when the load is light, the value of the friction coefficient increases significantly; when the load is high and as the load keeps increasing, at first, the value of the friction coefficient does not change too much. If it keeps increasing, the friction coefficient will drop gradually. For the Ree-Eyring fluid, when the rolling speed is not high, as the speed goes up, the value of the friction coefficient increases significantly, and if the speed increases more, the value of the friction coefficient increases much more slowly. The friction coefficient is almost linear with the logarithmic form of rolling speed. For the Ree-Eyring fluid, the value of the friction coefficient goes up when the slide/roll ratio increases. However, this trend becomes slower when the slide/roll ratio is high.

iii. For the Ree-Eyring fluid, as the amplitude of waviness increases, the friction coefficient first decreases a little or remains constant, and when the amplitude is high the friction coefficient increases gradually as the amplitude keeps increasing.

iv. For the Ree-Eyring fluid, compared with the isothermal solutions, the friction coefficients are smaller for the thermal solutions if the working condition is the same. This is caused by the decrease in equivalent viscosity within the nominal contact zone. When the thermal effect is considered, for the Ree-Eyring fluid, when the load is heavy and if the load keeps going up, the friction coefficient drops slightly which means that thermal effect is more evident for heavier loads. The value of the friction coefficient for the Ree-Eyring TEHL model first increases and then decreases as the rolling speed increases. This means that the thermal effect in high rolling speed cases would be more significant owing to the high sliding speed. The value of the friction coefficient of the Ree-Eyring TEHL model first increases and then decreases as the slide/roll ratio increases. This could also be explained by the variable sliding speed, which is a critical factor for the thermal effect.

In terms of the second objective - that is, the study of a comprehensive lubricated contact analysis of a spur gear pair - conclusions can be made as follows:

i. For the spur gear lubrication, if a quasi-steady load distribution is assumed for a spur gear pair with the contact ratio above unity, a transient fluid squeeze effect causes an opposite sudden fluctuation at the LPSTC and HPSTC where sudden load change occurs. For the given spur gear pair sample, along the LOA, the thinnest film thickness occurs at the approach point. The maximum temperature rise occurs at the approach point while the minimum temperature rise occurs at the pitch point owing to the zero slide/roll ratio. Along the LOA, not only the minimum film thickness but also the maximum temperature rise occurs at the approach point. This means that special attention should be paid to this meshing position, under the operating conditions considered.

In terms of the third objective - that is, the study of a coupled tribological-dynamic model for a gear pair - we conclude:

i. If the dynamic load effect is taken into account, then special attention should be paid using empirical formulae - such as the Dowson-Higginson formula - to evaluate the film thickness of a gear pair under high-speeds, especially within the resonance regions. Increasing the speed will not always increase the minimum film thickness since the vibration condition of the gear system might be harmful to the lubrication performance.

ii. Three methods are proposed to predict the normal contact stiffness of the spur gear pair based on deterministic tribological models. If surfaces are smooth, the EHL-based normal contact stiffness only very slightly differs from the dry-contact-based one. Surface roughness causes fluctuation of contact stiffness in the meshing period. Under dry contacts, the normal contact stiffness remains constant as the load or speed varies. Under EHL contacts, the normal contact stiffness varies as the load or speed changes.

In terms of those objectives, future work can be summarized as follows:

i. For the first objective, more detailed work is required for a better understanding of those coupled effects among the transient squeeze action, the working conditions, the thermal conditions, the surface roughness, fluid rheology behaviours and the dynamic conditions.

ii. For the second objective, the line contact is applied in this work to simulate the lubrication problem of spur gears. However, since there exist the assembly and the manufacture errors, the contact type will not exactly be the line contact problem. In addition, the surface topography should also be considered which requires a three-dimensional contact analysis instead of line contact analysis.

iii. For the third objective, a more comprehensive and coupled dynamic lubrication model is yet to be developed for a gear drive. Not only does the dynamic behaviour affects the lubrication performance of gears such as film thickness, traction, etc., but lubrication behaviours also affect the dynamic performance of gears such as mesh stiffness and mesh damping, etc.

iv. Generally, the numerical results lack experimental verification. More relevant experiments should be conducted to verify those numerical conclusions such as the prediction of pressure, film thickness, temperature field, stress field, and others.

References

[1] R. W. Snidle and H. P. Evans, "Some aspects of gear tribology," *Proceedings of the Institution of Mechanical Engineers Part C-Journal of Mechanical Engineering Science,* vol. 223, pp. 103-113, 2009.

[2] C. H. Venner and A. Lubrecht, *Multilevel method in lubrication*: Elsevier, 2000.

[3] P. Yang and S. Wen, "A generalized Reynolds equation for non-Newtonian thermal elastohydrodynamic lubrication," *Journal of Tribology,* vol. 112, pp. 631-636, 1990.

[4] Y. Z. Hu and D. Zhu, "A full numerical solution to the mixed lubrication in point contacts," *Journal of Tribology-Transactions of the Asme,* vol. 122, pp. 1-9, 2000.

[5] H. Liu, K. Mao, C. Zhu, and X. Xu, "Mixed lubricated line contact analysis for spur gears using a deterministic model," *Journal of Tribology,* vol. 134, pp. 021501-7, 2012.

[6] H. Liu, K. Mao, C. Zhu, X. Xu, and M. Liu, "Parametric studies of spur gear lubrication performance considering dynamic loads," *Proc. Inst. Mech. Eng. Part J: J Engineering Tribology,* 2012.

[7] H. Liu, K. Mao, C. Zhu, S. Chen, X. Xu, and M. Liu, "Spur gear lubrication analysis with dynamic loads," *Tribology Transactions,* vol. 56, pp. 41-48, 2013/01/01 2013.

[8] H. Hertz, *On the contact of rigid elastic solids*: Macmillan, 1896.

[9] F. P. Bowden and D. Tabor, "The area of contact between stationary and between moving surfaces," *Proceedings of the Royal Society of London. Series A. Mathematical and Physical Sciences,* vol. 169, pp. 391-413, February 7, 1939 1939.

[10] J. F. Archard, "Elastic deformation and the laws of friction," *Proceedings of the Royal Society of London. Series A. Mathematical and Physical Sciences,* vol. 243, pp. 190-205, December 24, 1957 1957.

[11]J. A. Greenwood and J. B. P. Williamson, "Contact of nominally flat surfaces," *Proc Roy Soc (London) Ser A,* vol. 295, pp. 300-319, 1966.

[12]K. L. Johnson, K. Kendall, and A. D. Roberts, "Surface energy and the contact of elastic solids," *Proceedings of the Royal Society of London. A. Mathematical and Physical Sciences,* vol. 324, pp. 301-313, September 8, 1971 1971.

[13]J. A. Greenwood and J. H. Tripp, "The elastic contact of rough spheres," *Journal of Applied Mechanics,* vol. 89, pp. 153–159, 1967.

[14]D. J. Whitehouse and J. F. Archard, "The properties of random surfaces of significance in their contact," *Proceedings of the Royal Society of London. Series A, Mathematical and Physical Sciences,* vol. 316, pp. 97-121, 1970.

[15]P. R. Nayak, "Random process model of rough surfaces in plastic contact," *Wear,* vol. 26, pp. 305-333, 1973.

[16]I. A. Polonsky and L. M. Keer, "Fast methods for solving rough contact problems: A comparative study," *Journal of Tribology,* vol. 122, pp. 36-41, 2000.

[17]J. A. Greenwood, "Problems with surface roughness," in *Fundamentals of Friction: Macroscopic and Microscopic Processes*, I. L. Singer and H. M. Pollock, Eds., ed Dordrecht: Kluwer, 1992, pp. 57-76.

[18]A. Majumdar and B. Bhushan, "Fractal model of elastic-plastic contact between rough surfaces," *Journal of Tribology,* vol. 113, pp. 1-11, 1991.

[19]W. T. Lai and H. S. Cheng, "Computer simulation of elastic rough surface contacts," *Trans. ASLE,* vol. 28, pp. 172-180, 1985.

[20]A. Brandt and A. A. Lubrecht, "Multilevel matrix multiplication and fast solution of integral equations," *Journal of Computational Physics,* vol. 90, pp. 348-370, 1990.

[21]T. Nogi and T. Kato, "Influence of a hard surface layer on the limit of elastic contact---Part I: analysis using a real surface model," *Journal of Tribology,* vol. 119,

pp. 493-500, 1997.

[22] S. Liu, Q. Wang, and G. Liu, "A versatile method of discrete convolution and FFT (DC-FFT) for contact analyses," *Wear,* vol. 243, pp. 101-111, 2000.

[23] H. Lu, M. Berzins, C. E. Goodyer, and P. K. Jimack, "High-order discontinuous Galerkin method for elastohydrodynamic lubrication line contact problems," *Communications in Numerical Methods in Engineering,* vol. 21, pp. 643-650, 2005.

[24] T. Almqvist and R. Larsson, "Thermal transient rough EHL line contact simulations by aid of computational fluid dynamics," *Tribology International,* vol. 41, pp. 683-693, 2008.

[25] A. A. Lubrecht, W. E. ten Napel, and R. Bosma, "Multigrid, an alternative method for calculating film thickness and pressure profiles in elastohydrodynamically lubricated line contacts," *Journal of Tribology,* vol. 108, pp. 551-556, 1986.

[26] D. Dowson, "Modelling of elastohydrodynamic lubrication of real solids by real lubricants," *Meccanica,* vol. 33, pp. 47-58, 1998.

[27] C. R. Evans, "Measurement and mapping of the rheological properties of elastohydrodynamic lubricants," PhD thesis, University of Cambridge, 1983.

[28] S. Bair, F. E. Lockwood, W. B. Anderson, Z. Q. Zhang, and D. Dotson, "Measurements of elasticity in multigrade motor oil at elevated pressure," *Tribology Transactions,* vol. 50, pp. 407-414, 2007.

[29] K. L. Johnson and J. L. Tevaarwerk, "Shear behaviour of elastohydrodynamic oil films," *Proceedings of the Royal Society of London. Series A, Mathematical and Physical Sciences,* vol. 356, pp. 215-236, 1977.

[30] H. Eyring, "Viscosity, plasticity, and diffusion as examples of absolute reaction rates " *J. Chem. Phys.,* vol. 4, pp. 1749836-44, 1936.

[31] T. Ree and H. Eyring, "Theory of non-Newtonian flow. I. Solid plastic system,"

Journal of Applied Physics vol. 26, pp. 793 - 800, 1955.

[32] T. Ree and H. Eyring, "Theory of non-Newtonian flow. II. Solution system of high polymers," *Journal of Applied Physics* vol. 26, pp. 800-809, 1955.

[33] K. L. Johnson and J. A. Greenwood, "Thermal analysis of an Eyring fluid in elastohydrodynamic traction," *Wear,* vol. 61, pp. 353-374, 1980.

[34] W. Hirst and A. J. Moore, "Non-Newtonian behaviour in elastohydrodynamic lubrication," *Proceedings of the Royal Society of London. Series A, Mathematical and Physical Sciences,* vol. 337, pp. 101-121, 1974.

[35] H. Liu, K. Mao, C. Zhu, X. Xu, and M. Liu, "Parametric studies of spur gear lubrication performance considering dynamic loads," *Proceedings of the Institution of Mechanical Engineers, Part J: Journal of Engineering Tribology,* May 9, 2012 2012.

[36] Y.-Q. Wang and X.-J. Yi, "Non-Newtonian transient thermoelastohydrodynamic lubrication analysis of an involute spur gear," *Lubrication Science,* vol. 22, pp. 465-478, 2010.

[37] S. Bair, "Rheology and high-pressure models for quantitative elastohydrodynamics," *Proceedings of the Institution of Mechanical Engineers Part J-Journal of Engineering Tribology,* vol. 223, pp. 617-628, 2009.

[38] S. Bair, "A Reynolds-Ellis equation for line contact with shear-thinning," *Tribology International,* vol. 39, pp. 310-316, 2006.

[39] R. C. Bhattacharjee and N. C. Das, "Power law fluid model incorporated into elastohydrodynamic lubrication theory of line contact," *Tribology International,* vol. 29, pp. 405-413, 1996.

[40] H. M. Chu, W. L. Li, and Y. P. Chang, "Thin film elastohydrodynamic lubrication - a power-law fluid model," *Tribology International,* vol. 39, pp. 1474-1481, 2006.

[41] L. M. Chu, W. L. Li, Y. P. Chang, and H. C. Hsu, "EHL of circular contacts lubricating with mixture of two lubricants," *Industrial Lubrication and Tribology,* vol. 62, pp. 83-90, 2010.

[42] P. Yang and X. Liu, "Effects of solid body temperature on the non-Newtonian thermal elastohydrodynamic lubrication behaviour in point contacts," *Proceedings of the Institution of Mechanical Engineers Part J-Journal of Engineering Tribology,* vol. 223, pp. 959-969, 2009.

[43] P. Kumar, P. Anuradha, and M. M. Khonsari, "Some important aspects of thermal elastohydrodynamic lubrication," *Proceedings of the Institution of Mechanical Engineers, Part C: Journal of Mechanical Engineering Science,* vol. 224, pp. 2588-2598, December 1, 2010 2010.

[44] L. Chang and C. Farnum, "A thermal model for elastohydrodynamic lubrication of rough surfaces," *Tribology Transactions,* vol. 35, pp. 281-286, 1992.

[45] L. Chang, "Traction in thermal elastohydrodynamic lubrication of rough surfaces," *Journal of Tribology,* vol. 114, pp. 186-191, 1992.

[46] P. R. Yang, S. Y. Qu, Q. Y. Chang, and F. Guo, "On the theory of thermal elastohydrodynamic lubrication at high slide-roll ratios - Line contact solution," *Journal of Tribology-Transactions of the Asme,* vol. 123, pp. 36-41, 2001.

[47] X. L. Liu and P. R. Yang, "Analysis of the thermal elastohydrodynamic lubrication of a finite line contact," *Tribology International,* vol. 35, pp. 137-144, 2002.

[48] F. Sadeghi and W. D. McClung, "Formulas used in thermal elastohydrodynamic lubrication," *Tribology Transactions,* vol. 34, pp. 588-596, 1991.

[49] F. Sadeghi and P. C. Sui, "Thermal elastohydrodynamic lubrication of rolling/sliding contacts," *Journal of Tribology,* vol. 112, pp. 189-195, 1990.

[50] H. Salehizadeh and N. Saka, "Thermal non-Newtonian elastohydrodynamic

lubrication of rolling line contacts," *Journal of Tribology,* vol. 113, pp. 481-491, 1991.

[51] S. Wang, C. Cusano, and T. F. Conry, "Thermal analysis of elastohydrodynamic lubrication of line contacts using the Ree-Eyring fluid model," *Journal of Tribology,* vol. 113, pp. 232-242, 1991.

[52] H. G. Elrod and D. E. Brewe, "Thermohydrodynamic analysis for laminar lubricating films," NASA Technical Memorandum 888451986.

[53] M. K. Ghosh and R. K. Pandey, "Thermal elastohydrodynamic lubrication of heavily loaded line contacts - An efficient inlet zone analysis," *Journal of Tribology-Transactions of the Asme,* vol. 120, pp. 119-125, 1998.

[54] L. Moraru and T. G. Keith, "Lobatto point quadrature for thermal lubrication problems involving compressible lubricants. EHL applications," *Journal of Tribology-Transactions of the Asme,* vol. 129, pp. 194-198, 2007.

[55] J. A. Greenwood and J. J. Kauzlari, "Inlet shear heating in elastohydrodynamic lubrication," *Journal of Lubrication Technology,* vol. 95, pp. 417-426, 1973.

[56] C. H. Hsu and R. T. Lee, "An efficient algorithm for thermal elastohydrodynamic lubrication under rolling/sliding line contacts," *Journal of Tribology,* vol. 116, pp. 762-769, 1994.

[57] W. R. Chang, I. Etsion, and D. B. Bogy, "An elastic-plastic model for the contact of rough surfaces," *Journal of Tribology,* vol. 109, pp. 257-263, 1987.

[58] K. L. Johnson, J. A. Greenwood, and J. G. Higginson, "The contact of elastic regular wavy surfaces," *International Journal of Mechanical Sciences,* vol. 27, pp. 383-396, 1985.

[59] P. Vergne, B. Villechaise, and D. Berthe, "Elastic behaviour of multiple contacts: asperity interaction," *Journal of Tribology,* vol. 107, pp. 224-228, 1985.

[60] Y. Zhao and L. Chang, "A model of asperity interactions in elastic-plastic

contact of rough surfaces," *Journal of Tribology,* vol. 123, pp. 857-864, 2001.

[61] A. E. H. Love, *A treatise on the mathematical theory of elasticity*: Dover Publications, 1944.

[62] N. Patir and H. S. Cheng, "An average flow model for determining effects of three-dimensional roughness of partial hydrodynamic lubrication," *ASME J. Lubricarion. Technol.,* vol. 100, pp. 12-17, 1978.

[63] D. Zhu, H. S. Cheng, and B. J. Hamrock, "Effect of surface roughness on pressure spike and film constriction in elastohydrodynamically lubricated line contacts," *Tribology Transactions,* vol. 33, pp. 267 - 273, 1990.

[64] D. Zhu and H. S. Cheng, "Effect of surface roughness on the point contact EHL," *Journal of Tribology,* vol. 110, pp. 32-37, 1988.

[65] D. Epstein, T. H. Yu, Q. J. Wang, L. M. Keer, H. S. Cheng, S. Liu, S. J. Harris, and A. Gangopadhyay, "An efficient method of analyzing the effect of roughness on fatigue life in mixed-EHL contact," *Tribology Transactions,* vol. 46, pp. 273-281, 2003.

[66] L. Moraru, T. G. Keith, and A. Kahraman, "Aspects regarding the use of probabilistic models for isothermal full film rough line contacts," *Tribology Transactions,* vol. 47, pp. 386-395, 2004.

[67] K. M. Phipps, "20 minutes with... Dr. Dong Zhu," *Ttribology and lubrication technology,* vol. 63, pp. 14-19, 2007.

[68] D. Dowson and G. R. Higginson, "A theory of involute gear lubrication," in *Proceedings of Institute of Petroleum, Gear Lubrication Symposium*, 1966.

[69] D. Dowson and G. Higginson, *Elastohydrodynamic lubrication*. Oxford: Pergamon Press, 1966.

[70] A. Gu, "Elastohydrodynamic lubrication of involute gears," *ASME Journal of Engineering for Industry,* pp. 1164-1170, 1973.

[71] J. P. Vichard, "Transient effects in the lubrication of hertzian contacts," *ARCHIVE: Journal of Mechanical Engineering Science 1959-1982 (vols 1-23),* vol. 13, pp. 173-189, 1971.

[72] E. J. Wellauer and G. A. Holloway, "Application of EHD oil flm theory to industrial gear drives," *Trans. ASME, J. Engn.for Industry,* vol. 98, pp. 626-634, 1976.

[73] A. Jackson and C. N. Rowe, "Application of EHL Theory to Gear Lubrication," *SAE Paper 800670,* 1980.

[74] K. L. Wang and H. S. Cheng, "Thermal Elastohydrodynamic Lubrication of Spur Gears," NASA CR-3241, Ohio CR-3241, 1980.

[75] M. Sato and S. Takanashi, "Thermo-elastohydrodynamic lubrication of an involute gear," *Tribology International,* vol. 15, pp. 23-30, 1982.

[76] Z. G. Lin and J. B. Medley, "Transient elastohydrodynamic lubrication of involute spur gears under isothermal conditions," *Wear,* vol. 95, pp. 143-163, 1984.

[77] A. K. Tieu and J. Worden, "Paper IX(ii) Transient oil film thickness in gear contacts under dynamic loads," in *Tribology Series*. vol. 11, ed: Elsevier, 1987, pp. 285-290.

[78] S. F. Wu and H. S. Cheng, "A friction model of partial EHL contacts and its applicatioin to power loss in spur gears," *Tribology Transactions,* vol. 34, pp. 398-407, 1991.

[79] D. Y. Hua and M. M. Khonsari, "Application of transient elastohydrodynamic lubrication analysis for gear transmissions," *Tribology Transactions,* vol. 38, pp. 905-913, 1995.

[80] R. Larsson, "Transient non-Newtonian elastohydrodynamic lubrication analysis of an involute spur gear," *Wear,* vol. 207, pp. 67-73, 1997.

[81] W. Scott and D. J. Hargreaves, "Specifying surface roughness for spur and

helical gears," in *Tribology Series*. vol. 34, ed: Elsevier, 1998, pp. 267-274.

[82] A. Mihailidis and K. Panagiotidis, "Transient thermo-elastohydrodynamic lubrication of gear teeth," *Lubrication Science,* vol. 15, pp. 295-310, 2003.

[83] J. Tao, T. G. Hughes, H. P. Evans, and R. W. Snidle, "Elastohydrodynamic lubrication analysis of gear tooth surfaces from micropitting tests," *Journal of Tribology-Transactions of the Asme,* vol. 125, pp. 267-274, 2003.

[84] Y. Wang, H. Li, J. Tong, and P. Yang, "Transient thermoelastohydrodynamic lubrication analysis of an involute spur gear," *Tribology International,* vol. 37, pp. 773-782, 2004.

[85] K. J. Sharif, H. P. Evans, and R. W. Snidle, "Prediction of the wear pattern in worm gears," *Wear,* vol. 261, pp. 666-673, 2006.

[86] P. Kumar, P. K. Saini, and P. Tandon, "Transient elastohydrodynamic lubrication analysis of an involute spur gear using couple-stress fluid," *Proceedings of the Institution of Mechanical Engineers Part J-Journal of Engineering Tribology,* vol. 221, pp. 743-754, 2007.

[87] S. Akbarzadeh and M. M. Khonsari, "Thermoelastohydrodynamic analysis of spur gears with consideration of surface roughness," *Tribology Letters,* vol. 32, pp. 129-141, 2008.

[88] H. P. Evans, R. W. Snidle, and K. J. Sharif, "Deterministic mixed lubrication modelling using roughness measurements in gear applications," *Tribology International,* vol. 42, pp. 1406-1417, 2009.

[89] J. A. Brandão, J. H. O. Seabra, and J. Castro, "Surface initiated tooth flank damage: Part I: Numerical model," *Wear,* vol. 268, pp. 1-12, 2010.

[90] J. A. Brandão, J. H. O. Seabra, and J. Castro, "Surface initiated tooth flank damage. Part II: Prediction of micropitting initiation and mass loss," *Wear,* vol. 268, pp. 13-22, 2010.

[91] S. Li and A. Kahraman, "A transient mixed elastohydrodynamic lubrication model for spur gear pairs," *Journal of Tribology,* vol. 132, pp. 011501-9, 2010.

[92] S. Li and A. Kahraman, "Influence of dynamic behaviour on elastohydrodynamic lubrication of spur gears," *Proceedings of the Institution of Mechanical Engineers, Part J: Journal of Engineering Tribology,* vol. 225, pp. 740-753, August 1, 2011 2011.

[93] P. Anuradha and P. Kumar, "Effect of lubricant selection on EHL performance of involute spur gears," *Tribology International,* vol. 50, pp. 82-90, 2012.

[94] H. P. Evans, R. W. Snidle, K. J. Sharif, and M. J. Bryant, "Predictive modelling of fatigue failure in concentrated lubricated contacts," *Faraday Discussions,* 2012.

[95] H. Liu, K. Mao, C. Zhu, X. Xu, and M. Liu, "Parametric studies of spur gear lubrication performance considering dynamic loads," *Proceedings of the Institution of Mechanical Engineers, Part J: Journal of Engineering Tribology,* vol. 226, pp. 731-737, 2012.

[96] M. N. Webster and R. S. Sayles, "A numerical model for the elastic frictionless contact of real rough surfaces," *Journal of Tribology,* vol. 108, pp. 314-320, 1986.

[97] X. Tian and B. Bhushan, "A numerical three-dimensional model for the contact of rough surfaces by variational principle," *Journal of Tribology,* vol. 118, pp. 33-42, 1996.

[98] C. H. Venner, "Multigrid solution of the EHL line and point contact problems," PhD Thesis, University of Twente, 1991.

[99] O. Reynolds, "On the theory of lubrication and its application to Mr. Beauchamp Tower's experiments, including an experimental determination of the viscosity of olive oil," *Proceedings of the Royal Society of London,* vol. 40, pp. 191-203, January 1, 1886 1886.

[100] C. H. Venner, W. E. ten Napel, and R. Bosma, "Advanced multilevel

solution of the EHL line contact problem," *Journal of Tribology,* vol. 112, pp. 426-431, 1990.

[101] B. J. Hamrock and D. Dowson, "Isothermal elastohydrodynamic lubrication of point contacts. 1. theoretical formulation," *Journal of Lubrication Technology,* vol. 98, pp. 223-229, 1976.

[102] H. Moes, "Discussion on a contribution by K. Jakobson and H. Christensen," *Proc. Inst. Mech. Eng., Part J: J. Eng. Tribol.,* vol. 183, pp. 205–206, 1969.

[103] H. Moes and R. Bosma, "Design charts for optimum bearing configurations—1: The full journal bearing," *ASME Jour. of Lubr. Tech.,* vol. 93, pp. 302-306, 1971.

[104] K. L. Johnson, *Contact mechanics*: Cambridge University Press, 1985.

[105] A. Brandt, "Rigorous local mode analysis of multigrid," in *Pre-lim. Proc. 4th Copper Mountain Conference on MultiGrid Methods*, Copper Mountain, Colorado, 1990.

[106] C. H. Venner, A. A. Lubrecht, and W. E. ten Napel, "Numerical simulation of the overrolling of a surface feature in an EHL line contact," *Journal of Tribology,* vol. 113, pp. 777-783, 1991.

[107] A. Brandt, "Rigorous quantitative analysis of multigrid, I: Constant coefficients two-level cycle with L2--norm," *SIAM Journal on Numerical Analysis,* vol. 31, pp. 1695-1730, 1994.

[108] P. W. Hemker, "On the order of prolongations and restrictions in multigrid procedures," *J. Comput. Appl. Math.,* vol. 32, pp. 423-429, 1990.

[109] A. A. Lubrecht and E. Ioannides, "A fast solution of the dry contact problem and the associated sub-surface stress field, using multilevel techniques," *Journal of Tribology,* vol. 113, pp. 128-133, 1991.

[110] I. A. Polonsky and L. M. Keer, "A numerical method for solving rough contact problems based on the multi-level multi-summation and conjugate gradient techniques," *Wear,* vol. 231, pp. 206-219, 1999.

[111] D. Dowson and G. R. Higginson, *Elasto-hydrodynamic lubrication*. New York: Pergamon Press, 1977.

[112] R. D. Britton, C. D. Elcoate, M. P. Alanou, H. P. Evans, and R. W. Snidle, "Effect of surface finish on gear tooth friction," *Journal of Tribology,* vol. 122, pp. 354-360, 2000.

[113] W. Z. Wang, S. Wang, F. H. Shi, Y. C. Wang, H. B. Chen, H. Wang, and Y. Z. Hu, "Simulations and measurements of sliding friction between rough surfaces in point contacts: From EHL to boundary lubrication," *Journal of Tribology-Transactions of the Asme,* vol. 129, pp. 495-501, 2007.

[114] E. Bou-Chakra, J. Cayer-Barrioz, D. Mazuyer, F. Jarnias, and A. Bouffet, "A non-Newtonian model based on Ree-Eyring theory and surface effect to predict friction in elastohydrodynamic lubrication," *Tribology International,* vol. 43, pp. 1674-1682, 2010.

[115] B. Jacod, C. H. Venner, and P. M. Lugt, "Influence of longitudinal roughness on friction in EHL contacts," *Journal of Tribology,* vol. 126, pp. 473-481, 2004.

[116] L. Chang and W. Zhao, "Fundamental differences between Newtonian and non-Newtonian micro-EHL results," *Journal of Tribology,* vol. 117, pp. 29-35, 1995.

[117] G. E. Morales-Espejel, A. W. Wemekamp, and A. Felix-Quinonez, "Micro-geometry effects on the sliding friction transition in elastohydrodynamic lubrication," *Proceedings of the Institution of Mechanical Engineers Part J-Journal of Engineering Tribology,* vol. 224, pp. 621-637, 2010.

[118] A. V. Olver and H. A. Spikes, "Prediction of traction in elastohydrodynamic

lubrication," *Proceedings of the Institution of Mechanical Engineers Part J-Journal of Engineering Tribology,* vol. 212, pp. 321-332, 1998.

[119] P. Kumar, S. C. Jain, and S. Ray, "Thermal EHL of rough rolling/sliding line contacts using a mixture of two fluids at dynamic loads," *Journal of Tribology-Transactions of the Asme,* vol. 124, pp. 709-715, 2002.

[120] A. Sottomayor, A. Campos, and J. Seabra, "Traction coefficient in a roller inner ring EHD contact in a jet engine roller bearing," *Wear,* vol. 209, pp. 274-283, 1997.

[121] D. Zhu, "A design tool for selection and optimization of surface finish in mixed lubrication," in *Tribology and Interface Engineering Series*. vol. Volume 41, M. P. G. D. D. Dowson and A. A. Lubrecht, Eds., ed: Elsevier, 2003, pp. 703-711.

[122] P. Yang, J. Wang, and M. Kaneta, "Thermal and non-Newtonian numerical analyses for starved EHL line contacts," *Journal of Tribology-Transactions of the Asme,* vol. 128, pp. 282-290, 2006.

[123] X. Liu, J. Cui, and P. Yang, "Size effect on the behaviour of thermal elastohydrodynamic lubrication of roller pairs," *Journal of Tribology,* vol. 134, pp. 011502-10, 2012.

[124] M. Kaneta and P. Yang, "Effects of thermal conductivity of contacting surfaces on point EHL contacts," *Journal of Tribology-Transactions of the Asme,* vol. 125, pp. 731-738, 2003.

[125] P. Yang, Z. M. Jin, F. Liu, and D. Dowson, "On the time-dependent, thermal and non-Newtonian elastohydrodynamic lubrication of line contacts subjected to normal and tangential vibrations," *Proceedings of the Institution of Mechanical Engineers Part J-Journal of Engineering Tribology,* vol. 218, pp. 71-82, 2004.

[126] P. Yang, *Numerical analysis of fluid lubrication (in Chinese)*. Beijing: National Defense Industry Press, 1998.

[127] Q. Liu, "Friction in mixed and elastohydrodynamic lubricated contacts including thermal effects," PhD Thesis, University of Twente, The Netherland, 2002.

[128] S. D. Kermans, "Model ter beschrijving van de wrijving in hoog belaste EHL kontakten," Master Thesis, University of Twente, The Netherlands, 1990.

[129] H. Forsman, P. Andersson, and G. Bäckström, "Thermal conductivity and heat capacity of n-heptane, n- and iso-propyl-alcohol at high pressure," *Physica B+C,* vol. 114, pp. 287-294, 1982.

[130] B. J. Hamrock, B. O. Jacobson, and S. R. Schmid, *Fundamentals of fluid film lubrication*: Marcel Dekker Inc, 2004.

[131] H. Moes, "Optimum similarity analysis with applications to elastohydrodynamic lubrication," *Wear,* vol. 159, pp. 57-66, 1992.

[132] H. N. Ozguven and D. R. Houser, "Mathematical models used in gear dynamics-A review," *Journal of Sound and Vibration,* vol. 121, pp. 383-411, 1988.

[133] J. Wang, R. Li, and X. Peng, "Survey of nonlinear vibration of gear transmission systems," *Applied Mechanics Review* vol. 56, pp. 309-329, 2003.

[134] H. N. Özgüven and D. R. Houser, "Dynamic analysis of high speed gears by using loaded static transmission error," *Journal of Sound and Vibration,* vol. 125, pp. 71-83, 1988.

[135] V. Atanasiu, D. Leohchi, and C. Rozmarin, "Dynamic transmission error prediction of spur gear pairs with friction consideration," in *SYROM 2009, Proceedings of the 10th IFToMM International Symposium on Science of Mechanisms and Machines*, I. Visa, Ed., ed: Springer Netherlands, 2009, pp. 243-252.

[136] D. C. H. Yang and J. Y. Lin, "Hertzian damping, tooth friction and bending elasticity in gear impact dynamics," *Journal of mechanisms, transmissions, and automation in design* vol. 109, pp. 189-196 1987.

[137] X. Tian, "Dynamic simulation for system response of gearbox including localized gear faults," Master's thesis, University of Alberta, Edmonton, Alberta, Canada, 2004.

[138] K. Mao, "Gear tooth contact analysis and its application in the reduction of fatigue wear," *Wear,* vol. 262, pp. 1281-1288, 2007.

[139] K. Mao, "An approach for powertrain gear transmission error prediction using the non-linear finite element method," *Proceedings of the Institution of Mechanical Engineers, Part D: Journal of Automobile Engineering,* vol. 220, pp. 1455-1463, October 1, 2006 2006.

[140] R. G. Parker, S. M. VIJAYAKAR, and T. IMAJO, "Nonlinear dynamic response of a spur gear pair: Modelling and experimental comparisons," *Journal of Sound and Vibration,* vol. 237, pp. 435-455, 2000.

[141] V. K. Tamminana, A. Kahraman, and S. Vijayakar, "A study of the relationship between the dynamic factors and the dynamic transmission error of spur gear pairs," *Journal of Mechanical Design,* vol. 129, pp. 75-84, Jan 2007.

[142] A. A. Lubrecht, C. H. Venner, and F. Colin, "Film thickness calculation in elasto-hydrodynamic lubricated line and elliptical contacts: the Dowson, Higginson, Hamrock contribution," *Proceedings of the Institution of Mechanical Engineers, Part J: Journal of Engineering Tribology,* vol. 223, pp. 511-515, 2009.

[143] P. Pan and B. J. Hamrock, "Simple formulas for performance parameters used in elastohydrodynamically lubricated line contacts," *Journal of Tribology,* vol. 111, pp. 246-251, 1989.

[144] A. Fabre, L. Barrallier, M. Desvignes, H. P. Evans, and M. P. Alanou, "Microgeometrical influences on micropitting fatigue damage: multi-scale analysis," *Proceedings of the Institution of Mechanical Engineers, Part J: Journal of Engineering Tribology,* vol. 225, pp. 1-9, 2011.

[145] A. Kahraman and R. Singh, "Interactions between time-varying mesh stiffness and clearance non-linearities in a geared system," *Journal of Sound and Vibration,* vol. 146, pp. 135-156, 1991.

[146] G. Pharr, W. Oliver, and F. Brotzen, "On the generality of the relationship among contact stiffness, contact area, and elastic modulus during indentation," *Journal of Materials Research,* vol. 7, pp. 613-617, 1992.

[147] U. Rabe, S. Amelio, E. Kester, V. Scherer, S. Hirsekorn, and W. Arnold, "Quantitative determination of contact stiffness using atomic force acoustic microscopy," *Ultrasonics,* vol. 38, pp. 430-437, 2000.

[148] X. Li and B. Bhushan, "A review of nanoindentation continuous stiffness measurement technique and its applications," *Materials Characterization,* vol. 48, pp. 11-36, 2002.

[149] J. Królikowski and J. Szczepek, "Prediction of contact parameters using ultrasonic method," *Wear,* vol. 148, pp. 181-195, 1991.

[150] H. A. Sherif, "Parameters affecting contact stiffness of nominally flat surfaces," *Wear,* vol. 145, pp. 113-121, 1991.

[151] J. Greenwood and J. Williamson, "Contact of nominally flat surfaces," *Proceedings of the Royal Society of London. Series A. Mathematical and Physical Sciences,* vol. 295, pp. 300-319, 1966.

[152] R. A. Onions and J. F. Archard, "The contact of surfaces having a random structure," *Journal of Physics D: Applied Physics,* vol. 6, p. 289, 1973.

[153] R. G. Parker, V. Agashe, and S. M. Vijayakar, "Dynamic response of a planetary gear system using a finite element/contact mechanics model," *Journal of Mechanical Design,* vol. 122, pp. 304-310, Sep 2000.

[154] I. Howard, S. X. Jia, and J. D. Wang, "The dynamic modelling of a spur gear in mesh including friction and a crack," *Mechanical Systems and Signal*

Processing, vol. 15, pp. 831-853, Sep 2001.

[155] T. Kiekbusch, D. Sappok, B. Sauer, and I. Howard, "Calculation of the combined torsional mesh stiffness of spur gears with two- and three-dimensional parametrical FE models," *Strojniski vestnik - Journal of Mechanical Engineering,* vol. 57, pp. 810-818, 2011.

[156] A. Majumdar and B. Bhushan, "Role of fractal geometry in roughness characterization and contact mechnaics of surfaces," *Journal of Tribology,* vol. 112, pp. 205-216, 1990.

[157] G. Lundberg, "Dynamic capacity of rolling bearings," *IVA Handlingar,* vol. 196, 1947.

[158] D. Yang and Z. Sun, "A rotary model of spur gear dynamics," *Journal of mechanisms, transmissions, and automation in design,* vol. 107, pp. 529-535, 1985.

[159] D. C. H. Yang and J. Y. Lin, "Hertzian damping, tooth friction and bending elasticity in gear impact dynamics," *Journal of mechanisms, transmissions, and automation in design,* vol. 109, pp. 189-196, 1987.